UNIVERSITY OF GRANADA
Applied Physics Deparment
Biocolloids and Fluids Physics Group

Interactions, Structure and Kinetic Properties of Colloidal Monolayers

Juan Carlos Fernández Toledano

Ph. Thesis

Editor: Editorial de la Universidad de Granada
Autor: Juan Carlos Fernández Toledano
D.L.: Gr. 292 - 2008
ISBN: 978-84-338-4774-4

Interactions, Structure and Kinetic Properties of Colloidal Monolayers

by

Juan Carlos Fernández Toledano

Licenciado en Física

SUPERVISORS

Dr. D. Arturo Moncho Jordá
Prof. Asociado de Física Aplicada

Dr. D. Francisco Martínez López
Prof. Titular de Física Aplicada

Dr. D. Roque Hidalgo Álvarez
Catedrático de Física Aplicada

A Fernando y Paqui
Mis padres
A los que tando debo

Agradecimientos

En esta memoria se recoge el trabajo realizado en los últimos 5 años en el grupo de Física de Fluidos y Biocoloides del Departamento de Física Aplicada de la Universidad de Granada. Durante este periodo, es mucha la gente que ha jugado un papel importante en el desarrollo de esta tesis tanto en el campo profesional como en el personal. Es por ello que me gustaría aprovechar estas líneas a modo de pequeño homenaje a esas personas.

En primer lugar, me gustaría agradecerle al profesor Roque Hidálgo la confianza depositada en mi desde aquel primer momento en el que atravesé la puerta de su despacho para hablar acerca del trabajo que podría desarrollar en el grupo un recién licenciado en Física. Él me abrió las puertas al mundo de la investigación y desde entonces he recibido su apoyo constante. Por supuesto, no olvido a la persona que me condujo a ese despacho, José Callejas, quien ha sido en todo momento un ejemplo de honradez y humildad, valores cada día más difíciles de encontrar.

Al poco de empezar esta nueva fase de mi vida, dos son las personas que se incorporaron a la formación de este nuevo aprendiz de científico: Arturo Moncho, quien me ensenãría los entresijos más técnicos del trabajo que iba a realizar, como el noble arte de la programación, así como mostró una confianza en mi trabajo que en muchos momentos superó incluso la que yo tenía. La otra persona fue Francisco Martínez, a quien he ido conociendo mejor año tras año. A él debo agradecerle el hacer una profunda revisión de esta memoria, además de haber sido capaz de decirme siempre lo que piensa sin filtros ni maquillaje.

Pero como buen becario, mi corazón estuvo siempre puesto en contacto con aquellos compañeros con los que he compartido este crecimiento como científico, pero sobre todo, como persona. Ellos fueron en muchos aspectos mis verdaderos maestros. Mucho ha llovido desde aquella primera etapa en el famoso despacho 13 (ahora me doy cuenta que esta será una de las

últimas tesis en la que se haga referencia a aquella habitación de la que tantos jóvenes científicos hemos/han surgido). A esta etapa pertenecen gente como Migue al que tanto tengo que agradecer como maestro tanto en lo profesional como en la Filosofía Cotidiana. También Alberto Martín, Catalina, Julia y Ceci con los que tantas cosas he vivido (a veces hasta altas horas de la madrugada), Juanjo, Ana Belén, Pedro Gea, José Manuel, Teresa, Joaquín y Roberto con los que tejimos esa maraña de apoyo mutuo e incondicional que de tantas situaciones nos sacó. Tras ellos vinieron Manolo, Miguel Peláez y Fernando Vereda y ahora las nuevas generaciones a las que toca recoger el relevo científico, Carlos, Miguel, Amelia y César, a los que les deseo lo mejor en este duro camino.

He creido conveniente separar a tres personas del parrafo anterior a las que quiero agradecer especialmente el que hayan estado a mi lado estos años. Sándalo, quizá el espíritu más científico que hasta ahora me he cruzado en mi camino, además de buen amigo, gran conversador y mejor profesor. A Fernando Martínez, compañero y hermano desde mis primeros meses en Granada, hace ya más de 10 años. Juntos hemos aprendido a crecer en todos los aspectos, y no hay palabras que hagan justo reconocimiento a la gratitud que siento que te debo. Finalmente al Moro por entre muchas otras razones, enseñarme a distinguir aquellas cosas que son realmente importantes de las que no son más que meras apariencias que, si no tenemos cuidado, pueden llegar a controlar nuestra vida.

Por supuesto, no puedo olvidar a la familia científica, a mi grupo, del que tanto cariño he recibido y que me han hecho sentir que formaba parte de él en todo momento. Especialmente a Miguel Cabrerizo, Maria José Gálvez, María, Juan Luis y Delfi.

Agradecer también a Emanuela Zaccarelli por la oportunidad de trabajar durante 3 meses en Roma en un campo hasta entonces desconocido para mi, pero que paso a paso me ha ido conquistando. Nunca olvidaré la cálida acogida que ella me brindó, así como aquella introducción que me dio de la Mode Coupling Theory sentados en el bordillo de un escalón en una de esas calurosas tardes de Agosto romana. Grazie mille Emanuella!!!

Fuera ya del ámbito científico, he de agradecer también a los que han sido mi familia granadina, los que me han dado otra vida fuera de la facultad y me eseñaron a valorar la amistad. Especialmente a Alberto y a Nico (no se que hubiera hecho sin ellos), Rocío (gracias por enseñarme que realmente otro mundo es posible), Evangelia (te debo mucho más de lo que nunca te haya dicho).

Finalmente, hay dos personas que han hecho que esto sea posible y son a quienes me gustaría dedicar esta tesis, pues es en gran parte fruto de su esfuerzo y sacrificio: a Fernando y a Paqui, mis padres, de los que tan orgulloso me siento de ser su hijo.

¡¡¡Gracias a todos!!!

Juan Carlos Fernández Toledano

Puertollano, 31 de Diciembre del 2007

Contents

Chapter 1

Introduction

Colloidal dispersions are defined as a substance consisting of particles that, although too tiny to be seen with the unaided eye (typically from 1 nanometre to 10 micrometres), are substantially larger than atoms and ordinary molecules and that are dispersed in a continuous phase (figure 1). Both the dispersed phase and the continuous phase may be solid, liquid, or gas. Examples include suspensions, aerosols, smokes, emulsions, gels, sols, pastes, and foams. Dyes, detergents, polymers, proteins, and many other important substances exhibit colloidal behaviour. Colloidal systems have been important for technological development through all of history, be it in the form of making ceramics, paints, inks or later to make steel.

The researcher who coined the word *colloid* was Thomas Graham who in 1861 studied solutions and classified them in two categories: the solutions that can pass through a semi–permeable membrane and the solutions that cannot. He called colloid the second ones (from the Greek $\kappa o \lambda \lambda \alpha$ that means glue).

Important experiments before Graham were also performed by Faraday (1791-1867) on gold sols which he flocculated by adding salt. Without salt however, they showed a quite stable behavior; several of Faraday's gold sols are still on display in the British museum. Faraday also discovered that small particles could be detected by focusing light into a conical region.

In 1827 the botanist Robert Brown studied the thermal motion of pollen grains using a microscope. Contrary to others who had tried to explain this erratic motion before him, he concluded by studying a range of finely divided substances that this motion had nothing to do with life or "life force".

In 1905 (the *annus mirabilis*), Einstein published three great papers. The

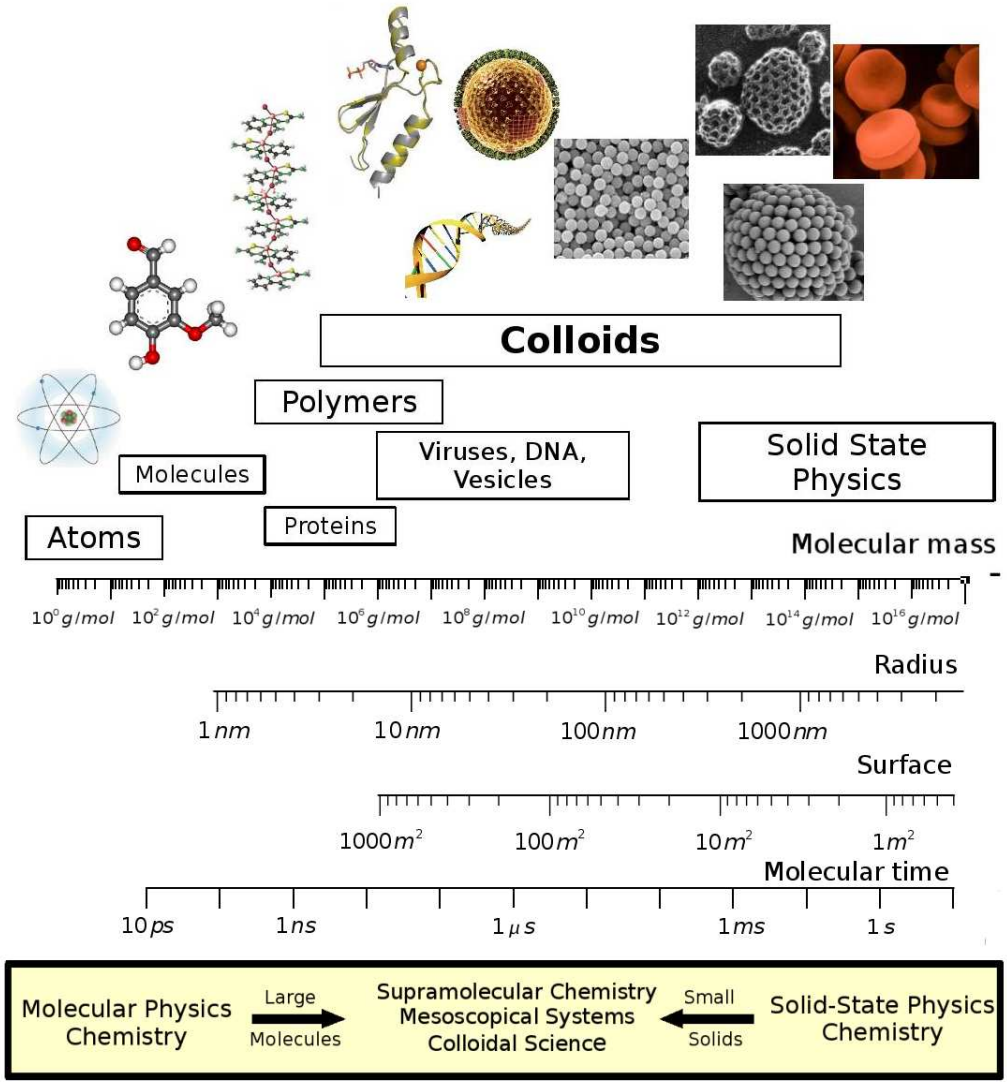

Figure 1.1: Colloids and their typical dimensions.

paper on relativity, the photoelectric effect and a third one where he examined the possibility that molecular motions could explain Brownian motion. One must remember that in 1905 many scientists did not believe in the existence of atoms. Einstein carried out a statistical analysis of molecular motion and its effect on particles suspended in a liquid. From this analysis he calculated the mean square displacement of these particles. As he says in ref [1]

"If the movement discussed here can actually be observed (together with the laws relating to it that one would expect to find), then classical thermodynamics can no longer be looked upon as applicable with precision to bodies even of dimensions distinguishable in a microscope; an exact determination of actual atomic dimensions is then possible. On the other hand, had the prediction of this movement proved to be incorrect, a weighty argument would be provided against the molecular-kinetic conception of heat"

In 1910 Perrin used the Einstein's results to experimentally determine the *Avogadro's number* by analyzing the diffusive motion observed through a microscope of a model dispersion of a monodisperse colloidal spheres [2]. He determined Avogadro's number from looking at how particles were distributed vertically when placed in colloidal suspensions. He prepared tiny spheres of gamboge, a resin, all of uniform size and density. He measured how the particles were distributed vertically when placed in water; calculating what forces would have to be in place to account for this keeping the particles suspended, he could calculate their average kinetic energy. If we know the mass and velocities, we can then determine the mass of a molecule of the fluid, and hence Avogadro's number, which is the molecular weight divided by the mass of a single molecule. Due to this and other experiments, he won the Nobel prize in Physics in 1926. His work contributed to put a definitive end to the controversy about the existence of molecules.

It took until after the development of Quantum Mechanics in the 1940's before the first general description of the interaction forces between two colloidal particles was given. This theory was developed independently by Derjaguin and Landau [3] and by Verwey and Overbeek [4] . This so–called DLVO theory describes the interactions between identical particles as the result of attractive Van der Waals forces and electrostatic repulsive forces produced by the charges residing on the particles surfaces. This potential is still a cornerstone of colloid science.

The formation of colloidal monolayers (colloidal particles which movement is restricted to a plane) is especially interesting due to the ability of colloidal particles to influence the stability of emulsions, foams and interfacial properties. Particularly, the study of aggregation in colloidal systems confined in two dimensions has drawn wide attention. The structure of the clusters and the kinetic properties of the coagulation process have been investigated by means of both, experiments and simulations [5, 6, 7, 8].

Theoretically, the success of techniques for treating phase transition phenomena has motivated the application of these idea for the analysis of some magnitudes in aggregating systems at long times, as the cluster–size distribution, to explain their power law behavior [9](*scaling properties*). The results showed that the morphology of colloidal clusters is fractal scale–invariant, and it is related to the time evolution of the cluster–size distribution.

Some years ago, other interesting aspects of colloidal coagulation have been studied in dense colloidal suspensions in two and three dimensions: the inter–cluster spatial [10, 11, 12, 13, 14, 15] and topological ordering [16, 17, 18]. These recent pictures complement the ones given by the kinetics and fractal growth description, and provide information about the organization of the colloidal clusters in the space. The topological properties have been found to reach a final stationary value in an aggregating system. This facts implies that the aggregation induces structuring not only inside the fractal clusters, but also in the the inter–cluster correlations. Therefore, the topological aspects have to be included in order to have a self–consistent theory of the aggregation phenomenon.

The aim of this work is to study the structural and kinetic properties of colloidal monolayers and their relationship with the interparticle interaction potential and with a possible external force. The main questions that we want to answer here correspond on each one of the chapters of this thesis:

1.- In **chapter 2** we present briefly the main theoretical aspects of the colloidal monolayers that are going to be useful in the develop of this thesis. The questions analysed here are:

   i.- ***How is the movement of the colloidal particles at the monolayers?*** We introduce the *Langevin* and the *Fokker–Planck equations* in order to describe the *Brownian motion* of the particles.

   ii.- When the particles coagulate between them, ***how is the structure of the resulting clusters?*** We will introduce the concept of

fractality.

iii.- After that, the following question is: ***how are the dynamics of the growing clusters and how that dynamics are affected by the interaction between the particles?*** To answer this question we introduce the *Smoluchowski equation*, that depends on the so–called *aggregation kernels* and we see the relationship between such kernels and the interaction potential.

2.- In **chapter 3** we answer the question: ***how is the interaction potential between colloidal particles trapped at a polar–non/polar interface?***. First, we present the typical model for colloids trapped at an interface (due to the surface tension) and how use the interaction potential between infinite half space to calculate the interaction between spheres through the *Derjaguin approximation*. After that, we comment on the different terms of the interaction potential:

i.- ***DLVO theory***: we introduce the electrostatic repulsion and the London–van der Waals attraction which are able to explain the presence of a primary minimum in the total interaction potential.

ii.- ***Non DLVO interactions***: the impossibility to explain some of the experimental results make necessary to introduce other interaction terms:

a.- ***Hydrophobic interaction***: it is due to the interaction of the colloidal particles with the surrounding molecules of fluid.

b.- ***Dipolar and monopolar potentials***: these are characteristic interactions between particles trapped at a polar–non polar interface induced by the presence of dipoles (even monopoles) in the non–polar phase. It was necessary to introduce them in order to explain the great stability of the colloids at interfaces in comparison with the three–dimensional case.

c.- ***Capillary interaction***: this interaction is the result of the distortion of the interface where the colloidal particles are trapped. The capillary interaction can be classified in two different categories: *flotation capillary forces*, when the interface deformation is provoked by the weight of the particles (and its considerate negligible for particles with radius $< 5\mu m$); and *immersion capillary forces*, when the deformation is due to the wetting properties

of the particle surface. This last interaction can be important in certain cases for the colloidal stability.

3.- In **chapter 4** we show the main mathematical tools used to study the aggregation process from a topological point of view. We define the *Voronoi diagram* which is used to describe a set of points over the planes (that, in our case, represents the mass center of our clusters) as a tessellation of the plane. Each cluster is represented by a cell which main properties (number of sides and area) are directly related with the properties of the aggregation process.

4.- In **chapter 5**, we use the Voronoi diagrams in order to study the topological properties of a system of colloidal clusters in two–dimensional DLCA simulations. Moreover, with the Voronoi diagrams is also possible to observe how the aggregation process tends to order the clusters and how this ordering increases with the surface packing fraction.

5.- In **chapter 6**, we study the influence of the interaction range of the repulsive interaction on the colloidal aggregation process. The particles are assumed to interact through a *Yukawa potential*. Three different kinetic region can be observed in the aggregation process depending on the parameters used on the Yukawa interaction. Moreover, we develop a new method to obtain the kinetic rate constants directly from the simulations. Using this kernel in the Smoluchowski equation, we are able to reproduce the simulated cluster size distribution.

6.- In **chapter 7** we show an experimental study of the formation of a loosely bound, internally ordered structures (usually called *mesostructures*) which have been tried to be explained in base of an unknown long–range attractive interaction. We see that the formation of such mesostructures is related to the presence of an oily contamination at the interface. The experiments show that mesostructures can be formed even with very small amounts of contaminant agent (silicon oil). Moreover, we present a simple model, based on oil droplets dispersed at an air–water interface, in order to explain the formation of such mesostructures. Finally, we show some *Monte Carlo simulation* of this model that can reproduce some of the colloidal mesostructures obtained in our experiments.

7.- In the **chapter 9** we extract the main conclusions of this thesis.

Chapter 2

Basic properties of the colloidal monolayers

2.1 Brownian motion of the colloidal particles

Many real-world phenomena which take place over time are not "deterministic". This means that even if we know exactly what has happened up to the present, we can't tell exactly what will happen next. The reason for this: *complexity* and *intrinsic indeterminability* is that there are so many factors involved that we can't effectively make an exact calculation. For example, if we drop a bucket of marbles into a bathtub, it is simply impossible to determine exactly where each marble will be after, say, a minute (actually, even after a much shorter time). Examples of "intrinsic indeterminability" come from Quantum Mechanics, where we simply can not know enough, even in the present, to make exact descriptions of submicroscopic events.

When we have non-deterministic phenomena, scientists and mathematicians are forced to describe their behavior not with certainly but only with likelihood, i.e. by giving probabilities. Non-deterministic phenomena described in this way are sometimes called stochastic processes.

In the early 19th century, the botanist Robert Brown observed strange random motion of microscopic pollen grains in water. They zig-zagged back and forth, almost as if they were alive. He described these movements carefully, but couldn't explain them. Nobody could until 1905 when Albert Einstein suggested that the motion was caused by hundreds-of-thousands of

invisible collisions between water molecules (too small to be seen, even in a microscope) and the tiny pollen grains. The water molecules themselves moved randomly, but at any given time, following the laws of probability, somewhat more in one direction hit the pollen than in other directions – the favored direction itself shifting randomly. Einstein's explanation described the *Brownian motion* perfectly, and was one of the first corroborations of the actual existence of atoms and molecules.

Brownian motion is a *Markov process*: the motion of a pollen grain is determined by a shifting imbalance in the forces of random collisions. Its direction and magnitude depend only on current collisions, not on those which happened in the past.

A refinement of Einstein's calculations was made by the physicist Paul Langevin. He gave the force on a *Brownian particle* as a sum of a **large external force** (gravity, magnetism or other attractive or repulsive deterministic forces), a **viscous force** (caused by friction between the particles) and a **random "noise"** (the unpredictable collisions with water molecules). Langevin's equation could theoretically predict, in a statistical sense, the likely position of a particle subject to these conditions. A modern computer can simulate these forces, hence simulate Brownian motion. Note that Langevin's equation describes the total force on a particle. Calculus, combined with **Newton's Laws of Motion** enables us to translate this force description into a formula for position in terms of time.

Many properties of colloidal monolayers are determined by the fact that the particles perform Brownian motion. Indeed, the colloidal size range (1 - 1000 nm) is defined such that the random displacements of the particles are significantly smaller than those of solvent molecules, but still large enough to affect suspension behavior on time scales of interest to humans.

In this section we describe Brownian motion which is based on the microscopic dynamics of a system composed of colloidal particles and solvent molecules. A full statistical mechanical description of this system would start with the *Liouville equation*. The solvent molecules are smaller than colloidal particles and they move on a smaller time scale. The characteristic time for colloids is 10^{-9} s and for molecules of water it is experimentally known to be around 10^{-14} s. Therefore, the positions and momenta of the solvent molecules can be integrated out. This results in a **Fokker-Planck equation** for the momenta and positions of the colloidal particles. In the Fokker-Planck time scale, the solvent molecules only cause small, rapidly fluctuating forces on the colloids by colliding with them.

2.1.1 The Langevin equation

Consider a colloidal particle with position coordinate $\vec{r}$, momentum $\vec{p}$, and mass m. A model that describe the motion of a particle assumes that the action of a net force, $\vec{f}_{net} = d\vec{p}/dt$, on a particle is the result of the sum of a systematic frictional force, $-(\gamma/m)\vec{p}$ (where γ is he friction coefficient) and a rapidly fluctuating force $\vec{f}(t)$. This model is the well-known *Langevin equation* [19, 20]:

$$\frac{d\vec{p}}{dt} = -\frac{\gamma}{m}\vec{p} + \vec{f}(t) \tag{2.1}$$

For a sphere of radius a, $\gamma = 6\pi\eta_0 a$ where η_0 is the viscosity of the fluid. The random force $\vec{f}(t)$ can only be prescribed in statistical sense and its average vanishes:

$$< \vec{f}(t) >= 0 \tag{2.2}$$

Since the random force fluctuates on a time scale much shorter than the time scale on which the Brownian particle moves it is usually assumed that its autocorrelation function vanishes identically, except at a time delay of zero, i. e. :

$$< \vec{f}(t)\vec{f}(t') >= \hat{G}\delta(t - t') \tag{2.3}$$

Here, δ is the Dirac delta function, and $\hat{G}$ a d–dimensional matrix.

The Langevin equation 2.1 is an Stochastic equation in the sense that it doesn't have a deterministic solution. The integration of this equation yield to:

$$\vec{p}(t) = \vec{p}(0)e^{-\gamma t/m} + \int_0^t d\tau \vec{f}(\tau)e^{-\gamma(t-\tau)/m} \tag{2.4}$$

In order to calculate the average time that the particle takes to change its momentum we can calculate the average of the momentum at time t:

$$\begin{aligned} < \vec{p}(t)\vec{p}(t) >= \vec{p}(0)\vec{p}(0)e^{-2\gamma t/m} \\ + \int_0^t d\tau < \vec{p}(0)\vec{f}(\tau) + \vec{p}(\tau)\vec{f}(0) > e^{-\gamma(2t-\tau)/m} \\ + \int_0^t d\tau_1 \int_0^t d\tau_2 < \vec{f}(\tau_1)\vec{f}(\tau_2) > e^{-\gamma(2t-\tau_1-\tau_2)/m} \end{aligned} \tag{2.5}$$

Using 2.2 and 2.3 we find:

$$< \vec{p}(t)\vec{p}(t) >= \vec{p}(0)\vec{p}(0)e^{-\gamma t/m} + \frac{\hat{G}m}{2\gamma}\left(1 - e^{-2\gamma t/m}\right) \tag{2.6}$$

In the long time limit the momenta must relax to those of an equilibrium system, given by the equipartition theorem:

$$\frac{<\vec{p}\vec{p}>}{2m} = \frac{1}{2}k_BT\hat{I} \quad \text{for } t >> \tau_{Br} \tag{2.7}$$

where $\hat{I}$ is the identity matrix, $\tau_{Br} = m/\gamma$ is the relaxation time[1] and k_B is the Boltzmann constant. Therefore, we find that:

$$\hat{G} = 2\gamma k_BT\hat{I} \tag{2.8}$$

The mean square displacement of the colloidal particles due to the collision with the molecules of the fluid can be calculated by integration of the Langevin equation 2.1:

$$\begin{aligned} \vec{r}(t) &= \int_0^t d\tau \frac{\vec{p}(\tau)}{m} \\ \Delta\vec{r}(t) &= \vec{r}(t) - \vec{r}(0) \\ &= \frac{\vec{p}(0)}{\gamma}\left(1 - e^{-\gamma t/m}\right) + \frac{1}{\gamma}\int_0^t d\tau \vec{f}(\tau)\left(1 - e^{-\gamma(t-\tau)/m}\right) \end{aligned} \tag{2.9}$$

Thus, the mean square displacement can be calculated using 2.2, 2.3 and 2.8:

$$\begin{aligned} <\Delta\vec{r}(t)\Delta\vec{r}(t)> &= \frac{\vec{p}(0)\vec{p}(0)}{\gamma^2}\left(1 - e^{-\gamma t/m}\right)^2 \\ &+ \frac{2mk_BT}{\gamma^2}\hat{I}\left(\frac{\gamma t}{m} + \frac{1}{2}\left[1 - e^{-2\gamma t/m}\right] - 2\left[1 - e^{-\gamma t/m}\right]\right) \end{aligned} \tag{2.10}$$

Thus, on a time scale much longer than the Brownian time ($t >> \tau_{Br}$), it is immediately shown that the particle moves diffusively:

$$<\Delta\vec{r}(t)\Delta\vec{r}(t)>^{=} \hat{I}\frac{2k_BT}{\gamma}t = \hat{I}2D_0t \tag{2.11}$$

where D_0 is the diffusion coefficient that can be written as

$$D_0 = \frac{k_BT}{\gamma} = \frac{k_BT}{6\pi\eta_0 a} \tag{2.12}$$

[1]The Brownian time which typically for colloidal particles is $\sim 10^{-9}$s

which is the Einstein relation.

We can estimate the Brownian length as the typical distance a particle moves in a time τ_{Br}. From equation 2.4 we obtain:

$$< \vec{p}(t) >= \vec{p}(0)e^{-\gamma t/m} \tag{2.13}$$

which could be integrated in order to calculate the Brownian length $l_{Br} = |\vec{p}(0)|/\gamma$, where $\vec{p}(0)$ can be calculated through the energy equipartition theorem 2.7:

$$l_{Br} \approx \frac{\sqrt{2mk_BT}}{\gamma} \tag{2.14}$$

This can be estimated to be around $\sim 10^{-10}$ m for typical values of the parameters. It is clear that this is a small fraction of the typical particle radius.

For processes in which a significant displacement of the colloidal particle is important a statistical description on the Brownian time scale, and its associated Brownian length scale, is sufficient as solvent molecules can be taken into account in an average sense by means of a fluctuating force. Since this is always the case for our study of colloidal particles we will only need to describe their dynamics using their position coordinates.

2.1.2 The Fokker-Planck equation

Considering the impracticability of describing in detail the motion of individual colloidal particles, it is useful to have equations for the distribution of such Brownian particles as a function of the position and time, $P(\vec{r}, t)$, which represents the probability to find a particle in a position $\vec{r}$ at time t. The Fokker-Planck equation[2] describes the time evolution of such probability density function.

If we restrict to the diffusive regime, the movement of the particle is determined by its position on the space $\vec{r}$ which is a stochastic variable. In this case, it can be demonstrated that the Fokker–Planck equation for the distribution function $P(\vec{r}, t)$ is [21]:

$$\frac{\partial P(\vec{r}, t)}{\partial t} = D_0 \nabla^2_{\vec{r}} P(\vec{r}, t) \tag{2.15}$$

[2] Also known as the *Kolmogorov Forward equation*

with the boundary conditions that at time $t = 0$ the particle is in the position $\vec{r}_0$:

$$P(\vec{r}, t = 0) = \delta(\vec{r} - \vec{r}_0) \tag{2.16}$$

It can be shown that the solution of the diffusive Fokker–Planck equation in a d–dimensional space with this boundary condition is the Gaussian distribution:

$$P(\vec{r}, t) = \frac{1}{(4\pi D_0 t)^{d/2}} e^{-|\vec{r}-\vec{r}_0|/(4D_0 t)} \tag{2.17}$$

If the colloidal particles interact among them through a interaction potential, or/and there is a deterministic external force (like a gravitational, electrostatic or magnetic force, for example), this force can be introduced in the Fokker–Planck equation as:

$$\frac{\partial P(\vec{r}, t)}{\partial t} = D_0 \nabla^2_{\vec{r}} P(\vec{r}, t) + \frac{1}{\gamma} \vec{F} \cdot \nabla_{\vec{r}} P(\vec{r}, t) \tag{2.18}$$

The solution of this differential equation, with the same boundary condition as in the case of absence of deterministic forces 2.16 yields:

$$P(\vec{r}, t) = \frac{1}{(4\pi D_0 t)^{d/2}} e^{-|\vec{r}-\vec{r}_0-\vec{F}t/\gamma|/(4D_0 t)} \tag{2.19}$$

Hence, the presence of a deterministic force acting on the particles provokes that the function distribution is not centered in the initial position of the particle, $\vec{r}_0$, but is displaced to $\vec{r}_0 + \vec{F}t/\gamma$.

In the next chapter we will study some of such deterministic forces whose origin is the pairwise interaction potential between the colloidal particles.

2.2 Fractal structure of the aggregates

The destabilization of a suspension of colloidal particles leads them to the formation of bigger units, which range from loose flocs at low solid contents to percolating particle networks at high solid contents. At low solid contents, the flocs are fractal objects, which the fractal dimension depends on the interaction potential, i.e. on the *sticking probability* between particles. In the so–called "fast" aggregation, where any two touching particles become bonded, the structure is open and has a low fractal dimension ($d_f \approx 1.44$ for a two–dimensional system). In contrast, for "slow" aggregating systems,

with sticking probability lower than 1, the particles can penetrate deeper into the already existing clusters leading to denser systems with relatively high fractal dimension ($d_f \approx 1.55$).

2.2.1 Fractals

The fractals are rough at every point, i. e., they are fractured at every point. This characteristics led Mandelbrot [22] to call them fractals (from the Latin: fractus). Some examples of well–known fractals are pictured in figures 2.1 and 2.2. Fractals are best constructed in a recursive way. Thus, for example, the Koch curve (figure 2.1) is constructed by starting with a unit segment. The middle third section of this segment is erased and replaced by two other segments of equal length 1/3. Next, the same procedure is repeated for each of the four resulting segments (of length 1/3). The process is iterated "ad infinitum". The limiting curve is of infinite length, yet it is confined to a finite region of the plane. The best way to characterize it is by using its Hausdorff–Besicovitch or *fractal dimension*, d_f. In a Koch curve magnified by a factor of three there are exactly four of the original curves. Therefore its fractal dimension is given by $3^{d_f} = 4$, or $d_f = \ln 4/\ln 3 = 1.262$.

The Sierpinski triangle of figure 2.2-a is constructed from an equilateral triangle, subdividing it into four smaller triangles and taking out the central triangle. This generator is iterated "ad infinitum". The resulting Sierpinski gasket has a fractal dimension given by $2^{d_f} = 3$ or $d_f = \ln 3/\ln 2 = 1.585$. Another famous example of a fractal is the Sierpinski's sponge (figure 2.2-b). It is constructed by starting from a cube, subdividing it into 3x3x3 = 27 smaller cubes, and taking out the central small cube and its six nearest neighbors. Each of the remaining 20 small cubes is processed in the same way, and the whole procedure is iterated "ad infinitum". After each iteration, the volume of the sponge is reduced by a factor of 20/27, while the total surface area increases. In the limit of the fractal sponge, the surface area is infinite, while the volume vanishes. This is consistent with the fractal dimension of the Sierpinski's sponge, which is given by $3^{d_f} = 20$, or $d_f = \ln 20/\ln 3 = 2.727$.

All of the above examples of fractals are deterministic fractals. That means they are constructed by a rigorous deterministic recursive law. This deterministic fractals are usually called self–similar fractals as one part of them is equivalent to the whole. However, in the nature there are many other objects that have the self–similarity property characteristic of fractals, but only in a statistical sense. It was first realized by Mandelbrot [22] that

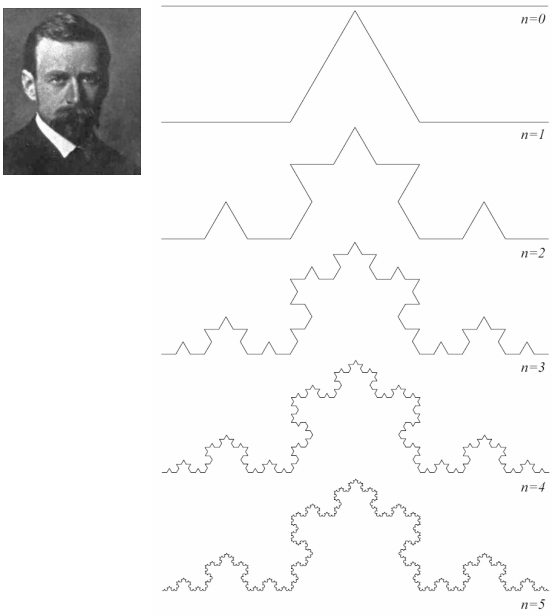

Figure 2.1: The construction of the Koch curve. The photograph corresponds to Helge von Koch.

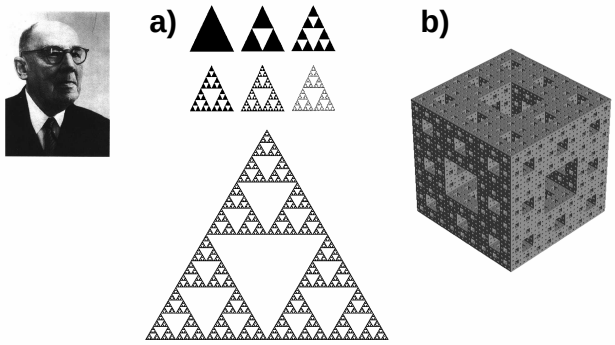

Figure 2.2: The most famous fractals of Sierpinski (in the photograph). *a*) The construction of the Sierpinski's triangle. *b*) The Sierpinski's sponge.

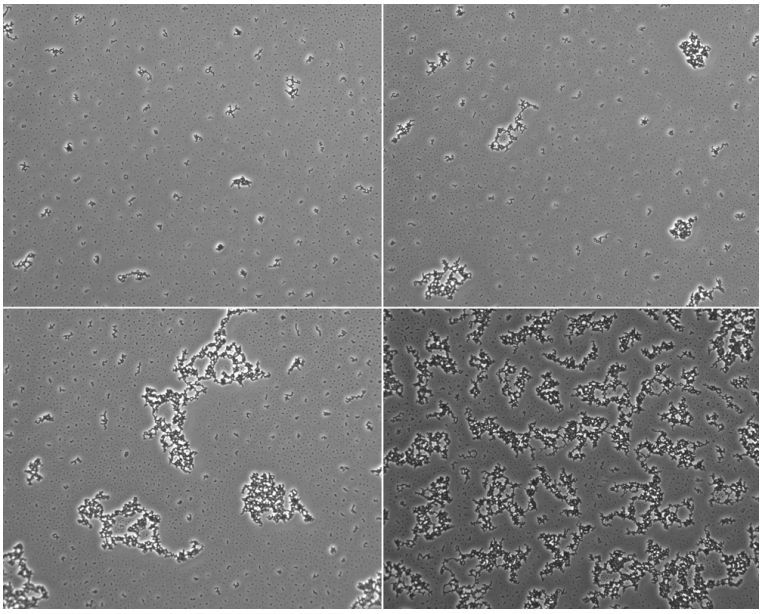

Figure 2.3: Examples of polystyrene aggregates at the air–water interface

many objects in nature are of a statistical–fractal shape. These range from polymers and coastlines to clouds and the pockmarked surface of the Moon.

A number of fractal models have been applied to physical problems: diffusion–limited aggregation [23] has been used as a model for real aggregates, dielectric breakdown, growth processes, viscous fingering, percolation theory, etc. This is also the case of the clusters formed by coagulation of spheres of polystyrene (see figure 2.3). The observations that the structure of clusters formed during an aggregation process exhibit fractal behavior, at least within certain length scales, has substantially simplified the description of the cluster geometry. It should be pointed out that clusters made of spherical primary particles are not fractal objects in the mathematical sense. This is because fractals are defined as a mathematical limit, and for natural fractals the self similarity property holds only over a limited range of sizes. In general, the self similarity property can be observed only for clusters containing a large number of primary particles. Furthermore, clusters are self similar only in a statistical sense, i.e. each individual cluster is not strictly self similar, but if one considers the average over clusters with the same mass, the self similarity holds true. For fractal clusters a fractal dimension d_f can be easily defined by the scaling of the cluster size i with its cluster radius of

gyration (R_g) defined as

$$R_g^2(i) = \left\langle \frac{1}{i} \sum_{k=1}^{i} \left[(\vec{r}_k - \vec{r}_{cm})^2 \right] \right\rangle \tag{2.20}$$

where $\vec{r}_k$ denotes the position of each particles in a cluster of size i and $\vec{r}_{cm}$ indicates the position of the center of mass of the cluster

$$\vec{r}_{cm} = \frac{1}{i} \sum_{j=1}^{i} \vec{r}_j \tag{2.21}$$

Computer simulations [24, 25] and experiments [26], indicate that the radius of gyration of fractal clusters is related with the cluster size i by

$$R_g(i) \sim i^{1/d_f} \tag{2.22}$$

where d_f is the fractal dimension.

The fractal dimension characterizes the inner structure of the cluster and it depends on both the clusters diffusion and the cluster–cluster interaction. Aggregation limited by the diffusion of the particles (DLCA) leads to more open structures ($d_f \approx 1.44$ for 2D–DLCA) than in the case of short–range likely repulsion ($d_f \approx 1.55$ in RLCA regime) [27]. For RLCA regime, clusters require multiple collisions between them before coagulation. Therefore, a higher interpenetration between clusters can occurs. This fact explains the formation of more compact aggregates under RLCA regime in comparison with those formed under DLCA regime.

2.3 Kinetic properties of the aggregation

2.3.1 Introduction

The groundwork for our present understanding of the process of particle aggregation is the result of the work published in 1916 by *von Smoluchowski* [28]. The *Smoluchowski equation* describes the kinetic aggregation in terms of the *reaction probability* (kernel k_{ij}) between clusters of sizes i and j (aggregates composed by i and j monomers, respectively). The physics of the coagulation process is embodied in this reaction probability, which depends

on the nature of the relative motion between the aggregates as well as the details of the pairwise interaction potential among the clusters.

In the last decade, both theory and experiment have shown the existence of two universal behaviors, independent of the particle nature, called *Diffusion–Limited Cluster Aggregation* (DLCA) and *Reaction–Limited Cluster Aggregation* (RLCA). The better known aggregation kinetic corresponds to the DLCA regime [29]. In this case, colloidal particles freely move by Brownian diffusion (without interparticle interactions) and they become irreversibly stuck after a collision. The kinetics properties of this aggregation process have been described using the Brownian kernel [30].

Another well known aggregation regime corresponds which colloidal particles that experiment short–range interparticle repulsions. These repulsions provoke a decrease of the aggregation rate. When the potential barrier is short–ranged (compared to the particle radius), the interaction between the particles can be approximated by a sticking probability defined as the fraction of collisions that effectively leads to the formation of new bonds. This is usually called Reaction-Limited Cluster Aggregation (RLCA) regime [31, 25].

When the range of the repulsive interactions is not negligible, the aggregation process cannot be modelled in terms of the sticking probability. In this case, it is necessary to include the effect of the interaction range in the kinetic model in order to describe properly the kinetics of the aggregation process.

2.3.2 Smoluchowski equation

The kinetic of an irreversible aggregation can be described as the pair reaction between aggregates composed by i–mers with aggregates of j–mers to form aggregates of size $i + j$. In a mean–field theory approach, one write down rate equations for this process, assuming that

$$A_i + A_j \xrightarrow{k_{ij}} A_{i+j} \tag{2.23}$$

where k_{ij} are the aggregation rates or kernel at which the aggregation process takes place. We denote by $c_i(t)$ the concentration of aggregates A_i at time t. The time evolution of the cluster size distribution is described by the Smoluchowski equation [28]

$$\frac{\partial c_k(t)}{\partial t} = \frac{1}{2} \sum_{i+j=k} k_{ij} c_i(t) c_j(t) - c_k(t) \sum_{i=1}^{\infty} k_{ik} c_i(t) \tag{2.24}$$

The aggregation kernel is directly related to the "*average life time*" $< t_{ij} >$, which represents the mean time used by aggregates of sizes i and j to diffuse and coagulate:

$$k_{ij} \sim \frac{1}{< t_{ij} >} \tag{2.25}$$

For certain aggregation kernels analytical as well as scaling solutions of equation 2.24 are available [30, 32]. However, in the general case only numerical solutions can be obtained.

The derivation of 2.24 involved certain hypotheses

1.- It considers only **binary collisions**.

2.- **The aggregation is irreversible**, i.e., the possibility of fragmentation and rearrangement of the particles in the aggregate is not taken into account.

3.- **The effect of the cluster morphology on the aggregation rates is taking into account implicitly in the expression for the kinetic rate constants, k_{ij}.**

4.- It assumes that **there is not spacial correlations** between the clusters. This is a good approximation when the transport mechanisms responsible for bringing the clusters to react are significantly faster than the reaction step.

Smoluchowski equation is a *mean–rate description* that predicts the evolution of the mass spectrum of a collection of particles due to successive mergers. It is widely used for modelling growth in many fields of science. Examples include planetesimals accumulation, mergers in dense clusters of stars, coalescence of interstellar dust grains, galaxy mergers in astrophysics, aerosol coalescence in atmospheric physics, colloids, and polymerization and gelation [33, 34, 35]. The first term of eq. 2.24 accounts for the creations of $k-$mers through collision of $j-$mers and $(k-j)$-mers and the second term represents the annihilation of $k-$mers due to a coagulation with other clusters.

A more general and realistic description of the aggregation process should include the possibility that the aggregates could break into smaller pieces or rearrangement. This is the well–known *reversible aggregation process*, which has been the subject of extensive theoretical and computational work [36, 37].

However, the experimental results for two–dimensional coagulation processes showed than the bonds formed by aggregation use to be so rigid that don't allow the rearrangement or the clusters break. Therefore, we only consider irreversible aggregation in this work.

The most important quantity that characterizes the kinetic properties of a coagulating system is the cluster size distribution $n_i(t) = c_i(t) \cdot S$, defined as the number of clusters containing i monomers at time t within the system with a total area S. The time evolution of the aggregation process is featured in global terms using the *number–average cluster size* $S_n(t)$ given by [38]:

$$S_n(t) = \frac{\sum_{i=1}^{\infty} i n_i(t)}{\sum_{i=1}^{\infty} n_i(t)} \tag{2.26}$$

Analogously, the *weight–average cluster size* is defined as

$$S_w(t) = \frac{\sum_{i=1}^{\infty} i^2 n_i(t)}{\sum_{i=1}^{\infty} i n_i(t)} \tag{2.27}$$

2.3.3 Scaling hypothesis

For long aggregation times, it has been demonstrated both by experiment and simulations that the weight–average cluster size develops a power-law behavior for long times

$$S_w(t) \sim t^z \tag{2.28}$$

where z is the so–called *kinetic exponent*.

It has been demonstrated also that if the function $S_w(t)^2 n_i(t)$ is plotted again the normalized cluster size, $i/S_w(t)$, all the curves scale into a single time–independent master curve $\Psi(i/S_w(t)) = S_w(t)^2 n_i(t)$. The shape of this master curve depends on the aggregation regime [39, 40].

Most kernels used in the literature are homogeneous functions of i and j. According to van Dongen and Ernst [41], this kind of kernels are characterized by two exponents, λ and μ, which are defined as:

$$\begin{array}{ll} k_{ai,aj} = a^{\lambda} k_{ij} & i, j >> 1 \\ k_{ij} \sim i^{\mu} j^{\lambda-\mu} & j >> i \end{array} \tag{2.29}$$

where a is a large positive constant. For $\lambda < 1$, the exponents z and λ are related by

$$z = 1/(1-\lambda) \tag{2.30}$$

2.3.4 Aggregation regimes

Brownian kernel

One of the most studied aggregation regimes is the *Diffusion–Limited Cluster Aggregation* (DLCA [42]), which can be considered a reference process because of its simplicity. In this regime, colloidal particles freely move by Brownian diffusion (without interparticle interactions) and they become irreversibly stuck after collision. Therefore, the aggregation process is totally determined by the time involved in the diffusion of the clusters before they collide to form a new larger cluster. The clusters formed under those conditions have an open structure, with a fractal dimension of 1.44 for two dimensions [43] and 1.55 for three dimensions [44, 45], while the master curve is bell shaped in both cases [9, 39], which means that the monomers and small-sized species are rapidly removed during the aggregation process to form larger clusters. For this regime, an explicit expression for the kernel may be obtained by estimating the rate of collisions for sufficiently long times. In a d-dimensional space, this reasoning yields [46]:

$$k_{ij}^{Br} \sim (D_i + D_j)(R_i + R_j)^{d-2} \tag{2.31}$$

where D_i and R_i are the diffusion coefficient and the radius of gyration of a clusters of size i, respectively.

We can assume that the average diffusion coefficient for a cluster with a characteristic radius of gyration R_g is given by $D \sim 1/R_g$ [47] (eq. 2.12). Then, inserting here the scaling behavior of the radius of gyration (eq. 2.22) one finally obtains for $d = 2$

$$k_{ij}^{Br} = \frac{k_{11}^{Br}}{2}(i^{-1/d_f} + j^{-1/d_f}) \tag{2.32}$$

This kernel is homogeneous, having $\lambda = \mu = -1/d_f = -1/1.44 \approx -0.69$.

Short–range interaction: RLCA regime

If the pairwise interaction potential $V_{11}(r)$ has a short–range repulsive component after the primary minimum, the kinetic of the coagulation regime corresponds to the *Reaction–Limited Cluster Aggregation* (RLCA) model. In this model aggregation is prevented by using a low *sticking probability* for two colliding aggregates [7]. In this case, the kinetics properties and

the cluster population is mainly determined by the cluster–cluster reaction time, which becomes much larger than the diffusion time. In this regime, the master curve shows a different shape: for two–dimensional aggregation the bell shaped form broadens significantly [48], while for three dimensions the master curve becomes a monotonous decreasing function of the cluster size [9]. That means that the reaction controlled cluster–cluster coagulation leads to more polydisperse cluster–size distributions and, therefore, to more disordered systems.

Considering primary particles, the reduced sticking efficiency due to repulsive forces for a three–dimensional colloidal aggregation can be expressed by the *Fuchs stability ratio*

$$W = 2a \int_{2a}^{\infty} \frac{\exp\left(V_{11}(r)/k_B T\right)}{r^2} dr \tag{2.33}$$

This expression applies only for primary particles and not for aggregates, which are composed of many primary particles. Unfortunately, the equation 2.33 is not longer valid for two–dimensional coagulation[3]. However, it has been verified experimentally, that the reactivity of aggregates increases with their mass [49, 9], and, therefore, an additional factor P_{ij} has been introduced into the aggregation kernel, leading to the following general RLCA kernel

$$k_{ij} = k_{ij}^{Br} P_{ij} \tag{2.34}$$

Int the rest of this section, we will review the various reported RLCA kernels and recast them in the previous form.

Using theoretical scaling arguments, Ball et al. [50] concluded that the efficiency of aggregation is determined by the larger of the two aggregating clusters through a power λ. This parameter accounts for the increased aggregation efficiency of larger clusters due to a larger number of contact possibilities on their surface, and it has been shown to be in the range $\lambda \epsilon [1, 1.1]$. The resulting kernel can be written in terms of P_{ij} as

$$P_{ij} = k^{\lambda} \quad \text{where } k = \max\{i, j\} \tag{2.35}$$

Other authors [31] used the product kernel, given by

$$P_{ij} = (ij)^{\lambda} \tag{2.36}$$

[3]The $2D$ diffusion equation has not a stationary solution

The parameter λ determines how fast the reactivity of clusters grows with size, and, therefore, it strongly affects the resulting cluster size distribution.

It is worth noting that, since DLCA represents the upper limit of the cluster aggregation rate[4] [51], all kernels must be corrected by restricting P_{ij} values to at most 1. This corresponds to the experimentally observed transition from RLCA to DLCA, which occurs as the cluster size increases [49, 52].

Moncho–Jordá et al. [27] proposed an extension of the product kernel that accounts intrinsically for the RLCA to DLCA transition mentioned earlier. This kernel is given by

$$P_{ij} = \frac{PN_{ij}}{PN_{ij} + (1 - P)} \tag{2.37}$$

where P is the *sticking probability* and N_{ij} is defined as the *number of collisions per encounter* between i and j–mers. The *encounter* is defined as a sequence of consecutive collisions between a given pair of clusters. This means that an encounter starts with the first collision and ends when the clusters aggregate or diffuse away.

Effect of the interaction with a non–negligible range over the aggregation rates

The effect of the interaction range on the coagulation process could be explained on the basis of the *superposition principle* applied to find the cluster–cluster interaction potential. This potential can be obtained as the sum of all the interactions between the monomers that compose the interacting clusters. Therefore, the total interaction between an i–mer and a j–mer can be calculated by:

$$V_{ij} = \sum_{k=1}^{i} \sum_{m=1}^{j} V_{11}(r_{km}) \tag{2.38}$$

where $V_{11}(r)$ is the monomer–monomer interaction potential and r_{km} is the center–to–center distance between the k–monomer of the i–cluster and the m–monomer of the j–cluster.

When we have colloidal particles that interact among them through a potential with a non–negligible interaction range, it is not possible to define

[4] In absence of attractive interactions.

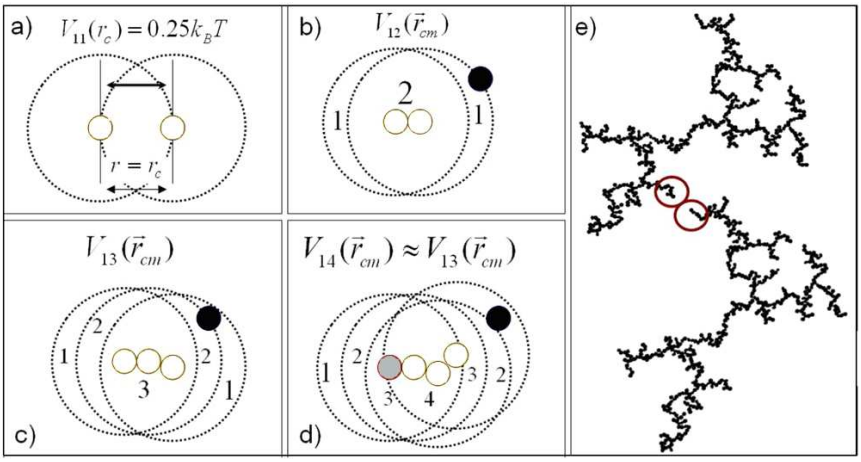

Figure 2.4: Scheme of cluster–cluster interactions. The monomers are represented as grey disks and their interaction regions are sketched by dashed circles. a) The monomer–monomer interaction is isotropic. When one of the monomers is outside the interaction region of the other monomer, the interaction potential is neglected. b) The dimer–monomer interaction is anisotropic. Around the dimer there is a region where the superposition of the two monomers interactions occurs (denoted as $I = 2$ in this scheme) and a region where the approaching monomer only feels the interaction of one of the monomers of the dimers($I = 1$). c) For trimer–monomer case, interaction is also anisotropic. Then, it appear a region where the approaching monomers feel the interaction with the three trimer particles. d) In this example, for the tetramer–monomer case, the approaching monomers does not interact with all the tetramer particles. e) The cluster–cluster interaction, only the monomers that are inside the circles participate in the interaction.

a collision between two clusters as usual. In this case, two approximating clusters "feel" each other before and after they collide. For this reason, it is necessary to define an interaction region between two monomers. This region is limited by a circle of radii r_{cut} centered in one of the monomers so that outside of this region, i. e., when the distance between the centers of the monomers is largest than r_{cut}, the interaction can be considered negligible. For a cluster, the interaction region is given by the union of all the interaction region of each one of its particles.

In figure 2.4 we show a sketch of these interaction regions as the size of the cluster increases. Since r_{cut} is finite, when the clusters become big enough the interaction between two of them is determined by only a fraction of its particles, the nearest ones.

Now, we redefine an *encounter* between two clusters as the even that begins when any monomer of one aggregate cross the interaction region of some monomer of the other aggregate. The encounter finishes when these clusters coagulate or when one of the clusters diffuses away from the interaction region of the other.

A dimer is formed when two monomers collide, forming a strong bond. For experimental colloidal aggregation, the van der Waals interactions is the bond forming force. This strong bond would not allow each of the particles to roll over around the other, due to the roughness of their surfaces. In figure 2.4-b we represent the interaction between a dimer and a monomer. As the interaction range is larger than the particle diameter, there is some region around the dimer where the pairwise interactions are summed due to the superposition principle. Therefore, we can distinguish two different regions around a dimer: a more repulsive region[5] (depicted as $I = 2$ in figure 2.4-b) due to the overlapping of the repulsive interactions of the two monomers that compose the dimer, and a less repulsive region (depicted as $I = 1$ in figure 2.4-b) where there is no overlapping of the interaction regions. Hence, the resulting interaction potential V_{12} is anisotropic, what means that when a monomer interacts with a dimer, there is a convenient orientation between them which minimizes the repulsive interaction. So, the coagulation is easier when they approach through the less repulsive region $I = 1$.

Using the same idea, three different spatial regions appear when a trimer interacts with a monomer, depending on the number of superposed monomer–monomer interactions. In figure 2.4-c they are represented as $I = 1$, $I = 2$

[5]If we consider repulsive long–range forces.

and $I = 3$ regions. Again, the aggregation will occur preferently through a low–number region (less repulsive region). The $I = 1$ regions are usually at the extremes of the aggregates, so it is easier that monomer coagulates in such extremes, and therefore, the small aggregates tend to develop a linear structure (chains).

In the case of the tetramer–monomer interaction (figure 2.4-d), the monomer can coagulate through an interaction region with $I < 4$. This means that not all the monomers forming the tetramer participate in the interaction (the monomer can aggregate with the tetramer without feeling the interaction of the whole cluster). Therefore, we can define a *critical cluster size*, i_0, as the maximum size that all the monomers forming the cluster participate in the interaction with an approaching monomer. The interaction between a monomer and a cluster of size i becomes more repulsive with the increasing of i until it reaches the critical size i_0. After that, the monomer–cluster interaction becomes independent on the cluster size.

When two clusters with a size larger than the critical one approach each other, not all the monomers participate in the interaction. So, there is not any "privileged" direction and the clusters with a size $i > i_0$ begin to lose their linearity. In figure 2.4-e two interacting big clusters are shown. In this case, the monomers that participate in the interaction are those inside the circles.

Therefore, when colloidal particles interact through a potential with a non–negligible range (as compared with the particle diameter) three kinetic regions can be distinguish:

i.- *First region.* For small aggregates, the cluster–cluster repulsion increases with the cluster size due to the superposition of the interactions. Therefore, the function P_{ij} (equation 2.34) decreases with the clusters size. In this region, the cluster–cluster interaction is anisotropic and this causes the formation of chains, which is the preferred configuration to minimize the repulsive interaction between two approaching clusters.

ii.- *Second region.* When the size of the interacting clusters is bigger than the critical size, i_0, the cluster–cluster interaction potential becomes size independent since not all the monomers that form the aggregates participate in the interaction. Since the range of the cluster–cluster interaction does not grow anymore with the cluster size, the probability to overlap the repulsive barrier tends to be also size–independent. Under

this situation we can use again the term "*collision*" between clusters. Moreover, the interaction is more isotropic than in the previous region and the chains coagulate to form clusters with higher fractal dimensions. Although the collision efficiencies are constant, the probability P_{ij} of coagulation of two clusters with sizes larger than i_0 still grows with the size, due to the increase of the cluster cross section. Hence, the typical coagulation kinetics for the RLCA regime is recovered.

iii.- *Third region.* For long enough aggregation times, the cross section of the clusters is so large that the number of consecutive collision per encounter between a pair of neighboring clusters is usually very high. This implies that two colliding big clusters are not able to diffuse away and finally end up forming a bond. Hence, in this region a cluster coagulate almost certainly during its first encounter with another cluster and the aggregation rate becomes diffusion controlled (DLCA). However, there is a finite time between the encounter and the coagulation that prevent reaching completely the DLCA regime. Therefore, the kernel for this third region will be:

$$k_{ij} = A \cdot k_{ij}^{Br} \tag{2.39}$$

where A is a constant with values $0 \leq A \leq 1$.

Hence, the coagulation of the large clusters is controlled by the Brownian diffusion and then the kinetic exponent z of equation 2.27 and the fractal structure of the final clusters will be the same as in a typical DLCA coagulation regime.

Chapter 3

Interactions in colloidal systems trapped at interfaces

3.1 Introduction

Particle monolayers are formed when small colloidal solid particles adsorb at liquid–vapour or liquid–liquid interfaces. Typical examples are latex monolayers at the air–aqueous salt solution [53] and oil–water interfaces [54, 55]. The interaction between particles within the monolayer is dependent on both the properties of the fluids that make up the interface and on the nature of the adsorbed particles. Therefore, a detailed analysis of the interactions in colloidal monolayers is quite complex and distinctions must be made to take into account the different components of the monolayer.

The total interaction between particles in the monolayer determines their *stability behavior*. Thus, examples of stable monolayer systems with particles that remain independent for a long time have been reported [56], in spite of the fact that in a thermodynamic sense, colloidal particles are not stable because of their great surface to volume ratio. Some monolayer systems show a triangular structure suggesting the existence of long–ranged particle interactions. In other reported systems, however, it has been found that particles are unstable and aggregate to form fractal structures [6] or even became organized to form the so–called *mesostructures* [57, 58]. When fractal structures appear, the particle interaction potential is short ranged and has a minimum at very short distances. In the other cases, the formation of mesostructures can be explained if the interaction energy between the particles has a min-

imum at a typical average distance between particles of the order of a few times the particle diameter [59].

The different colloidal stability behavior shown experimentally by particle monolayers has fundamental importance in a wide set of industrial applications. Typical examples are the manufacture of emulsion polymers in stirred–tank reactors [60] and separation processes such as froth and solvent extraction. In these cases, it is found that $2D$ colloidal aggregation can occur with different consequences. When manufacturing emulsion polymers, it is important to prevent aggregation because it has a negative effect on the characteristics of the synthesized particles as increasing the particle polydispersity increases. However, in separation processes, the aggregation of the colloidal particles is accelerated by the re–dispersion of aggregates formed at the bubble surfaces. This foaming action [61] of colloidal particles at the bubble surfaces is dependent on the degree of surface aggregation [62] and finally on the interfacial properties of the particles.

Thus, a correct description of interactions between colloidal particles in monolayers is of great interest and could enable us to understand these kinds of processes and to improve the use of colloidal particles for industrial applications. In this chapter, a detailed discussion of the theory of interactions in colloidal monolayers is presented. The theory considers *Derjaguin–Landau–Verwey–Overbeek* (DLVO), capillary, hydrophobic, monopolar and dipolar interactions between the particles. The contribution of these terms to the total interaction energy has been computed numerically using typical values for most of the parameters included in the theory.

3.2 Theoretical Model

As stated in the introduction, the interaction between particles forming monolayers is dependent on the particle characteristics and on the properties of the fluids defining the interface where colloidal particles are trapped.

3.2.1 Model of the colloidal particles

The shape, size, chemical composition and internal and surface structural properties of the particles must be given in order to have a complete model of them. Although it is not infrequent to find works reporting experimental results using ellipsoidal particles, here we only consider spherical particles

with radius a. This does not represent an important limitation as most applications make use of spherical particles since they are easily synthesized.

Due to their surface properties, colloidal particles are strongly trapped at an interface by capillary and electrostatic forces [63]. Thus, the *contact angle* θ is the main parameter that determines the position of the particles at the interface, i.e. the immersed fraction of the particles. Its value is given by Young's law equation:

$$\cos\theta = \frac{\gamma_{PA} - \gamma_{PL}}{\gamma} \tag{3.1}$$

Here, γ is the interfacial tension between the fluid phases and γ_{PL} and γ_{PA} and γ are the interfacial energies between the colloidal particle and phases L and A, respectively.

Usually, ionic surface groups on colloidal particles can become dissociated when they are in polar media and then produce dipoles or even monopoles that give rise to long–ranged interactions. The formed dipoles originate at least in part from the counterions in the polar phase and they can become exposed to the non-polar phase because of thermal fluctuations that are able to rotate the colloidal particles. For example, this is the case of colloidal latex particles at the air–water surface. As the dipole number depends on the number of ionic surface groups on the particles, it is expected that its maximum amount is not directly related to the ionic strength of the polar phase. The monopoles, like the dipoles, come from the dissociated surface groups of the particles and they can be exposed to the non-polar phase across the interface; however, it is not so clear how they can remain stable without attaching counter charges as some experimental work has reported [64].

Internal properties of the colloidal particles, i.e., chemical composition and structure, affect their interaction both in dispersion and at the interface when they form monolayers. The chemical composition and structure of the particles determine the strength of the dispersion forces and even the existence of a dipolar type interaction, as might be the case for magnetic particles. There is also the possibility that particles have not a smooth surface but a surface that can be structured or rough. This fact can affect the particle arrangement at the interface and the inter–particle interactions and consequently the colloidal stability. Despite the number of possible choices, we take a particle model that considers spherical particles with radius a, contact angle θ, a uniform chemical composition and carrying some dipoles and monopoles on their surfaces.

3.2.2 The model of the fluid phases

The simplest model for the fluid phases assumes a uniform continuous polar or non–polar medium characterized by some physical average properties like the *mass density* (ρ) and the *dielectric constant* (ϵ).

3.2.3 Derjaguin approach

For the sake of simplicity, some of the interaction terms between particles at the interface have been computed with the assumption that interaction occurs only between their emergent parts and between their immersed parts, respectively, and that the interaction between the emergent part of one particle and the immersed part of another one can be neglected. This is also the case of the dispersion and double layer interaction (DLVO interaction) and of the dipolar and monopolar interactions.

As the model considers spherical colloidal particles, the computation of their potential of interaction, $V_{sph-sph}$, can be done in some cases using the *Derjaguin approximation* [65]

$$V_{sph-sph}(h_0) = \int V_{flat}(h) dS(h) \tag{3.2}$$

which makes use of the corresponding interaction potential per unit area between infinite half spaces, V_{flat}. The integration must be done over the particle surface. Here h_0 is the minimum distance between the particles and h is the local distance between the different surface elements. The Derjaguin approximation is useful to estimate the total interaction when the range of interaction is small compared to the radius of curvature of the particle.

To compute the pair interaction potential by using the Derjaguin approximation presents two main problems. The first one is related to the determination of the particle surface fraction above and below the interface which must be taken into account to calculate the interaction. The second one relates to the specific expression of the interaction potential per unit area between half spaces, V_{flat}, that depends on the kind of the interaction. The first problem is solved with the help of the *flat meniscus approximation*. With this assumption, the calculation of the immersed and emergent particle surface fraction becomes easier. Figure 3.1 sketches the variables used to calculate both emergent and immersed parts of the particle. The ratio between both parts depends on the value of the contact angle θ. Indeed, the

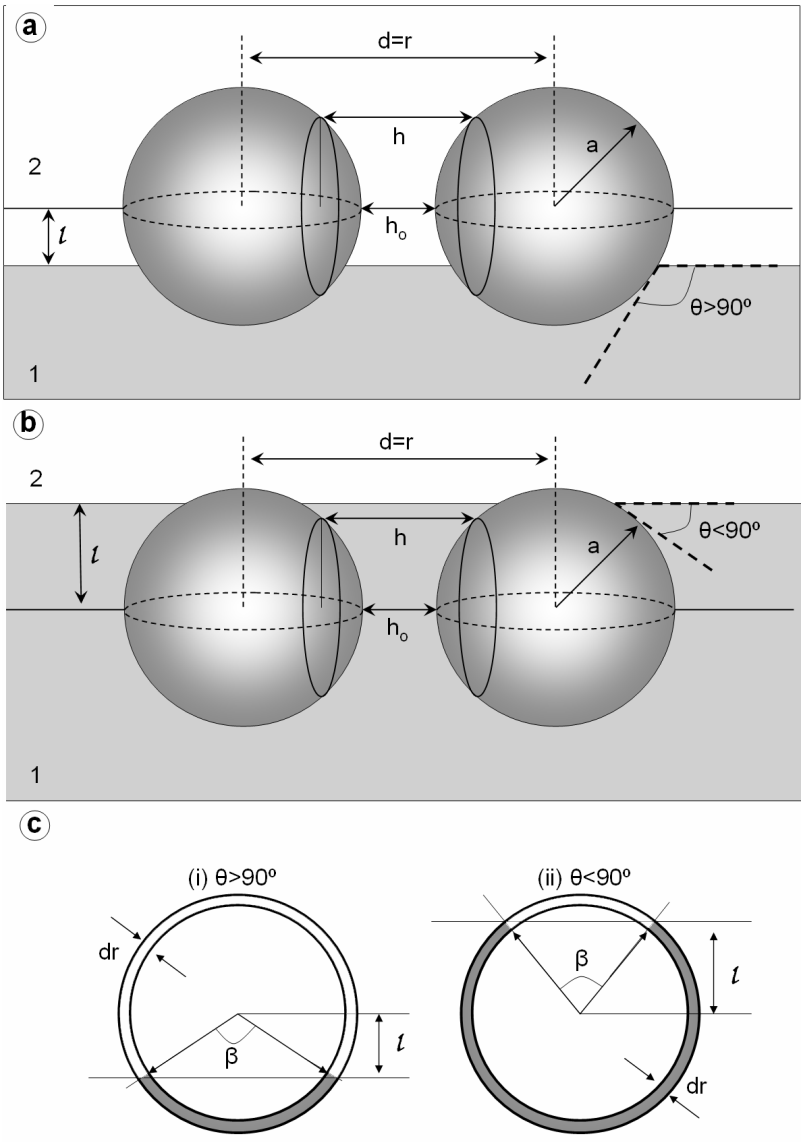

Figure 3.1: Sketch of the colloidal particle arrangement at the interface between phases 1 and 2 for (a) $\theta > 90°$and (b) $\theta < 90°$. The particle surface fraction included into each phase depends on the particle hydrophobicity, i.e., on the contact angle θ. The immersed part is indicated in (c) by a thick black line for $s > l$.

immersed part increases as the contact angle decreases. For $\theta > \pi/2$ the emergent part of the particle is larger than the immersed one (figure 3.1*a*) while for $\theta < \pi/2$ the inverse occurs (figure 3.1*b*). This dependence with the contact angle has a great importance on the value of the different terms of the interaction.

3.3 The Energy of Interaction

The calculation of the total pair energy is quite difficult and it is mainly determined by the particle accommodation at the interface. Thermodynamics limits the form that the interface can adopt, in such a way that the interface near the particle surface forms a curved meniscus contacting the surface of the particle at a well-defined angle, the *contact angle* θ; θ depends on the properties of the particle surface and on the nature of the fluids that form the interface as indicated by *Young's equation*. Nevertheless, for colloidal particles whose size ranges from a few nanometres to some micrometres, the meniscus can be considered approximately flat. This is true because the Bond number ($= \Delta\rho g a^2/\gamma$) for these systems is very small [66], usually of the order of 10^{-8} for colloidal particles of many hundred nanometres radius at the air–water surface. Here $\Delta\rho$ is the difference of densities between the two fluid phases and g is the gravity constant. The flat meniscus approximation helps us to simplify the computation of the immersed part of the particle. It also implies that capillary interaction is practically negligible for particles of colloidal size.

3.4 Terms of the energy of interaction

There are different terms of the interaction energy that must be taken into account for interfacial particles in order to explain their stability properties. Usually, the DLVO theory [67, 39] allows to study the stability behavior of colloidal particles in bulk ($3D$ stability). However, this is not the case for colloidal particles at an interface ($2D$ stability). Furthermore, in two dimensions there are new elements like capillary attraction, intrinsic to interfacial phenomena, which have no analogy in bulk aggregation. Besides, the DLVO expressions for the double layer and dispersion interactions have to be corrected in order to account for the presence of the interface that reduces the

degrees of freedom for the movement of the colloidal particles.

The different terms of the inter-particle interaction energy that we will consider here are: double layer and dispersion interactions ($2D$ DLVO), capillary interaction, hydrophobic interaction and monopolar and dipolar interactions. These terms have a different order of contribution to the total interaction energy, which depends on the specific values of the parameters included in the theoretical model. Here, typical values from the literature have been assigned to the parameters in order to account for most of the experimentally reported situations and to have as correct as possible weighting of the different energetic contributions.

3.5 The DLVO approximation at the interface

The DLVO approximation for colloidal interaction at the interface considers only two energetic terms: the electrical double layer interaction between that part of the particles in the polar phase and the dispersion van der Waals interaction that, in our approximation, takes place between the immersed parts and between the emergent parts of the particles through the different fluid media, i.e. with a different *Hamaker constant* for each fluid.

3.5.1 Electrostatic interaction between the double layers of the particles

In order to determine the electrostatic interaction between the double layers of the colloidal particles at the interface, the *Poisson–Boltzmann* (PB) equation for the electrostatic potential Ψ in the polar phase

$$\nabla^2\Psi = -\frac{1}{\epsilon\epsilon_0}\sum_i n^0 e z_i e^{-z_i e\Psi/k_B T} \tag{3.3}$$

should be solved simultaneously with the *Laplace equation* in the dielectric non–polar phase

$$\nabla^2\Psi = 0 \tag{3.4}$$

where n^0 is the salt concentration, z_i the valence of the salt, k_B the Boltzmann constant, T the temperature and e the electron charge. This was done by Lyne [68] and Levine [69] who demonstrated the accuracy of the Derjaguin

approximation for the case of thin to moderate double layers ($\kappa a > 5$), where κ is the inverse Debye screening length given by

$$\kappa = \left(\frac{e^2 2 z^2 n^0}{\epsilon k_B T} \right)^{1/2} \tag{3.5}$$

where ϵ is the dielectric constant of the polar phase and φ_0 the potential at the particle surface

Thus, the potential of interaction between half spaces can be obtained for symmetric electrolytes using the PB equation and the assumption that the double layers do not overlap significantly [4]. Within these approximations the electrostatic interaction potential per unit area between half spaces separated a distance h is

$$V_{flat}(h) = \frac{64 n^0 k_B T Z^2}{\kappa a} e^{-\kappa h} \tag{3.6}$$

where ($Z = tanh(\nu e \varphi_0 / 4 k_B T)$).

.

3.5.2 Dispersion van der Waals interaction

The van der Waals interaction is completely understood under quantum mechanics formalism. It originates from the fluctuations of the electron clouds around the atomic nucleus. These fluctuations produce temporary dipoles that are able to induce the formation of new dipoles in the neighboring atoms, giving rise to an attraction between them. To calculate the van der Waals interaction energy we have used the Derjaguin approximation. The expression for the interaction potential per unit area between half spaces separated a distance h was obtained from Gregory [70] and Overbeek [71]

$$V_{flat}(h) = -\frac{A}{12\pi h^2} \frac{1}{1 + bh/\lambda} \tag{3.7}$$

It takes into account the retardation effect due to the limit on the speed of light. In this expression, the constants b and λ have values 5.32 and 100 nm, respectively. Furthermore, the Hamaker constant A was assigned different values for both fluid phases. For the case of polystyrene particles at the air–water surface the values of the Hamaker constants were taken to be $A_{air} = 6.6\text{x}10^{-20}$ J and $A_{water} = 0.95\text{x}10^{-20}$ J.

Table 3.1: Typical parameter values for the hydrophobic interaction potential between half spaces.

Parameter	Hydrophilic particles	Hydrophobic particles
λ_0 (nm)	0.6–1.1	1–2
W_0 (mJm^{-2})	3–30	-20 to -100

3.6 Non–DLVO interactions

3.6.1 The hydrophobic interaction

The interaction of the colloidal particles with the surrounding fluid molecules is the origin of the so–called structural forces. This interaction affects the structure of the fluid near the particle surface, giving rise to an increase or decrease of its order as compared with the fluid structure far away from the particles surface. Therefore, structural forces can be regarded as entropic interactions. The character of this interaction allows solid particles to be classified as *lyophilic* or *lyophobic* depending on whether they have or do not have affinity for the liquid in which they are dispersed, respectively. When the fluid is water, the colloidal particles are designated as *hydrophilic* or *hydrophobic*.

Hydrophobic particles repel water from their surface so when dispersed in water they experience an attraction. However, the interaction of hydrophilic particles with the fluid produces a layered arrangement of the nearest fluid molecules that prevent the approach of the colloidal hydrophilic particles, i.e. they feel a net repulsion. Besides the dependence of the structural forces on the chemical properties of the particles surface and the fluid, they are also affected by the surface roughness [72] and the wetting degree of the particles. For example, colloidal particles at the air–water surface that are partially wetted will experience less interaction than fully wetted ones. As our model for the particles considers that they have smooth surfaces, the effect of roughness will not be explicitly taken into account, although the effect of the wetting degree is considered through the contact angle.

Experimentally, the hydrophobic attraction is detectable when the contact angle is greater than 64° [73], while the hydrophilic repulsion is important when the contact angle is lower than 15° [74]. For contact angle values ranging from 15° to 64° the hydrophobic interaction is negligible and the

DLVO theory is sufficient to explain the colloidal stability in solution. Christenson and Claesson [75] have shown that the hydrophobic interaction decays exponentially for plane surfaces. Thus, because of the short range of this interaction, the Derjaguin approximation is useful to estimate the hydrophobic interaction between two partially immersed particles. The expression used for the hydrophobic interaction potential per unit area between half spaces separated by a distance h is

$$V(h) = W_0 e^{-h/\lambda_0} \tag{3.8}$$

where W_0 and λ_0 are constants related to the strength and range of the interaction. Typical values for these parameters obtained from ref. [76] are given in Table 3.1.

3.6.2 The monopolar and dipolar interactions

The proposed model for the particle at the interface includes the possibility of some kind of charges, monopoles and dipoles, in the non–polar fluid phase. The most important question now is to understand how these dipoles and residual charges can arise in this part of the particle surface. The origin of this charge and dipoles can be understood if one takes into account the rough character of the particles at a molecular level and the process of monolayer formation, i.e. the so–called spreading process.

Usually, particle monolayers are formed from a particle suspension using a spreading agent like methanol, which helps the formation of a uniform surface distribution of colloidal particles at the interface. The spreading process is rather turbulent because of the spreading agent effect that allows the colloidal particles to rotate and even penetrate into the sub–phase, i.e. the polar fluid phase that is most frequently water. This process is so vigorous that particles can trap traces of polar fluid at their surfaces around the hydrophilic surface charged groups [54, 77, 78]. Therefore, there is not a complete dewetting of the part of the particle lying above the water level. This water could be in the form of either small droplets or as a thin layer of water around the particle surface in the non–polar medium (air, oil, etc.). The presence of the polar liquid at this part of the particle surface can affect the configuration of their surface chemical groups, which can be found in the following three possible configurations in the non–polar phase (see figure 3.2):

1.- *Non–dissociated*: most of the surface groups remain neutral and do not contribute to the interaction potential.

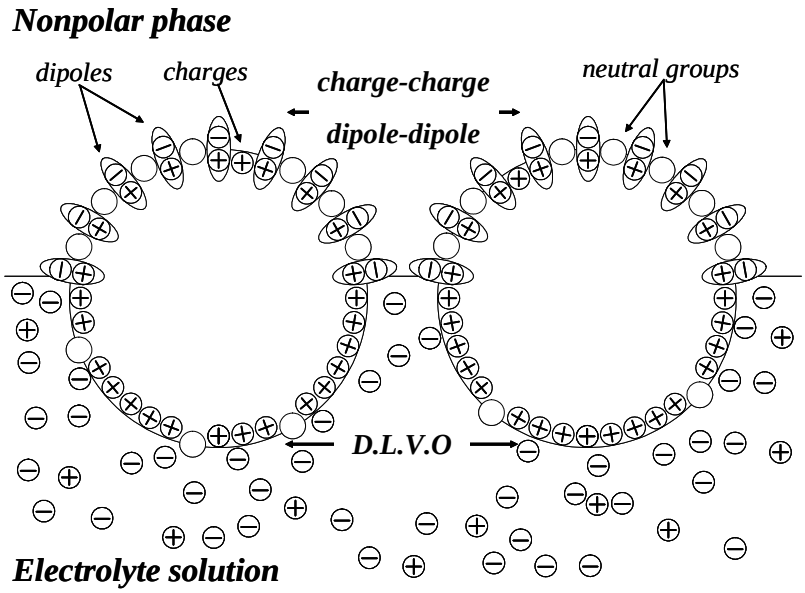

Figure 3.2: Illustration of the particle–particle interactions through the non–polar phase (charge–charge and dipole–dipole) and the polar phase (DLVO forces) for particles at a liquid interface.

2.- *Forming dipoles*: some wetted surface groups, even though dissociated, can form dipoles together with the counterions from the polar phase. These dipoles are effectively screened in the polar phase as a cloud of ions is formed around the particle. However, this does not occur in the non–polar phase, as usually it has no dissolved salt. Hence, the dipoles at the surface of particles can give rise to a total dipole moment and to quite strong dipole–dipole repulsion between particles that is mediated through the non–polar phase. To account for the number of dissociated groups on the particle surface we define the *fraction of dipoles*, f_d, as the percentage of them forming dipoles in relation to the total surface groups above the polar liquid (water) level.

3.- *Totally dissociated*: only a few of the total surface groups acquire a net charge and form monopoles. Analogously to f_d, the *fraction of monopoles*, f_c, is defined as the percentage of dissociated groups forming monopoles. Since the non–polar phase has generally a low dielectric constant, these charges generate a monopole Coulombic repulsive potential which is very intense and long ranged, even for very small monopole fraction values f_c.

Since the number of initially dissociated ionic surface groups above the water level is expected to be small, most of the groups will be neutral, i.e. $f_c,\ f_d << 1$. The exact location of these dipoles and charges is still unclear. However, because of the turbulent nature of the spreading process, it is usually assumed that they are homogeneously distributed at the part of the particles exposed to the non–polar fluid phase. The presence of dipoles and monopoles on the upper surface of the particle causes the appearance of three contributions to the total potential energy: the monopole charge–charge ($V_{cc}(r)$), the monopole–dipole ($V_{cd}(r)$) and the dipole–dipole ($V_{dd}(r)$) potentials.

However, in a first approximation, the monopole–dipole interaction has an asymptotic behavior that can be written as

$$V_{cd}(r) = k' \frac{\vec{P} \cdot \hat{r}}{r^2} \tag{3.9}$$

where k' includes the monopole charge and some constants and $\hat{r} = \vec{r}/r$ where $\vec{r}$ is the position vector of the charge taken from the net dipole moment of the particle $\vec{P}$ and r is its modulus. If the particle has a homogeneous surface dipole distribution, $\vec{P}$ is always normal to the interface and also to the vector

$\vec{r}$. Therefore, under this approximation, the monopole–dipole interaction potential term is zero and does not contribute to the total energy. Thus we will only consider the contribution of the dipole–dipole interaction, $V_{dd}(r)$, and monopole–monopole interaction, $V_{cc}(r)$.

It should be emphasized that the total surface area exposed to the non-aqueous phase depends on the contact angle. Therefore, the dipole–dipole and charge–charge repulsions change if the particle hydrophobicity is varied. This effect has been experimentally observed in colloidal monolayers formed by polystyrene spheres trapped at the air–water surface, where adding small amounts of surfactant to the aqueous phase (around $10^{-5}M$) leads to a reduction of the stability of the monolayer, inducing aggregation [77]. At the oil–water interface, the particle hydrophobicity has also a significant role in the spatial distribution of the colloidal particles [79]. Very hydrophobic particles with large contact angles (above 129°) lead to well-ordered hexagonal monolayers. On the contrary, the monolayers of less hydrophobic particles with contact angles below 115° are completely disordered or aggregated. Between 115° and 129°, a disorder–order coexistence region occurs. Of course, these intervals can be different if we change the non–polar medium or the surface density of charged groups in the colloidal particles.

The repulsion produced by the charge–charge and dipole–dipole pair interactions is in general very strong, and dominates over the other energetic contributions even for very small values of f_c and f_d. Consequently, the stability of colloidal monolayers for a given contact angle will be essentially ruled by the surface charge and surface dipole percentages f_c and f_d, respectively.

3.6.3 Dipolar electrostatic interaction between the emergent parts of the particles

To estimate numerically this dipolar interaction we have supposed that the part of the particle exposed to the non–polar phase has a uniform distribution of dipoles. As the dipoles are originated from the surface groups of the particles and the counterions from the solution, we can consider them as two unit charges with opposite sign separated by a distance, d_{dip}, equal to the sum of the radius of typical anions and cations, i.e. of the order of 0.3 nm. This parameter can be changed in the calculation but there is no apparent reason to do it.

To calculate the dipolar interaction energy the emergent surface has been

divided into different parts with a surface dS and charge $f_d\sigma dS$, where σ is the surface charge density and f_d is the fraction of the surface groups forming dipoles, as was indicated above. At a distance d, equal to the dipole length from these surface elements, we have considered the existence of a charge of equal magnitude and opposite sign that forms part of the dipole. Therefore, the total charge on the emergent dipole is zero. The interaction between these pairs of charges for two particles allows the dipolar interaction energy to be determined. This calculation implies a $4D$ integration given by

$$V(h_0) = \int d\theta_1 \int d\theta_2 \int d\phi_1 \int d\phi_2 V(\theta_1, \theta_2, \phi_1, \phi_2) \tag{3.10}$$

where $V(\theta_1, \theta_2, \phi_1, \phi_2)$ depends on the particle radius a, the distance between particles h_o, the spherical coordinates θ_1, θ_2, ϕ_1 and ϕ_2, taken with origin at each particle, the surface charge density σ, the dipole fraction f_d and the dipole length d_{dip}. The expression for $V(\theta_1, \theta_2, \phi_1, \phi_2)$, obtained using *Coulomb's law*, has the form

$$V(\theta_1, \theta_2, \phi_1, \phi_2) = \frac{f_d^2 \sigma^2 a^4}{4\pi\epsilon\epsilon_0} \sin\theta_1 \sin\theta_2 G(a, d_{dip}, \theta_1, \theta_2, \phi_1, \phi_2) \tag{3.11}$$

where

$$\begin{aligned} G(a, d_{dip}, \theta_1, \theta_2, \phi_1, \phi_2) = \frac{1}{F(a,a)} - \frac{1}{F(a+d_{dip}, a)} \\ - \frac{1}{F(a, a+d_{dip})} + \frac{1}{F(a+d_{dip}, a+d_{dip})} \end{aligned} \tag{3.12}$$

and the function F reads

$$F(A, B) = \sqrt{X^2 + Y^2 + Z^2} \tag{3.13}$$

where

$$\begin{aligned} X = A\sin\theta_1\cos\phi_1 - B\sin\theta_2\cos\phi_2 - 2a - h_0 \\ Y = A\sin\theta_1\sin\phi_1 - B\sin\theta_2\sin\phi_2 \\ Z = A\cos\theta_1 - B\cos\theta_2 \end{aligned} \tag{3.14}$$

Here ϵ is the dielectric constant of air and ϵ_0 is the permittivity of vacuum.

3.6.4 Monopole–monopole interaction

The dipole–dipole interactions arising between colloidal particles trapped at interfaces account for the higher electrolyte concentrations needed to induce aggregation in such a kind of 2D system, as compared to colloidal systems in bulk dispersion. For large surface packing fractions of particles, the dipole–dipole interactions seems to give a fair description of the spatial ordering and the experimental surface pressure–area curves obtained by compressing the colloidal monolayers at the air–water and oil–water interfaces. However, for dilute systems, i.e. large inter–particle distances, the particle monolayers exhibit a long–range repulsion, which cannot be explained assuming dipole repulsive interactions between the emergent parts of the particles [54, 76].

In this respect, Sun and Stirner [80] performed molecular dynamic simulations including charge–charge interactions besides the dipole–dipole contribution in order to account for the experimental results obtained by Aveyard et al. [54] in colloidal monolayers of polystyrene particles trapped at the octane–water interface. The net dipole moment and total charge densities were taken as fitting parameters. They observed that each mechanism gives rise to a specific surface pressure–area behavior. The dipole–dipole interactions were only able to reproduce the experimental data for high coverage (above 0.45) but not for more dilute regimes. Analogously, they showed that the charge–charge interactions could describe the data for low particle densities. Clearly, all these results point out that the short-range repulsion between colloidal particles is mainly mediated by dipole–dipole interactions, depending asymptotically on the inter-particle distance r as $V_{dd}(r) \propto 1/r^3$. Analogously, they found that the long–range repulsion is governed by charge–charge Coulombic interactions through the oil phase, $V_{cc}(r) \propto 1/r$. According to their calculations, about 0.4% of the maximum charge on the upper part of the particle is sufficient to explain the long–range repulsion through the oil phase.

The existence of Coulombic long–range forces between colloids at interfaces has also been supported by other experiments in stable polystyrene particle monolayers at the air–water surface, even at quite low particle surface packing fractions (around 0.01).

The dipole–dipole interaction energy dominates at short distances, and it has to be calculated integrating numerically over the whole distribution of dipoles. In principle, $V_{cc}(r)$ should also be determined in the same way. However, since this potential has a longer range than the dipole–dipole con-

tribution, it is worth simplifying the calculations assuming that the total charge of the upper part of the spherical particle is concentrated in its center. This approximation fails at short inter–particle distances, where the specific details of the surface charge and dipole distributions have to be considered in order to obtain accurate values for the interaction potentials. Nevertheless, for such small distances, $V_{dd}(r)$ dominates over the other terms and the correction introduced by the exact calculation of $V_{cc}(r)$ becomes negligible. According to this, the charge– charge interaction between two colloidal particles reads [54]

$$V_{cc}(r) = \frac{q^2}{4\pi\epsilon_r\epsilon_0}\left(\frac{1}{r} - \frac{1}{\sqrt{4\zeta^2 + r^2}}\right) \tag{3.15}$$

Here, r is the distance between the centers of the particles, ϵ_r is the relative dielectric constant of the non–polar phase, and $\zeta = a(1 - cos\theta)/2$, where θ is the contact angle. The net charge of the particle above the water level, q, is given by

$$q = A\sigma f_c = 2\pi a^2(1 - cos\theta)\sigma f_c \tag{3.16}$$

Here, A is the area of the particle exposed to the non–polar medium and σ is the surface charge density. The first term in equation 3.15 is the usual Coulombic interaction energy through the non–aqueous phase between two identical point charges of value q, separated by a distance of r. The second term corresponds to the interaction between the second particle and the image charge of the first one, located at a distance $\sqrt{4\zeta^2 + r^2}$ from the second one, symmetrically with respect to the interface that divides both media. For large inter-particle distances, equation 3.15 takes the form

$$V_{cc}(r) = \frac{q^2}{4\pi\epsilon_r\epsilon_0}\frac{2\zeta^2}{r^3} \tag{3.17}$$

One of the most important experimental results that support the presence of unscreened Coulombic pair inter–particle interactions acting through the non-polar phase are those obtained using optical tweezers [55]. In such experiments, a couple of particles at the interface are originally entrapped inside two laser beams well removed from each other. Then, the inter–particle distance is decreased until one of the particles is released from the beam. At this point, the inter–particle force is equal to the trapping force of the

laser. By repeating the same procedure for several laser powers, the force can be determined as a function of the particle separation. The experimental data showed that colloidal particles at the oil–water interface interact with a long–range repulsive force that scales with the inter–particle distance as $F(r) \sim r^{-4}$, but does not depend on the ionic strength in the water phase. These results agree with the interaction potential given in equation 3.17 and points out the fact that charge–charge interactions are involved in the stability of the colloidal monolayers at the oil–water interface.

3.7 Contact angle dependence of the interaction potential

As stated previously, the contact angle value is the main parameter controlling the behavior of colloidal particles at the interface. So, as a practical application, we study the different terms of the interaction and the total pair energy for the case of colloidal particles with different hydrophobic properties and the same radius (300 nm) at the air–water surface. For the sake of simplicity, we have not included the monopolar interaction, analyzed in detail in the previous sub–section.

The theoretical conditions of the computed potential values correspond with experimental systems for which it is hoped that no monopoles appear; i.e. for high salt concentration. In the computation we have used standard constant values as those already indicated. In this section we will not consider the capillary interaction because it is negligible for colloidal particles, as will be shown in Section 3.8.

The first analyzed interaction is the van der Waals interaction. In figure 3.3 we show the dependence of the van der Waals interaction energy on the separation distance between particles for different contact angles taking into account the retardation effect. The effect of the contact angle on the van der Waals interaction for different fixed values of the separation distance is shown in figure 3.4. This interaction potential changes abruptly at short distances when the contact angle goes from values lower than 90° to values greater than 90°, contrary to the predicted soft dependence reported by Williams [81].

The dependence of the double layer electrostatic interaction between the immersed parts of the particles on the contact angle at fixed separation is

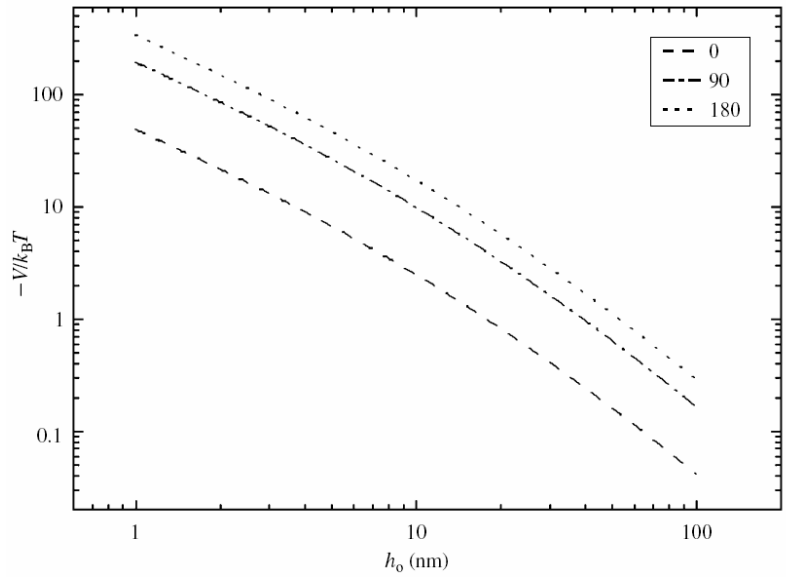

Figure 3.3: Retarded van der Waals interaction energy between particles at the air–water surface as a function of the inter–particle distance for three values of the contact angle (given in degrees) and particle radius $a = 300$ nm.

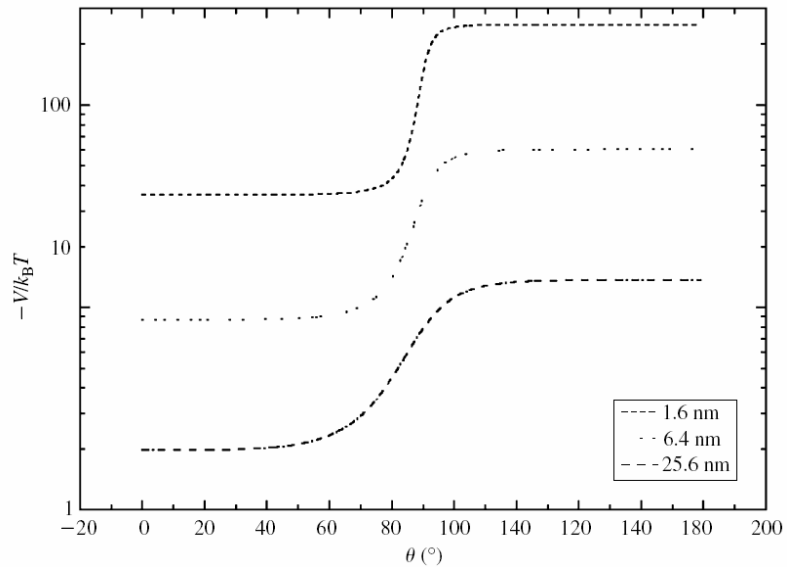

Figure 3.4: van der Waals interaction energy between particles at the air–water surface as a function of contact angle for different inter–particle separation values h_0 (given). It should be noted that this interaction is a very sensitive function of the contact angle.

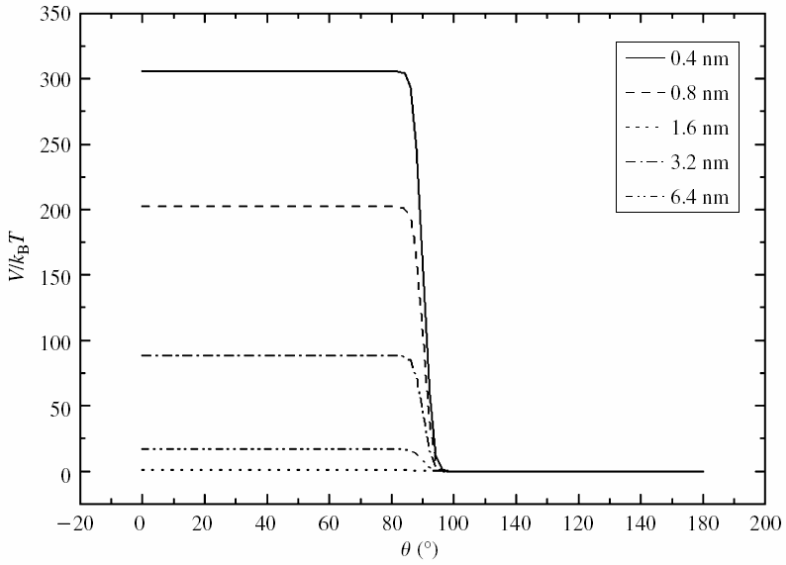

Figure 3.5: Double layer interaction energy between immersed parts of the colloidal particles as a function of contact angle for different inter–particle distances (given). The dependence on the contact angle has a similar critical behavior to that of the van der Waals interaction at $\theta = 90°$.

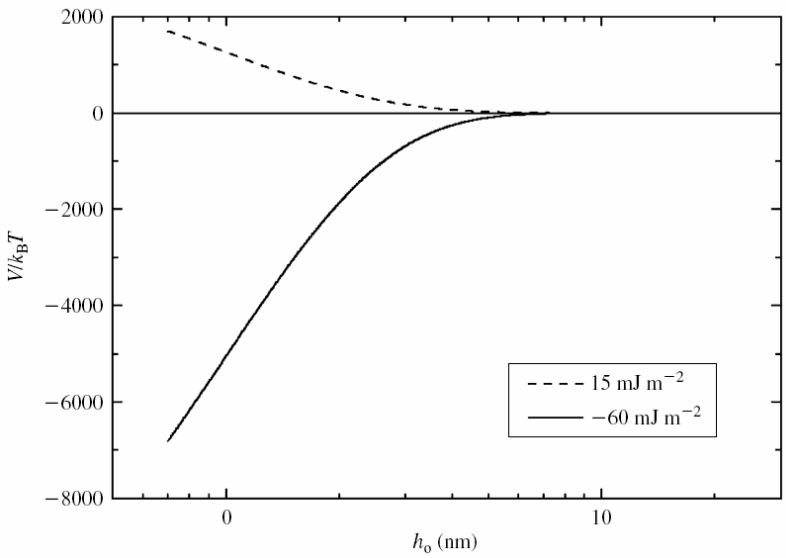

Figure 3.6: Hydrophobic interaction versus inter–particle distance for two values of W_0 (given) with $\lambda_0 = 1$ nm. The interaction range extends to a few nanometres.

shown in figure 3.5.

In this case, there is also a critical dependence with the contact angle value. The interaction strength is considerable for contact angles below 90°, while for values above 90°it is negligible. This energetic term decays strongly with the separation between the particles (compare 0.4 and 6.4 nm).

The decaying behavior of the hydrophobic interaction with the separation between particles is shown in figure 3.6. This behavior is similar to that of the electrostatic interaction in the sub–phase as could be expected, since both interactions have the same dependence on the inter–particle distance. The dipolar repulsion is shown in figures 3.7 and 3.8 as a function of the contact angle at different distances and as a function of the separation between particles for different contact angles, respectively. As a general behavior, the curves have a maximum near $\theta = 90°$.

For partially immersed particles at the air–liquid surface, the van der Waals interaction between colloidal particles is enhanced due to the partial particle exposure to the air phase. The increase of the van der Waals attraction coupled with the decrease of the electrostatic repulsion due to the electrical double layer overlapping does not account for the great stability

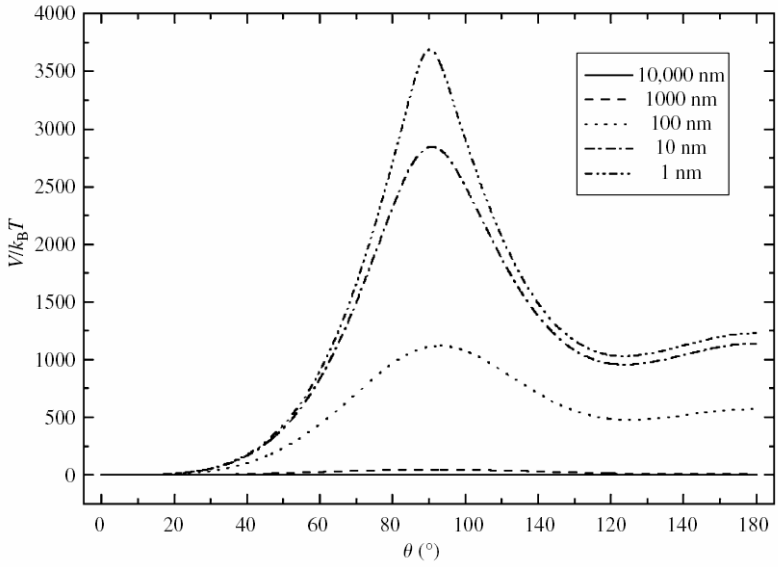

Figure 3.7: Dependence of the dipolar interaction energy on the contact angle θ for different inter–particle distances (given). A typical maximum near $\theta = 90°$ is found in all cases. The values used in the computation were $\sigma = 0.6\mathrm{e}^{-}\mathrm{nm}^{-2}$, $f_d = 1$ and $d_{dip} = 0.3$ nm.

experimentally observed in colloidal monolayers. The sum of these terms, i.e. electrostatic interaction between the sub–phase double layers and van der Waals interaction, that constitute the DLVO approximation, is shown in figure 3.9. As can be seen, the change of the contact angle can drastically reduce the repulsive energy barrier of the interaction potential between colloidal particles at the interface. This reduction is so important that increasing the surface potential and decreasing the Hamaker constant values in the DLVO interaction potential are not enough to justify the great stability of colloidal particles at the interface even for 1 M salt concentration.

This difficulty is overcome by adding the hydrophobic and dipolar interaction terms to the DLVO interaction. Figures 3.10–*a* and –*b* show this total contribution for both hydrophobic and hydrophilic particles, respectively. As expected, the hydrophobic interaction gives a potential with a minimum and repulsion at short distances for hydrophilic particles while there is a stronger attraction at short distances for hydrophobic ones. When the dipolar repulsion term is included, the interaction pair energy shows a repulsive barrier

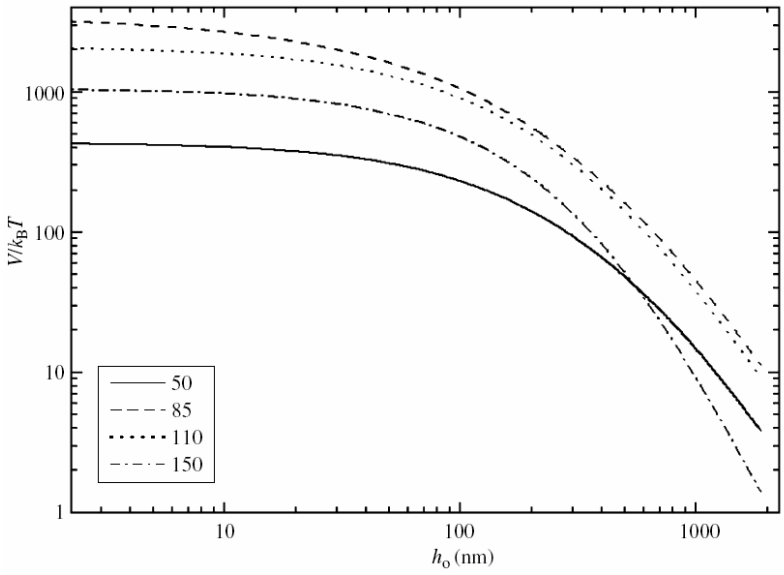

Figure 3.8: Dipolar interaction energy as a function of the inter–particle distance for different values of the contact angle (given in degrees). The asymptotic dipolar behavior as h_0^{-3} is observed at long distances. The values used in the computation were $\sigma = 0.6\mathrm{e}^{-}nm^{-2}$, $f_d = 1$ and $d_{dip} = 0.3$ nm.

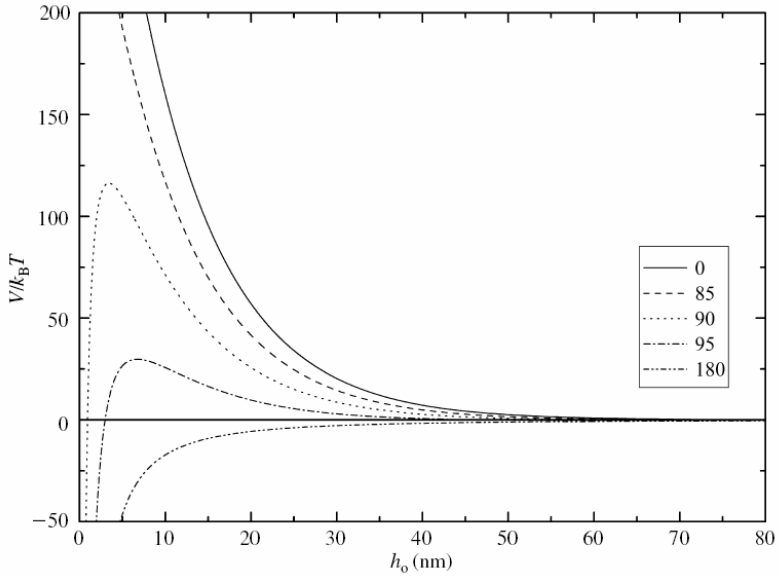

Figure 3.9: Dependence of the DLVO interaction energy between interfacial particles on the inter–particle distance for different values of the contact angle (given in degrees). When changing θ from 0° to 180°, the repulsive barrier disappears. The plotted data were obtained for a 1 mM salt concentration and $\varphi = -40$mV. The Hamaker constants were those indicated in section 3.5.2

that prevents the aggregation of the colloidal particles. The dipolar interaction strength can be changed by varying the dipole fraction on the particle surface. This effect is shown in figure 3.11 where the dependence of the total pair energy on the dipole fraction is indicated for hydrophobic particles. The number of dipoles is indicated as a percentage of the maximum quantity that corresponds with all the surface groups forming dipoles. For 100% of dipoles, it is practically impossible that the potential barrier could be overcome by the particles and so they remain stable without aggregating. Thus, it can be concluded that the dipolar interaction is the most important contribution to the stability of colloidal particles at the air–liquid surface for high salt concentration in the sub-phase.

The dipolar interaction allows one to explain quantitatively why the CCC (the Critical Concentration Coagulation), i.e. the lower salt concentration for which fast colloidal aggregation occurs, is much lower for colloidal particles in dispersion than for aggregation at the interface. Thus, this term justifies the great stability found for colloidal particles at the air–liquid interface.

The shape of the pair interaction potential curves is different for hydrophobic and hydrophilic particles (figure 3.10). Hydrophobic particles can aggregate at a primary minimum while for hydrophilic ones aggregation occurs at a secondary minimum. This difference could explain the restructuring phenomena observed by Hórvölgyi et al. for glass beads of lower hydrophobicity [82], which aggregate at larger distances. The aggregates formed by these particles are re–structured and become more compact.

3.8 The capillary interaction

The capillary interaction has no equivalent in bulk dispersions. When a particle contacts the boundary between two fluid phases, their different interactions with both phases causes the perturbation of the interface from its original form. Usually, the interface is flat and the effect of the particle is to depress or elevate the interface around it to form the so–called meniscus. When particles placed at an interface approach each other, their menisci overlap generating an interaction that can enhance or impede their further approach.

The capillary interaction can be classified in two different categories: *flotation and immersion capillary forces*, depending on whether the interfacial deformation is produced by the weight of the particle or by the wetting

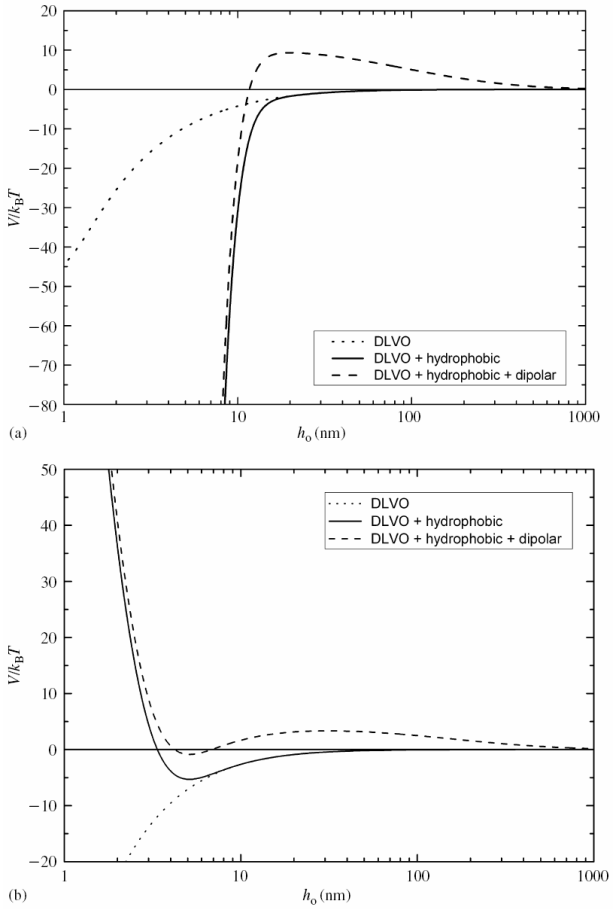

Figure 3.10: Addition of the hydrophobic and dipolar interactions to the DLVO interaction energy for (a) hydrophobic and (b) hydrophilic particles respectively. The parameters used were: (a) $\theta = 82°$, salt concentration = 1M of 1 : 1 electrolyte, $\varphi_0 = 40$mV, surface density of dipoles = 0.18dipoles nm^2. Hydrophobic character is characterized by $W_0 = 60\text{mJm}^{-2}$ and $\lambda_0 = 1$ nm. (b) $\theta = 50°$, salt concentration = 1M of 1 : 1 electrolyte, $\varphi = 56$mV, surface density of dipoles = 0.18 dipoles nm^{-2}. Hydrophobic character is characterized by $W_0 = 3\text{mJm}^{-2}$ and $\lambda_0 = 1$ nm

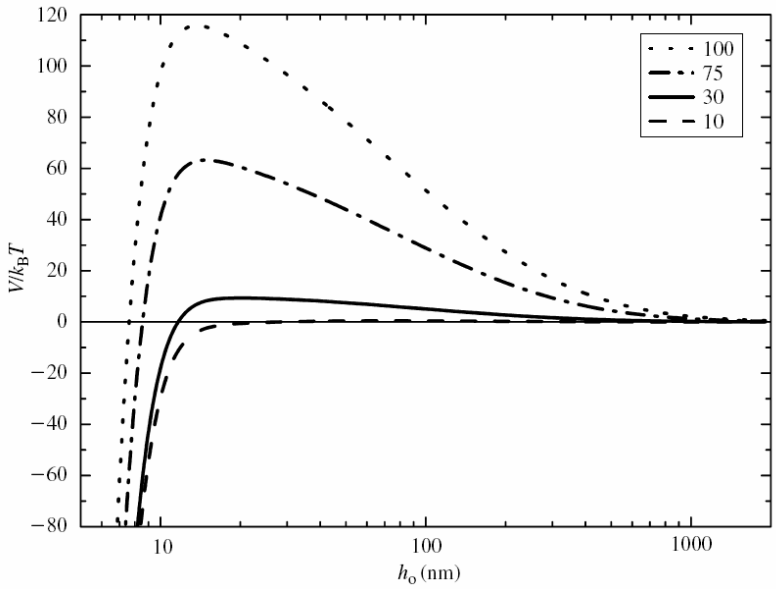

Figure 3.11: Effect of the dipole fraction on the total pair potential for hydrophobic particles at the air–water surface. The values given of 100, 75, 30 and 10 correspond to the percentages of the groups forming dipoles at the surface. The contact angle used and the surface potential were 90° and −40mV, respectively. The salt concentration is 1M of a 1 : 1 electrolyte. Full coverage corresponds to $\sigma = 0.6$ e$^-$nm^{-2} forming dipoles in the air phase.

properties of the particle surface that, in turn, are functions of the position of the contact line and the value of the contact angle rather than gravity. A theoretical description of lateral capillary forces requires to solve the *Laplace equation of capillarity* and to determine the *meniscus profile around the particle*. This can be done by means of an energy approach that accounts for the contributions due to the increase of the meniscus area, gravitational energy and/or wetting energy. Flotation and immersion forces have a similar behavior on the inter-particle separation but very different dependencies on the particle radius and the surface tension of the interface. The flotation capillary forces appear in systems formed by particles trapped at a liquid–fluid interface. This is a long–range interaction and negligible for particles of small size (radius below 10 μm). Immersion forces arise when particles are trapped at a liquid interface over a substrate or in a thin liquid film, and they are long–range interactions that can be very important even for small particles (radius between few nanometres to micrometres). Recent studies have shown that immersion forces can also arise in floating particles when these particles display an irregular meniscus over their surface [83, 84] or when there is an external electric field that pushes the particle into the liquid sub–phase, so-called electrodipping [85, 86, 87, 88]. These immersion interactions between particles trapped at interfaces were used to explain the unexpected long range attractive interaction reported in recent experiments of colloidal particles spread on interfaces [57, 58, 59, 83, 85, 89, 90].

3.8.1 Calculation of the capillary interaction potential

The thermodynamic approach to calculate the capillary interaction potential, V_{men}, between particles at an interface uses the change of free energy that occurs when the colloidal particles approach each other. Its value is given by

$$V_{men}(d) = \hat{F} - F_1 - F_2 = \hat{F} - 2F_1 \tag{3.18}$$

where $\hat{F}$ is the free energy of the equilibrium configuration for the two colloidal particle system and F_1 ($= F_2$) is the single particle equilibrium free energy. In order to calculate the pairwise capillary potential, the terms F_1 (due to the presence of one particle alone at the interface) and $\hat{F}$ have to be determined. These three contributions depend, in turn, on the interface profile near the particles, characterized through the distortion of the meniscus, $\zeta(r)$. $\zeta(r)$ is defined as the difference between the real profile $z(r)$ and

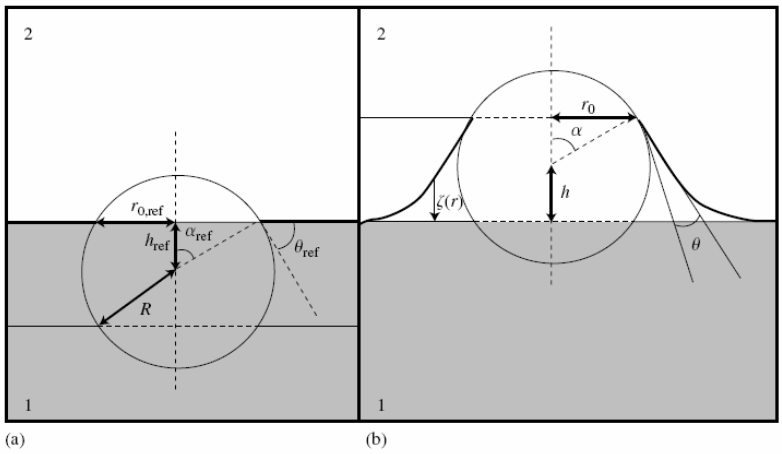

Figure 3.12: (a) Description of the reference state for a colloidal particle confined at an interface where θ_{ref} is the equilibrium contact angle. (b) Description for the deviations from the reference state where ζ is the meniscus profile and h is the height from the particle center to the interface.

a reference profile with flat meniscus, z_{ref}: $\zeta(r) = z(r) - z_{ref}$, where r is the distance between any point of the interface and the center of the particle. We detail the calculations of these three contributions for the free energy below.

One particle at the interface

To compute the capillary free energy of a colloidal particle at the interface it is necessary to consider a reference state, with respect to which changes in free energy will be measured. Usually, the reference state has a planar meniscus with the colloidal particle at such a height h_{ref} that Young's law is satisfied (figure 3.12), i.e. the contact angle θ formed by the planar interface and the single particle surface is given by Young's law in the equilibrium state: $cos\theta = (\gamma_1 - \gamma_2)/\gamma$.

The capillary free energy, F_1, of a single particle at a liquid interface will depend on the meniscus profile $\zeta(r)$, i.e. on the distortion of this meniscus from the reference state. According to ref. [88], the free energy may be separated into the following terms

$$F_1 = F_{cont} + F_{men} + F_{grav} + F_{\Pi} + F_{coll} \tag{3.19}$$

Next, we analyze each of these five contributions separately.

i.- F_{cont} is the free energy due to the change of the areas of the particle exposed to each phase

$$F_{cont} = \gamma_1 A_1 + \gamma_2 A_2 - (\gamma_1 A_{1,ref} + \gamma_2 A_{2,ref}) \tag{3.20}$$

Here, A_i is the surface area of the particle that is in contact with the phase i, and $A_{i,ref}$ is the same area but for the reference case. By using the fact that $A_{1,2} = 2\pi a^2(1 \mp cos\alpha)$ and $A_{1,2,ref} = 2\pi a^2(1 \mp cos\theta)$ together with Young's law (eq. 3.1), equation 3.20 becomes

$$F_{cont} = \pi a^2 \gamma[(cos\theta - cos\alpha)^2 + sin^2\alpha + sin^2\theta] \tag{3.21}$$

This expression can be written in terms of the deformation of the interface at contact $\zeta(r_0)$ by replacing $sin\alpha = r_0/a$, $cos\alpha = (\zeta(r_0) - h)/a$, $sin\theta = r_{0,ref}/a$ and $cos\theta = -h_{ref}/a$. Assuming that the distortion of the meniscus is small, we can approximate the real deformation $\zeta(r_0)$ by the one corresponding to the reference contact line, i.e., $r_0 \approx r_{0,ref}$. Therefore, we approximate $\zeta(r_0) \approx \zeta(r_{0,ref})$ (see figure 3.12)

$$F_{cont} \approx \pi\gamma\left[\zeta(r_{0,ref}) - \Delta h\right] - \pi\gamma(r_0^2 - r_{0,ref}^2) \tag{3.22}$$

where $\Delta h = h - h_{ref}$.

ii.- F_{men} is the free energy contribution due to the change of the meniscus area, given by

$$F_{men} \approx \gamma \int_{S_{men}} dA\sqrt{1 + |\Delta\zeta(r)|^2} - \gamma \int_{S_{men,ref}} dA \tag{3.23}$$

where S_{men} and $S_{men,ref}$ are the meniscus areas (excluding the area occupied by the particle) in the perturbed and the reference system, respectively. For small slopes of the meniscus deformation $\zeta(r)$, i.e. for $|\Delta\zeta(r)|^2 << 1$, and with the approximation $S_{men} \approx S_{men,ref}$, we have

$$F_{men} \approx \gamma\pi(r_{0,ref}^2 - r_0^2) + \frac{1}{2}\int_{S_{men,ref}} |\Delta\zeta(r)|^2 dA \tag{3.24}$$

iii.- F_{grav} represents the change in the gravitation potential energy with respect to the reference state due to displacements of the volumes of the fluid phases

$$F_{grav} \approx \frac{1}{2}\gamma \int_{S_{men,ref}} q^2\zeta(r)^2 dA \qquad\qquad q = \sqrt{\Delta\rho g/\gamma} \tag{3.25}$$

Here, q^{-1} symbolizes the characteristic capillary length which determines the action range of the capillary forces. The capillary length has the typical value $q^{-1} = 2.7$ mm for the air–water surface (and it is higher than any other characteristic length of the system) and $\Delta\rho = \rho_2 - \rho_1$ is the difference between the densities of the fluid phases 1 and 2.

iv.- F_Π accounts for the presence of external fields acting perpendicularly to the fluid interface. Its origin can be diverse. It can be produced by the disjoining pressure between two adjacent phases across the liquid film, by the electrostatic pressure caused by an electric external field, etc. By defining $\Pi(r)$ as the force per unit area, this energetic contribution reads

$$F_\Pi \approx -\int_{S_{men,ref}} \Pi(r)\zeta(r)dA \approx 2\pi \int_{r_{0,ref}}^{\infty} r\Pi(r)\zeta(r)dr \tag{3.26}$$

v.- F_{coll} is the free energy change due to the vertical displacement of the particles

$$F_{coll} = -f\Delta h \tag{3.27}$$

where f is the total force acting on the particle perpendicularly to the interface.

By adding these five terms, we finally obtain the total free energy F_1, calculated with the approximation of small slope of the meniscus ($|\Delta\zeta|^2 << 1$) and assuming $S_{men} \approx S_{men,ref}$

$$\begin{aligned} F_1 \approx 2\pi\gamma \int_{r_{0,ref}}^{\infty} r\left(\frac{1}{2}\left(\frac{d\zeta}{dr}\right)^2 + \frac{q^2\zeta^2}{\gamma} - \frac{1}{\gamma}\Pi\zeta\right)dr \\ +\pi\gamma(\zeta(r_{0,ref}) - \Delta h)^2 - F\Delta h \end{aligned} \tag{3.28}$$

We can find the shape of the meniscus that minimizes the free energy by solving the so–called linearized Young–Laplace equation [91]

$$\left|\frac{dF_1}{d\zeta}\right|_{\zeta_{min}} = 0 \quad \Rightarrow \quad \frac{d^2\zeta}{dr^2} + \frac{1}{r}\frac{d\zeta}{dr} = q^2\zeta - \frac{\Pi(r)}{\gamma} \tag{3.29}$$

The last expression is the key equation giving a theoretical description of the capillary interactions. This equation governs the meniscus shape for a

given configuration of particles at an interface. In order to solve this differential equation, two boundary conditions are necessary. First, the slope of the meniscus height just at the contact line $r = r_0 \approx r_{0,ref}$ has to be [88]

$$\left|\frac{d\zeta}{dr}\right|_{r=r_{o,ref}} = \frac{\zeta(r_{0,ref})}{r_{0,ref}} \tag{3.30}$$

The second requirement comes from the fact that the meniscus has to be asymptotically flat at sufficiently large distances from the particle surface

$$\lim_{r\to\infty} \zeta(r) = 0 \tag{3.31}$$

The solution of the differential equation 3.29 with the boundary conditions (eqs. 3.30 and 3.31) may be expressed in the following general form [88]

$$\begin{aligned}\zeta(r) = \frac{1}{\gamma} I_0(qr) \int_r^\infty s\Pi(s) K_0(qs) ds \\ + \frac{1}{\gamma} K_0(qr) \left(C + \int_{r_{0,ref}}^r s\Pi(s) I_0(qs) ds \right)\end{aligned} \tag{3.32}$$

where $K_0(x)$ and $I_0(x)$ are the modified Bessel functions of zero order of first and second kind, respectively [92], and C is an integration constant which can be obtained with the boundary condition given by equation 3.30. By replacing the explicit form for $\zeta(r)$ into equation 3.8.1 we finally obtain the free energy of one particle, F_1.

Two particles at the interface

In order to calculate the effective pairwise interaction potential, $V_{men}(d)$, between two identical particles at a liquid interface at a fixed lateral distance d in equilibrium, it is necessary to find out the free energy of this configuration. According to Oettel et al. [88] this free energy may be approximated as

$$\begin{aligned}\hat{F} \approx \gamma \int_{S_{men,ref}} dA \left(\frac{1}{2} |\Delta\hat{\zeta}|^2 + \frac{q^2 \hat{\zeta}^2}{2} - \frac{1}{\gamma} \hat{\Pi}\hat{\zeta} \right) \\ + \sum_{\alpha=1,2} \left[\frac{\gamma}{2 r_{0,ref}} \oint_{\partial S_\alpha} dl (\Delta\hat{h}_\alpha - \hat{\zeta})^2 - \hat{F}_\alpha \Delta\hat{h}_\alpha \right]\end{aligned} \tag{3.33}$$

Here, $\hat{\zeta}(r)$ is the meniscus shape in the presence of two particles, $\Delta\hat{h}_\alpha$ are the corresponding heights of each particle, $\hat{\Pi}$ is the vertical force per unit area acting on the interface due to external fields and $\hat{F}_\alpha$ is the force acting on each particle perpendicularly to the interface. S_α is the area of the circular disk defined by the contact line around each particle while ∂S_α are the contact lines (counter-clockwise). In this context, the area of the meniscus in the reference system (flat interface) is defined as $S_{men,ref} = \mathbb{R}^2 - (S_1 \bigcup S_2)$.

By minimizing $\hat{F}$ with respect to ζ as in equation 3.29 the following second order partial differential equation is found

$$\nabla^2\hat{\zeta} = q^2\hat{\zeta} - \frac{\hat{\Pi}}{\gamma} \tag{3.34}$$

This equation has to be solved again imposing two boundary conditions. The first one is the transversality conditions at the boundary defined by the contact lines defined by [88]

$$\partial S_1 \bigcup \partial S_2 \tag{3.35}$$

$$\frac{\partial\hat{\zeta}}{\partial n_\alpha} = \frac{\hat{\zeta}(\vec{r}) - \bar{\zeta}_\alpha}{r_{0,ref}} - \frac{f}{2\pi\gamma r_{0,ref}} \tag{3.36}$$

where $\partial/\partial n_\alpha$ is the derivative in the outward normal direction of ∂S_α, and

$$\bar{\zeta}_\alpha \equiv \frac{1}{2\pi r_{r,ref}} \oint_{\partial S_{alpha}} dl\hat{\zeta} \tag{3.37}$$

is the mean height of the distortion of the meniscus at the contact line.

The second boundary condition tells us again that the meniscus has to be asymptotically flat at sufficiently large distances from the particle surface

$$\lim_{r\to\infty} \hat{\zeta}(\vec{r}) = 0 \tag{3.38}$$

The final solution of equation 3.34 with the boundary conditions given by equations 3.36 and 3.38 is a very complex analytical problem that can only be solved in the homogeneous case, i.e. for $\hat{\Pi} = 0$ [93]. The general problem is solved introducing the approximation of superposition, valid in the limit of large interparticle separation ($d >> a$) [94]

$$\begin{aligned} \hat{\zeta}(r) &\approx \zeta_1(r) + \zeta_2(r) \\ \hat{\Pi}(r) &\approx \Pi_1(r) + \Pi_2(r) \\ F(r) &\approx F_1(r) \approx F_2(r) \end{aligned} \tag{3.39}$$

where ζ_α, Π_α, F_α, with $\alpha = 1, 2$, are the meniscus profile, the stress of the interface and the force acting on the interface due to each particle in analogo to the case of one particle at the interface. The effective potential between two particles due to the interface deformation that they produce can be calculated now using equation 3.18. Oettel et al. [88] calculated an approximate general form for the effective potential due to the meniscus deformation using the assumption of superposition

$$\begin{aligned} V_{men}(d) \approx &- \int_{S_{men,ref}} \Pi_1 \zeta_2 dA + \int_{S_1} \Pi_2 \zeta_2 dA - \gamma \oint_{\partial S_1} \frac{\partial(\zeta_1\zeta_2)}{\partial n_1} dl \\ &- \frac{1}{2}\gamma \oint_{\partial S_1} \frac{\partial(\zeta_2^2)}{\partial n_1} dl + \frac{\gamma}{r_{0,ref}} \oint_{\partial S_1} |\bar{\zeta} - \zeta_2|^2 dl - 2f\bar{\zeta} \end{aligned} \tag{3.40}$$

where $\bar{\zeta} \equiv \frac{1}{2\pi r_{0,ref}} \oint_{\partial S_1} \zeta_2 dl$, is the mean height of the single particle meniscus with respect to the contact line of the other colloidal particle. There are two different asymptotic behaviors of the effective potential ($a << d << q^{-1}$), depending on the relation between the dimensionless quantities ϵ_Π and ϵ_F, defined as

$$\begin{aligned} \epsilon_F &\equiv \frac{-f}{2\pi\gamma r_{0,ref}} \\ \epsilon_\Pi &\equiv \frac{1}{2\pi\gamma r_{0,ref}} \int_{S_{men,ref}} \Pi dA \end{aligned} \tag{3.41}$$

All the forces acting on the particles are included in ϵ_F, while the stress over the interface is included in ϵ_Π. Thus, the ratio between ϵ_F and ϵ_Π is directly related ti that between f and Π. If $\epsilon_\Pi \neq \epsilon_F$, V_{men} reads

$$\begin{aligned} V_{men}(d) &\approx -2\pi\gamma r_{0,ref}^2 (\epsilon_F - \epsilon_\Pi)^2 K_0(qd) \\ &\approx -2\pi\gamma r_{0,ref}^2 (\epsilon_F - \epsilon_\Pi) \ln \frac{2e^{-\gamma_E}}{qd} \end{aligned} \tag{3.42}$$

where $\gamma_E = 0.577216$ is the Euler's constant. This is a long-range (logarithmic) attractive effective potential that does not depend on the sign of the forces and stress acting on the system. If $\epsilon_\Pi = \epsilon_F$, then

$$V_{men}(d) \approx -2\Pi(d) \textstyle\int_{S_{men,ref}} \zeta dA \quad \text{with } S_1 = S_2 = S \tag{3.43}$$

In this case, $V_{men}(d)$ has the same dependence on the distance as the stress. It is a short-ranged interaction that can be attractive or repulsive depending on the form of $\Pi(d)$. Typically $\Pi(d) \sim d^{-n}$ so $V_{men}(d) \sim d^{-n}$.

Capillary flotation forces

In this particular case, there are no stresses acting at the meniscus ($\Pi = 0$) and the force f on the particles is due to their weight and the buoyancy force. Thus, we are in the case $\epsilon_F \neq \epsilon_\Pi$ with $\epsilon_\Pi = 0$. Using equation 3.43 we obtain

$$V_{men}(r) \approx -2\pi\gamma r_{0,ref}^2 \epsilon_F^2 K_0(qr) = -2\pi\gamma Q^2 K_0(qr) \tag{3.44}$$

where $Q = r_{0,ref}\epsilon_F$ is the so-called "capillary charge" [84, 91, 94] by analogy with the $2D$ electrostatic problem. The dependence of the capillary charge on the particle radius a is easily obtained from equation 3.41

$$Q = r_{0,ref}\epsilon_F = \frac{-F_g}{2\pi\gamma} \propto m \propto a^3 \quad \Rightarrow \quad Q^2 \propto a^6 \tag{3.45}$$

Thus, the capillary flotation interaction strongly depends on the particle radius a. The "capillarity charges" for floating particles can be expressed in terms of a and the three-phase contact angle, θ, through the expression [95]

$$Q = \frac{1}{6} q^2 a^3 (2 - 4D + 3con\theta - cos^3\theta) \tag{3.46}$$

where $D = (\rho_S - \rho_1)/(\rho_2 - \rho_1)$ and ρ_S is the density of the colloidal particle. The values for the flotation capillary interaction for two spherical particles at contact ($d = 2a$) trapped at an air–water surface are plotted in figure 3.13 versus the particle radius. As can be seen, the flotation capillary interaction is negligible, i.e. $V(2a) << k_B T$, for particles with a $a < 10$ μm. In other words, the weight of floating micrometers (or submicrometrers) sized particles is too small to create any surface deformation.

Capillary immersion forces

Long–range attractive forces between micrometer–sized particles at a fluid interface were experimentally detected [58, 57, 59, 83, 85, 96, 90] and attributed to immersion capillary interactions. Usually, these kind of capillary interactions come out when colloidal particles are trapped in a thin liquid film [91, 97] or at a liquid interface formed over a substrate [98]. Nevertheless, it has been reported recently that the immersion capillary interactions between floating particles may also appear when the three–phase contact line (particle–liquid–fluid) is irregular rather than flat due to the non-homogeneous wetting of the particle surfaces [83, 84] or when there is an

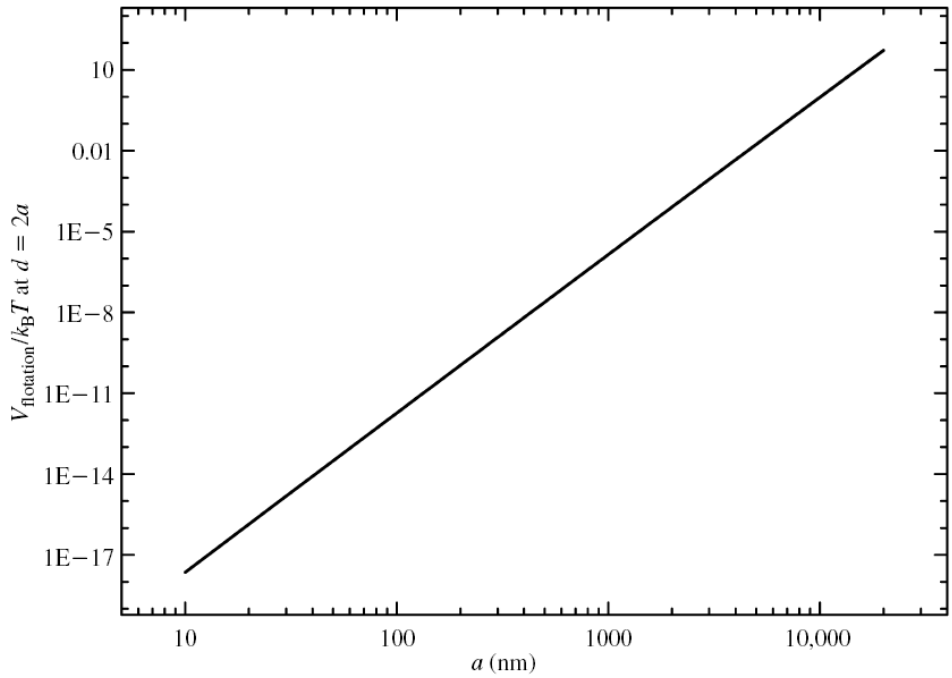

Figure 3.13: Floating capillary interaction energy between two spherical colloidal particles in contact ($d = 2a$) trapped at the air–water surface versus the particle radius, for a contact angle $\theta = 82°$. As can be seen, the interaction is negligible for particles with radius under 10 μm

electrical stress that causes an immersion of the particles into the liquid phase [85, 86, 87]. However, some of these models are still nowadays incomplete and none of them could explain all the characteristics of the mesostructures found experimentally[1]. Here, we will comment on these immersion capillary interactions between floating particles. Then, we will focus on the long-range behavior of those interactions used here to explain the attractions reported experimentally for large inter-particle distances.

Roughness of the particle surface

Notwithstanding, we have not considered particle roughness in our model. The surface deformation of the meniscus could appear even with small particles (submicrometer–sized) if the phase contact line on the particle surface is irregular rather than circular (see figure 3.14-A). This is the case of colloidal particles with an irregular shape with surface roughness, chemical inhomogeneities, etc. In such cases, the meniscus shape around the colloidal particles is described by the expression [83]

$$\zeta(r,\varphi) = \sum_{i=1}^{\infty} K_i(qr)(A_i cos(i\varphi) + B_i sin(i\varphi)) \tag{3.47}$$

which is the solution of the linearized Young–Laplace equation for small meniscus slopes in cylindrical coordinates (r, φ). Here A_i, B_i are integration constants and $K_i(x)$ is the modified Bessel function of order i. For $qr << 1$, $K_i(qr) \propto (qr)^{-i}$, in this case the equation 3.47 reduces to a multipolar expansion (analogue to an electrostatic multipolar expansion in 2D).

The capillary forces between particles with an irregular contact line could be considered as a kind of immersion force insofar as they are related to the particle wettability, rather than to the particle weight. A theoretical description of the lateral capillary force between colloidal spheres with an undulated contact line was recently given by Stamou et al [83]. They realized that the leading multipole order in the capillary force between such particles is the quadrupole–quadrupole interaction ($i = 2$ in equation 3.47) (see figure 3.14-B). The capillary interaction energy is given by

$$V_{rough}(d) \approx -12\pi\gamma H^2 cos(2(\varphi_A + \varphi_B)) \left(\frac{r_c}{d}\right)^4 \quad \text{for } i = 2;\ d >> 2r_c \tag{3.48}$$

[1]We will see a complete description of such mesostructures in chapter 7

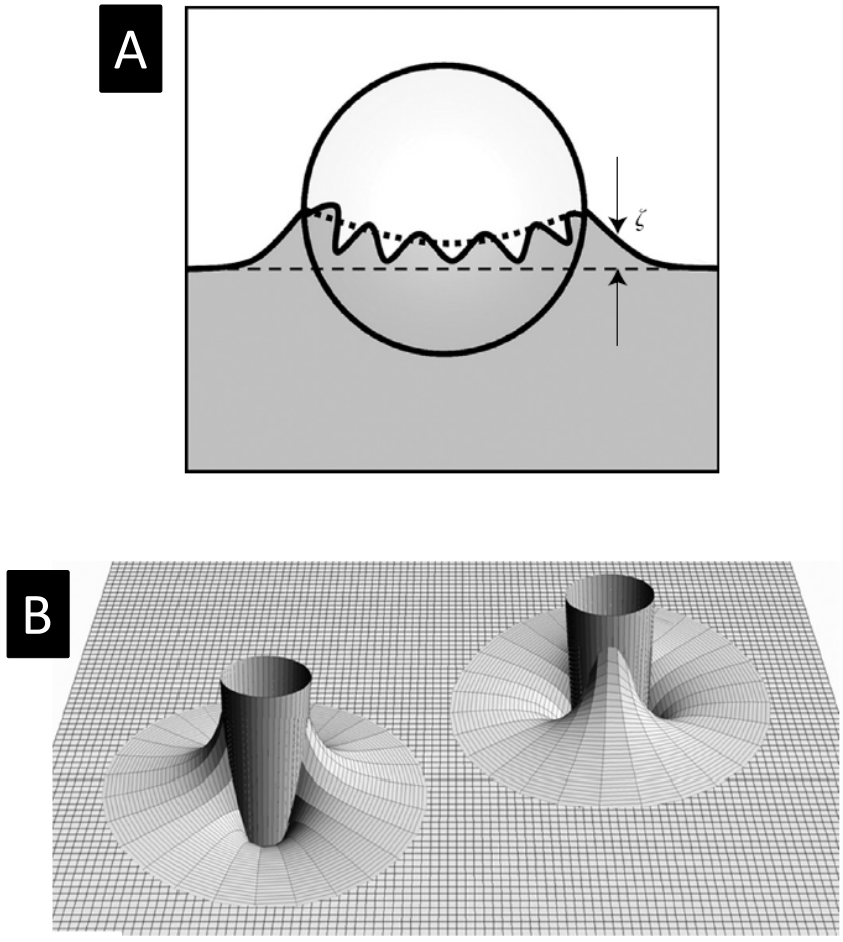

Figure 3.14: (A) Sketch of the contact line for a colloidal particle at a fluid interface. The dashed line is the ideal flat contact line, the continuous line corresponds of the undulated contact line and the dotted line is the quadrupoles contribution of the irregular contact line. (B) Representation of the quadrupolar term for two colloidal cylindrical particles trapped at a fluid interface. The total interface deformation, which is due to the presence of the particles, depends on the mutual orientation between them.

where H is the maximum amplitude of the deformation of the contact line at the particle surface, $r_c = a \cdot sin\theta$ is the contact radius and φ_A and φ_B are subtended angles between the diagonals of the respective quadrupoles and the line connecting the centers of both particles. Thus, the pairwise interaction potential at long distances could be a combination of $V_{rough}(d)$ together with the dipolar interaction $V_{dip}(d)$.

$$V_{d>>a}(d) = V_{dip}(d) + V_{rough}(d) \approx \frac{A}{d^3} - \frac{Bcos(2\varphi_A + 2\varphi_B)}{d^4} \tag{3.49}$$

where A and B are constants independent of both the inter–particle distance (d) and particle orientation ($\varphi_A + \varphi_B$). In this way, even a minimal roughness of the contact line could be sufficient to produce a significant capillary attraction [83]. For multipoles, the sign and the magnitude of the capillary force depend on the particular mutual orientation. So, quadrupoles tend to assemble in a square lattice [84].

This model is, however, rather incomplete since the meniscus deformation is calculated with the approximation of the absence of stress and perpendicular forces acting on the interface and the particles, respectively (i. e. $\Pi = 0$ and $F = 0$). According to these approximations, the effective potential associated with this deformation is obtained and added to the dipolar interaction. So, for a correct analysis, it is necessary to introduce the electrostatic stress due to the dipolar field in the Young–Laplace capillary equation. This adds new terms to the effective interaction potential with the same dependence on the distance as that found by Stamou et al. [83]. Therefore, the introduction of this new term does not change quantitatively the interaction potential: the dependence of the dipolar interaction with the distance is like $1/r^3$ and the attractive interaction has again an asymptotic behavior like $1/r^4$.

Meniscus deformation due to an electric field

The mechanical equilibrium of the colloidal particle at the interface (figure 3.12-a) is given by the counterbalance of a normal external force and the surface tension force $f(= 2\pi r_c \gamma \sin\theta)$. In the case of floating capillary forces, the normal force is due to gravity and the magnitude of the surface distortion decreases rapidly when decreasing the particle size, becoming negligible for particles with a radius $a < 10$ μm.

Nevertheless, for such small particles, Nikolaides et al. [85] suggested that the normal force f could have also an electric origin, f_{el}, rather than only

gravitational, f_g. They proposed that the asymmetric charging of the particles absorbed at interfaces could produce a dipolar field. The electrostatic force associated with this field could be responsible for the interfacial deformation and the lateral capillary interactions. With these considerations, and neglecting the electrostatic stress acting on the interface ($\Pi_{el}(r) = 0$), they finally obtained a long–range (logarithmic) capillary attraction. However, if we take this stress into account the situation changes drastically. Then, the new dependence [86, 85] on the inter–particle distance is $1/d^6$ rather than logarithmic, i.e. it is a short–range interaction that does not explain completely the origin of the secondary minimum.

In turn, Danov et al. [87] reported experimental results showing that the interfacial deformation around glass particles (with radius between 200 and 300 nm) at the oil–water interface is dominated by an electrical force. They called this effect electrodipping[87]. In that work, they suggested that this force is due to charges at the particle–oil boundary (or, in general, at the particle-non-polar phase boundary in general). They solved numerically the electrostatic boundary problem which gives rise to a long-range (logarithmic) electric field than induces the capillary attraction between two floating particles. However, they calculated the pairwise effective potential solving the Young–Laplace capillary equation only in the presence of gravity ($\Pi = 0$, $F_{el} = 0$, $F_g \neq 0$) with the superposition approximation as usual the solution even in the case of $\Pi \neq 0$. Hence, the solution given in ref. [87] appears inaccurate because the approximation of superposition is not correctly applied and new terms arise when the capillary equation with $\Pi \neq 0$ is formally solved. Moreover, Danov et al. solve the electrostatic problem using the asymptotic behavior ($r >> r_{0,ref}$) of $\Pi(r)$, but the dominant contribution to the interaction potential due to the meniscus deformation stems from points $r \approx r_{0,ref}$. Accordingly, they obtain a non–vanishing pre-factor of the logarithmic term in the interaction potential. Therefore, the presence of charges at the particle–non–polar phase boundary cannot explain an attractive logarithmic interaction.

Oettel et al. [88] proposed a logarithmic long–range attractive attraction tuned by a small external electrostatic field. However, this attraction is only possible if the net force acting on the system does not vanish. In order to show this, they considered the total stress tensor $\hat{T}$ which consists of the Maxwell stress tensor (due to the electrostatic field) and a diagonal osmotic pressure tensor (due to the electrolyte). The total force acting on the whole system (interface and particles) perpendicularly to the interface can be calculated

through.

$$f_z = \hat{e}_z \cdot \oint_{S_{tot}} d\vec{A} \cdot \hat{T} = 2\pi\gamma r_{0,ref}(\epsilon_\Pi - \epsilon_F) \tag{3.50}$$

where $S_{tot} = S_{men} + S_1 + S_2$. In the absence of external forces, $f_z = 0$, we are in the case of $\epsilon_\pi = \epsilon_F$ and we have to apply equation 3.43 which gives a short–range interaction. Thus, the existence of a net force acting on the interface is necessary to have an attractive logarithmic (long–range) interaction. If $f_z \neq 0$, then $\epsilon_\pi \neq \epsilon_F$ and so we have to use equation 3.8.1 which gives a long–range interaction. Therefore, in the presence of an external electric field, the values of ϵ_π and ϵ_F; can be calculated numerically solving the electrostatic boundary problem. Subsequently, the interaction potential due to the interfacial deformation, $V_{men}(d)$, can be theoretically obtained by using equation 3.8.1.

Oettel et al. calculated the external electric field necessary to obtain the long–range attractive interaction shown in ref [85] and they obtained a relatively small value $E \approx 1.8\text{x}10^{-4}$ Vm^{-1}. Indeed, an electric field $E \sim 10^{-3}$ Vm^{-1} is enough to provoke a secondary minimum of about 1 k_BT. These calculations indicate how sensitive the system can be to spurious external electric fields that give the required long-range attraction. This model, however, is not able to explain such an attraction for isolated systems ($f_z = 0$). In view of these conclusions, further effort (theoretical and experimental) is needed to achieve a complete understanding of the interactions that appear when colloidal particles are spread at a liquid interface.

3.9 Conclusions

The interactions between particles in monolayers have been theoretically discussed. These interactions are dependent on both the properties of the fluids that make up the interface and on the nature of the adsorbed particles. We can distinguish three different stability behaviors: particle monolayers that remains stable for a long time, unstable monolayers with clusters of fractal structure and the mesostructure formation. In the first case some very regular geometrical structures have been observed suggesting the existence of long-ranged particle interactions. When the structures are fractal in character the interparticle repulsions are short–range, and the total interaction potential shows a minimum at very short distances. The third case, the formation of mesostructures, is still a controversial subject and we will study

them in chapter 7.

The different terms of the inter-particle interaction energy are double layer and dispersion interactions (2-D DLVO), capillary interactions (which are intrinsic to interfacial phenomena and have no analogy in the 3-D case), structural forces and monopolar and dipolar interactions. These terms have a different weight in the total interaction energy. The capillary interaction involved the flotation and immersion capillary forces, depending on whether the interfacial deformation is produced by the weight of the particle or by the wetting properties of the particle surface that, in turn, are functions of the position of the contact line and the value of the contact angle rather than gravity. Immersion forces are long-range interactions and play an important role in the behavior of colloidal monolayers even for small particles.

Chapter 4

Voronoi diagrams

4.1 Introduction

A very useful tool to determine the correlations and ordering in space–filling systems is the one based on the topological properties. *Topology is the mathematical study of the properties that are preserved through deformation, twistings, and stretching of objects.* The study of the topological properties of such systems can be achieved with the help of the *Voronoi construction*, which creates a division of the whole space in irregular partitions (*cells*). Such a method has been successfully used to describe the evolution of many natural systems, as soap froths [99, 100, 101, 102, 103], propagation of defects in foams [104, 105], metallurgical grains [106], biological tissues [107], crack patterns in ceramics [108], etc. Even though these systems differ in the way how they evolve (mitosis for biological tissues, diffusion of gas between neighbor cells for soap froths,...), it is found that most of them arrive at a final stationary state where topological properties remain constant. Moreover, this state is described by the same common laws, that come from maximum entropy predictions [109, 110]. However, all these works are essentially mean field studies and only account for the correlations between adjacent cells. In recent times, the description of the long–range topological ordering and the correlation between non–nearest neighbors have attracted interest and new theoretical methods based on shell structure have been applied to the understanding of the evolution of cellular systems [111, 112, 113, 114, 115, 116].

4.2 Voronoi diagrams

There is a one–to–one correspondence between many–particle systems, such as simple fluids or granular materials, and cellular systems. Mathematical tools provide the geometric duality between the spatial distribution of particles and a cell structure. For instance, the Voronoi construction method provides a unique map of an arbitrary arrangement of points named generators to a cellular tessellation of space. To each generator a Voronoi cell is assigned containing all points closer to this generator than to any other. If all generators are located on a Bravais lattice, the Voronoi cells are identical with the Wigner–Seitz cells. Therefore, the Voronoi construction, which is applicable to any distribution of generators, can be regarded as a natural generalization of the Wigner–Seitz construction for crystal lattices.

The number of sides of a cell, n, informs about the number of closest neighboring generators, while the area of the cell, A, is related to the total area filled by each generator. Hence, the Voronoi diagram of a set of points give us a tool to study the repartition of the space by these generators.

4.2.1 Definition

For any (topologically) discrete set $P = \{p_1, p_2, ..., p_n\}$ / $p_i \, \epsilon \, \mathbb{R}^D$ of points in Euclidean space and for almost any point x, there is one point of P closest to x. The word *almost* is occasioned by the fact that a point x may be equally close to two or more points of P.

In general, the set of all points closer to a point p_k of P than to any other point of P is the interior of a (in some cases unbounded) convex polytope called the *Dirichlet domain* or Voronoi cell $V(p_k)$ for p_k.

$$V(p_k) = \{x \epsilon \mathbb{R}^D : |p_i - x| \leq |p_j - x| \forall j \neq i\} \tag{4.1}$$

The set of such polytopes tessellates the whole space, and it is called the Voronoi tessellation corresponding to the set P. If the dimension of the space is only $D = 2$, then it is easy to draw pictures of Voronoi tessellations, and in that case the set of Voronoi cells $V(p_i)$ is called *Voronoi diagram* $V(P)$.

The dual graph for a Voronoi tessellation corresponds to the *Delaunay triangulation* of the same set of points P. It is obtained by connecting generators of neighboring Voronoi cells, as illustrated in figure 4.1. The resulting structure represents a tessellation of the plane by triangles of different shapes.

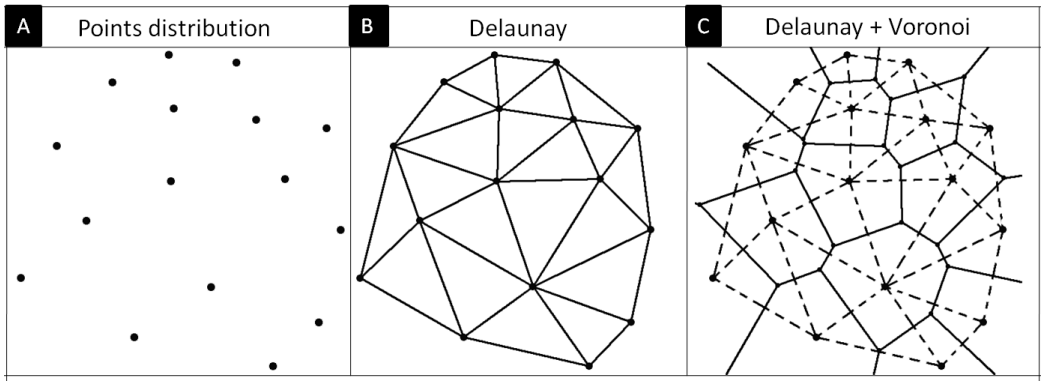

Figure 4.1: A) Set of random points. B) Delaunay triangulation of such points. C) Voronoi diagram (continuous lines) and Delaunay triangulation (dashed lines) of the set of points.

The nodes, located on the positions of generators of the Voronoi cells, have a varying coordination in the triangulated structure.

In figure 4.2 examples of construction of some Voronoi diagrams are shown:

***a) 2 points diagram*:**

If P contains only two points, p_1 and p_2, then the set of all points equidistant from p_1 and p_2 is a hyperplane – an affine subspace of co–dimension 1. That hyperplane is the boundary between the set of all points closer to p_1 than to p_2, and the set of all points closer to p_2 than to p_1. It is the perpendicular bisector of the line segment from p_1 and p_2.

***b) 3 points diagram*:**

If P contains three points p_1, p_2, p_3, the Voronoi diagram is formed by the three perpendicular bisectors to the segments $\overline{p_1p_2}$, $\overline{p_2p_3}$ and $\overline{p_1p_3}$. The intersection between the three bisectors is a *Voronoi vertex*.

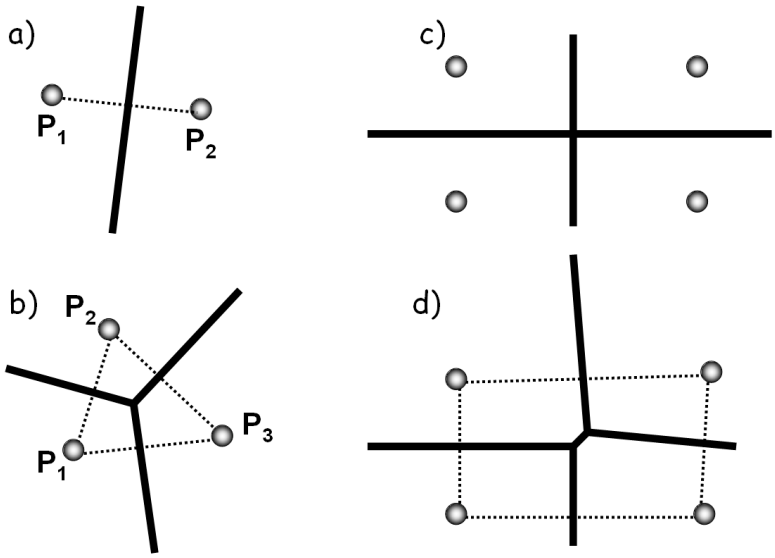

Figure 4.2: Diagram associated to *a*) two points. *b*) three points. *c*) four points with degeneration (the Voronoi vertex is of fourth order. *d*) four points without degeneration (two vertex of third order)

***c and d) 4 points diagram*:**

If P is composed by four points p_1, p_2, p_3, p_4 that are the vertex of a rectangle, the resulting Voronoi diagram is showed in figure 4.2–*c*. In this diagram, the four bisectors intersect among them in the same vertex. Therefore, this is a Voronoi vertex of order 4 (*degenerate vertex*). A small displacement of any point of P modifies the diagram and causes the apparition of two non–degenerated vertex of order 3 (figure 4.2–*d*). In this work, we will consider only non–degenerated Voronoi diagrams where only three edges meet in a vertex.

4.3 Statistical properties of the Voronoi diagrams

In two–dimensional coagulation, the center of masses of the growing clusters can be used to build the Voronoi diagram, where each cell represents a single cluster (figure 4.3). The number of sides (n) and the area (A) of the cells

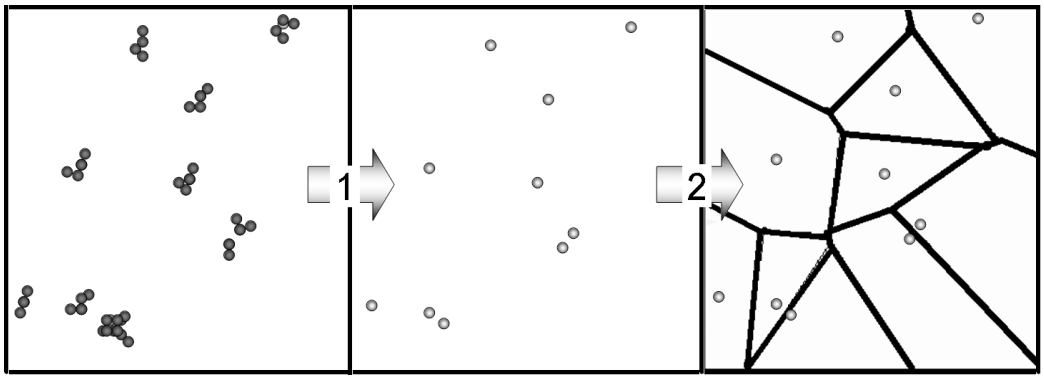

Figure 4.3: (1) Each aggregate i is substituted by its mass center p_i. Therefore, in each instant of the coagulation process we will have a set of points $P = \{p_i\}_{i=1,N_c}$. (2) We associate to each point of the set P_i its Voronoi cell defined as the region of the space that is closer to p_i than to the other points of P.

are related to the number of nearest neighbors and the size of the clusters, respectively. The evolution of the cellular pattern is ruled by two independent processes. The first one is the diffusive motion of the clusters in the plane: every time a cluster moves a large enough distance, a new rearrangement of the cells is found in terms of a local side switching (also called T1 process). The second process takes place when two clusters coagulate together to form a larger cluster; here, one of the cells disappears and the surrounding cells are accommodated to the new configuration (T2 process) [102]. Both processes (figure 4.4) induce a topological restructuring of the two–dimensional froth that is connected in general, to the physical conditions of the aggregating system, and more specifically to the aggregation regime and the particle packing fraction φ.

The number of sides and area of the cells will be statistical properties distributed according to $P(n, A)$, defined as the probability of finding a cell of n sides and area A. This probability is normalized in the form:

$$\int_A \sum_n P(n, A) = 1 \tag{4.2}$$

The probability to find a n-sided cell is given by

$$P(n) = \int_A P(A, n) dA \tag{4.3}$$

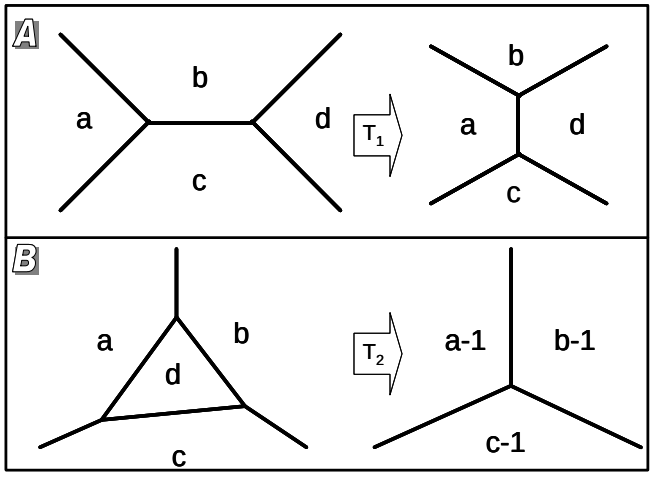

Figure 4.4: (A) T_1 process: topological transformation consisting of an exchange of neighbors between four cells. (B) T_2 process: topological transformation where a cell is created or destroyed.

Analogously, the area distribution $P(A)$ is obtained by the summation over all number of sides:

$$P(A) = \sum_n P(A, n) \tag{4.4}$$

The average area per cell, $< A >$, is just given by the total area of the tessellation divided by the total number of cells:

$$< A >= \sum_n \int_A AP(n, A)dA = \frac{A_0}{N_c} \tag{4.5}$$

where A_0 is the area of the whole froth, and N_c is the total number of cells.

4.3.1 Euler's theorem

In a Voronoi diagram composed by a large number of cells ($N \to \infty$), the number of vertex V and the number of edges E are related through the Euler's formula [117]:

$$N - E + V = \chi \tag{4.6}$$

where χ is a topological invariant that has a constant value which depends on the dimension of the space where the Voronoi diagram is defined. Moreover, as each edge represent the boundary between two cells. The number of cells and edges are related through:

$$E = \frac{1}{2}\sum_{i=1}^{N} N(n)n \tag{4.7}$$

where $N(n)$ is the number of n–side cells.

In this work we consider that the Voronoi vertex are not degenerated, and so, these vertex have order 3 (they are formed by the intersection of 3 edges). Therefore, the vertex and the edges numbers are related by

$$V = \frac{1}{3}\sum_{i=1}^{N} N(n)n \tag{4.8}$$

If we introduce 4.7 and 4.8 in 4.6, we obtain the following relationship for the average cell edge number:

$$< n >= \sum_{i=1}^{N} nP(n) = \sum_{i=1}^{N} n\frac{N(n)}{N} = 6 - 6\chi/N \xrightarrow{N\to\infty} 6 \tag{4.9}$$

As conclusion, for a Voronoi diagram composed by infinite cells without degenerated vertex, each cell has in average 6 nearest neighbors.

The general property 4.9 of planar cell structures greatly simplifies their analysis. It should be kept in mind that only the average cell topology is fixed. In natural and constructed cell structures, the appearance of cells with topologies $n \neq 6$, is the rule rather than the exception. The deviation from the *ideal froth* where there are only 6–sided cells can be measurement using the second central moment of the side number distribution $P(n)$ defined as:

$$\mu_2 =< n^2 > - < n >^2 = \sum_{n=3}^{\infty}(n-6)^2 P(n) = \sum_{n=3}^{\infty} Q_n^2 P(n) \tag{4.10}$$

where we defined the topological charge of an n–sided cell as $Q_n = 6 - n$.

In the literature, the variance μ_2 of the cell topologies is frequently used as measures of the degree of disorder in the froth.

4.3.2 Lewis's law

Investigating the cell structure of cross–sections of different biological tissues, the American botanist Lewis [118] discovered a linear increase of the mean area of a cell with the edges number n:

$$< A(n;t) >= k(t)(n - n_0(t)) \tag{4.11}$$

The Lewis's law has been confirmed for many natural and constructed cell structures, except for cells with $n = 3$ or 4 sides.

The linearity predicted by 4.11 has long been matter of controversy. Various "derivations" of this law have been proposed [117, 109, 119], mostly involving the maximization of an entropy defined as a functional of the probability edges distribution, $P(n)$. None of these derivations, however, is based on first principles, and Chiu [120, 121] has shown that entropy arguments of this kind do not allow firm conclusions. Moreover, significant deviation from the Lewis's law has been observed in binary and fractal tessellations.

4.4 Neighboring correlations: the Aboav–Weaire law

The topological correlations between neighboring cells are contained in the topological two-point function $p^{(2)}(n,k)$, defined as the probability that an arbitrarily chosen edge separates a k- and an n-sided cells. Consequently, the probability that one side of an arbitrarily chosen edge belongs to an n–sided cell is:

$$p^{(1)}(n) = \sum_k p^{(2)}(n,k) \tag{4.12}$$

This distribution differs from the n–sided cell distribution $P(n)$ since each n–sided cell is counted n times. Therefore, the relation between $p^{(1)}(n)$ and $P(n)$ is:

$$p^{(1)}(n) = \frac{n}{< n >} P(n) \tag{4.13}$$

We can define now the *topological pair correlation function for neighboring cells*[1], $g(n,k)$, as the function that relates the two–point function $p^{(2)}(n,k)$

[1] $g(n,k)$ is a particularization of the general topological pair correlation function (that will be defined in section 4.5.4), $C_j(n,k)$, for $j = 1$

with the one–point function $p^{(1)}(n)$ as:

$$p^{(2)}(n,k) = g(n,k)p^{(1)}(n)p^{(1)}(k) \tag{4.14}$$

Insertion of 4.14 in equation 4.12 yields to:

$$p^{(1)}(n) = \sum_k g(n,k)p^{(1)}(n)p^{(1)}(k) \;\; \Rightarrow \;\; \sum_k g(n,k)p^{(1)}(k) = 1 \tag{4.15}$$

The effective correlation between two adjacent cells characterized by a topological charge of Q_n and Q_k, respectively, can be defined as:

$$\rho := \frac{<< Q_n Q_k >> - << Q_k >>^2}{<< Q_k >>^2} \tag{4.16}$$

where the brackets corresponds to the average of all pairs of neighbors cells ($<< ... >> = \sum_{n,k} p^{(2)}(n,k)$).

Now, we can calculate the average number of sides of the neighbor cells of n-sided cell, $m(n)$, as:

$$m(n) = \sum_k k g(n,k) p^{(1)}(k) \tag{4.17}$$

In the case of the *topological gas* (TG) the cell structure is uncorrelated, i. e., $g(n,k) = 1 \; \forall k,n$, and using 4.10 and 4.13:

$$\begin{aligned} m^{TG} = \sum_k k p^{(1)}(k) = \frac{1}{<n>} \sum_k k^2 P(k) = \\ \frac{1}{<n>} \sum_k ((k - <n>)^2 - <n>^2 + 2k<n>) P(k) = \\ \frac{1}{<n>}(\mu_2 + <n>^2) = <n> + \frac{\mu_2}{<n>} \end{aligned} \tag{4.18}$$

An exact identity can be derived from equations 4.17, 4.10 and 4.15:

$$\begin{aligned} \sum_n p^{(1)}(n) m(n) = \sum_{n,k} g(n,k) k p^{(1)}(n) p^{(1)}(k) = \\ \sum_k k p^{(1)}(k) \sum_{n,k} p^{(1)}(n) g(n,k) = \sum_k k p^{(1)}(k) = \\ \frac{1}{<n>} \sum_k k^2 P(k) = m^{TG} \end{aligned} \tag{4.19}$$

where is interesting to see that,

$$\sum_n nm(n)P(n) = \sum_k k^2 P(k) \tag{4.20}$$

This relationship is known as the *Weaire's sum rule* [122]. Now, using the equations 4.4, 4.10, 4.13, 4.14, 4.15 and 4.17:

$$<< Q_k >>= \sum_n \sum_k p^{(2)}(n,k)Q_k = \underbrace{< n > \sum_n \sum_k p^{(2)}(n,k)}_{I} - \underbrace{\sum_n \sum_k kp^{(2)}(n,k)}_{II} \tag{4.21}$$

$$I =< n > \sum_n \sum_k p^{(2)}(n,k) =< n > \sum_n p^{(1)}(n) \sum_k g(n,k)p^{(1)}(k) = \sum_n nP(n) =< n > \tag{4.22}$$

$$II = \sum_n \sum_k kp^{(2)}(n,k) = \sum_k kp^{(1)}(k) \sum_k g(n,k)p^{(1)}(n) = \frac{1}{< n >} \sum_k k^2 P(k) =< n > + \frac{\mu_2}{< n >} \tag{4.23}$$

$$I + II = -\frac{\mu_2}{< n >} \tag{4.24}$$

$$<< Q_n Q_k >> - << Q_k >>^2 = \sum_n \sum_k p^{(2)}(n,k) - << Q_k >> \sum_k \sum_n p^{(2)}(n,k)Q_k = \sum_n \sum_k p^{(2)}(n,k)(Q_k Q_n - << Q_k >> Q_n) \tag{4.25}$$

Therefore, the correlations ρ defined in 4.16 can be rewritten as:

$$-\rho\frac{\mu_2^2}{< n >} =< n > \sum_{n,k} p^{(2)}(n,k)(<< Q_k >> -Q_k)Q_n =$$

$$\sum_n P(n)(nm(n) - nm^{TG})Q_n \tag{4.26}$$

$$\tag{4.27}$$

Finally, it is reduced to:

$$nm(n) - nm^{TG} = -\rho\frac{\mu_2}{< n >}Q_n \tag{4.28}$$

Originally, the linear variation of $nm(n)$ with n has been discovered empirically by Aboav, analyzing the cross–sections of poly–crystals. Later, the relation 4.28, known as the Aboav–Weaire law [123, 122, 117], has been confirmed in high accuracy by experiments and simulations. Usually, the Aboav–Weaire parameter a is used instead of the correlations ρ. The relation between both parameters is:

$$a \equiv -\frac{\mu_2}{< n >}(\rho - 1) \tag{4.29}$$

Therefore, the usual expression for the Aboav–Weaire law is:

$$m(n) = 6 - a + \frac{6a + \mu_2}{n} \tag{4.30}$$

The number of sides of adjoined cells are correlated: many–sided cells have few–sided neighbors and vice versa. The various derivations of 4.30 that one can find in the literature involve approximations (usually of the mean–field kind) or hypotheses whose general validity is subject to caution (we consider the "maximum entropy method" to be in this class). The dominant view today is probably that 4.30 is not exact, but merely a good approximation to some unknown "true" curve, which need not be the same for all cellular systems. Finite system size effects caused $m(n)$ to depart significantly from this law when $n \geq 9$. The exact calculation made by Hilhorst [124] has explained both qualitatively and quantitatively this fail: the exact asymptotic formula for $m(n)$ exhibits an inverse square root decay with n. This large n behavior represents a new paradigm in the field of planar cellular systems.

4.5 Long–range topological correlations of the Voronoi construction

As we have seen in the previous section, the analysis of two–dimensional cellular patterns can be performed by means of several laws regarding the evolution of the probability $P(n)$ and the correlations between adjoining cells (Aboav–Weaire law). However, these descriptions are mean field treatments and do not include the correlations between non–adjoining cells. In order to describe the correlations between any pair of cells in the whole system, we need the *topological distance*. In general, any froth can be studied by means of a shell structure around a central cell (seed). The first layer (with $j = 1$) corresponds to the nearest neighbor cells, the second layer corresponds to the cells adjoining the first layer, and so on (figure 4.5). Therefore, we can define the topological distance, j, between two cells as the minimum number of edges that it must to be crossed to put them in contact.

In the shell structure, the cells forming the layer j can be divided into two categories. Some cells simultaneously have neighbors in the layers $j-1$ and $j+1$. These cells form closed layers and constitute the *skeleton* (sk) of the shell structure. Other cells are inclusions between the layers of the shell skeleton (they have neighbors in the layer $j-1$ or other topological inclusions but not in the layer $j+1$). These cells are called *topological defects*. These topological defects has a great importance in the statistical properties of the Voronoi diagrams as we will see in section 4.5.3.

This decomposition of the plane in concentric regions allows us to systematically explore the long–range ordering induced by the coagulation process and to measure the topological distances at which a colloidal cluster "feel" the presence of a second cluster. In a topological point of view, what we are looking for is to describe how the fact of having an n-sided cell affects the whole froth, and to give an estimation of the topological distance $j = \xi$ where the correlations vanish. When ξ is large, the cells in the froth are strongly correlated and a mean field models break down. On contrary, if $\xi = 1$, only the adjoining cells are influenced by the central seed, and for $\xi = 0$ we find a totally uncorrelated system (topological gas).

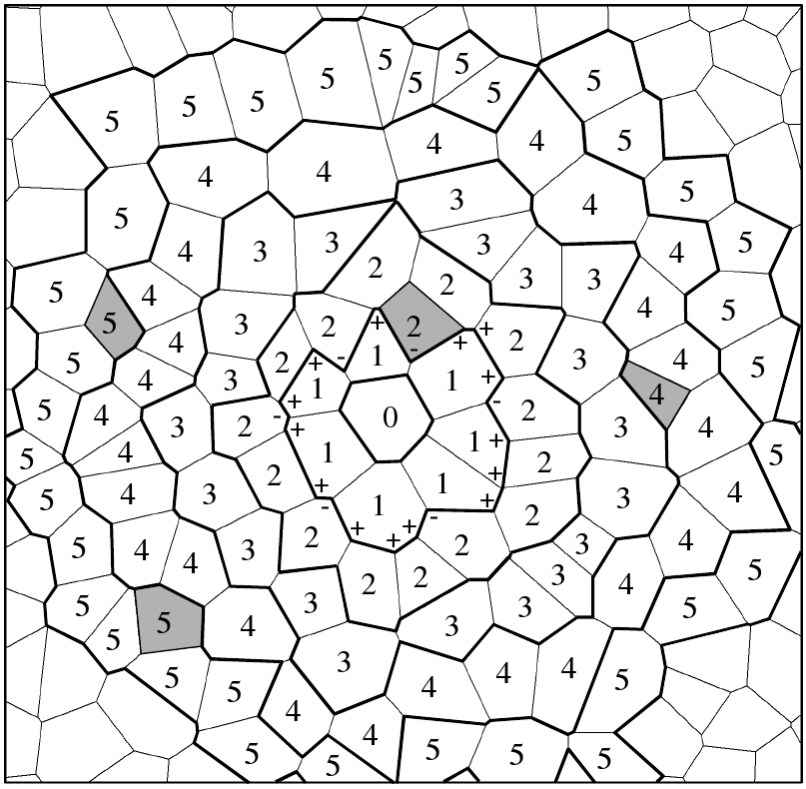

Figure 4.5: Cell structure and defects around a given central cell. The number inside the cells is the topological distance from the central cell. The grey cells represent topological defects. The '+' ('-') symbol represents the convex (concave) vertexes of the first layer.

4.5.1 Important definitions

Some j–dependent topological quantities are required in order to describe the structure of concentric shells. Here we will follow the notation introduced by Aste et al. [113]:

- $K_j(n)$: average number of cells in the j-layer around an n-sided central cell.
- $m_j(n)$: average number of sides of the cells in the j-layer around an n-sided central cell.
- $q = 6 - n$: topological charge of an n-sided cell.

- $Q_j(n) = \sum_{i \leq j}(6 - m_i(n))K_i(n)$: total topological charge of the cells that go from the central seed to the j-layer.
- $C_j(n, m)$: probability of finding a m-sided cell at a distance j from an n-sided cell.
- $V_j^+(n)$: average number of convex vertexes going from the j–layer to the $(j+1)$–layer around an n-sided central cell (represented as + symbols in figure 4.5).
- $V_j^-(n)$: average number of concave vertexes going from the j–layer to the $(j-1)$–layer around an n-sided central cell (represented as - symbols in figure 4.5)
- $\Gamma_j(n) = Q_j(n) - < Q_j >= Q_j(n) - \sum_n Q_j(n)P(n)$: fluctuation part of the topological charge $Q_j(n)$ with respect to its average value $< Q_j >$.

4.5.2 Shell–Structured–Inflatable froths

We defined a Shell–Structured–Inflatable froth (SSI) as the Voronoi diagrams free of topological defects. For SSI froths the shell structure and its skeleton coincide.

The total topological charge of cells bounded by the shell j can be written in terms of vertex coming into and going out from the shell j

$$Q_j(n) = \sum_{i=1}^{j}(6 - m_i)K_i = \sum_{i=0}^{j}(6 - n_i) = 6 - V_j^+(n) + V_j^-(n) \qquad (4.31)$$

where the sum runs over all the cells i in the cluster and n_i is the number of sides of the cell i. Equation 4.31 is a general expression which is valid also for non–SSI systems. It states that the total topological charge inside a cluster depends only on its boundary. For SSI froths, Eq. 4.31 can be rewritten as

$$Q_j(n) = 6 - K_{j+1}(n) + K_j(n) \qquad (4.32)$$

We can find the inverse of this expression using the following iterative process

$$K_j(n) = 6 + K_{j-1}(n) - Q_{j-1}(n) = \\ (6 - Q_{j-1}(n)) + (6 + k_{j-2}(n) - Q_{j-2}(n)) = \ldots \qquad (4.33)$$

and therefore,

$$K_j(n) = 6(j-1) + n - \sum_{i=1}^{j+1} Q_i(n) \tag{4.34}$$

First shell (j=1)

The number of cells around an n–sided cell is

$$K_1(n) = n \tag{4.35}$$

and the topological charge inside the first shell is

$$Q_1(n) = (6-n) + (6-m_1(n))K_1(n) \tag{4.36}$$

The average of the topological charge in the first layer can be calculate using the Weaire's sum 4.20 and the Euler's theorem 4.9

$$< Q_1 >=< (6-n) > + < (6-m_1(n))K_1(n) >=< (6-n)n >= -\mu_2 \tag{4.37}$$

We can express the topological charge in the first layer, Q_1, in terms of the fluctuation of the charge in this layer, $\Gamma_1(n) \equiv Q_1(n) - < Q_1 >$, where the average of the fluctuation has to satisfied $< \Gamma_1 >= 0$

$$Q_1(n) = (6-n) + (6-m_1(n))n = -\mu_2 + \Gamma_1(n) \tag{4.38}$$

This is a relationship between the number of sides n of a cell and the average number of sides of the adjacent neighbors. The Aboav–Weaire's law (eq. 4.30) can be obtained from this expression by imposing a linear form in the fluctuation part

$$\Gamma_1(n) = (1-a)(6-n) \tag{4.39}$$

This linear dependence can be interpreted in terms of the screening of the central charge $Q_0 = 6 - n$ by the charges of the first layer. The total screening charge in the first layer is $(6 - m_1(n))n$ and its deviation from the average value is

$$(6-m_1(n))n - < (6-m_1)n >= \mu_2 - a(n-6) - \mu_2 = -a(n-6) \tag{4.40}$$

This expression give us the interpretation of the Aboav–Weaire parameter a as a screening factor of the internal topological charge. When $a = 0$ there is no screening and when $a = 1$ all the charge of the central cell is screened.

Generic shell

The Weaire's sum 4.20 can be generalized introducing the topological distance j as [113]

$$< (6-m_j)K_j >=< (6-n)K_j > \tag{4.41}$$

where $< ... >= \sum_n P(n)....$

We can express the portion of charge inside the layer j in terms of the topological fluctuations using the generalized Weaire identity 4.41, 4.34 and the Euler's theorem 4.9

$$\begin{aligned} &< (6-m_j)K_j >=< (6-n)K_j > \\ &= 6j < (6-n) > - < (6-n)^2 > - \sum_{i=1}^{j-1} < (6-n)\Gamma_i > + \\ &\sum_{i=1}^{j-1} < Q_i >< (6-n) >= -\mu_2 - \sum_{i=1}^{j-1} < (6-n)\Gamma_i > \end{aligned} \tag{4.42}$$

Hence, the total charge inside a generic shell j is

$$< Q_j >= \sum_{i=1}^{j} < (6-m_i)K_i >= -\mu_2 j - \sum_{i=1}^{j-1}(j-i) < (6-n)\Gamma_i > \tag{4.43}$$

In the case of the absence of fluctuations ($\Gamma_i(n) = 0\ \forall i$), the topological charge decreases linearly with the distance j and each shell has a constant topological charge value equal to $-\mu_2$.

We can rewrite the expression 4.34 for $K_j(n)$ in terms of the fluctuation using eq. 4.43

$$\begin{aligned} K_j(n) &= 6j - (6-n) - \sum_{i=1}^{j-1} Q_i(n) \\ &= 6j - (6-n) - \sum_{i=1}^{j-1} \Gamma_i(n) + \sum_{i=1}^{j-1} < Q_i > \\ &= 6j - \sum_{i=0}^{j-1} \Gamma_i(n) + \sum_{i=0}^{j-2} \frac{(j-i)(j-i-1)}{2} < (6-n)\Gamma_i > \end{aligned} \tag{4.44}$$

All the relations showed for $K_j(n)$, $Q_j(n)$ are exact results valid for any SSI froth.

Minimum correlation length

In a froth where the cells are uncorrelated after a topological distance ξ, the average number of edges per cell, $m_j^{unc}(n)$, in a layer $j > \xi$ has to be independent of the edges number of the central cell ($m_j^{unc}(n) = m_j^{unc}$). Therefore

$$< m_j^{unc} K_j >= m_j^{unc} < K_j > \tag{4.45}$$

Using the generalize Weaire rule 4.41

$$\begin{aligned} m_j(n) = m_j^{unc} = \frac{< m_j^{unc} K_j >}{< K_j >} = \frac{< nK_j >}{< K_j >} = \frac{< -(6-n)K_j > +6 < K_j >}{< K_j >} \\ = 6 - \frac{< (6-n)K_j >}{< K_j >} \text{ (for } j > \xi) \end{aligned} \tag{4.46}$$

According to 4.31, the topological charge inside the layer j is

$$\begin{aligned} Q_j(n) - Q_{j-1}(n) = (6 - m_j(n))K_j(n) \\ =< Q_j > - < Q_{j-1} > +\Gamma_j(n) - \Gamma_{j-1}(n) \\ =< (6 - m_j)K_j(n) > +\Gamma_j(n) - \Gamma_{j-1}(n) \\ =< (6-n)K_j(n) > +\Gamma_j(n) - \Gamma_{j-1}(n) \end{aligned} \tag{4.47}$$

Hence,

$$\Gamma_j = \Gamma_{j-1} + (6 - m_j(n))K_j(n) - < (6-n)K_j > \tag{4.48}$$

Introducing eq. 4.5.2 here, we obtain

$$\Gamma_j = \Gamma_{j-1} + < (6-n)K_j > \left(\frac{K_j}{< K_j >} - 1 \right) \tag{4.49}$$

In the case of a topological gas which is completely uncorrelated ($\xi = 0$) and for $j = 1$

$$\begin{aligned} \Gamma_1 = (6-n) + < (6-n)n > \left(\frac{n}{6} - 1 \right) \\ = (6-n)(1 + \frac{\mu_2}{6}) \end{aligned} \tag{4.50}$$

where we have used that $K_1(n) = n$ and $\Gamma_0(n) = 6 - n$. If we compare this expression with eq. 4.39, we obtain that the value of $a = -\mu_2/6$ for a froth completely uncorrelated.

Now, we will demonstrate that for a SSI froth with $\mu_2 \neq 0$ where the Aboav–Weaire's law is verified, the cells must be correlated at least to the third layer ($\xi \geq 3$). So, if we take the average value of $K_j(n)$ of the eq. 4.34 we obtain

$$< K_j >= 6j - \sum_{i=1}^{j-1} < Q_j > \tag{4.51}$$

It must be a minimum topological distance ν in order to fill the $2D$ space, i. e., $< K_j > \propto j$ for $j \geq \nu$. Therefore, in base of eq. 4.51, the average charge inside the layer j must be equal to zero for $j \geq \nu$. Using the definition of the topological charge and eq. 4.5.2 we obtain

$$< Q_j > - < Q_{j-1} >=< (6-m_j)K_j >= -\mu_2 - \sum_{i=1}^{j-1} < (6-n)\Gamma_i >= 0 \tag{4.52}$$

Hence, the following condition

$$\sum_{i=1}^{\nu-1} < (6-n)\Gamma_i >= -\mu_2 \text{ for } \nu \geq 1 \tag{4.53}$$

is imposed to the fluctuation, and to keep the topological charge independent of the topological distance it must be verified

$$< (6-n)\Gamma_j >= 0 \text{ for } j \geq \nu \tag{4.54}$$

For a froth which topological correlations vanish for layers $j \geq \xi$ the relation 4.5.2 must be satisfied. Therefore

$$< (6-n)\Gamma_j >=< (6-n)\Gamma_{j-1} > + \frac{< (6-m_i)K_j >^2}{< K_j >} \tag{4.55}$$

Now the question is: which distance is greater? ξ or ν?. If we suppose that $j = \nu > \xi$, and we introduce equations 4.52 and 4.54 into 4.55 we obtain

$$< (6-n)\Gamma_{\nu-1} >= 0 \tag{4.56}$$

In this case, contrary to the definition of ν as the topological distance afterward the topological charge per layer remains constant (eq. 4.52), we have that this charge is constant too in the layer $\nu' = \nu - 1$. As conclusion,

$\xi \geq \nu$. If the Aboav–Weaire's law 4.30 is satisfied, we have $\Gamma_1 = (1-a)(6-n)$ (eq. 4.39), so, if $\nu = 1$, using the eq. 4.54 we obtain

$$< (6-n)\Gamma_1 >=< (6-n)(1-a)(6-n) >= (1-a)\mu_2 = 0 \tag{4.57}$$

Expression that is verified only for $\mu_2 = 0$ (perfect hexagonal array) or $a = 1$ (total screening of the charge of the central cell). If $\nu = 2$, using the eq. 4.53 we have

$$< (6-n)\Gamma_1 >=< (6-n)(1-a)(6-n) >= (1-a)\mu_2 = -\mu_2 \tag{4.58}$$

This expression is verified only for $\mu_2 = 0$ or $a = 2$. In other case, the parameter a is restricted to fixed values for $\mu_2 \neq 0$. It follows that if a must be a free parameter for the froth, then $\nu \geq 3$ and $\xi \geq 3$. Thus, using equations 4.49 and 4.53 we have

$$\Gamma_j(n) = 0 \quad \text{for } j \geq \nu \tag{4.59}$$

Statistic for SSI froths with minimal correlation length ($\xi = 3$)

For a SSI froth where $\nu = \xi = 3$ (and then, $\Gamma_i = 0$ for $i > 3$) and the Aboav–Weaire's law is satisfied, we have that eq. 4.53 remains as

$$< (6-n)\Gamma_1 > + < (6-n)\Gamma_2 >= -\mu_2 \tag{4.60}$$

Using that $\Gamma_1 = (1-a)(6-n)$ we obtain

$$\begin{gathered}(1-a) < (6-n)^2 > + < (6-n)\Gamma_2 >= \\ (1-a)\mu_2 + < (6-n)\Gamma_2 >= -\mu_2 \end{gathered} \tag{4.61}$$

$$\tag{4.62}$$

A solution for this equation is given by

$$\Gamma_2(n) = (a-2)(6-n) \tag{4.63}$$

Using 4.59 and 4.63 equations and the general expression 4.5.2 for the number of cells per layer $K_j(n)$ we can find

$$\begin{gathered} K_1(n) = n \\ K_2(n) = (2-a)(n-6) + 12 + \mu_2 \\ K_j(n) = (6 + (3-a)\mu_2)j - (5-2a)\mu_2 \text{ for } j \geq 3 \end{gathered} \tag{4.64}$$

Then, we can calculate the topological charge, using eq. 4.32 into eq. 4.5.2, as

$$\begin{aligned} Q_1(n) &= -\mu_2 + (1-a)(6-n) \\ Q_2(n) &= -(3-a)\mu_2 + (a-2)(6-n) \\ Q_j(n) &= -(3-a)\mu_2 \text{ for } j \geq 3 \end{aligned} \tag{4.65}$$

4.5.3 Shell–Structure froths with topological defects

Topological defects[2] are roughness of the shell structure and their number, as μ_2, give an estimation of the disorder degree of the froth. Indeed, they are not present in perfectly ordered froths (as hexagonal or rectangular lattices), but only in such systems where the Voronoi diagram is not constituted by regular cells. In our case, the Voronoi construction derived for a time–dependent two–dimensional system of aggregating clusters is definitively a non–ordered process, so the quantification of the number of defects during the coagulation will give a characterization of the evolution of the cluster–cluster correlations.

We use use the notation $K_j(n)$, $Q_j(n)$ and $m_j(n)$ for the global froth (skeleton and topological defects), $K_j^{sk}(n)$, $Q_j^{sk}(n)$ and $m_j^{sk}(n)$ for the quantities associated with the shell skeleton. The symbols $K_j^d(n)$ and $m_j^d(n)$ are associated to the number of defective cells and their average number of sides. Thus, the total number of cells at topological distance j from the central cell is

$$K_j(n) = K_j^{sk}(n) + K_j^d(n) \tag{4.66}$$

Some of the equation obtained in the previous section are still valid for the skeleton when topological defects are included in the froth. In particular, the equations 4.32 and 4.34

$$Q_j(n) = 6 - K_{j+1}^{sk}(n) + K_j^{sk}(n) \tag{4.67}$$

and

$$K_j^{sk}(n) = 6(j-1) + n - \sum_{i=1}^{j+1} Q_i^{sk}(n) \tag{4.68}$$

The expression 4.31 for the total topological charge as a function of the concave and convex vertex remains unchanged

$$Q_j(n) = 6 - V_j^+(n) + V_j^-(n) \tag{4.69}$$

[2]also known as *topological inclusions*

Without defects the outgoing convex vertexes from the j–layer are equal to the incoming concave vertexes to the $(j+1)$–layer, i.e. $V_j^+(n) = V_{j+1}^-(n)$. However, if topological defects are present in the froth, part of the outgoing vertexes are trapped in the defective cells. In this case, the previous relation does not hold any more and a correction must be included in order to consider the lost of outgoing vertexes. One obtains

$$V_{j+1}^- = V_j^+ - \eta K_{j+1}^d \tag{4.70}$$

where η is the average number of sides lost in one defect[3]

The number of concave vertex (V_j^-) are related only with the number of skeleton cells in this layer. Moreover, it can be demonstrate that

$$V_j^- = K_j^{sk} \tag{4.71}$$

Thus, if we introduce this property plus the equation 4.70 into equation 4.69, we obtain

$$Q_j(n) = 6 - K_{j+1}^{sk}(n) + K_j^{sk}(n) - \eta K_{j+1}^d(n) \tag{4.72}$$

which is a generalization of eq. 4.32. Now, the substitution of eq. 4.67 into 4.72 leads to the following general expression

$$Q_j(n) = Q_j^{sk}(n) - \eta K_{j+1}^d \tag{4.73}$$

Hence, the topological charge inside the shell j is equal to the charge associated with the shell skeleton minus a contribution due to the defects attached to the external shell and so, the defects present in the internal layers do not contribute to the total charge. It is interesting to see that the defects always decrease the total topological charge.

The average value of the topological charge can be calculated using the definition of the charge ($Q_j(n) = \sum_i (6 - m_j(n))K_j$), the Weaire's sum 4.20

[3]Please note that we have explicitly omitted the dependence of η on the number of sides of the central seed (n) and the topological distance j since the value of this quantity is found to be rather constant for all the defects in the whole system and close to 1

and the expression 4.68 for $K_j^{sk}(n)$

$$< (6-m_j)K_j >=< (6-n)K_j >=< (6-n)K_j^d > + < (6-n)K_j^{sk} >$$
$$=< (6-n)K_j^d > - \sum_{i=0}^{j-1} < (6-n)Q_i^{sk} >$$
$$=< (6-n)K_j^d > - \sum_{i=0}^{j-1}(< (6-n)Q_i > + < (6-n)\eta K_{i+1}^d >)$$
$$=< (6-n)K_j^d > - \sum_{i=0}^{j-1}(< (6-n)\Gamma_i > + < (6-n)\eta K_{i+1}^d >) \qquad (4.74)$$

Hence,

$$< Q_j >= \sum_{i=1}^{j}(6-m_j(n))K_j) = \sum_{i=1}^{j} < (6-n)K_j^d > -$$
$$\sum_{i=1}^{j}\sum_{i'=0}^{j-1}(< (6-n)\Gamma_{i'} > + < (6-n)\eta K_{i'+1}^d >) =$$
$$\sum_{i=0}^{j-1}[< (6-n)K_{i+1}^d > -(j-i)(< (6-n)\Gamma_i > + < (6-n)\eta K_{i+1}^d >)] \qquad (4.75)$$

We can use this expression together with equations 4.68 and 4.68 in order to calculate[4] the average number of cells of the shell skeleton at topological

[4]For simplify the notation, the n dependence of the magnitudes considered are omitted

distance j

$$K_j^{sk} = 6j - \sum_{i=0}^{j-1} Q_i^{sk} = \sum_{i=0}^{j-1}(Q_i + \eta K_{i+1}^d)$$
$$= 6j - \sum_{i=0}^{j-1}(\Gamma_i + < Q_i > + \eta K_{i+1}^d)$$
$$= 6j - \sum_{i=0}^{j-1}(\Gamma_i + \eta K_{i+1}^d + \sum_{i'=0}^{i-1}[< (6-n)K_{i'+1}^d >$$
$$-(i-i')(< (6-n)\Gamma_{i'} > + < (6-n)\eta K_{i'+1}^d >)])$$
$$= 6j - \sum_{i=0}^{j-1}(\Gamma_i + \eta K_{i+1}^d + (j-i) < (6-n)K_i^d >)$$
$$+ \sum_{i=0}^{j-2} \frac{(j-i)(j-i-1)}{2}(< (6-n)\Gamma_i > + < (6-n)\eta K_{j+1}^d >) \qquad (4.76)$$

This expression is a generalization of equation 4.5.2. Following the same procedure than is the section 4.5.2, it can be shown that, for a SSI froth with topological inclusions for which the Aboav–Weaire's law is verified, the system can be uncorrelated after the first neighbors ($\xi \geq 1$). Hence, the reduction of the correlations due to the presence of topological defects shows the relationship between the raise of the disorder of the cells distribution and the increase of the topological defects.

If we have a system that the adjoining cells verify the Aboav-Weaire law and the cell–cell correlations vanish after the second layer $\xi = 2$ (the froth has short–range correlations), then it is possible to find simple approximated expressions for $K_2(n)$ and $K_3(n)$ through equation 4.5.3 and using the reasonable assumptions that the first shell have a small number of defects ($K_1^d << 1$)

$$K_2(n) \approx 12 + \mu_2 + (2-a)(n-6) + (1-\eta)K_2^d(n)$$
$$K_3(n) \approx 18 + (4-a)\mu_2 + (3 - 2a + \frac{(2-a)^2\mu_2}{12+\mu_2})(n-6)$$
$$-\eta K_2^d(n) + (1-\eta)K_3^d(n) \qquad (4.77)$$

In a Euclidean $2D$ froth, the number of cells per layer grows linearly with the distance for $j >> 1$. So, if there is a topological distance ξ afterward there

is no correlations, the slope of this linear dependence must be independent of the number of sides, i. e., for $j \geq \xi$ the number of sides of the central cell has not influence on the number of cells for long distances due to the absence of long correlations. Therefore,

$$K_j(n) = C \cdot j + B(n) \text{ for } j >> 1 \tag{4.78}$$

From equations 4.5.3, we can obtain an explicit expression for the asymptotic value of the average topological charge, $< Q_j >$. Using the definition of the topological charge and the generalized sum rule of Weaire (eq. 4.28), we obtain

$$< Q_j > - < Q_{j-1} > = < [6 - m_j(n)]K_j(n) > = < [6 - n]K_j(n) > \tag{4.79}$$

In the asymptotic limit, $K_j(n)$ is given by eq. 4.78. Hence, we have

$$\begin{gathered} < Q_j > - < Q_{j-1} > = \\ < (6-n) > Cj + < (6-n)B(n) > = < (6-n)B(n) > \text{ for } j \geq \xi \end{gathered} \tag{4.80}$$

Thus, the difference $(< Q_j > - < Q_{j-1} >)$ is independent of the topological distance for large j. In other words, the topological charge inside a layer is constant. Assuming now that this is true for $j = 2$ and using eqs. 4.5.3, we have

$$\begin{gathered} < Q_2 > - < Q_1 > = \\ < Q_j > - < Q_{j-1} > = < (6-n)K_2(n) > = -(2-a)\mu_2 \text{ for } j \geq 2 \end{gathered} \tag{4.81}$$

where the contribution of the defects has been neglected. By iterating last expression, we obtain

$$< Q_j > = -(2-a)\mu_2(j-1) + < Q_1 > \tag{4.82}$$

where $< Q_1 >$ is the average topological charge contained up to the first layer; which is given by $< Q_1 > = < 6 - n > + < [6 - m_1(n)]n > = < (k-n)n > = -\mu_2$. So, finally, $< Q_j >$ is given by

$$< Q_j > = -\mu_2(2-a)j + (1-a)\mu_2 \tag{4.83}$$

By combining eqs. 4.69, 4.70, and 4.71, the following expression for the average topological charge in the j layer is found

$$\begin{aligned} < Q_j > &= < 6 - V_j^+ + V_j^- > \\ &= 6 + < -V_{j-1}^- - \eta K_{j-1}^d + V_j^- > \\ &= 6 + < K_j - K_{j+1} - K_j^d + (1-\eta)K_{j+1}^d > \end{aligned} \tag{4.84}$$

We can deduce an analytic expression for C, the slope of $K_j(n)$ for large j, by taking the asymptotic limit $j >> 1$ and using eqs. 4.78 and 4.83 in eq. 4.5.3

$$-(2-a)\mu_2 j = 6 - C + (1-\eta)K_{j+1}^d - K_j^d \tag{4.85}$$

It is appropriate to define the proportion of defects in the j layer as the ratio $\Lambda_j =< K_j^d > / < K_j >$. With this definition and using eq. 4.78, the last equation can be written as

$$\begin{aligned} -(2-a)\mu_2 j = [(1-\eta)\Lambda_{j+1} - \Lambda_j]Cj + (6-C) \\ +(1-\eta)\Lambda_{j+1}(B+C) - \Lambda_j B \end{aligned} \tag{4.86}$$

In the asymptotic limit, the proportion of defects converges to a constant value independent of j, $\lim_{j\to\infty}\Lambda_j \equiv \Lambda$. Hence,

$$-(2-a)\mu_2 j = \eta\Lambda C j + const \tag{4.87}$$

where *const* is a value independent of j. The matching of both terms for $j >> 1$ imposes the following identity for the slope C:

$$C = \frac{(2-a)\mu_2}{\eta\Lambda} \tag{4.88}$$

which predicts that C is directly correlated to the short– and long–range disorder of the froth (μ_2 and Λ, respectively).

Finally, for large j, we have that

$$< K_j^{sk} >= (1-\Lambda) < K_j > \tag{4.89}$$

therefore, as $K_j(n)$ is linear, $< K_j^{sk} >$ also has a linear behavior with j. This implies that

$$\begin{aligned} < (6-m_j)K_j >=< Q_j - Q_{j-1} > \\ =< Q_j^{sk} - Q_j^{sk} > - < \eta K_{j+1}^d - \eta K_j^d > \\ = \eta < K_j^d - K_{j+1}^d >= \eta\Lambda < K_j - K_{j+1} > \\ = \eta\Lambda C \end{aligned} \tag{4.90}$$

that is, the charge decreases linearly with j with a decrement of $\eta\Lambda C$ per layer.

Taking into account that $C =< K_{j+1}(n) - K_j(n) >$ and using the expressions obtained in 4.5.3, we can obtain finally an approximate theoretical expression for $\eta\Lambda$ through equation 4.5.3.

$$\eta\Lambda \approx \frac{< (6 - m_j)K_j >}{C} = \frac{(2-a)\mu_2}{6 + (3-a)\mu_2 - < K_2^d >} \tag{4.91}$$

4.5.4 Topological pair correlations

The two–cell topological correlation function defined in section 4.5.1 , $C_j(n, m)$, is the probability of finding a cell with m sides at a topological distance j from a cell with n sides. The two–cell topological correlation function is equal to the total number, $N_j(n, m)$, of couples of cells with, respectively, n and m sides that are at a relative distance j, divided by the number of all couples of cells at a relative distance j

$$C(n, m) = \frac{N_j(n, m)}{\sum_{n,m} N_j(n, m)} \tag{4.92}$$

We consider the n– and m–sided cells as distinguishable. Therefore, each couple is counted twice and $N_j(n, m)$ and $C_j(n, m)$ are symmetric in n and m, that is , $C_j(n, m) = C_j(m, n)$.

By definition, for uncorrelated systems the correlation function must factorize as

$$C_j(n, m) = s_j(n)s_j(m) \tag{4.93}$$

The normalization and the symmetry of $C_j(n, m)$ imply that $\sum_m s_j(m) = 1$, consequently $s_j(n) = \sum_m C_j(n, m)$.

Consider two cells with n and m sides that are at a relative topological distance j. Such a pair, connected by a path of length j, can be seen as a "string" with n– and m–sided terminations. Clearly the number of these strings in the cellular system is $N_j(n, m)$ (where each string is counted twice since the terminations are distinguishable cells). The number of strings of length j with a termination in a cell with n sides and the other termination free is given by $\sum_m N_j(n, m)$. The same quantity is equal to the number of n–sided cells in the system $N(n)$ multiplied by the average number of strings of length j which terminate in one n–sided cell $K_j(n)$. Therefore,

$$\sum_{m=3}^{\infty} N_j(n, m) = N(n)K_j(n) \tag{4.94}$$

Finally, the total number of strings of length j is equal to the total number of cells (N_T) multiplied by the average number of strings of length j that terminate in any given cell ($< K_j >$). Thus, we have

$$\sum_{n,m} N_j(n,m) = \sum_n N(n)K_j(n) = N_T \sum_n \frac{N(n)}{N_T} K_j(n) = N_T \sum_n P(n)K_j(n) = N_T < K_j > \tag{4.95}$$

The probability to find a string of length j with a termination in a cell with n sides is consequently given by the ratio

$$s_j(n) = \frac{\sum_m N_j(n,m)}{\sum_{n,m} N_j(n,m)} = \frac{N(n)K_j(n)}{N_T < k_j >} = P(n)\frac{K_j(n)}{< K_j >} \tag{4.96}$$

Thus, for a complete uncorrelated system

$$C_j^{des}(n,m) = s_j(n)s_j(m) = \frac{K_j(n)K_j(m)}{< K_j >^2} P(n)P(m) \tag{4.97}$$

Even when the system is uncorrelated, taking two cells at distant j, the probability to have one cell with m sides and the other cell with n sides is not given by the simple product of the probabilities of finding independently an n– and an m–sided cell $P(n)P(m)$. The factor $K_j(n)K_j(m)/ < K_j >^2$ in Eq. 4.97 indicates that a cell in a froth (even in an uncorrelated one) cannot be topologically independent of its neighbors.

In order to study the long–range topological correlation in a system, we will study the $\beta_j^{n,m}$ functions defined as

$$\beta_j^{n,m} = C_j(n,m)/C_j^{des}(n,m) \tag{4.98}$$

For an uncorrelated system, we have that $\beta_j^{n,m} = 1$ for all j.

4.6 Relations between topology and the number–average cluster size

The topological magnitudes are related with the kinetic magnitudes of the colloidal aggregation. So, if as for example, we can consider the number–average cluster size, $S_n(t)$ (eq. 2.26)

$$S_n(t) = \frac{N_0}{N_C(t)} \tag{4.99}$$

where N_0 is the total number of particles and $N_c(t)$ the number of clusters at time t. Introducing in this expression the equation 4.5, we can connect $S_n(t)$ with the average area of the cells

$$S_n(t) = \frac{N_0}{A_0} \sum_n P(n,t) A(n,t) \tag{4.100}$$

And, now, using the Lewis' law 4.11, we have

$$S_n(t) = \frac{N_0}{A_0} \sum_n P(n,t) k(t) (n - n_0(t)) = \frac{N_0}{A_0} (6 - n_0(t)) = \frac{N_0}{A_0} A(6;t) \tag{4.101}$$

so if the system satisfies the Lewis's law at all times, only the six–sided cells are needed to know the temporal evolution of $S_n(t)$.

Usually, $n_0(t)$ is independent on the time, and therefore, the scaling properties of $S_n(t)$ is also expected for $k(t)$

$$S_n(t) \propto \frac{1}{N_C(t)} \propto A(n,t) \propto k(t) \Rightarrow k(t) \propto t^z \tag{4.102}$$

Chapter 5

Topological order induced by cluster diffusion and aggregation

5.1 Introduction

The aim of this chapter is to study how the aggregation process affects the topological properties of a system of colloidal clusters. The topological correlations will be then a direct consequence of the spatial structuring of the space–filling system of clusters. We have neglected the particle–particle interactions in order to pick up solely the effects of the pure diffusive aggregation (DLCA) and the monomer concentration on the behavior of the topological properties. For this purpose, the growing clusters are substituted by convex non–overlapping polygonal domains (cells) that form a tessellation of the space where aggregation takes place. The number of sides and area of each cell denote the number of nearest neighbors and area filled by the real cluster together with its surrounding depletion region, respectively. In our study we go further the nearest neighbor clusters and investigate the short and long–range ordering created by the aggregation process and how this structuring is related to the surface packing fraction of particles.

5.2 Connections between topology and aggregation

The kinetics of aggregation processes are usually described in terms of the cluster–size distribution $\{n_i(t)\}$, defined as the number of cluster formed by i individual colloidal particles (see section 2.3.2). The time evolution of the cluster–size distribution is strongly connected to the particle–particle interactions, the spacial dimensionality and the geometry of the clusters. One of the most studied property derived from $\{n_i(t)\}$, is the weight–average cluster size, S_w (equation 2.27)

The kinetic aspects are essential to understand the *affinity* between clusters with different sizes and to give an estimate of the total aggregation rate. However, the cluster size distribution, $n_i(t)$, only gives information about the population of the different species formed during the aggregation process, but not about the structure and distribution of these clusters in the space. In order to understand the short and long–range structure of the whole system of clusters confined in two dimensions, a topological description is needed. By means of the Voronoi construction, each cluster is replaced first by a point representing its center of mass, and then, the space around each point is partitioned into convex, irregular polygons, called *cells*. What we obtain after this mapping is a disordered tessellation or *froth*, where the original clusters are represented by non-overlapping cells. Figure 5.1 illustrates a typical snapshot of the colloidal clusters and the froth derived from this method during the coagulation process.

The number of sides of a cell, n, informs about the number of closest neighboring clusters, while the area of the cell, A, is related to the total area filled by the colloidal cluster and its depletion region. The relative distance between two non–neighboring clusters is now represented by the topological distance, j that, as we saw in section 4.5. is defined as the minimum number of cells that we must go through from a starting cell to a given final cell. The topological distance allows us to consider the froth as a collection of concentric shells which are at the same topological distance from a central seed. The main advantage of using the topological distance, j, instead of the metric distance, r, is the fact that j gives an unambiguous and time-independent measurement of the coordination shell at which a cluster is localized in relation to a central one. For a system of growing clusters, however, the typical metric distance of a certain coordination shell is not a constant quantity, but

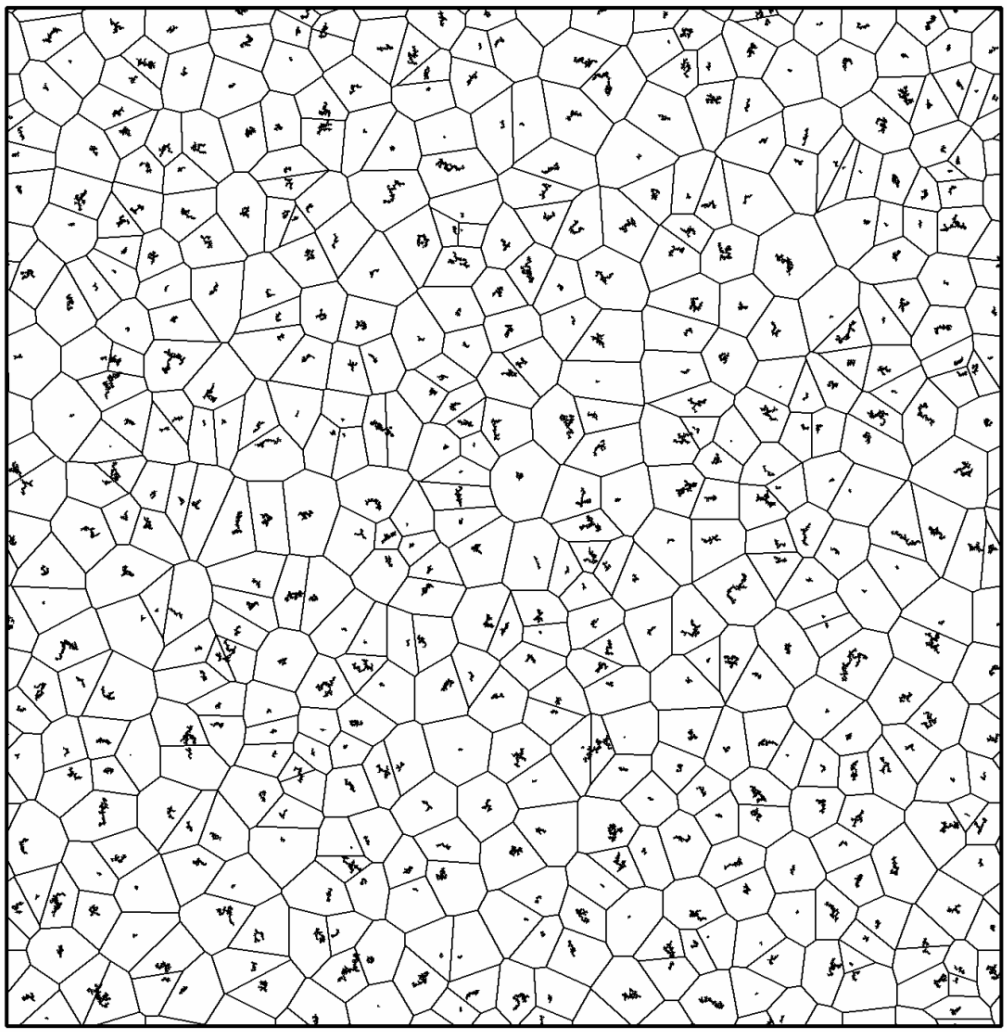

Figure 5.1: Typical snapshot of a two–dimensional system of aggregating clusters, and the subsequent Voronoi diagram built up from their center of masses.

it increases as the aggregation proceeds. The topological distance also gives a good characterization of the correlation between any couple of cells of the froth (i.e. correlation between two colloidal clusters). Indeed, any modification in the shape or the number of sides of a particular central cell produced by the motion and/or aggregation of the colloidal clusters will have more influence on the cells placed at small topological distances. For large j the statistical properties of the cells become independent on the central one. In fact, as we will see later, the cell–cell correlations are negligible for $j > 2$.

As we saw in section 4.3, in two–dimensional coagulation the evolution of the cellular pattern is ruled by two independent processes. The $T1$ process, where every time a cluster moves a large enough distance, a new rearrangement of the cells is found in terms of a local side switching and the $T2$ process when two clusters coagulate together to form a larger cluster and one of the cells disappears. Therefore, the surrounding cells are accommodated to the new configuration. Both topological processes induce a topological restructuring of the two–dimensional froth that is connected in general, to the physical conditions of the aggregating system, and more specifically to the aggregation regime and the packing fraction of particles φ.

Since the aggregation process induces a disordered froth with irregular cells, the number of sides and area of the cells will be statistical properties distributed according to $P(n, A)$ (the probability of finding a cell of n sides and area A).

One of the most interesting quantities derived from the probability distribution $P(n)$ (equation 4.3) is its second central moment, μ_2 (eq. 5.6), which can be understood as an estimate of the degree of the disorder in the froth.

In principle, n and A are both important to give a complete description of the froth. However, only one of them is really necessary since these quantities are in fact strongly correlated through the Lewis' law (see section 4.3.2), that states that the mean area of the n-sided cells shows a linear dependence on n, $A(n) = \kappa(t)(n - n_0)$ [118]. Here, $\kappa(t)$ increases with the aggregation time whereas n_0 is found to be a constant value [18]. Hence, the number of sides n is sufficient to give a good representation of the froth and the cluster-cluster correlations.

The study of correlations between the shapes of two neighboring cells in the froth can be easily done with the help of $m_1(n)$, defined as the average number of sides of the adjacent cells of n-sided cells. From space–filling conditions follows the result that large cells (i.e. with many sides) tend to be surrounded by small cells. This intuitive property can be expressed in a

semi–empirical law called the *Aboav-Weaire law* [125, 126] (see section 4.4), that states that on average $m_1(n)$ is linear in $1/n$:

$$m_1(n) \approx (6 - a) + \frac{6a + \mu_2}{n} \tag{5.1}$$

where μ_2 is again the second central moment and a is the screening factor.

5.3 Simulations

Brownian Dynamics off–lattice DLCA simulations were done in a square box of side L by considering a total number of monomers of $N_0 = 30000$ with a particle diameter $d = 735\ nm$, and for five different packing fractions: $\varphi = N_0\pi r^2/L^2 = 0.005$, 0.01, 0.03, 0.06 and 0.1. In the initial state, monomers were placed at random avoiding particle–particle overlapping. Periodic boundary conditions are imposed at the boundaries of the simulation surface. The simulations were stopped when the number of clusters was around 1500 aggregates. For the entire surface packing fractions considered this condition is good enough to reach the scaling time and it is a warranty to have good statistics for all aggregation times.

The diffusion coefficient (D) of a single cluster is obtained from its radius of gyration (R_g) assuming the Stokes' law $D \sim 1/R_g$. To move the clusters they are selected one by one for a movement test. A random number ξ uniformly distributed in $[0; 1]$ is generated. If $\xi \leq D/D_{max} = (R_g)_{min}/R_g$, the cluster is moved in a random direction. If $\xi > D/D_{max}$, the cluster does not move. D_{max} is the largest diffusion coefficient and $(R_g)_{min}$ the smallest radius gyration in the whole system of clusters. Whether the cluster moves or not, the time is increased by

$$\Delta t = \frac{1}{N D_{max}} \tag{5.2}$$

A collision is considered to occur when a moved aggregate overlaps another one. Then, the position of the moved cluster is corrected backwards along the direction of the movement as far as the surfaces of both clusters are in contact. These contacting clusters are joined to form a larger cluster that will continue the diffusive motion in the following time step. For DLCA every collision produces coagulation.

The programs used in this chapter for the DLCA aggregation and to obtain the topological properties of the Voronoi diagrams associated to this

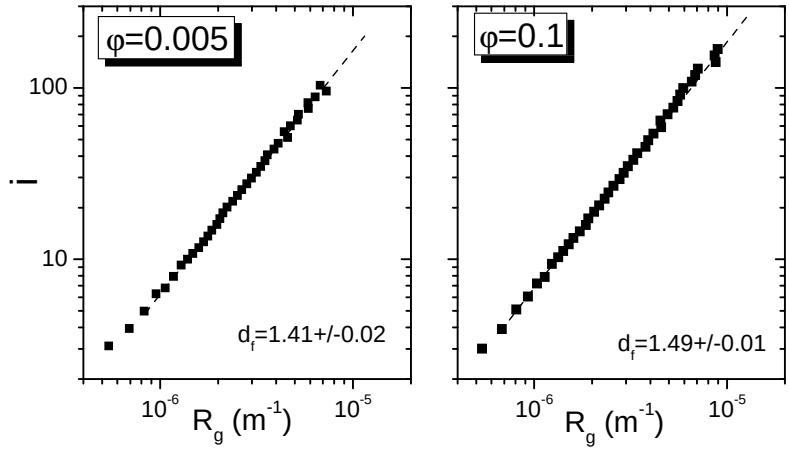

Figure 5.2: Cluster size i versus the gyration radius R_g for $\varphi = 0.005$ on the left and $\varphi = 0.1$ on the right. As expected, we obtain a behavior in power as $i \sim R_g^{d_f}$.

aggregation process were developed by the Dr. Arturo Moncho Jordá and has been used successfully in previously works [18, 27, 127, 128].

5.4 Structural and kinetic properties of the DLCA regime

The representation of the number of monomers of the aggregate versus its gyration radius is shown in figure 5.2 for $\varphi = 0.005$ and 0.1. As predicted by the scaling law 2.22 we obtain a power law dependence where the scaling exponent is the fractal dimensions. In figure 5.3 shows the fractal dimensions for the DLCA simulation as a function f the packing fraction φ. For all cases, we obtained values close to the typical fractal dimension characteristic for the two–dimensional DLCA coagulation (~ 1.44). However, we can discern an increasing of the fractal dimension with the packing fraction.

In figure 5.4, the weight–average cluster size is plotted as a function of the aggregation time for the five surface packing fractions. $S_w(t)$ monotonically increases as time goes on, and after the so called scaling time t_{sc} (see cross symbols), it reaches the scaling behavior given by a power–law growth: $S_w(t) \sim t^z$. For higher particle concentrations the aggregation process is

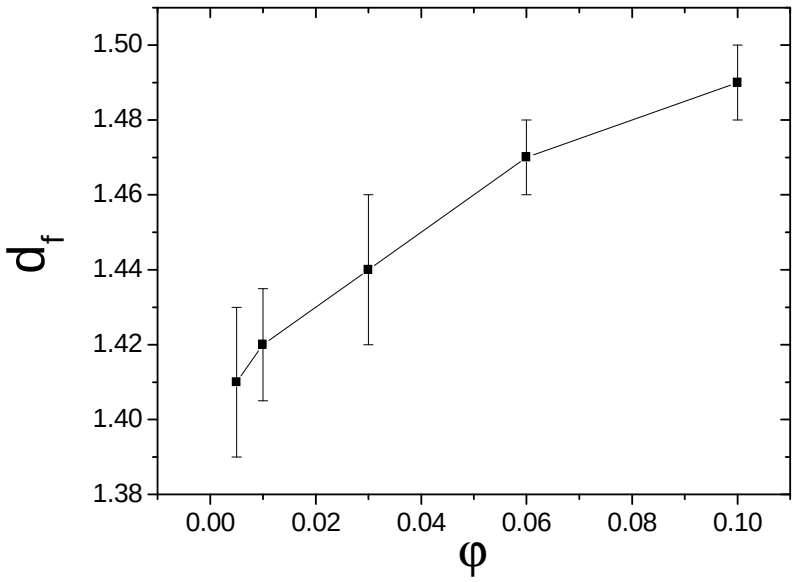

Figure 5.3: Dependence of the fractal dimension of the aggregates, d_f, versus the packing fraction, φ. Although the values are close to the result expected for DLCA regime (~ 1.44), we observed an increase of the fractal dimension with φ.

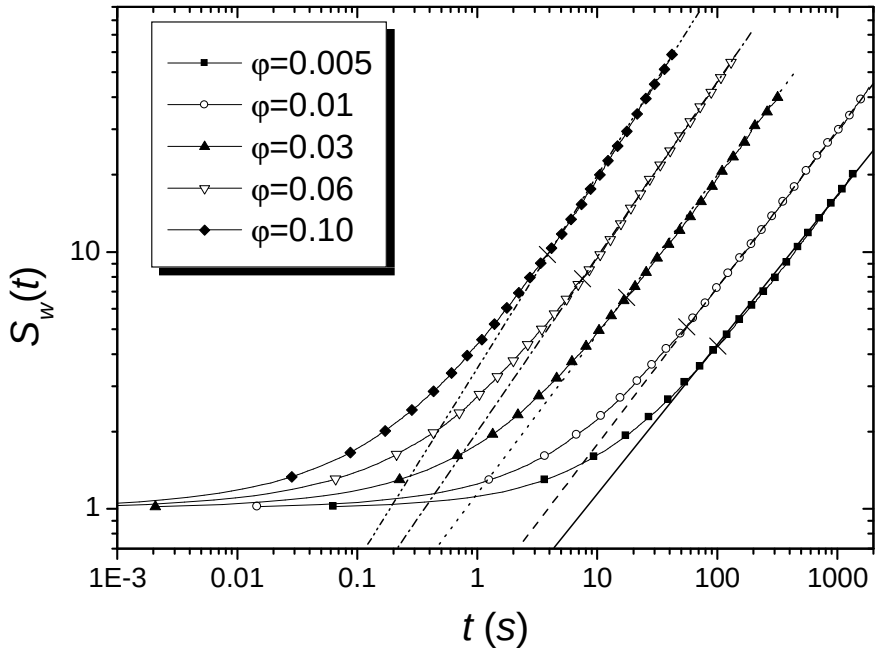

Figure 5.4: Time evolution of the weight–average cluster size obtained from DLCA simulations for five surface packing fractions. At long times, $S_w(t)$ shows a power–law behavior (scaling). The cross symbols represent the scaling time t_{sc}.

faster, and consequently the scaling region is manifested at shorter times with a larger kinetic exponent z [129] (see Table 5.1).

5.5 $P(n)$ and μ_2

After this brief description of the kinetic properties, we will focus on the topological aspects of the aggregation process. For all the studied situations (i.e. different times and initial particle concentration conditions), the probability of number of sides $P(n)$ is a centered distribution around the maximum value at $n = 6$, and the first moment verifies the Euler theorem ($< n >= 6$). The time evolution of $P(n)$ for four different packing fractions is shown in figure 5.5. We observed that the probability of finding cells with $n = 6$ increases with time. Also, $P(n)$ becomes tighter when the particle concentration is

φ	z (± 0.01)	$t_{sc}(s)$
0.005	0.60	101.7
0.01	0.61	55.8
0.03	0.63	17.1
0.06	0.68	7.4
0.10	0.76	3.8

Table 5.1: Kinetic exponent z and scaling time t_{sc} for the five surface packing fractions studied in this work.

increased. For long aggregation times, $P(n)$ becomes independent on time.

The second central moment, μ_2, determines the dispersion of $P(n)$, so it can be regarded as the key quantity to characterize the global topological disorder of the system of clusters. As shown in figure 5.6, μ_2 decreases with time for all cases for short times. However, after certain time which corresponds to the scaling time t_{sc} it finally reaches a roughly time–independent value. This long–time behavior has been previously observed by several authors [100, 16, 17]. Indeed, experiments on soap froths indicate that, as time goes on, there is a final state where the topological properties reach stable values [113]. Some experiments of two–dimensional colloidal coagulation performed by Earnshaw and Robinson also show similar topological results for $t > t_{sc}$ [17].

The decrease of μ_2 reveals that the clusters formed in the DLCA regimen tend to adopt an hexagonal-like structure as the aggregation proceeds, i. e. the aggregation process induces a topological ordering that is intimately related to the spatial organization of the clusters in the plane. As soon as the scaling of the cluster–size distribution is manifested, the topological ordering ends and the system of aggregating clusters reaches a final stationary state with constant μ_2. Therefore, the dynamic scaling can be understood as a "stationary" state in a topological point of view. Our simulation results also show that the final stationary value of μ_2 decreases as the particle concentration increases (from $\mu_2 = 1.42$ for $\varphi = 0.005$ to $\mu_2 = 1.07$ for $\varphi = 0.1$), which means that aggregation induces stronger topological ordering for dense colloidal suspensions than for the dilute ones. Figure 5.7-A represents the slope of the $\mu_2(t)$ versus the aggregation time. As it can be observed, this slope is independent The final stationary value, however, decreases with the particle packing fraction (figure 5.7-B). This clearly shows that the intercluster

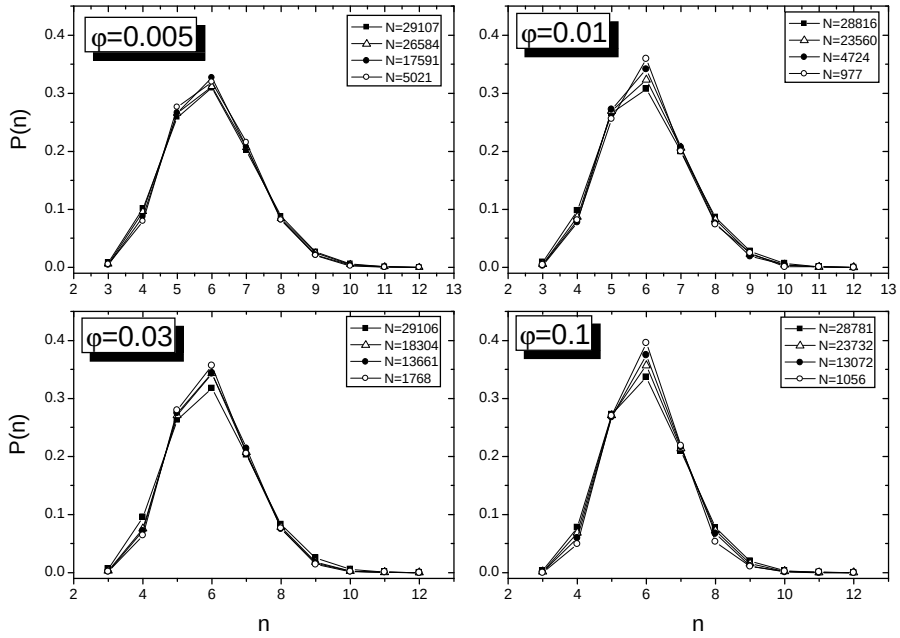

Figure 5.5: $P(n)$ versus n for four different packing fractions.

ordering induced by the aggregation process is stronger for dense colloidal suspensions.

This ordering is linked to the growth of the colloidal clusters and the existence of free space between them. Clusters are non–compact fractal–type structures with a special ability to fill the space even for relatively small number of particles. The typical distance between the surfaces of two nearest neighbor clusters ($r_s(t)$) is given by

$$r_s(t) = r_{cc}(t) - 2R(t) \tag{5.3}$$

where $r_{cc}(t)$ is the average distance between centers of the clusters and $R(t)$ is the characteristic cluster radius. r_s is a measure of the size of the depletion zone around a cluster. The cluster growth is achieved at the expense of the surrounding particles/clusters, which are mopped up after diffusion through this depletion distance. When the dynamic scaling is established, the fractal dimension of the clusters d_f is a well–defined quantity and $R(t)$ scales with the number–average cluster size as $R(t) \sim S_n(t)^{1/d_f}$. The center–to–center distance is, however, given by $r_{cc}(t) \sim S_n(t)^{1/2}$. Since $d_f < 2$, we observe that $R(t)$ grows faster than $r_{cc}(t)$. At very low particle concentrations, this effect

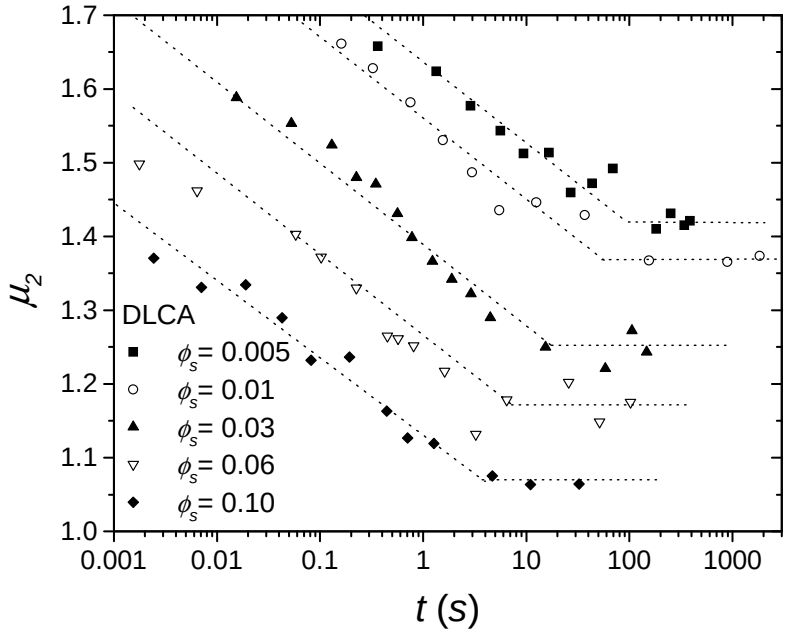

Figure 5.6: Second central moment of $P(n)$ as a function of the aggregation time for five surface packing fractions. After the scaling time μ_2 reaches a final stationary value (dashed lines are only guides for the eyes).

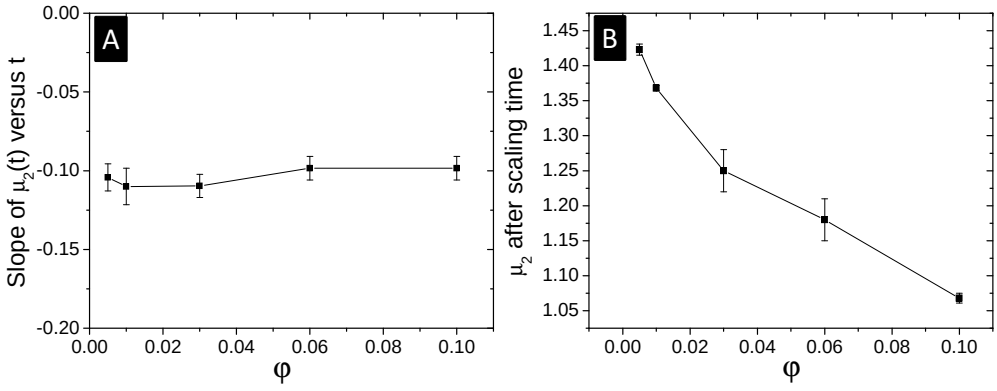

Figure 5.7: A) The slope of $\mu_2(t)$ versus the aggregation time before the scaling time remains independent of the packing fraction φ. B) The final stationary value of $\mu_2(t)$ decreases with the packing fraction.

is not really important since the average cluster–cluster distance is much larger than the cluster radius at any aggregation time. However, for higher particle densities, the free space available between a cluster and its nearest neighbors becomes rapidly small compared to the effective surface filled by the fractal clusters. Then, the cluster structure is able to induce spatial order in the cluster localization: the surrounding clusters around a central one tend to adopt a more closely packed two–dimensional structure (the more particle density we have, the stronger is the inter–cluster ordering). Topologically, it yields the increase of 6 sided cell probability and the subsequent reduction of μ_2 for more dense systems and long aggregation times. Since this effect is a consequence of the trend of fractal clusters to fill up the whole space, we do not expect the same spatial organization when clusters are not fractal. This is the case of aggregation into a finite energy minimum, which allows the colloidal particles to rearrange inside the cluster and to form more compact structures [130].

The final stationary value for μ_2 obtained during the scaling regime (figure 5.7-B) seems to be an intrinsic property of the self–assembly of the clusters linked to the value of the average fractal dimension of the cluster. In fact, we expect departures from our results for μ_2 at very high particle densities and long times, when the aggregating system is close to undergo gelation ($r_s \approx 0$)), since the clusters lose their individual fractal character and become homogeneous structures (with $d_f = 2$).

5.6 Lewis's law

As we see in section 4.3.2, there is a linear behavior of the mean area of the cells versus the edges number as $A(n,t) = k(t)(n - n_0)$. This relationship is the Lewis's law. Here, we corroborate this law for a Voronoi diagram of an aggregating system. In figure 5.8 we represent the mean area of the cells, $A(n;t)$ versus the number of sides n for different times for the simulation of $\varphi = 0.06$. We observed the linearity behavior for all the simulations.

In figure 5.9 we represent $k(t)$ as a function of time obtained from the simulations. In all cases, $k(t)$ collapse in a common curve after the scaling time independently of the packing fraction, with a power law dependence with time that can be fitted with an exponent close to the kinetic exponent.

As we saw in section 4.6, the area of the 6–sided cells scale with time through the kinetic exponent. In figure 5.10, the quantities $\rho \cdot A(6;t)$ (ρ is the

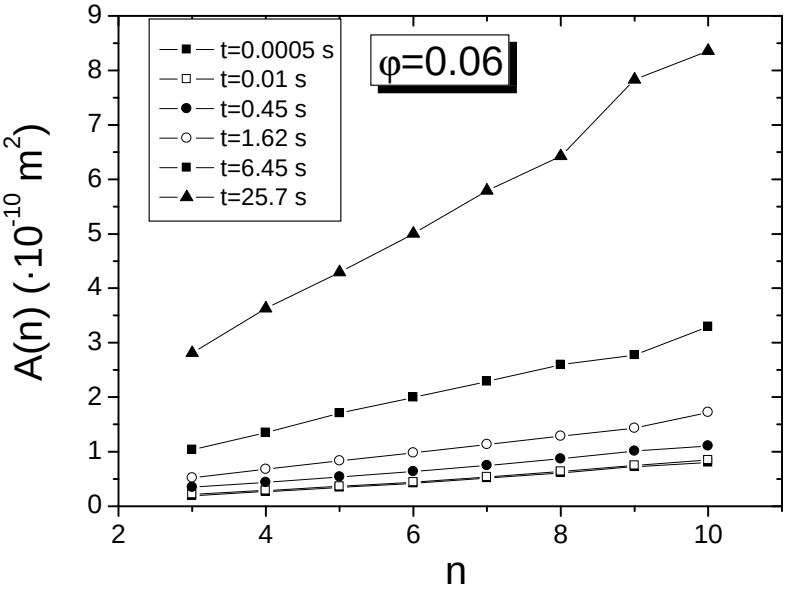

Figure 5.8: An example of the dependence of $A(n;t)$ versus n for different times and $\varphi = 0.06$. The linearity can be explained in base of the Lewis law $A(n;t) = k(t)(n - n_0)$

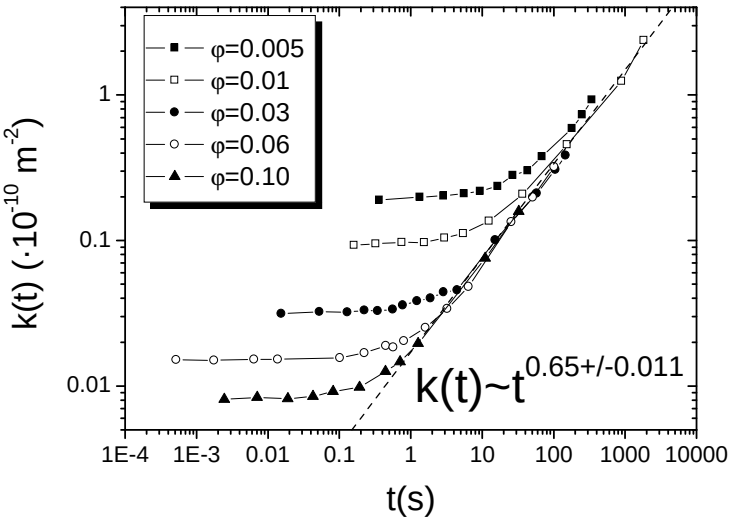

Figure 5.9: Scaling behavior of $k(t)$ for the different simulations. After the scaling time, all curves overlap in the same common curve with a power law dependence similar to the one observed for $S_n(t)$.

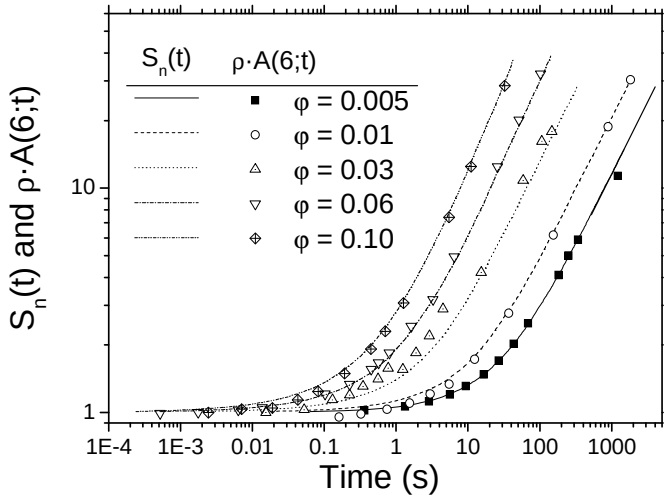

Figure 5.10: The relationship 4.101 between $S_n(t)$ and $\rho{\cdot}A(6;t)$ is checked. In all the cases a good agreement is found for the five different packing fraction.

particle surface density) is plotted against the aggregation time and compared to the mean cluster size, $S_n(t)$. There is a perfect agreement between both, as expected by equation 4.101. Therefore, if we know the time dependence of the area of the 6–sides cells, we have completely determined the growth of the mean cluster size.

5.7 Topological ordering between nearest neighbor clusters

A similar steady state behavior is found for the screening factor a obtained fitting the results to the the Aboav–Weaire law for the average number of sides of the nearest neighbor cells of an n–sided cell, $m_1(n)$. Figure 5.11 shows $m_1(n)$ as a function of $1/n$ for the particular case of $\varphi = 0.01$ at four different times (similar curves are found for the rest of particle concentrations and aggregation times). The increase of $m_1(n)$ as a function of $1/n$ means that large clusters (with many number of sides) tend to be surrounded by

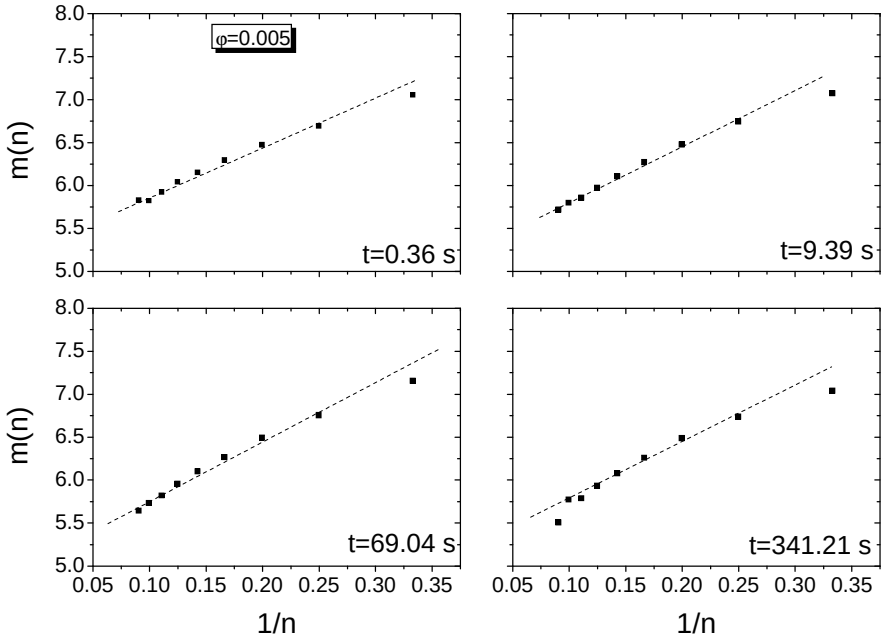

Figure 5.11: Example of $m(n)$ versus $1/n$ for $\varphi = 0.005$ and 4 different times. The linearity predict by the Aboav–Weaire's law is verified except for the cells with large number of sides. The dashed lines represent the fits using the Aboav–Weaire law.

small ones (with low n). Together with the simulated data, we represent the fit using the Aboav–Weaire law given by Eq. 5.1 (solid line). As observed, simulated and theoretical $m_1(n)$ agree well, except for the cells with large number of sides ($n > 9$) where departures from the Aboav–Weaire prediction are found. This departure from the linear behavior can be explained in terms of an exact asymptotic formula for the first–neighbor correlation of Poisson–Voronoi cells as $m(n) \sim 1\sqrt{n}$ (instead of $m(n) \sim 1/n$) predicted by Hilhorst [124] .

The screening factor a obtained from the fits of $m_1(n)$ is not an independent property but it is also strongly correlated to the topological order of the system. In fact, for most of the froths with weak and moderate disorder, a is a positive quantity and grows as μ_2 decreases [131]. This behavior is also found for the particular case of two–dimensional colloidal coagulation. Indeed, as observed from figure 5.12, the parameter a first increases for times below the scaling time and arrives at a rather stationary state when the dynamic scal-

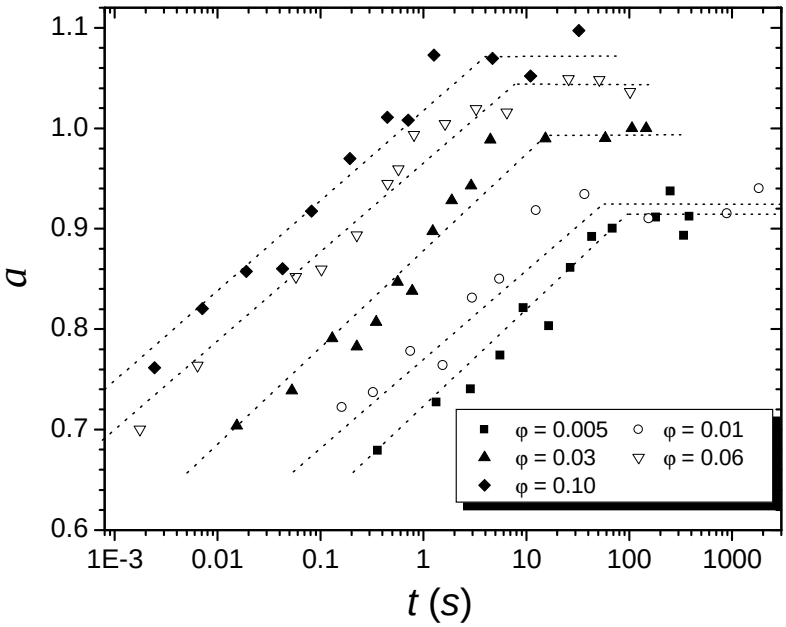

Figure 5.12: Screening factor a calculated by fitting $m_1(n)$ according to the Aboav–Weaire law (cf. Eq. 5.1). After the scaling time a also reaches a stationary value (dashed lines are only guides for the eyes).

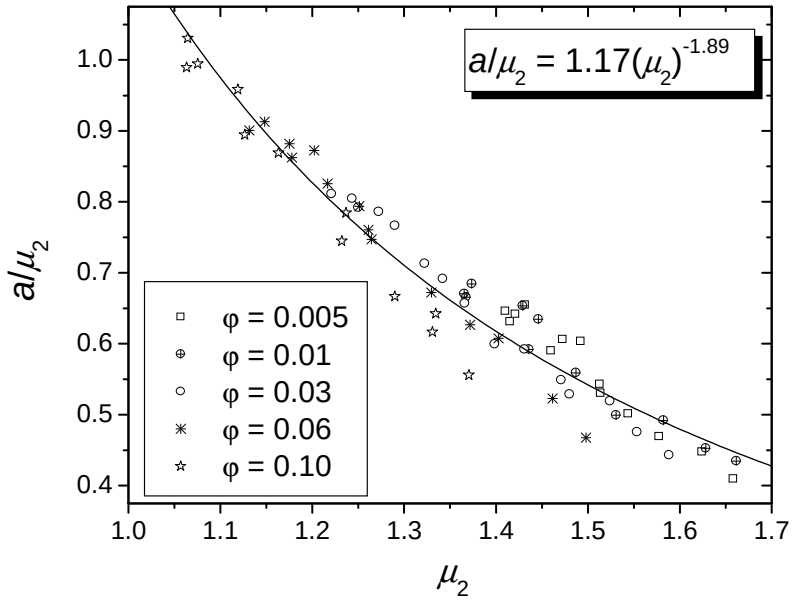

Figure 5.13: The simulated μ_2 and a/μ_2 data at any time and for the five studied particle concentrations lie in a universal common form: $a/\mu_2 = 1.17(\mu_2)^{-1.89}$. In this plot, the μ_2-axis is representative of the time-axis, but in the opposite direction.

ing is established. The final value of a increases with particle density, going from $a = 0.91$ for $\varphi = 0.005$ to $a = 1.07$ for $\varphi = 0.1$. Moreover, if we plot the simulated values of a/μ_2 for all times and for the five different surface packing fractions of particles as a function μ_2, the results lie in a universal curve (see figure 5.13), given by $a = D(\mu_2)^w = 1.17(\mu_2)^{-0.89}$. A similar universal behavior is found for other natural or computer simulated froth systems but with different values of D and w [131, 116]. Since the exponent w may be considered as a universality class feature of the froth evolution, we deduce that the topological structuring induced by two–dimensional aggregation processes correspond to a unique universality class ($w = -0.89$) which does not longer depend on the monomer density, but it is a general property linked to the space–filling aspects of the cluster growth.

5.7.1 Correlations between non–adjacent clusters.

This section extends the study of the topological properties beyond the first nearest neighbor cells.

$K_2(n)$ and $K_3(n)$

First we investigate the average number of cells around an n-sided cell for the two nearest non–adjacent layers around the central seed: $K_2(n)$ and $K_3(n)$. Figure 5.14 shows an example of the dependence of the simulated $K_2(n)$ and $K_3(n)$ on the number of sides (symbols) together with the theoretical prediction (lines) deduced for froths where the cell–cell topological correlations vanish after the second layer (see Eq. 4.5.3) and where the first cell is correlated according to the Aboav-Weaire law. As observed, this theoretical model reproduces fairly well the simulation data, although some departures are found for cells with $n \geq 9$ as a consequence of the failure of the Aboav–Weaire law for such many–sided cells (see figure 5.11.) Although the complete set of results is not shown, similar agreement between theory and simulation was found for all aggregation times and particle densities, supporting the idea that the aggregation process is not able to produce correlations for $j > 2$. Moreover, the values of $K_2(n)$ and $K_3(n)$, that characterize the shape of the second and third layer of the shell structure, are basically given by topological properties related to single cell averages and first layer correlations, as the second central moment μ_2 and a.

Asymptotic behavior of $< Q_j >$

In the next step we go beyond the first 3 nearest layers with the aim of studying the long–range topological properties and their asymptotic limit. Using the quantities defined in Section 4.5.1, we can describe the long–range ordering of the froth induced by the aggregation process. First of all, we start our analysis with the average topological charge $< Q_j >$. Figure 5.15 shows typical examples of the dependence of $< Q_j >$ on the topological distance for the particular case of $\varphi = 0.005$. The topological charge decreases linearly with j. Moreover, $< Q_j >$ is well described by the theoretical prediction $< Q_j >= -\mu_2(2-a)j$ given in Eq. 4.83 for froths where the cell–cell correlations vanish after the second layer. Similar results are found for all times and other particle densities.

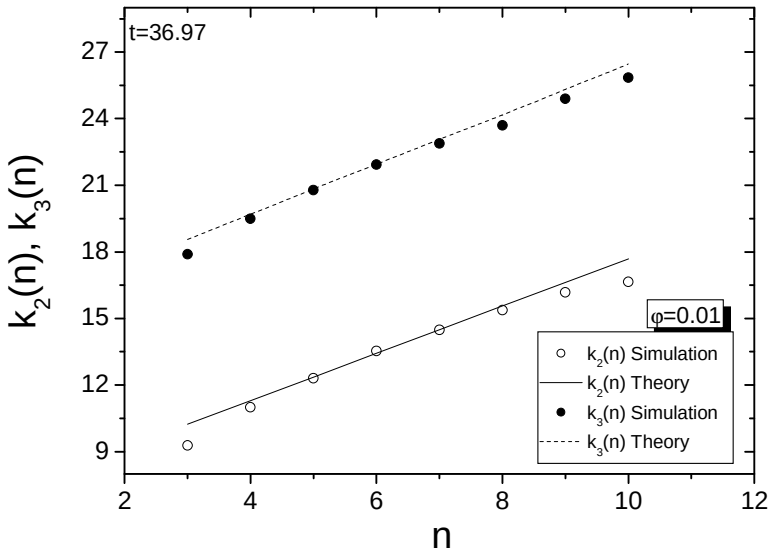

Figure 5.14: Dependence of the average number of cells in the closest non–adjacent layers to the central one, $K_2(n)$ and $K_3(n)$, on the sides number n for DLCA simulation with $\varphi = 0.01$ after the scaling time. The solid lines represent the theoretical expectations obtained using Eqs. 4.5.3. Similar fittings are obtained for all simulations.

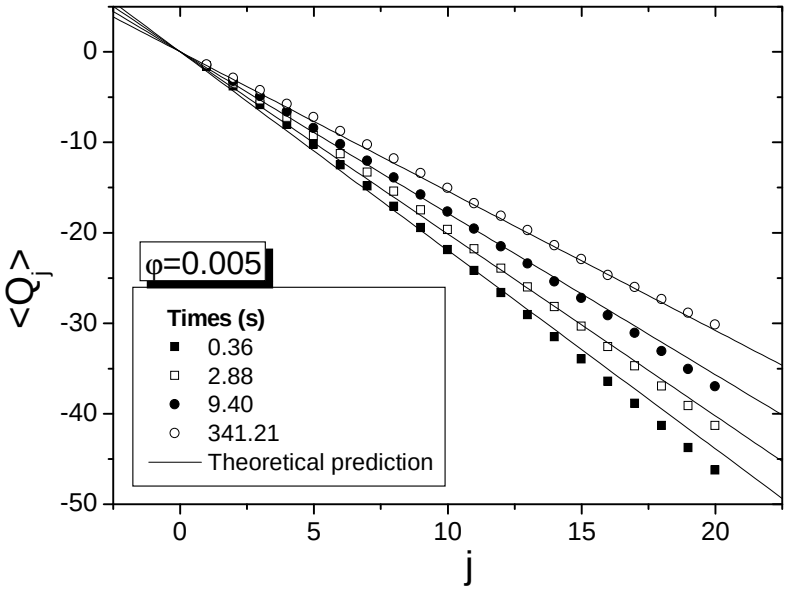

Figure 5.15: Dependence of the average topological charge $< Q_j >$ on the topological distance j for DLCA simulation with $\varphi = 0.06$ for different times. The straight line are the theoretical predictions $< Q_j >= -\mu_2(a-2)j$.

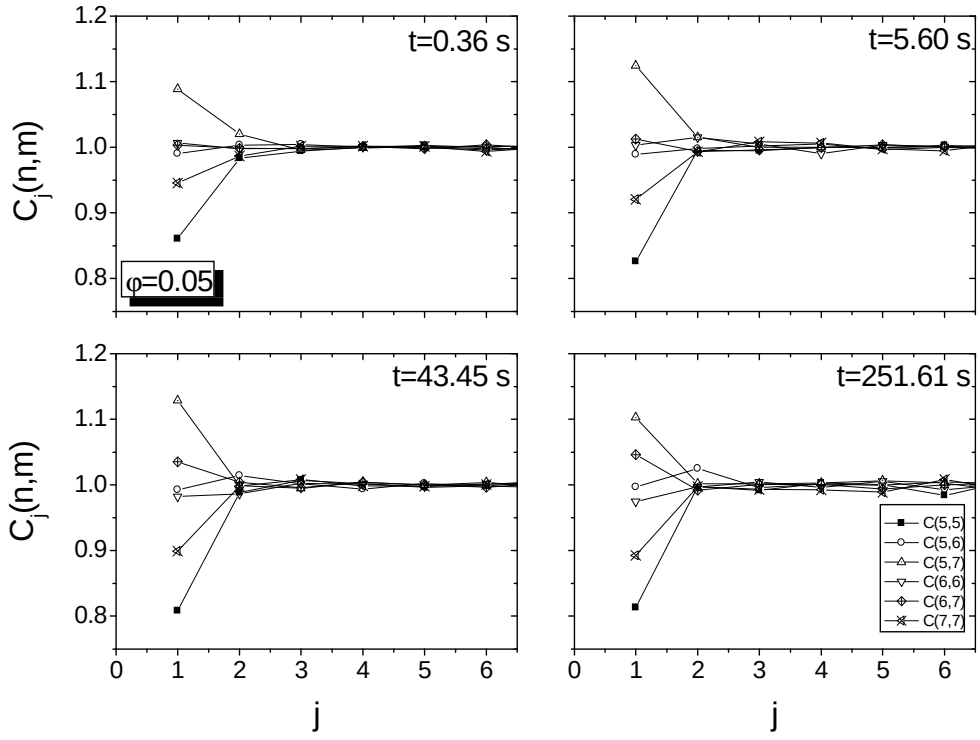

Figure 5.16: $C_j(n,m)$ $(n,m = 5,6,7)$ for $\varphi = 0.05$ and different times. The topological correlations vanish for $j > 2$.

The result corroborate an already mentioned fact: the spatial and topological correlations between two clusters are negligible if the topological distance between them is larger that 2. This conclusion has been independently confirmed by measuring the probabilities $C_j(n,m)$ defined in section 4.5.4 for several values of n and m (see figures 5.16 and 5.17).

Indeed, the amplitude of the oscillations of $\beta_j^{n,m} = \frac{C_j(n,m)}{C_j^{un}(n,m)}$ (eq. 4.98) is only important for $j = 1,2$, and becomes insignificant for $j > 2$. Furthermore, since Eq. 4.83 holds for all particle concentration and aggregation times (before and after the scaling), we conclude that the aggregation process is only able to induce short–range inter–cluster correlations (up to $j = \xi = 2$) even at high particle packing fraction: clusters in the third layer do not feel the presence of a given central cluster.

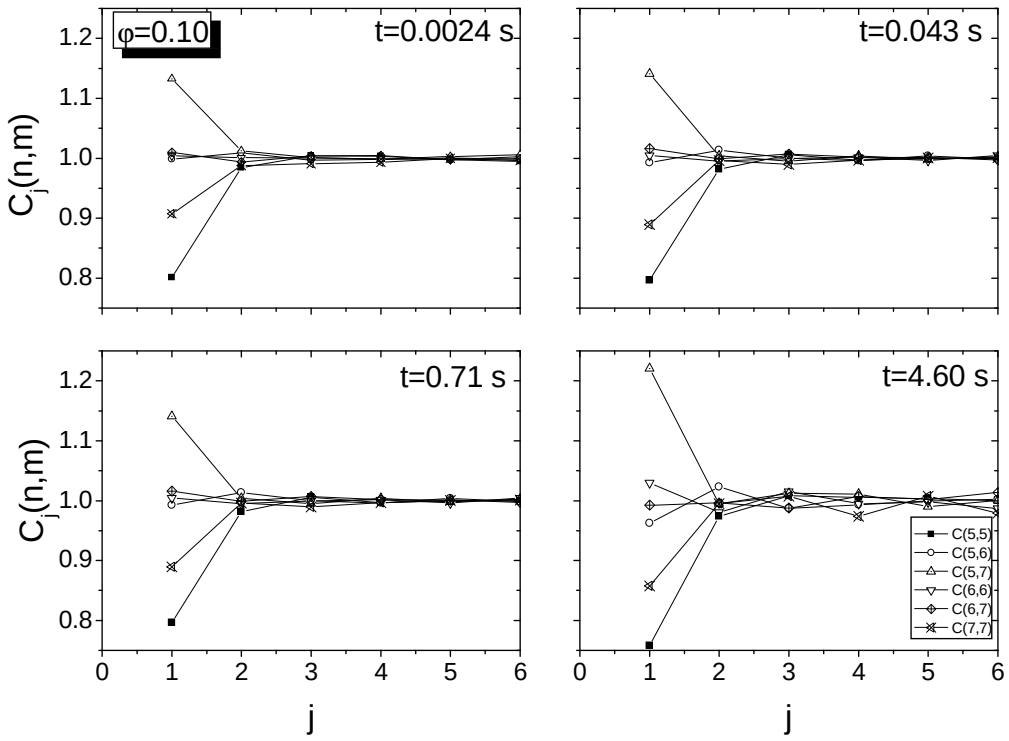

Figure 5.17: $C_j(n,m)$ $(n,m = 5,6,7)$ for $\varphi = 0.1$ and different times. The topological correlations vanish for $j > 2$.

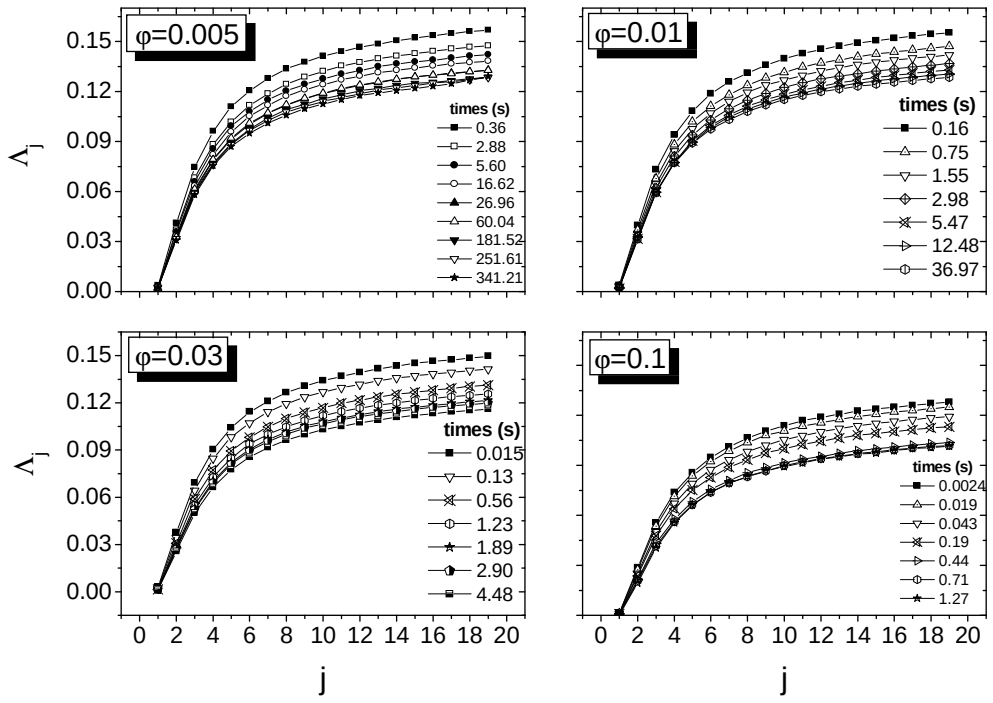

Figure 5.18: Proportion of defects as a function of the topological distance obtained for DLCA simulations with $\varphi = 0.005$, 0.01, 0.03 and 0.1. After the scaling regime the curves become time–independent.

5.7.2 Topological defects

We now turn to the study of another important aspect of the froth: the topological defects. Their presence in the shell structure has a dramatic influence on the cell assembly. In fact, for froths with large values of the proportion of defects, Λ_j, the cell–cell correlations drop off very fast with the topological distance j. It means that cluster–cluster correlations beyond nearest neighbors are mainly dominated by the percentage of defects.

Figure 5.18 shows the proportion of defects as a function of j for several aggregation times for $\varphi = 0.005$, 0.01, 0.03 and 0.1. In all cases Λ_j increases with j, and for large distances it reaches an asymptotic constant value, Λ, that features the long-range shell structure. As the coagulation progresses, the whole curves go down and reach lower values of Λ. This decrease of the defect concentration as time evolves clearly indicates that the aggregation

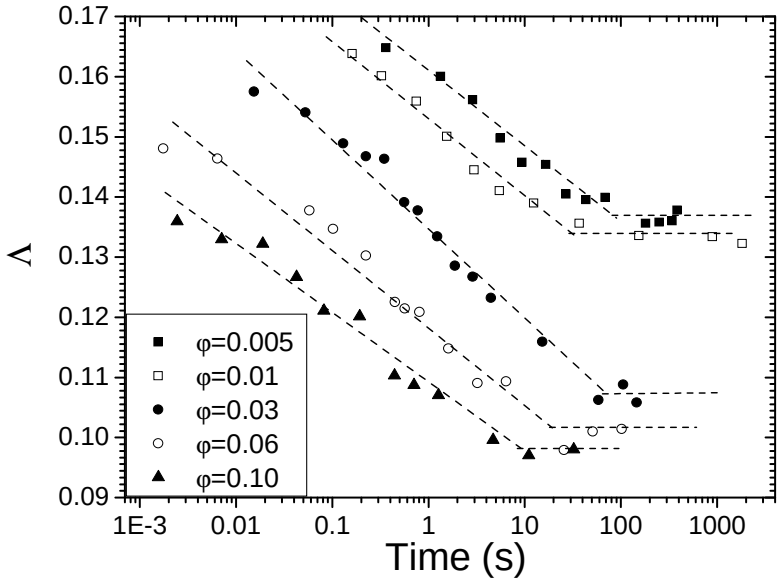

Figure 5.19: Asymptotic value of the proportion of defects as a function of the aggregation time for the five studied surface packing fractions. After the scaling time Λ reaches a final stationary value (dashed lines are only guides for the eyes).

process induces ordering not only between nearest neighbors ($j = 1$), but also between well removed clusters ($j >> 1$). It is remarkable that, for times beyond the scaling time the curves saturate and the topological ordering of the froth arrives at a stationary state.

This behavior can be better observed if we represent the asymptotic value of the proportion of defects Λ as a function of time. Unfortunately, our simulated data go up to topological distances $j \leq 19$ and we do not have valuable information at larger distances. This is mainly due to the poor statistics that we have for such large distances, especially for long aggregation times, where the number of clusters is small and the analysis becomes affected by the boundaries of the simulation box. Nevertheless, although the defect concentration shown in figure 5.18 does not reach completely this asymptotic value, there is a clear trend that points out the existence of a constant value for large enough topological distances. This constant value is rather logical[1]

[1]We refer the reader to ref [113], where a similar behavior for the proportion of defects

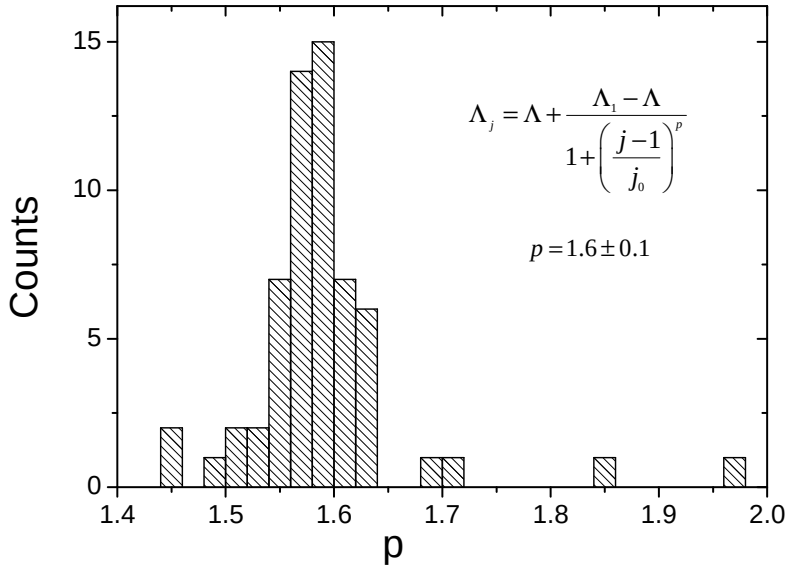

Figure 5.20: Histogram of the values obtained for the parameter p for all times and surface packing fractions.

since there is not difference between any shell and the next one for large values j. In this respect, our asymptotic value is in fact an extrapolation of the simulated data for large j.

In order to estimate this parameter, the simulated data have been fitted according to the following empirical law:

$$\Lambda_j = \Lambda + \frac{\Lambda_1 - \Lambda}{1 + \left(\frac{j-1}{j_0}\right)^p} \tag{5.4}$$

where Λ is the asymptotic value for $j >> 1$, Λ_1 is the percentage of defects for the first layer and p and j_0 are fitting parameters. The regression coefficient was $r > 0.99$ in all fittings and, as we can see in figure 5.20, the value for the parameter $p = 1.6 \pm 0.1$ for all times and surface packing fractions.

In figure 5.19 the asymptotic behavior of the topological defects is shown. What we obtain is a plot which resembles the one obtained for μ_2 (figure 5.6), i.e. Λ decreases with the aggregation time for $t < t_{sc}$ and becomes constant for $t > t_{sc}$. Once again, the arrangement provoked by the aggregation is

is observed and a final asymptotic stabilization is found.

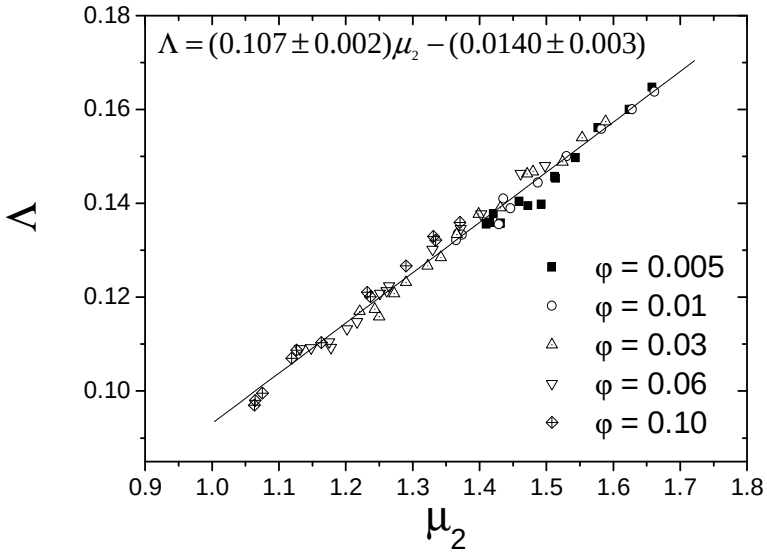

Figure 5.21: Asymptotic value for the topological defects, Λ, versus μ_2 for all the packing fraction considered. As we can see, there is a linear dependence between these magnitudes.

more important for higher particle concentrations: the average value found in the scaling regime decreases as we increase the surface packing fraction up to $\varphi = 0.1$. As discussed in Section 5.7 for μ_2 and a parameters, the decrease of the number of defects at all topological distances also accounts for the fact that fractal cluster growth at high particle concentrations leads to a stronger density modulation of the system and so, to more structured close–packed structures (an ideal hexagonal froth has $\mu_2 = 0$, $a = 0$ and $\Lambda = 0$).

In figure 5.21, we represent Λ versus μ_2 for the different simulations. As can be observed, there is a linear dependence between both magnitudes which slope do not depend on time.

By using the simulated values of Λ, μ_2 and a into expression 4.91 we can calculate theoretically the average number of sides lost in the defective cells, η. The behavior of η does not show clear tendencies with the aggregation time or particle density. On the contrary, it remains roughly constant for all the studied situations, and given by $\eta = 1.30 \pm 0.05$ (figure 5.22).

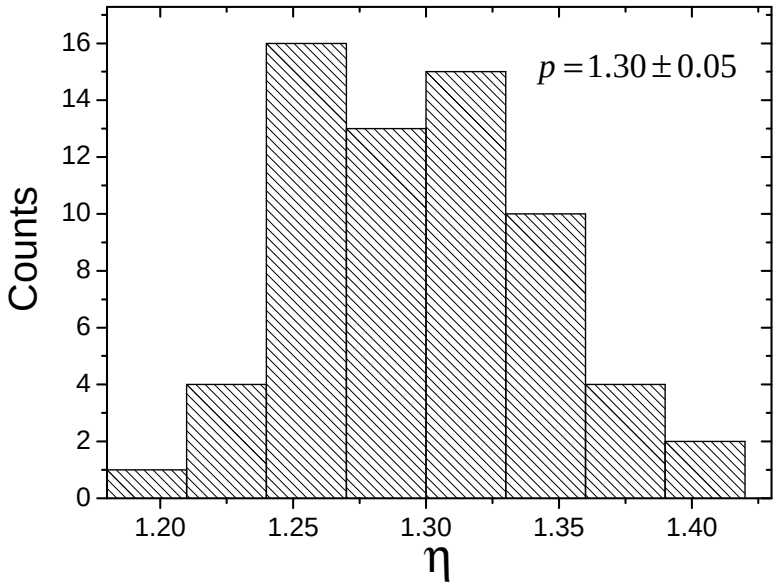

Figure 5.22: Histogram for η values obtained for all times and surface packing fractions.

$< K_j >$

Finally, we study the behavior of the slope C, obtained from the fitting of $< K_j >$ (eq. 4.78) in the asymptotic limit. Figure 5.23 shows a typical examples of the dependence of $< K_j >$ on the topological distance for the particular case of $\varphi = 0.06$. The values obtained for C are shown in figure 5.24 for the five studied particle densities and times before and after the scaling. Again we observe different behavior between the early stages of the aggregation (where C decreases monotonically with t) and the final stationary value found in the scaling regime. Particularly, C takes values close to 11 at the beginning of the coagulation and decays to a final value that is smaller at higher particle concentrations (from $C = 9.57$ for $\varphi = 0.005$ to $C = 8.82$ for $\varphi = 0.1$).

The quantity $C \cdot j$ can be understood as the average perimeter of a j–layer. For perfect spherical layers the value of C should be $2\pi \approx 6.28$. However, the C–values calculated from the DLCA computer simulations are always higher at all aggregation times and particle densities, what is an evidence for the roughness of the shell structure, due not only to the fact that the cells do not

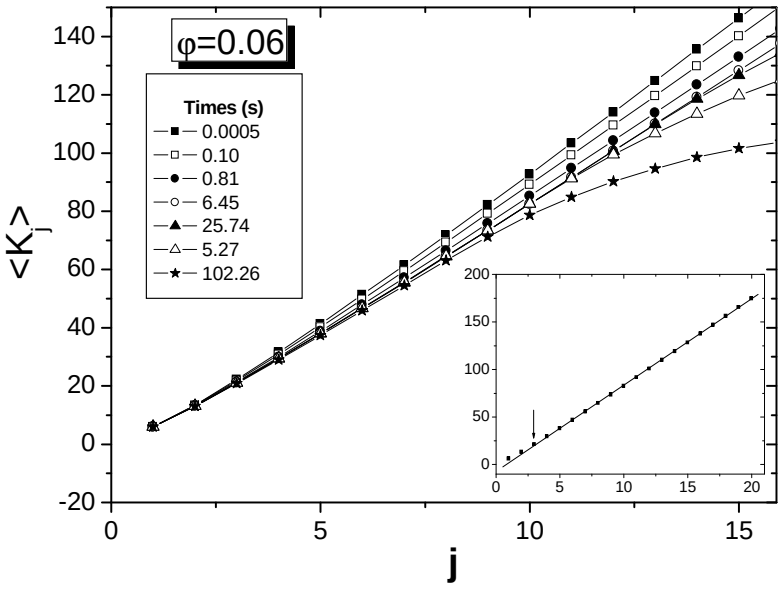

Figure 5.23: Dependence of the average number of cells $< K_j >$ on the topological distance j for DLCA simulation with $\varphi = 0.06$ for different times. Inset: $< K_j >$ grows linearly for $n > 3$.

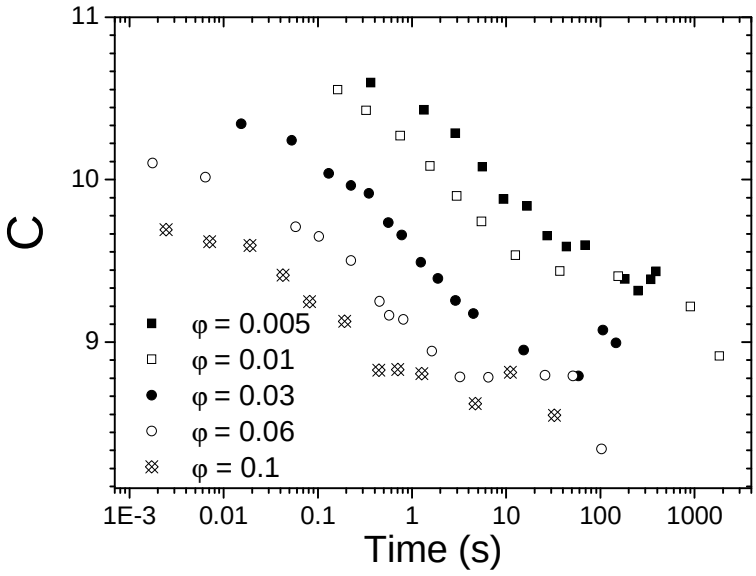

Figure 5.24: Time evolution of the slope C of $< K_j >$ for the five studied surface packing fractions. After the scaling time C also has a constant value.

form a smooth circle, but also to the presence of topological defects. Indeed, shell structures with many defective cells will have layers of larger perimeter and higher values of C. This fact establishes a connection between C and the defect concentration Λ (C decrease with Λ). Therefore, the long–range topological order induced by the aggregation process is also the responsible of the decrease in C with t during the pre–scaling regime.

The comparison between the simulated results for C and the theoretical prediction given in Eq. 4.88 for froths uncorrelated after the second layer, is generally in good agreement. Although some departures are observed between simulated data and theory, they are mainly due to statistical errors in the determination in the parameters involved in such expression. It proves that C is not an independent variable, but it is attached to the values of μ_2, a and Λ. Similar dependencies have been observed for several topological quantities, as $K_2(n)$, $K_3(n)$ and $< Q_j >$. Since the asymptotic value of the defect concentration Λ is also linked to the global disorder in the froth (set by μ_2), we conclude that all the short and long–range topological properties in the system of aggregating clusters are controlled by the screening factor a and the second central moment μ_2. Both parameters are mean field

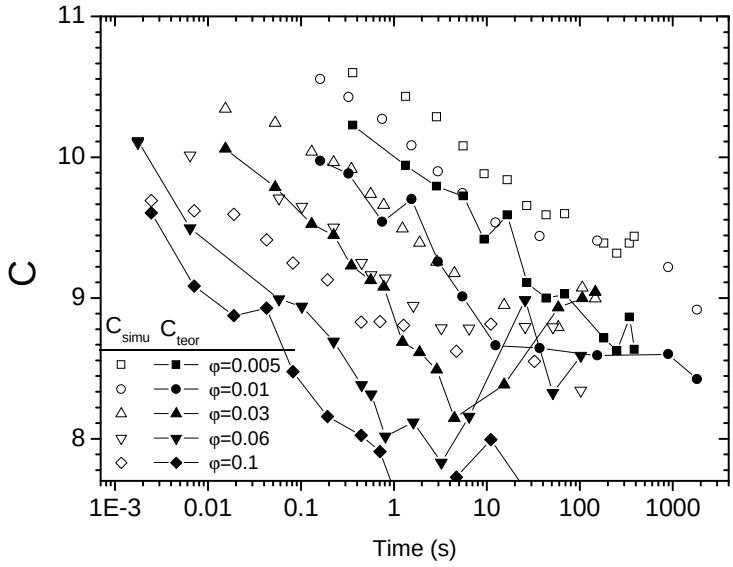

Figure 5.25: Comparisons of the C values obtained from the simulation and the theoretical results.

properties that characterize the global disorder and the correlation between nearest neighbor clusters, but do not give any information about the long–range structure. Thus, we find the surprising fact that the long–range order is determined by average properties involving only single cells and nearest neighbors correlations.

In our opinion, the fact that the long-range correlations are determined by average properties as the second central moment μ_2 and the parameter a, is basically a consequence of the lack of cell-cell correlations for topological distances beyond the second concentric layer, $j > 2$. It allows us to express the topological properties for $j > 2$ as functions of the properties for $j \leq 2$, that are mainly given by μ_2 and a. One good example of this may be seen in the study of the average topological charge $< Q_j >$ (see Eqs. 4.5.3, 4.82 and 4.83), where the lack of cell-cell correlations for $j > 2$ leads to an expression for $< Q_j >$ only in terms of properties of the cells with $j \leq 2$, as $K_2(n)$ and $< Q_1 >$ that, in turn, are given in terms of μ_2 and a. For such froths where the topological correlations reach larger distances, this simple scheme will not hold and a more sophisticated description will be called for.

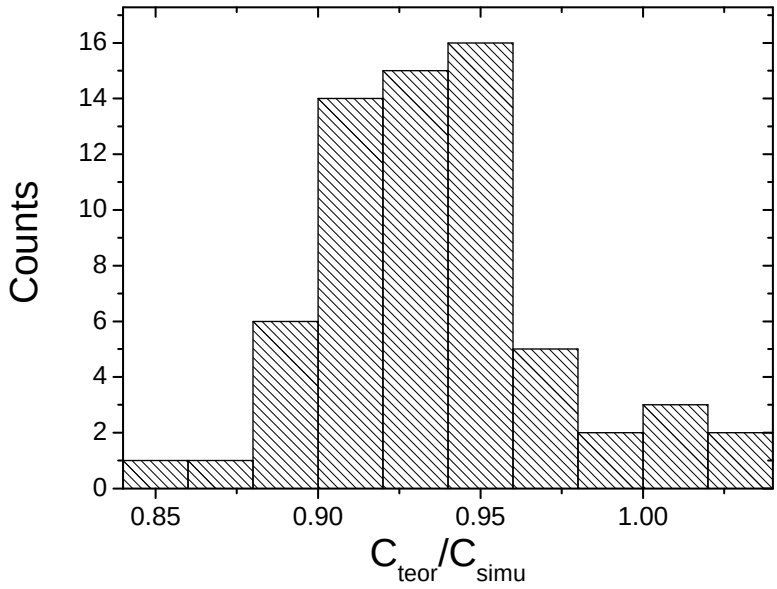

Figure 5.26: Histogram for the ratio C_{teo}/C_{simu}. Although there is significant differences between C_{teo} and C_{simu}, the simple model for C (equation 4.88) is able to reproduce quite well the simulation results.

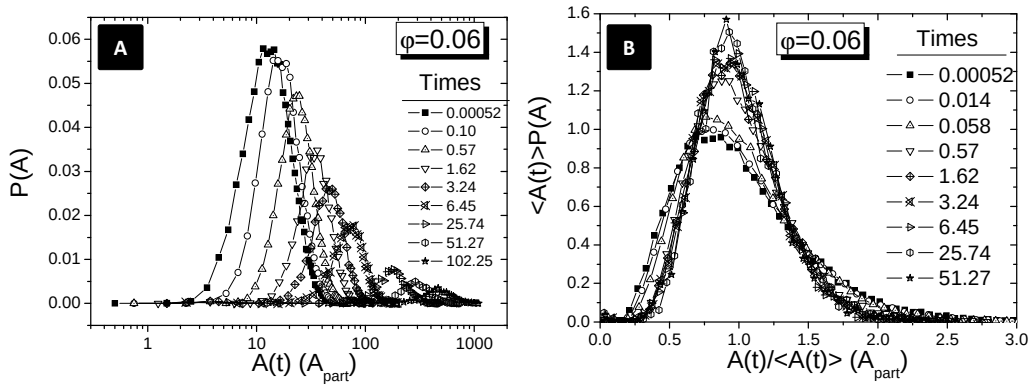

Figure 5.27: A) $P(A)$ distribution obtained for $\varphi = 0.06$ for different times. B) Representation of $< A(t) > P(A)$ versus $A/ < A(t) >$ for the same simulation. We can see that the area distribution becomes more symmetric when the time increases to reach a time, after that, the area distribution remains constant.

It should be noted that these results obtained for two–dimensional cluster–cluster aggregation can not be, in principle, extrapolated to other types of space–filling structures. For instance, the correlations between biological cells can be important even for $j > 2$, and then all the theoretical expressions shown above will break down.

5.8 Area distribution

Here, we study of the area distribution of the cells $P(A)$ (defined as $P(A) = \sum_{n=3}^{\infty} P(n, A)$) of a system of clusters under coagulation in two dimensions. The area of the cells is the area filled by the real cluster together with its surrounding depletion region. In figure 5.27-A we show the distribution $P(A)$ versus the area expressed in particle area units ($A_{part} = \pi R_p^2$) for the simulation $\varphi = 0.06$. In all cases, $P(A)$ is asymmetric [2] respect to the mean value $\bar{A}$. This means that there is a higher probability to find a cell with an area a above the mean value $\bar{A}$ than under it.

In section 5.7, we showed that the number of sides distribution ($P(n, t)$) was time independent after the aggregating system reaches the scaling regime.

[2]Note that the time is presented in logarithmic scale

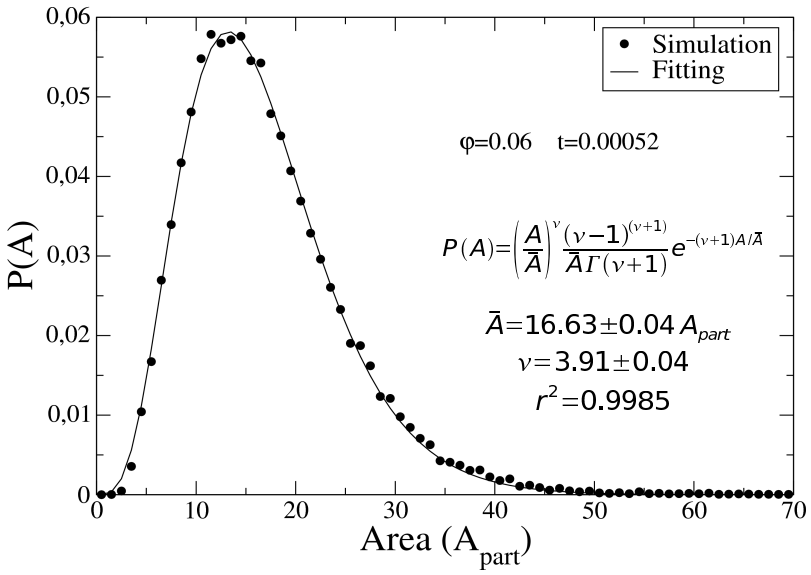

Figure 5.28: Example of fitting of $P(A)$ with a Schultz distribution.

Here, we observed a similar behavior for the area distribution $P(A,t)$. As it can be observed in figure 5.27-B, the function $f(x) =< A(t) > P(A,t)$ with $x = A/ < A(t) >$ is also invariant [132]. We also observe that the area distribution becomes more symmetric with the time to reach the scaling time, afterward, it remains roughly constant.

The distribution $P(A)$ can be fitting with good accuracy using a Schultz distribution (figure 5.28), which is usually employed to determine the polydispersity index of colloidal dispersions

$$P_{Schultz}(A) = \left(\frac{A}{\bar{A}}\right)^{\nu} \frac{(\nu-1)^{\nu+1}}{\bar{A}\Gamma(\nu+1)} e^{-(\nu+1)A/\bar{A}} \tag{5.5}$$

where $\bar{A}$ is the mean value of the distribution and ν represents its asymmetry. In the fitting process, we used the values of $< A(t) >$ obtained from the simulations and we use as a free parameter ν. The ν parameter is relate to the polydispersity index *ind* as

$$ind = \frac{1}{\sqrt{1+\nu}} = \frac{\int_0^\infty a^2 P(a)da - \left(\int_0^\infty aP(a)da\right)^2}{\int_0^\infty aP(a)da} = \frac{\sigma^2}{\bar{A}} \tag{5.6}$$

The obtained values for ν (figure 5.29) grow with time to reach a constant value after the scaling time, that is, the polydispersity index *ind* decrease

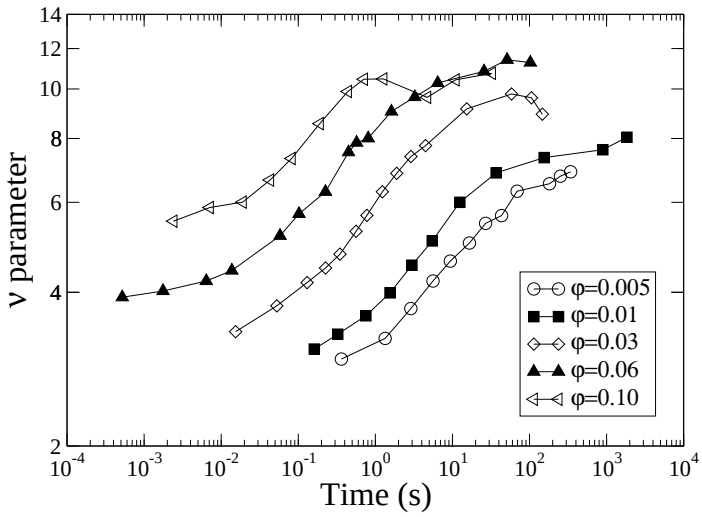

Figure 5.29: Time dependence of the ν parameter.

with time. In other words, the DLCA aggregation process tends to make more uniform the size of the cells before the scaling time. Afterward, the polydispersity of the system remains constant.

The behavior of the ν parameter is similar to the one observed for the second moment of the side distribution, μ_2, and it is possible to find a relationship between them as $\nu = 14.67\mu_2^{-2.56}$ as we see in figure 5.30

5.9 Conclusions

We studied the time evolution and the topological properties of computer–simulated two–dimensional aggregating systems for several surface packing fractions of particles. We assumed the simplest case of freely Brownian diffusive sticking particles without interactions (DLCA). The topological properties have been measured with the help of the Voronoi construction, which replaces the original system of aggregating cluster by an equivalent system of convex non–overlapping regions (cells) that completely tessellate the plane, each cell representing a single cluster of the system and its surrounding depletion zones. The study of the correlations between non–adjacent cells was

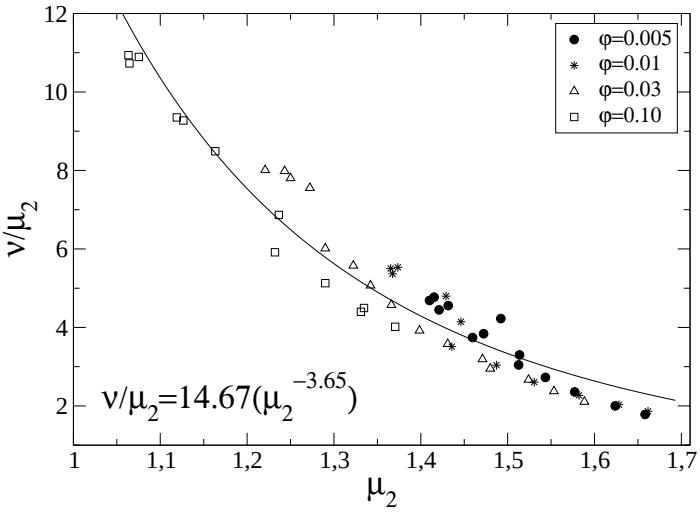

Figure 5.30: The simulated μ_2 and ν/μ_2 data at any time and for the five studied particle concentrations lie in a universal common form: $\nu = 14.67\mu_2^{-2.56}$. In this plot, the μ_2-axis is representative of the time-axis, but in the opposite direction.

achieved by analyzing the system as structured in concentric layers around a given central one. This method allows us to go beyond the internal fractal structure of the clusters and to study the external inter–cluster properties. Indeed, it determines the short and long–range spatial organization and the cluster–cluster "interactions" induced by the mutual competition between neighboring depletion regions that occurs when the fractal–like clusters fill up the whole space.

We found that the topological aspects of the aggregation are strongly connected to the kinetic ones . In all cases, we obtained a continuous ordering of the cell structure as aggregation proceeds. Specifically, clusters tend to adopt a more ordered hexagonal organization in the plane, what topologically means a reduction in both, the second central moment of the number of sides distribution μ_2 and the proportion of defects Λ. This ordering is more important for higher particle densities, where the already small free space existing between growing clusters becomes rapidly shrunk due to the fractal growth. This ordering finishes as soon as the scaling of the cluster–size distribution is reached ($t > t_{sc}$). Since all the studied topological properties ($P(n)$, μ_2, a, $< K_j >$, $< Q_j >$ and Λ) remain constant in this final scaling limit, it can be regarded as a topological invariant state. We also found that the whole coagulation process (after and before the dynamic scaling) lies in a universal topological class independent on the particle concentration, given by the general relation $a \sim \mu_2^{-0.89}$.

After the comparison of the simulated data and the theoretical expressions, we concluded that colloidal aggregation in two dimensions is only able to produce short–range inter–cluster correlations (up to the second layer of clusters around a central one, $j = 2$) even for the very high packing fraction of particles. However, the ordering is manifested in the whole shell structure at any topological distance in terms of a decrease of the proportion of defective cells Λ_j. We have also shown that the main topological property that controls the degree of structuring at short and long inter–cluster distances is the second central moment μ_2, which is a measurement of the global order in the whole system.

Finally, in a logical step forward, it is highly interesting to extend the topological/structural description to three–dimensional aggregating systems of dense colloidal suspensions and to colloidal systems with interacting particles as those with long–range particle–particle repulsive interactions. Note the difference between our results and earlier results in 3D [14, 15], where it is found that, after the depletion region, the particle-particle correlation

function tends to the value one after reaching the nearest neighbor clusters, without further oscillations in this function (besides those coming for the statistical uncertainties). It is possible that the clusters in 3D, due their ability to interpenetrate more easily without touching [129], “feel a lower repulsion between them”, while in 2D the greater ”repulsion” would make the clusters to become more ordered, increasing in this way the ξ to a value equal to two. Absence of further oscillations could also be due to having considered the particle–particle correlations function and not the cell–cell correlations as in the present work. All this merit a similar study for the three dimensional case, as stated above.

Chapter 6

Effect of repulsive interaction with non–negligible range

We have studied the effect of the interaction's range in computer–simulated two–dimensional aggregating colloidal system [128]. For this purpose, we considered that the particles of the system interact among them through a repulsive Yukawa potential which depends on two parameters: the value of the interparticle interaction potential at contact $V_0 > 0$ and the range of the interaction κ^{-1}. We observed that the increase of the interaction range provokes the arrangement of the small aggregates in linear structures. The repulsive interactions also have a strong influence on the kinetic behavior of the coagulation process. Indeed, they induce the transition between two different aggregation regimes. In the first regime (at early states) the aggregation is dominated by the range of the repulsive forces, and the cluster–cluster repulsion increases with the cluster size. The second regime (at intermediate times) is reached when the average cluster size is larger than the interaction range. In this regime, the strength and the range of the cluster–cluster repulsion becomes nearly independent of the cluster size, so the probability of overcoming the repulsive barrier is the same for all clusters. This corresponds with the so called RLCA regime, where more than one collision is needed to form a bond.

6.1 Introduction

A previous simulation work [133], using a *Metropolis Monte Carlo Procedure*, was successfully reproduced the low cluster fractal dimensions experimentally obtained for a two–dimensional colloidal aggregating systems [134], whose particles were assumed to interact via a repulsive medium–range potential. However, that work was restricted to the analysis of the structural behavior, while the dynamics was set aside.

In this chapter we report kinetics and structural results from two dimensional colloidal aggregation simulations using a medium–range repulsive interaction potential. The repulsive interaction considered is the Yukawa potential, which has been used in many fields to model screened interactions.

The kinetics results were fitted using the general form for the coagulation kernel $k_{ij} = k_{ij}^{Br} P_{ij}$ (see section 2.3.4), where no purely diffusive aggregation (DLCA–regime) contributions are included in the P_{ij} functions.

6.2 Simulations description

*Brownian Dynamics off-lattice simulation*s were performed in a square box of side L with periodic boundary conditions. A total number of monomer particles $N_0 = 21904$, with a particle radius $a = 300$ nm, were used. The length of the box L was fitted to have a packing fraction $\varphi = N_0 \pi a^2 / L^2 = 0.005$. Initially, monomers were placed at random avoiding particle–particle overlapping. The simulations time step Δt was set a constant value so that the mean square displacement of a particle is given by $\Delta r^2 = 2 k_B T \Delta t / (3 \pi \eta a)$ where T is the temperature and η the viscosity.

The interaction potential between the particles was the Yukawa potential. This potential represent the analytical solution for the Poisson–Boltzmann equation (3.3) in the framework of the Debye–Hückel approximation[1]:

$$V_{11} = \frac{V_0}{r^*} e^{-\kappa d (r^* - 1)} \tag{6.1}$$

where $r^* = r/d$ is the distance between the centers of the particles expressed in units of the particle diameter d, V_0 is the value of the potential at contact

[1] That is obtained from the linearization of the Poisson–Boltzmann equation, which is valid when the electrostatic energy is small compared with the thermal energy

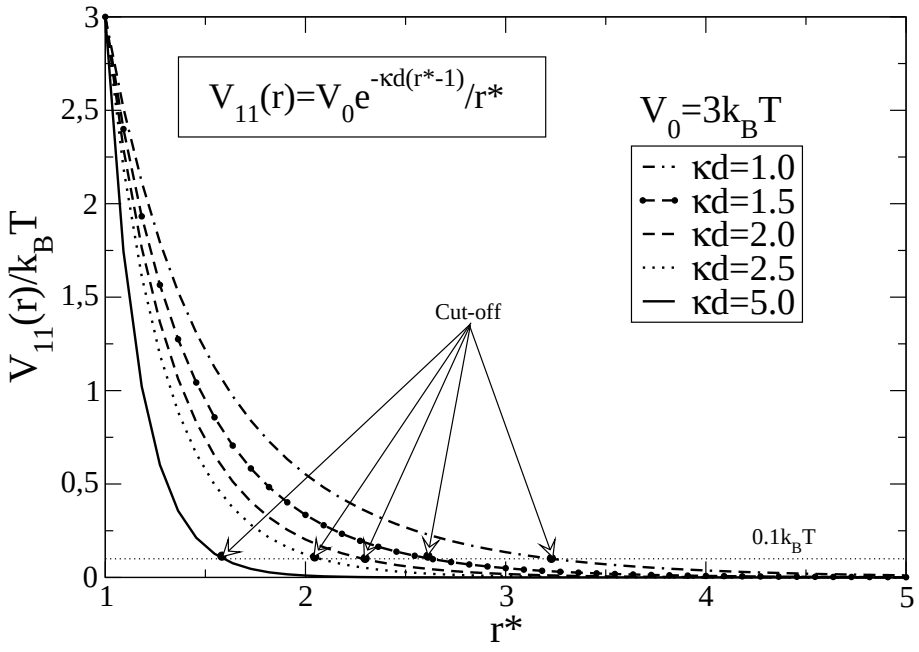

Figure 6.1: Interaction potentials used in the simulations with $V_0 = 3k_BT$ and $\kappa d = 1.0, 1.5, 2.0, 2.5$ and 5.0

($r^* = 1$), and $1/(\kappa d)$ is related to the range of the potential. In our simulations, we fixed $V_0 = 3$ k$_B$T and we used $\kappa d = 1.0$, 1.5, 2.0, 2.5 and 5.0. The resulting potential interactions are showed in figure 6.1. In practice, the Yukawa potential of interaction was cut at a cut–off length r^*_{cut} such as $V_{11}(r^*_{cut}) = 0.1k_BT$.

In the simulations, the movement of the aggregates was performed picking cyclically each cluster and determining the total force $\vec{F}_{ext}$ acting on it. This force is the result of the interaction of each particle of the cluster with the particles of the neighbor clusters that are closer than the cut-off length r^*_{cut}.

$$\vec{F}_{ext} = -\sum_{particles} \vec{\nabla} V_{11} \tag{6.2}$$

In order to have a good sampling of the interaction range, the time step

of the simulation was taken so that $r^*_{cut}/\Delta r \approx 30$. In this way, we guarantee that a cluster needs to make a lot of steps to contact with another cluster.

The motion is assumed to be governed by the *Langevin equation* (see section 2.1.1). This equation 2.1 is solvable and the probability density function in the diffusive time scale, defined as the probability to find a cluster at the position $\vec{r}$ at time t when it was in $\vec{r}_0$ at time t_0, is given by:

$$P(\vec{r},t) = \frac{1}{4\pi D\Delta t} e^{-|\vec{r}-\vec{r}_0-\vec{F_{ext}}t/\gamma|^2/(4D\Delta t)} \tag{6.3}$$

where D is the cluster's diffusion coefficient, $1/\gamma = D/(k_B T)$, k_B is the Boltzmann constant and T is the temperature. Thus, the center of mass of the cluster is moved by a vector $\vec{d} = (d_x, d_y)$ where d_x and d_y are numbers distributed according to this Gaussian probability distribution 6.3.

Coagulation occurs when a cluster overlaps another one. Then, the position of the cluster is corrected in the opposite direction of its movement just to put them in contact. Afterwards, these clusters becomes joined to form a larger cluster that will continue the movement in the following time step.

Finally, the simulations were stopped when the number of clusters was smaller than 200 aggregates. For all the performed, this is enough to reach the scaling time and to have a good statistics for all aggregation times.

The algorithms used were already applied to show the existence of dynamic scaling in both DLCA and RLCA regimes [27, 18, 127].

6.2.1 Obtaining the aggregation kernel

Due to the cut–off of the interaction potential each monomer has associated an interaction region defined by a circle centered on it and with radius r^*_{cut}. Outside this region, the interaction potential with another monomer is neglected ($V_{11}(r^* > r^*_{cut}) < 0.1 k_B T$). So we will consider that a collision occurs between two clusters, if the particles of one of them overlap the interaction region of one (or more) particles of the other one. We also define an encounter between two clusters as the set of consecutive collisions between them before they coagulate or one of them diffuse to collide with a different cluster (figure 6.2).

We define N_{ij} as the number of encounters between clusters of size i with clusters of size j, and C_{ij} as the number of coagulations between i–clusters with j–clusters. Therefore, we can calculate the "*probability of coagulation*

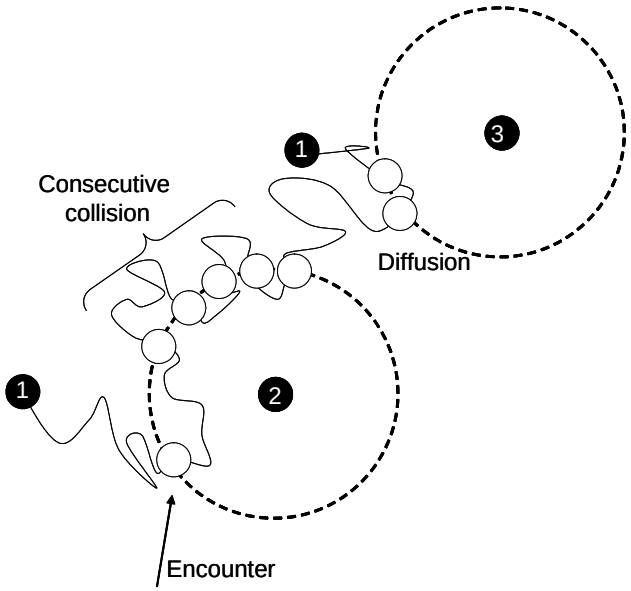

Figure 6.2: In this scheme we depicted three monomers labeled as 1, 2 and 3. The dashed circles around the monomers 2 and 3 of radii r^*_{cut} represent the interaction regions around them. First, the moving particle 1 crosses the interaction region of particle 2 several times (first encounter). This encounter finishes when the particle 1 diffuses away from particle 2 to collide with particle 3.

per encounter" (PE_{ij}) as:

$$PE_{ij} = \frac{C_{ij}}{N_{ij}} \tag{6.4}$$

If we consider the same cutoff radius, r^*_{cut}, for the DLCA coagulation process we found that $PE^{DLCA}_{ij} < 1$, because not all encounters lead to coagulation. In order to account only the effect of the interaction potential (not the diffusion effect), we need to correct the probability of coagulation by encounter using the PE^{DLCA}_{ij} values. Therefore, the functions P_{ij} may be obtained as the ratio:

$$P_{ij} = \frac{PE_{ij}}{PE^{DLCA}_{ij}} = \frac{k_{ij}}{k^{Br}_{ij}} \tag{6.5}$$

Hence, as both PE_{ij} and PE^{DLCA}_{ij} values can be obtained from the simulations, **we are able to estimate the effect of the interaction on the coagulation kinetics**.

6.3 Solving the Smoluchowski equation

In order to solve the *Smoluchowski equation* 2.24, we need to know the explicit expression of the coagulation kernel, k_{ij}, given by $k_{ij}^{Br}P_{ij}$, where k_{ij}^{Br} is the *Brownian kernel* (eq. 2.32 with $k_{11} = 4.5 \cdot 10^{-12}\ m^2/s$) and P_{ij} are obtained in our case from the simulation results as previously indicated (section 6.2.1). The numerical integration of these equations was done using a fourth–order *Runge-Kutta technique* with an adaptive time step [135], with $c_k(t)$ evaluated sequentially at each time step.

We truncated the infinite differential equation system to have only 500 equations. So, we reach a good accuracy and we are able to compare with simulation results for which a weight average cluster size of $S_w \sim 200$ is obtained.

The program code has been tested using both: the constant and the sum kernels [30]:

1.- *Constant kernel*. If the kernel has a constant value for all aggregate sizes, $k_{ij} = k_{11}$, the analytical solution is

$$c_i(t) = c_0 \frac{(k_{11}c_0t)^{i-1}}{(1 + k_{11}c_0t/2)^{i+1}} \tag{6.6}$$

2.- *Sum kernel*. It corresponds to the kernel $k_{i,j} = (k_{11}/2)(i + j)$. In this case, the analytical solution is given by

$$c_i(t) = c_0 \frac{(1 - [1 - e^{-k_{11}c_0t/2}])(i[1 - e^{-k_{11}c_0t/2}])^{i-1}e^{-i(1-e^{-k_{11}c_0t/2})}}{i!} \tag{6.7}$$

Figure 6.3 shows the analytical and numerical solutions for several cluster sizes and both kernels. The perfect agreement between them demonstrates the correctness of our numerical method to solve the Smoluchowski equation.

6.4 Results and discussion

6.4.1 Structure

The characterization of the structure of the colloidal clusters is strongly related to the study of the aggregation kinetics. The fractal dimension fea-

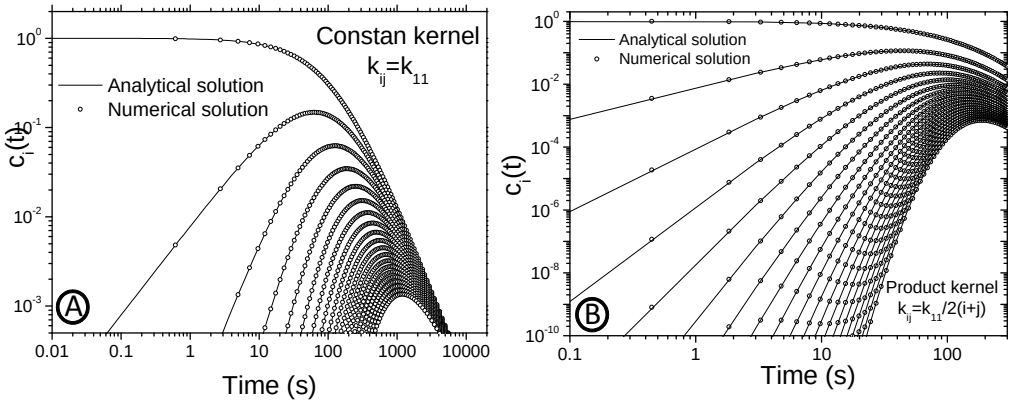

Figure 6.3: Analytical and numerical solutions for the Smoluchowski equation for: A) the constant kernel. B) the sum kernel.

tures the inner structure of the cluster. It is well known that DLCA aggregation leads to more open structures ($d_f \sim 1.44$ for $2D - DLCA$) than those obtained with short interparticle repulsive interactions ($d_f \sim 1.55$for $2D - RLCA$) [27]. Here, we want to analyze here is **the effect that a pairwise interaction with a non-negligible range has on the fractal structure o the formed clusters.**

We have used the *radius of gyration method* (eq. 2.22) in order to calculate the fractal dimension (figure 6.4). For the longest interaction range case ($\kappa d = 1.0$), two different regions with different slopes can be distinguished in the behavior of i vs R_g, one for clusters composed by less than 15 monomers (***small aggregates region***) and the other for clusters composed by more that 15 monomers (***big aggregates region***). This fact reveals that the structure of the aggregates depends on their sizes. Although it is not possible to define the fractal dimension for clusters before the scaling region, this slope is clearly related to the structure of these small clusters. The value of the slope in the first region ($d_f = 1.16$) clearly points out an enhancement of the linear conformation of the small clusters while the fractal dimension associated to the big clusters region ($d_f = 1.55$) recovers the typical fractal dimension of the RLCA aggregation regimen. As the interaction range decreases, the slope of the first region increases (figure 6.5), i.e., small clusters are less linear, and the differences between the first and the second regions become less pronounced. Therefore, the origin of the first region is a di-

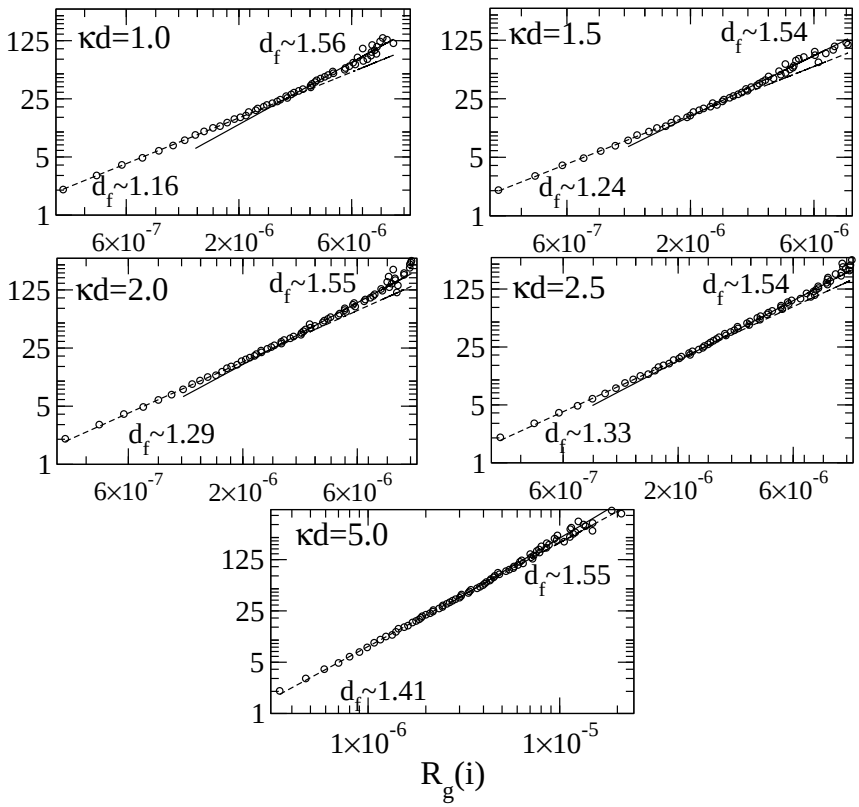

Figure 6.4: The cluster size versus the radius of gyration for the different simulations performed. Two different regions can be distinguished, with different slopes, for all the cases. The small aggregates tends to be more linear when the interaction range is increased as is demonstrated by the decreasing of the slope of i vs R_g as κd decreases.

rect consequence of the repulsive interaction potential with a non–negligible range. The structure of the big clusters, as indicated by the fractal dimension, is similar for all the interaction ranges and comparable to that of the RLCA aggregation regime.

A direct confirmation of the high linearity of the small clusters is given in figure 6.6 where we can see typical fractal clusters formed in the simulations. For the longest interaction range ($\kappa d = 1.0$), we observed a high linearity of the small clusters, for the big ones. When the interaction range decreases, the small clusters become more ramified, but they still are more linear than the big ones. This fact is demonstrated by the increase of the fractal dimension, compared with the smallest clusters, when changing the interaction range from $\kappa d = 1.0$ to $\kappa d = 5.0$.

In conclusion, the formation of linear small clusters is a consequence of the range of cluster–cluster repulsions, according to the discussion of section 2.3.4. Indeed, a non negligible interaction range induces an anisotropic cluster–cluster interaction potential, that depends on the relative orientation between the clusters. In this case, the orientation that minimize this repulsion between clusters give rise to the formation of linear structures, since two clusters tend to coagulate setting their monomers as separated as possible. When the clusters are large enough (larger than a *critical size* i_0), their interaction potential becomes nearly independent on the cluster size, as not all the monomers that form the clusters participate in the cluster–cluster interaction. For medium–size clusters, there is not a privileged orientation of aggregation so the interaction potential becomes more and more isotropic as the cluster size increase. Thus, finally the fractal dimension for RLCA regime is recovered.

In order to demonstrates this important property of the cluster–cluster interactions the *average interaction potential*, $< V_{ij} >$ was calculated. $< V_{ij} >$ using 50 different clusters of size i and j selected from the simulations. The total interaction was averaged over their relative orientations and shapes. The $< V_{ii} >$ potentials ($i = 1, 2, \ldots, 9$) for different interaction ranges are shown in figure 6.7. We observe that the interaction potential $< V_{ii} >$ becomes independent of i being the critical size values $i_0 = 6, 5, 4$ and 3 for $\kappa d = 1.0, 1.5, 2.5$ and 5.0, respectively. This supports that the reactions between clusters larger than i_0 do not depend on their size. As the interaction potential becomes independent of the cluster's size and the interaction range, the fractal cluster dimension value approach that of the RLCA regime.

For long enough aggregation times, the mean cluster size is so big that the

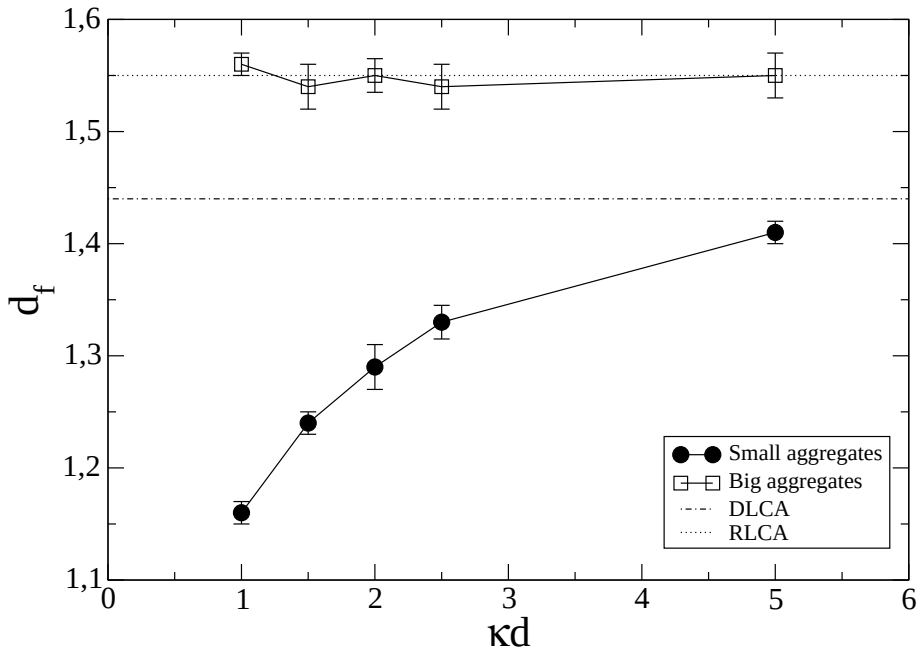

Figure 6.5: Fractal dimension versus κd obtained by the fitting of the radius of gyration in the small clusters region (fill symbols) and in the big clusters region (open symbols). The linearity of the small aggregates decreases as the interaction range is reduced, however the fractal dimension for the big clusters is constant and compatible with the typical value for the RLCA aggregation regime (~ 1.55).

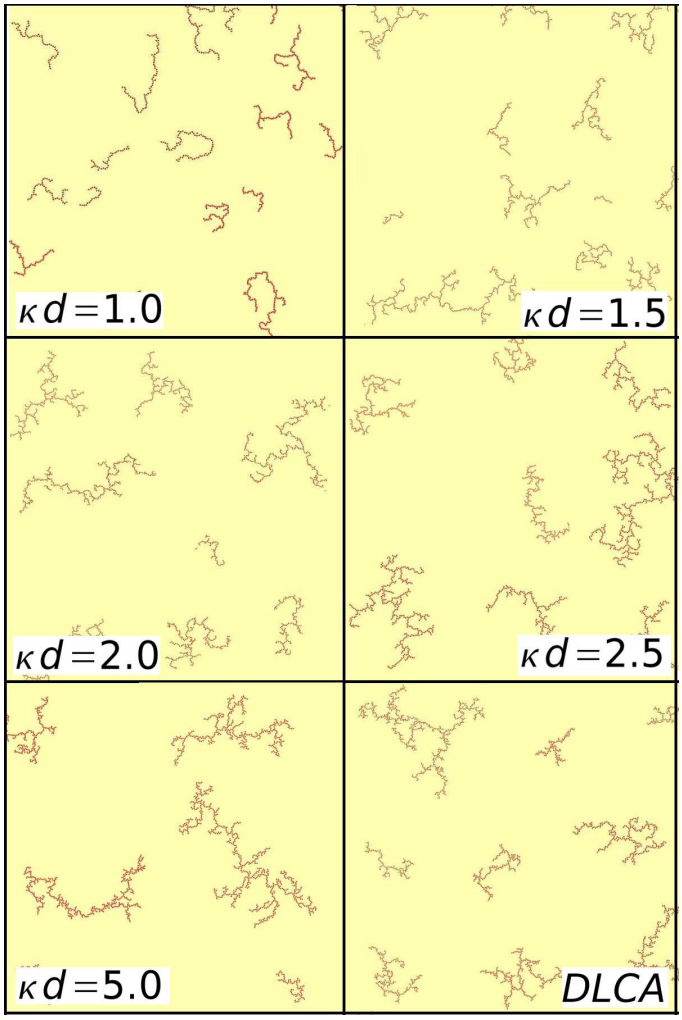

Figure 6.6: Typical fractal clusters formed in the simulation of the aggregation with a Yukawa potential for different interaction ranges and $V_0 = 3$ k_BT. For the longest range ($\kappa d = 1.0$) we can observe a high linearity of the clusters structure. As the interaction range is decreased we observe that the smallest clusters have a low fractal dimension but, when they grow up, the bi clusters become more ramificated. After that, the "fractal dimension" of the small clusters increases continuously as the interaction range decreases and the big clusters reach a fractal dimension value equal to that of the RLCA case.

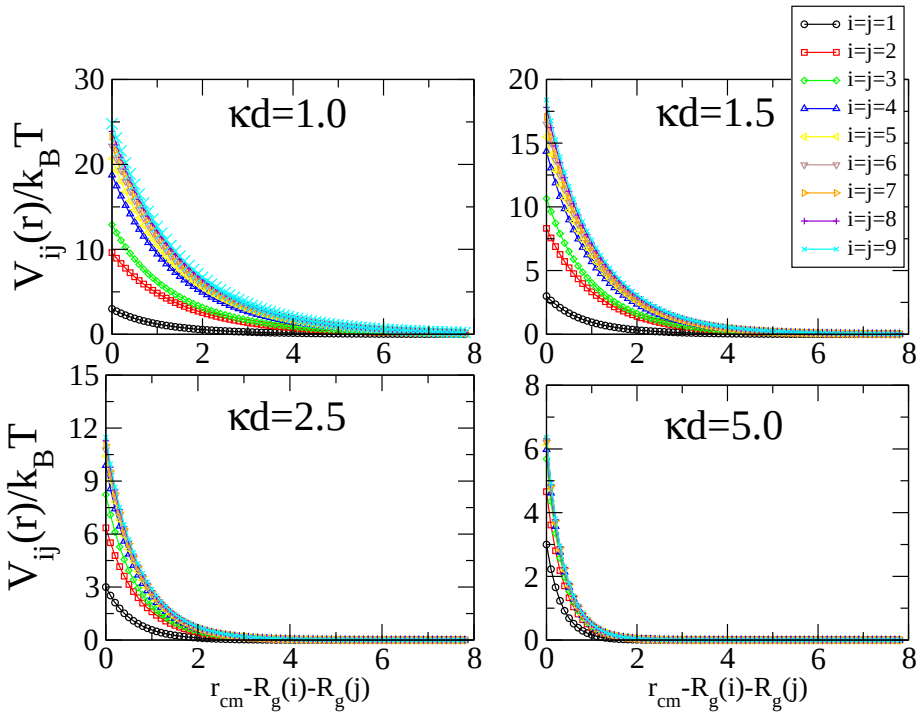

Figure 6.7: Average of the i-mer/i-mer interaction potential versus the cluster–cluster separation, $r = r_{cm} - R_g(i) - R_g(j)$ for different interaction ranges. Here, r_{cm} is the distance between the center of mass of the clusters and $R_g(i)$ and $R_g(j)$ are the radius of gyration of the clusters i and j, respectively. Each point was obtained averaging with 50 different cluster shapes and orientations. We observed that the interaction becomes more repulsive with the increase of the cluster size i. After reaching the critical size, $i = i_0$, the interaction becomes independent on i. All distances are expressed in particle radius units.

coagulation should be dominated by the diffusion (transition from the RLCA to the DLCA regime) as commented in section 2.3.4. However, this transition has been observed only for the shortest interaction range ($\kappa d = 5.0$), but not for the other simulations. This could means that not enough big cluster size was reached in order to observe the crossover to DLCA regime.

Thus, the formation of chains clusters and the transition to the RLCA regimen can be explained on the basis of the superposition of the cluster–cluster interactions with a non–negligible range and their dependence of such interactions on the size of the involved clusters.

The formation of chains has also been observed in experiments [136] and simulations [137, 138] for $3D$–colloidal systems when the particles interact among them with a potential that prevents the aggregation in the primary minimum. However, in the refered works, the potential has a secondary minimum induced by the presence of non–adsorbing polymers (depletion interactions), That provokes a non–truly irreversible aggregation. In this situation, the clusters are not rigid but they fluctuate around typical configurations and the rearrangement of the particles provokes the formation of the so called *Bernal spirals* [137, 138].

6.4.2 Kinetics

Figure 6.8 shows the evolution of the *mean cluster size*, $S_n(t)$ (Eq. 2.27), versus the aggregation time for the simulations performed varying κd. We can distinguish two different kinetic regions in the behavior of $S_n(t)$. In the first region (***range effect region***), the mean cluster size increases very slowly with the time. Here, the growth of the clusters is strongly dependent on the parameters of the interaction potential. This range-effect region is widther more clear for the longer interaction range. In the second region, the growth of the cluster is faster and the kinetics exponent tends to the characteristic values of the ***RLCA regime*** ($z_{RLCA} \sim 0.67$)[27]).

The kinetics results are consistent with the effect of the interaction range as considered in section 2.3.4. For small aggregates (with sizes $i < i_0$) the cluster–cluster repulsion increases with the cluster size. That explains the first kinetics region where the growth of the clusters is very slow. When the mean cluster size reach the critical size, i_0, the interaction becomes independent of the size and the interaction range looses its main importance to control the aggregation kinetic. Then, the aggregation rate becomes faster due to the increase of the cross section of the clusters, while the interaction

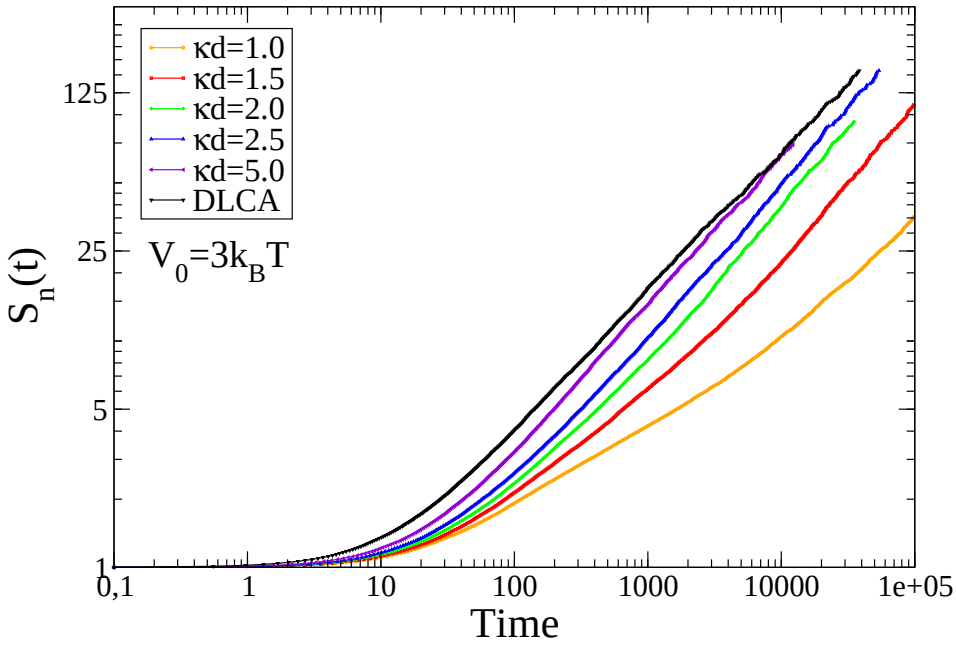

Figure 6.8: Mean cluster size for the different performed simulations.

potential remains constant: this corresponds to the RLCA region. When the aggregates are large enough, every encounter between clusters provokes coagulation after some collisions. So, a transition towards a DLCA regime, displaced in time, is expected to occurs. However, we are not able to observe this third region in our simulations except for the case of the shorter interaction range ($\kappa d = 5.0$).

6.4.3 Coagulation kernels

The aggregation rate constants k_{ij} account for all the relevant physical and chemical effects on the kinetics of the aggregation process. The influence of the pairwise interaction potential between the particles on the coagulation kinetics is included into the P_{ij} functions ($k_{ij} = k_{ij}^{Br} P_{ij}$). The P_{ij} values can be computed from the ratio between the probability of coagulation per encounter (PE_{ij}) for the considered potential and the PE_{ij}^{DLCA} values corresponding to the DLCA case, which can be determined during the simulations.

The computed *probability of coagulation per encounter* for the monomers, PE_{11} is showed in figure 6.9 for $V_0 = 3k_BT$, $\kappa d = 5.0$ and the DLCA simulations. As can be seen, after a transitory region, these probabilities fluctuate around a constant value. In order to solve the Smoluchowski equation 2.24, this constant values were used to calculate the ratios $P_{ij} = PE_{ij}/PE_{ij}^{DLCA}$ for all interaction ranges κd and for $i, j = 1, ..., 9$.

In figure 6.10 we show the P_{ij} values obtained from our simulations against the sizes of the reacting clusters i and j. For the shorter interaction range ($\kappa d = 5$), the kernel increases with i and j until it reaches a constant value. In this case, the range of the interaction is very short and the cluster–cluster interaction potential V_{ij} does not depend on the clusters sizes for i and $j > 2$. The P_{ij} functions grows with the cluster sizes i and j due to the increase of the clusters effective cross section because the number of particles that can collide per encounter increases with their sizes. This is the typical RLCA aggregation regime which kernel is given by the equation 2.34.

When the interaction range is enlarged, the cluster–cluster interaction potential becomes more repulsive as the increase of clusters grow till the critical size i_0. This causes the decrease of P_{ij} with i and j for small clusters. This effect can be clearly observed in the figure 6.10. For large enough aggregates ($i, j \geq i_0$), V_{ij} becomes independent on i and j so the functions P_{ij} start to grow with the cluster sizes due to the increase of the cross section of the cluster.

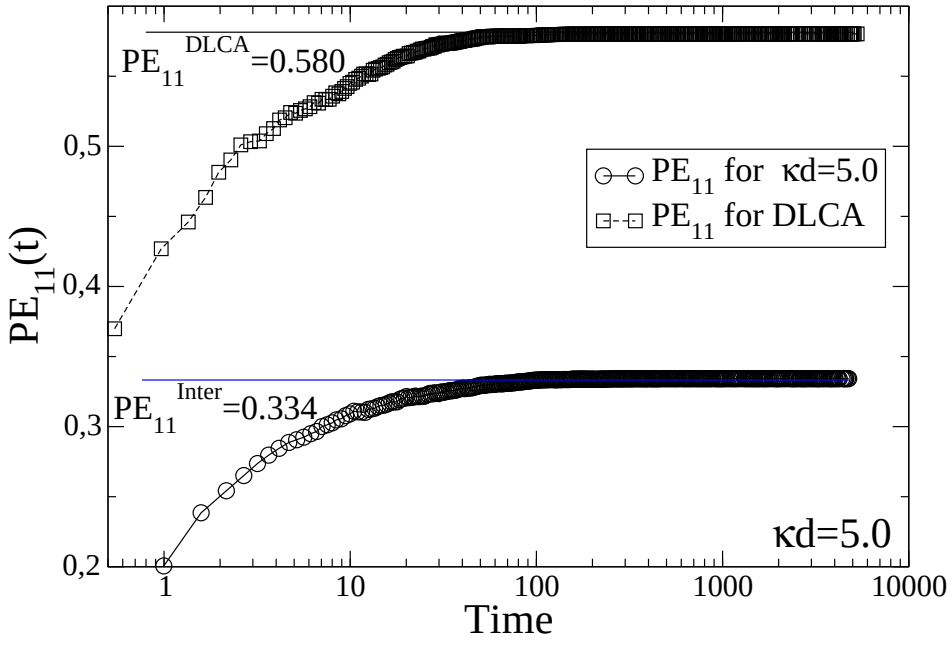

Figure 6.9: Time dependence of $PE_{11}$for DLCA and the simulation with $V_0 = 3k_BT$ and $\kappa d = 5.0$.

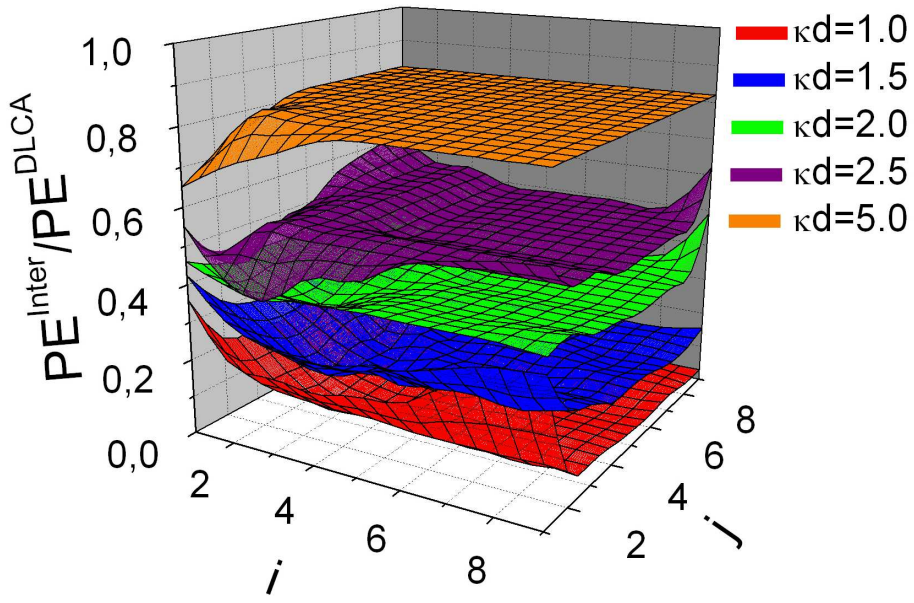

Figure 6.10: P_{ij} functions obtained from the simulations for $V_0 = 3k_BT$ and $\kappa d = 5$, 2.5, 2.0, 1.5, and 1.0.

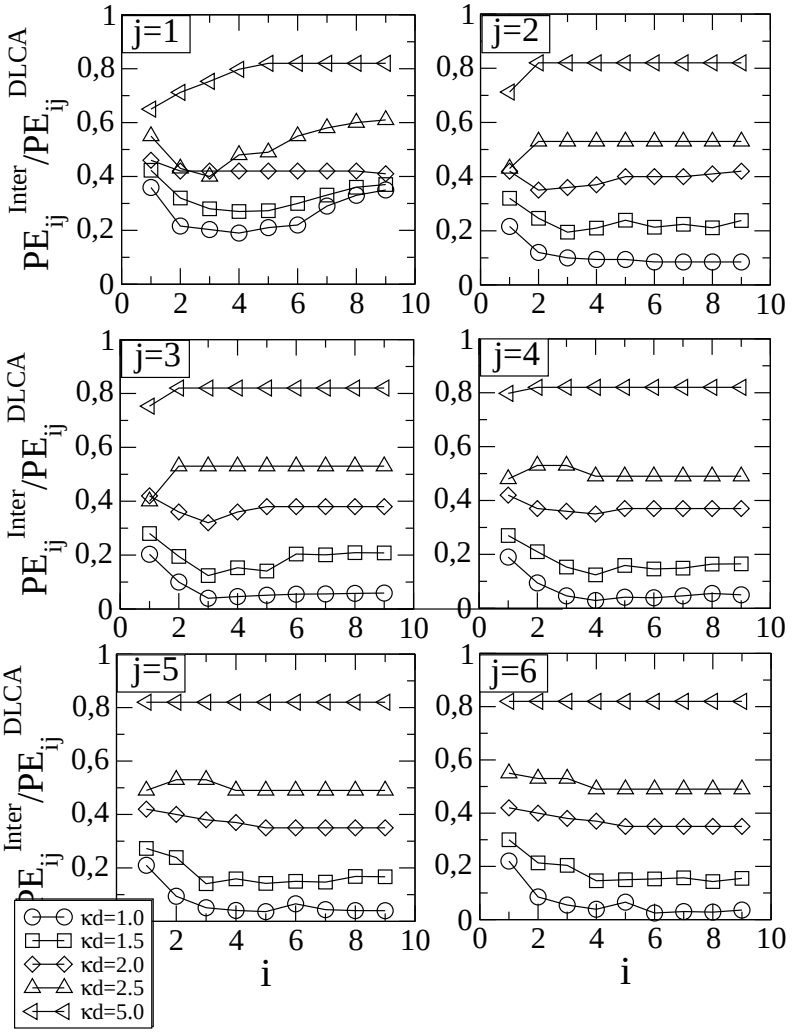

Figure 6.11: P_{ij} functions for fixes j versus i for $V_0 = 3k_BT$ and all the κd used values.

The quantitative dependencies of the P_{ij} functions with the interaction range κ^{-1} are shown in figure 6.11. Each inset shows P_{ij} versus i for a fix j and for the simulations with $V_0 = 3k_BT$ and $\kappa d = 1.0$, 1.5, 2.0, 2.5 and 5. Two different kinetics regions can be clearly observed: the first one controlled by the interaction range, and the second one by the cluster cross section. The P_{ij} dependence for small values of i and j is enhanced for long range repulsions. This is joined to the growth of the critical size i_0 with the interaction range.

By solving the Smoluchowski equation (eq. 2.24) with this aggregation kernel we are able to fit the average cluster number size (figure 6.12) and the cluster size distributions (figure 6.13) with good accuracy for all the simulations.

6.5 Conclusions

We studied the effect of the interaction range on the kinetic properties and the structure of the aggregates formed by computer simulation of two–dimensional colloidal system.

Two different regions can be distinguished on the time dependence of the number–average cluster size $S_n(t)$, that correspond with two different kinetics. In the *region controlled by the interaction range* the cluster–cluster interaction potential, V_{ij}, becomes more repulsive as the cluster size increases, due to the range of the particle–particle repulsion. In this region, the clusters aggregates forming a linear structures. This phenomenon is verified by the direct observation of the small aggregates from the simulations. *RLCA region*: when the reacting clusters reach sizes above the critical size i_0, not all the monomers that compose the clusters participate in the interaction. Therefore, V_{ij} becomes independent on i and j (for $i, j > i_0$), and the cluster–cluster interaction recovers in average its isotropy. The chains formed in the previously region coagulate to form fractal aggregates with a fractal dimension typical for the RLCA coagulation regime. In this region, the growth of the clusters is faster than in the previous region. At long times a *RLCA–DLCA transition* is expected, because the diffusion coefficients of the reacting clusters are very low and so, it is easier for two interacting large clusters to collide between them many times and coagulate than to diffuse away to collide with another cluster. Hence, for large enough clusters all "encounter" between of them end up in coagulation after some time and their coagulation becomes

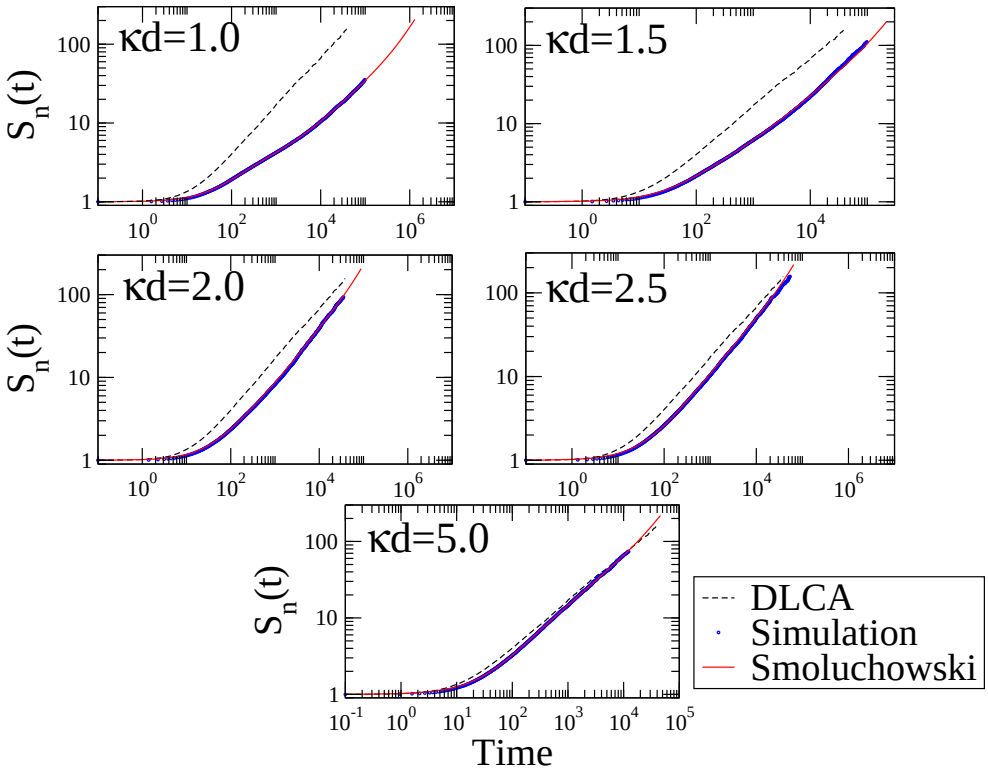

Figure 6.12: Average cluster size in number $S_n(t)$ given by the simulations (circles) and the numerical results calculated by solving the Smoluchowski equation (black line) with the obtained kernels for $V_0 = 3k_BT$ and $\kappa d = 1.0$, 1.5,1.0, 2.5, and 5.0. The dashed line represents the DLCA simulation

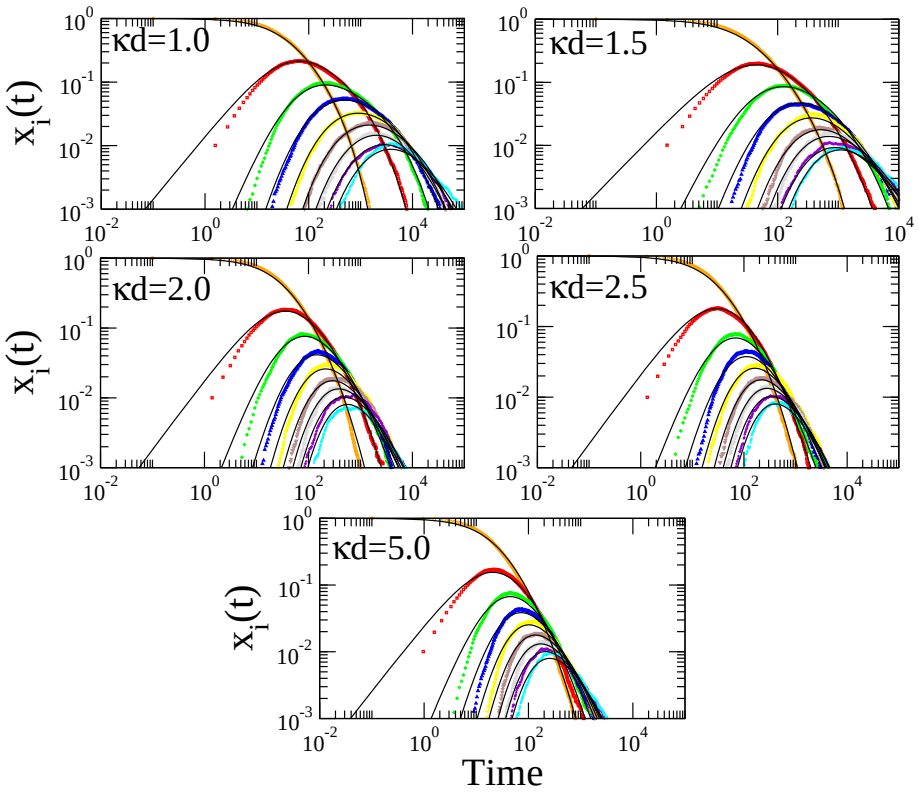

Figure 6.13: Cluster size distribution $x_i(t) = n_i(t)/N_0$, given by the simulations and the numerical results computed by solving the Smoluchowski equation with the obtained kernels for $V_0 = 3k_BT$ and $\kappa d = 1.0$, 1.5, 2.0, 2.5, and 5.0.

limited by the Brownian diffusion (DLCA). However, we need to make simulations with more particles and longer aggregation times to reach aggregates with sizes large enough to observe this crossover.

A new method has been developed to obtain the aggregation rate constants kernel directly from the simulations. Then, the kernel was introduced in the Smoluchowski equation 2.24 and the resulting cluster size distribution was found to be in good agreement with the simulation results.

Therefore, we have connected the new kinetics region induced by the range of the interaction with the well–known RLCA–DLCA crossover. Hence, we have a complete description of the kinetics behavior of a two–dimensional aggregating system composed by colloidal particles that interact with a medium–range pairwise repulsive interaction. We have observed that the range of the interaction modifies the kinetics of the coagulation process at short times and also the structure of the small aggregates formed in this process.

Chapter 7

Colloidal mesostructures

7.1 What are mesostructures?

We can distinguish three different types of experimental colloidal monolayers depending on the morphology of the structures formed by the spread colloidal particles

One type is found when the colloidal particles that form the monolayer are not stable and can aggregate. The formed clusters have usually a fractal character featured through a fractal dimension[139, 140]. The formation of fractal aggregates can be explained using the DLVO theory of interactions. Another type occurs when the colloidal particles remains homogeneously distributed over the interface without coagulate (stable colloidal monolayer). This stability is due to the dipolar and monopolar interactions between colloids trapped at the interface between a polar and a non–polar fluids[1] (see section 3.6.2). Finally, it has been reported since 1995 the formation of some colloidal loosely bound structures, those are internally well ordered, when particles are spread at an air–water surface [57, 58, 59, 89, 141] or at an oil–water interface [85]. In order to distinguish such ordered structures from the random fractal objects formed in colloidal aggregation processes, Ghezzi and Earnshaw [89] proposed to call them colloidal mesostructures.

The diverse morphology of the mesostructures arising at an interface is surprisingly rich. We can distinguish between circular patterns of particles, voids, line patterns, soap froths and loops [59, 141] (see figure 7.1).

A common feature of all these colloidal mesostructures is the significant

[1]For example, particles at an air–water interface.

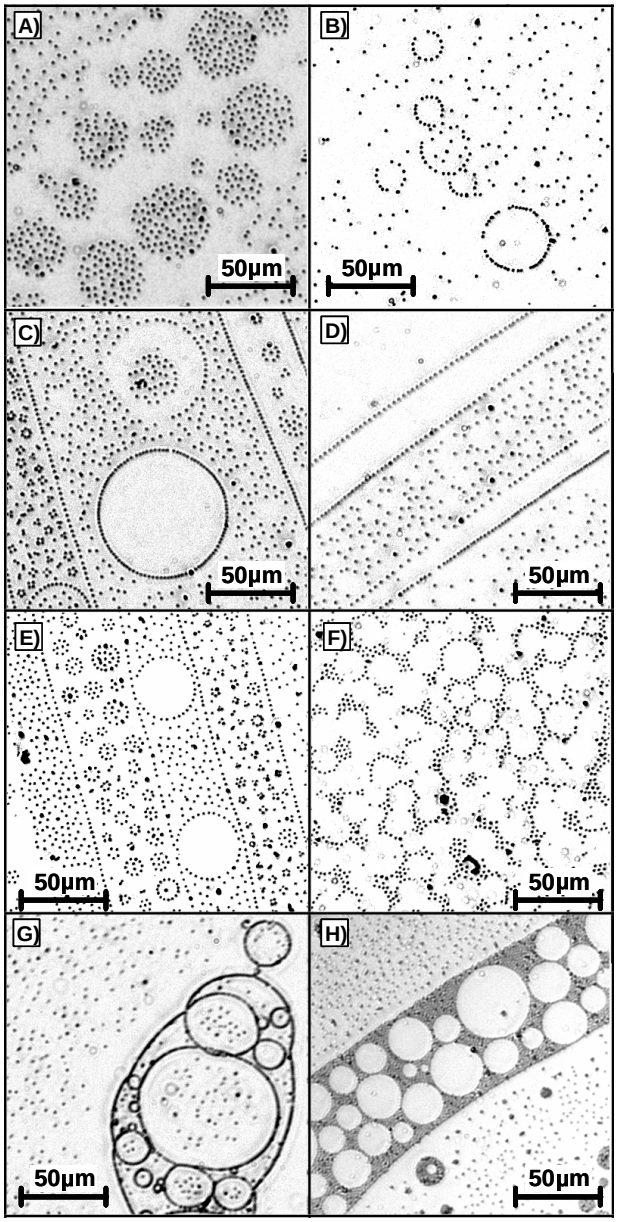

Figure 7.1: Different patterns of mesostructures formed by polystyrene colloidal particles at the air–water interface. A) Circular clusters. B, C) Rings. D) Lines. E) Coexistence of lines, circular clusters and rings. F) Foams. G) Loops. H) Voids [141, 142].

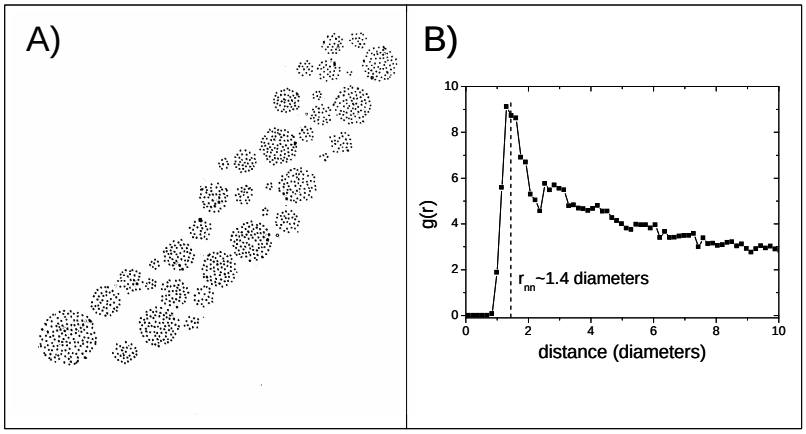

Figure 7.2: A) Example of a mesostructure foamed by circular clusters. B) Computed $g(r)$ for the particles of the clusters on image A). The main peak is around $d_m \approx 1.45$ diameters. In general, $d_m \epsilon [1, 2]$ diameters for all the circular clusters obtained in our experiments.

separation between the constituent particles, which in most of the cases is about the particle diameter, $2a$ (see figure 7.2). Another important characteristic of the mesostructures is that they arise immediately after spreading the particles at the interface and then evolve in different ways. So, for instance, the evolution from void structures to soap froths after some hours has been reported[58]. Likewise, a change from circular arrays of particles to a stable colloidal monolayer was reported[89] (after several hours). This slow evolution indicates that the mesostructure are not stable but metastable.

7.2 Origin of mesostructures: long–range attractive interaction?

At this point, the question that arises is what is the origin of the mesostructures? The fact that for all the observed mesostructures the average distance between neighboring particles is typically constant and of the order of the particle diameter, suggest that the inter-particle interaction potential should have a secondary minimum located at that distance. Figure 7.3 depicts the pairwise interaction potential used to explain the origin of mesostructures [58, 59, 89, 85]. According to this, the secondary minimum explains why the

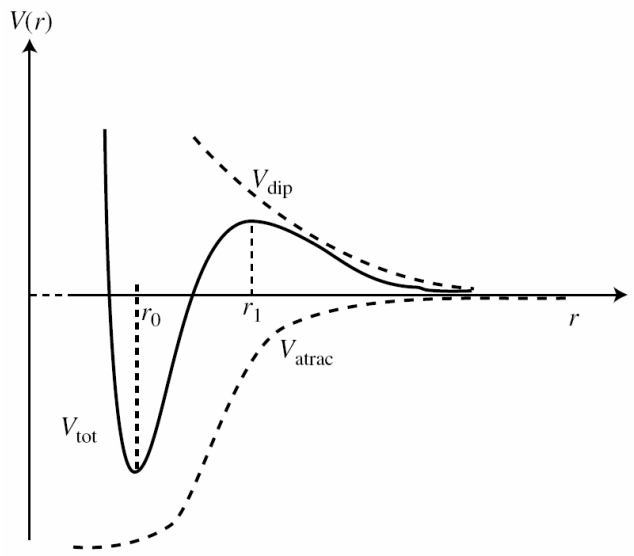

Figure 7.3: Shape of pairwise interaction potential used to explain the formation of circular clusters. It has a secondary minimum at distances around the particle diameter, which could explain the characteristic distance between particles in the mesostructures. Besides, there is a repulsive barrier after the secondary minimum that prevents the coagulation of the mesostructures.

inter–particle distance is roughly constant, while the small potential barrier, situated at a larger distance prevents the collapse of the individual structures. The spreading process is quite turbulent, and the particles may be forced to approach each other very closely, passing over the potential barrier to become temporarily trapped in the secondary minimum at r_0. The barrier at r_1 cannot be very high, as the metastable mesostructures disaggregate on timescales of the order of hours due to thermal energy at room conditions.

In order to obtain this secondary minimum both an attractive and a repulsive interactions, which sum does not vanish at such distance, are necessary. On the one hand, there is only one repulsive interaction that can be important at distances around the particle radius that is the dipolar interaction. On the other hand, until our knowledge, all the attractive interactions vanish at such distances. So, the proposed pairwise interaction potential could not be explained using the known interactions.

Some theoretical models have tried to explain the formation of these

mesostructures, i.e. the origin of the long range attractive interaction, on the basis of capillary immersion forces (section 3.8.1) [83, 84, 85, 87, 88]. In order to have a complete description of the interactions between colloidal particles at interfaces, it is essential to understand the origin of these structures. A great effort has been done to provide a theoretical model for this long–range attraction, but none of the suggestions explains the totality of the experimental results. However, in our recent experimental work [141] we suggested that these mesostructures can be caused by the non–homogeneous surface tension of the interface due to the presence of polluting agents like silicone oil. As we will see in section 7.4, with this assumptions, our model is able to explain the great variety of mesostructures.

7.3 Experiments

This section is devoted to understand the causes underlying the self–assembly of colloidal particles in order to form mesostructures. It will be shown that no long–range force at the interface exists and that the physical reason for the formation of mesostructures is given by the interfacial tension.

7.3.1 Colloidal system

In all the performed experiments we have used polystyrene microspheres particles synthesized by Dr. Arturo Moncho Jordá. This system has a great stability at the air–water interface, even at high particle concentration. Moreover, the colloidal monolayer remain stable independently on the ionic strength of the subphase. Therefore, this is an optimal system to prepare stable monolayers at the air–water interface.

The colloidal particles were synthesized from styrene by free–emulsifier polymerization [143] with potassium persulfate ($K_2S_2O_8$) as an initiator and potassium bicarbonate ($KHCO_3$) as a buffer. They were cleaned by steam stripping and then with serum replacement and mixed-bed ion–exchange resin following the work in ref [144]. The average particle diameter and polydispersity index (measured by Transmission Electronic Microscope: TEM) were 600 ± 25nm and 1.004, respectively. Therefore, this system can be considered as very monodisperse.

The particles have a maximum surface charge density of $\sigma = -5.3 \pm 0.5$ μC/cm^2, as it was determined by conductometric titration.

7.3.2 Experimental setup

Microscopy is a very common technique used in many scientific applications. With the microscopy help, one gets very accurate two–dimensional information because we can observe directly the behavior of the particles at the interface. In order to observe polystyrene particles, it is necessary a contrast phase microscope because the refraction index of the polystyrene is very similar to the refraction index of the water. The microscope used in our experiments was a Nikon Optiphot–2. The magnification of the objective was fixed to 10×.

The self–assembly process was monitored using a CCD camera (model CCD–1300D) attached to the microscope. This camera has a resolution of 1280x1024 and a frequency of capture of 12.5 images per second. The images were stored on a PC using a Frame–Grabber PCimage–SDIG/AIAZ and further processed in the computer.

The particles were deposited in a cell designed as shown in figure 7.4. It consists of a small cylindrical cell of Teflon (area, 2.01 cm^2; height, 1.0 cm) glued to a microscopy slide. After forming the monolayer, the Teflon cell is covered using a cover glass that is put on a auxiliary external ring that encloses the cell. This cover prevents contamination of the monolayer and the convective fluxes produced by the air motion.

The effects of external vibrations were avoided by placing the system formed by the cell, microscope, and camera on an antivibratory table.

The images acquired by the microscope were calibrated with the help of a ruler (figure 7.5-A). The calibration gives us that the pixel width is about 462 nm. Therefore, each pixel is approximately as wide as a particle.

7.3.3 Preparation of the dispersions and deposition

In order to prepare the air–water interface, we fill with water the Teflon cell. The interface has to be as planar as possible to prevent the particle emigration as a consequence of gravity during the experiments. However, as the Teflon is very hydrophobic, a curved meniscus is formed when we introduce the water into the cell. Hence, we used a syringe to extract water in order to flatten the interface (figure 7.6).

The colloidal suspensions were prepared in a solution of ultra–pure water (from a Millipore Milli-Q system) and methanol and were sonicated for 5 min to assure a good initial monodispersity. The methanol was used as spreading

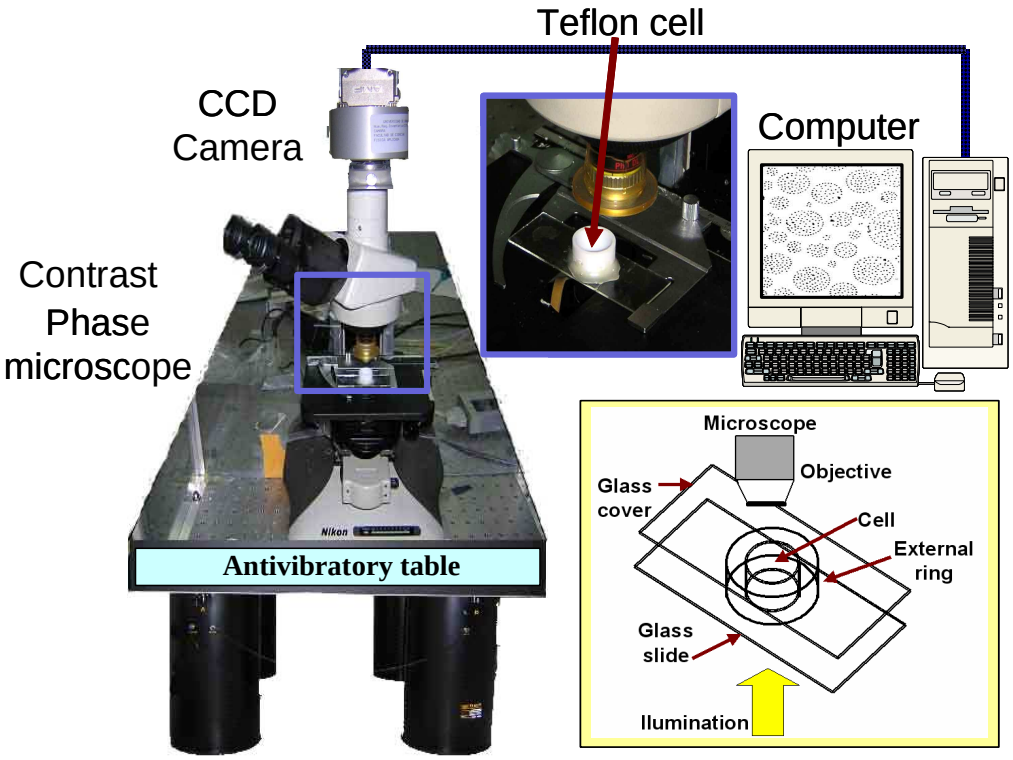

Figure 7.4: Scheme of the experimental setup.

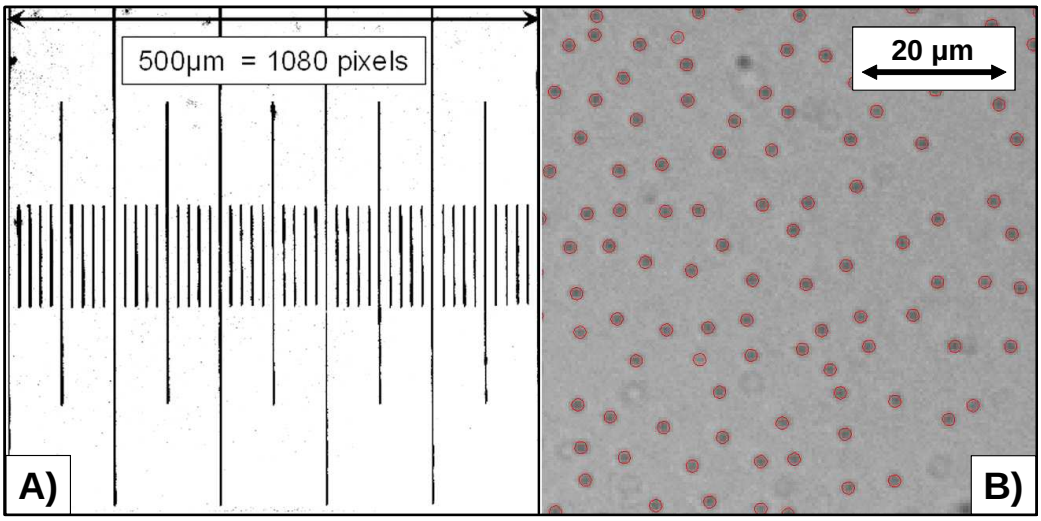

Figure 7.5: A) The ruler used to calibrate the microscope image resolution, i.e., the size of a pixel. We have obtained that one pixel corresponds with 462 nm. B) A detail of a colloidal monolayer and particles of radius equal to 300 nm that has been transformed in pixels with the performed calibration. As we can see, the equivalence between a particle and a pixel is almost perfect.

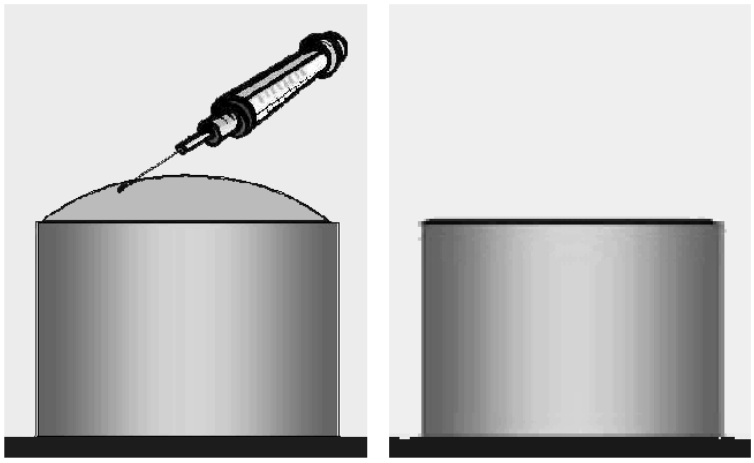

Figure 7.6: Due to the hydrophobicity of the Teflon cell, when we fill it with water a curve meniscus appears. In order to flatten it we extract water using a syringe of $1ml$.

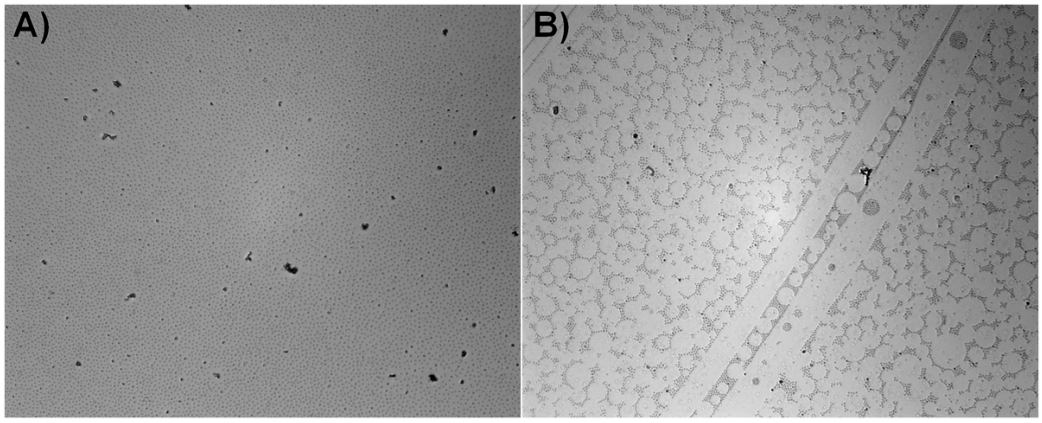

Figure 7.7: Two different runs of a typical experiment performed with the same dispersion under identical experimental conditions at the stationary state. A) Stable monolayer $\varphi = 0.081\%$. B) Mesostructures $\varphi = 0.078\%$

agent in order to avoid the immersion of latex beads into water. It should be noted that the use of methanol in the deposition procedure is essential for obtaining a uniform monolayer. In all the performed experiments we have used 80% of methanol and 20% of water mixtures.

The latex particles were placed at the liquid–air interface using a Hamilton micro–syringe. After methanol evaporation, the cell was covered by a thin glass plate to prevent the contamination of the monolayer and the convective fluxes produced by the air motion.

7.3.4 Experimental results

Low reproducibility of the experiments

Figure 7.7 shows two pictures from two different runs of a typical experiment performed under identical experimental conditions. The images corresponds to the stationary state which is reached after 30 min from deposition. The liquid subphase was in both cases ultrapure water without an additional electrolyte. The microspheres were spread on the air–water interface using a syringe (1 ml Plastipak) and a needle (Microlance 3). After some experiments, we observed that the morphology of the colloidal monolayers at the air-water interface was dependent on the number of times that we used the same needle and syringe. At the beginning, we always observed sta-

ble monolayers (see figure 7.7–A). However, after a certain number of uses, we observed the spontaneous formation of mesostructures (see figure 7.7–B), and that phenomenon was more evident with the repeated use of the same syringe and needle.

Once the cause of the spontaneous formation of mesostructures was experimentally confirmed to be the repeated use of the same syringe and needle, we decided to contact with the manufacturer of both materials in order to check if some kind of contaminant agent from the syringes or the needles could affect the monolayers formation. The manufacturer of the syringes and needles informed us that they were made with an internal silicone oil coating.

This information suggested us that as a consequence of the aging the needles and syringes could loose their internal silicon oil coating. The liberated silicon oil could affect the interfacial properties (surface tension) of monolayer giving rise to the formation of the mesostructures. To test this hypothesis, the surface tension values of a water drop were measured using the axisymmetric drop shape analysis (ADSA) technique[145] (see figure 7.8-A). We observed that the surface tension of a water drop changed from 73 to 62 mJ/m^2 as a result of the contact with an aged needle for 1 s (figure 7.8–B). However, the surface tension of the water-air interface remained constant when it was put in contact with a needle, which had been previously washed with toluene. We never observed the formation of mesostructures using glass syringes and the washed needle.

It should be noted that the silicone oil is partially miscible in methanol [146], and that this alcohol is very often used as the spreading agent in the formation of colloidal monolayers trapped at the air-water interface. So, it is feasible that some silicon oil molecules (even drops!) can remain at the interface after evaporation of the methanol for most of the reported works on mesostructures. The hypothetical presence of some contaminant oily film (say from dissolved styrene oligomers) as a possible cause for the mesostructure formation was already pointed out by Kralchevsky and Denkov [97]. In our case, we cleaned the latex particles by steam stripping, so the residual monomers were removed. Therefore, we excluded that some oily film from the dissolved styrene oligomers could be present on the interface when spreading the suspension of latex particles with the methanol/water mixture help.

The pattern formations of stable colloidal monolayers or mesostructures were reproducible for six different experiments. The surface particle density

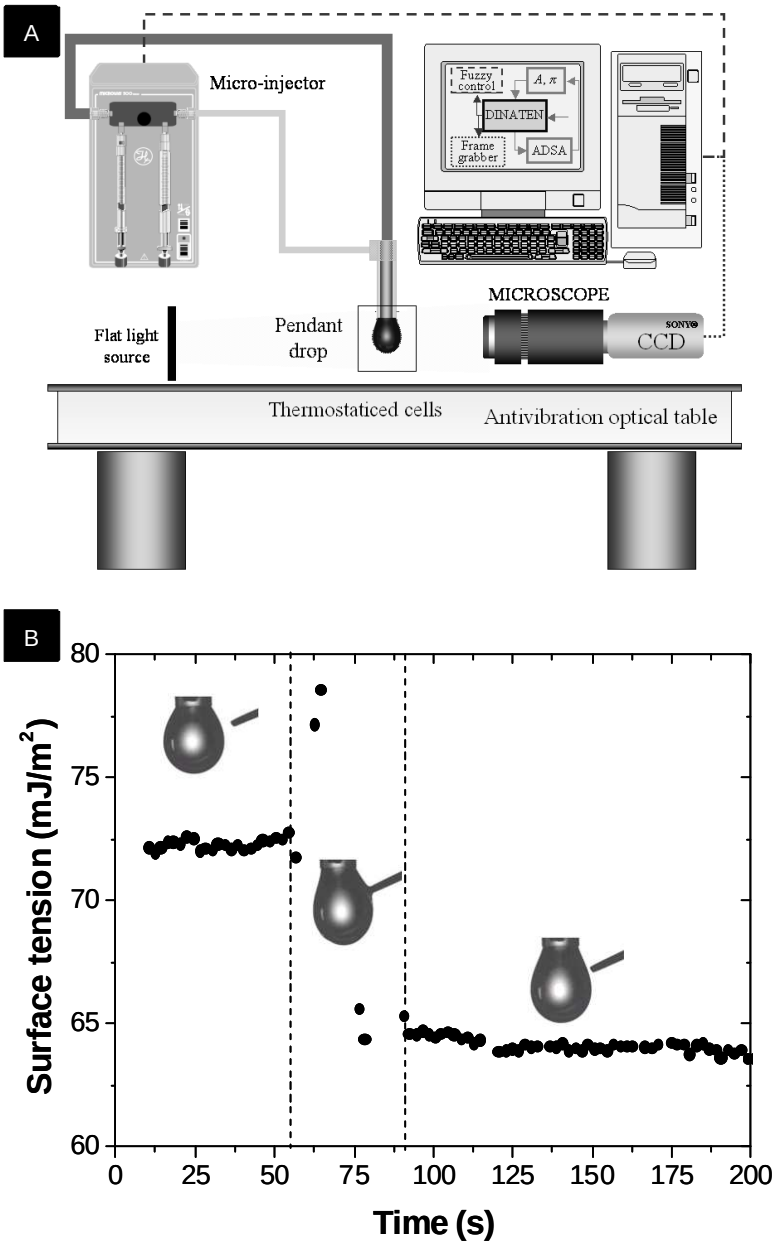

Figure 7.8: A) Sketch of the ADSA technique used to determine the interfacial tension values of liquids. B) Variation of the interfacial tension of a drop of water when put in contact with an old needle. The interfacial tension changes from 73 mJ/m^2 to 62 mJ/m^2.

of the formed colloidal monolayers was between 0.6 and 0.8%.

Effect of the silicon oil impurities

To check the effect of silicone oil on the spontaneous formation of mesostructures, we performed some experiments where the colloidal particles were contaminated with silicone oil (AR200 from Fluka; density, 1.042 g cm^{-3}; refractive index, 1.450) dissolved in methanol.

First, we dissolved 5 μl of silicon oil in 5 ml of extra–pure methanol and the solution was sonicated for 15 min to assure a good dissolution. Thus, the contaminated methanol (CONT–meth) has a concentration of silicon oil of $\phi_{vol} = 0.001$ in volume. After that, we used this contaminated methanol to prepare 6 different dispersions. We deposited 5 μl of each dispersion over the interface in all the experiments performed. Assuming that the silicon oil was homogeneously dispersed in the solution and that all the silicon oil deposited is going to remain at the interface, we can made an approximate calculus of the silicon oil mass concentration at the interface (ρ_{SO}) for each experiment. In table 7.1, the composition of the different dispersion used in our experiments is resumed.

N°	CONT–meth (μl)	ρ_{SO} (μgcm^{-2})
1	0.5	$\sim$ 1.3x10^{-3}
2	1.0	$\sim$ 2.5x10^{-3}
3	1.5	$\sim$ 3.8x10^{-3}
4	2.5	$\sim$ 5.0x10^{-3}
5	5.0	$\sim$ 12.7x10^{-3}
6	20.0	$\sim$ 25.4x10^{-3}

Table 7.1: The different dispersions were obtained by addition of 1 ml of latex solution (composed by 0.125 ml of the original polystyrene solution (AMJ2), 0.125 ml of ultrapure water and 0.750 ml of methanol) and an increasing amount of CONT-meth (as indicated).

Figure 7.9 shows some mesostructures obtained by this procedure for the different silicone oil concentrations. For the lowest solutions 1 and 2 (figures 7.9-A and B), the particles are distributed homogeneously at the interface forming a uniform monolayer. When the silicon oil concentration is

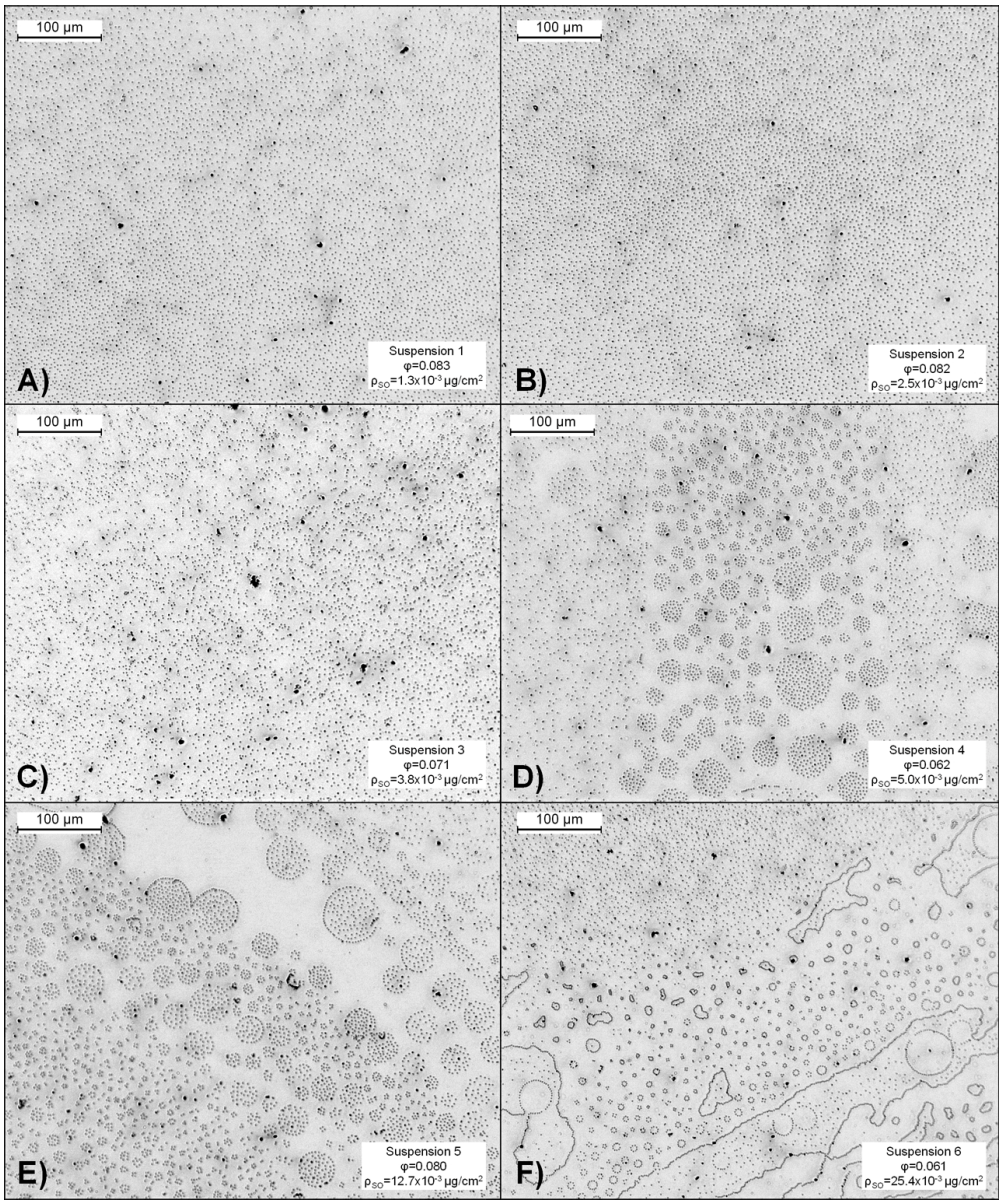

Figure 7.9: Formation of colloidal mesostructures when the concentration of silicon oil impurities is increased from 1.3x10^{-3} μg/cm^2 (A) to 25.4x10^{-3} μg/cm^2 (F).

increased (figure 7.9-C), the monolayer becomes less homogeneous and then appear arrays of three or four particles forming circumference arcs. This is the first step of the self–assembly of the particles to form mesostructures. If we still increase the silicon oil concentration (figures 7.9-D and E), circular clusters and voids appear and the isotropy of the monolayer is completely lost. Finally, for the highest silicon oil concentration, the particles tend to adopt complex structures as loops and other irregular shapes 7.9-F. Hence, the pattern of these structures depends on the number of silicone oil molecules that are present at the air–water interface. In addition, the molecular weight of the silicone oil might also affect the geometric pattern of mesostructures. This is likely to explain the great number of geometric patterns found by different authors [58, 89, 90, 57, 147, 59].

Figure 7.10 shows until our knowledge the first experimental evidence of the time evolution of a uniform colloidal monolayer to form a colloidal mesostructures. The picture shows the evolution from a thin and long cluster, that turns into an elliptical cluster and which finally becomes an almost spherical mesostructure with voids and other smaller clusters. The evolution from an elliptical shape to a more circular structure can be explained in terms of the surface energy minimization of the silicon oil drops that drag the particles inside to form a circular array of particles. It should be noted that, in our experiments, these mesostructures appear spontaneously at the interface without applying external fields to the system, in contrast to the experiments reported by Chen et al. [148]. They supplied kinetic energy to the system by pipetting periodically a small amount of water, in order to overcome the repulsions and to obtain colloidal rings and circular patterns. The simulated colloidal rings, circular clusters, and voids are quite similar to those experimentally obtained.

The spontaneous formation of mesostructures can be explained in terms of the difference between the surface tension of the water (73 mJ/m^2) and silicon oil (35 mJ/m^2). Even a very small amount of silicone oil is able to change the surface tension of the air–liquid interface and to lead to the formation of a two–dimensional emulsion with hydrophobic (silicone oil droplets) and hydrophilic patches (water surface) with different interfacial tensions. When the polystyrene microspheres (hydrophobic in character) are spread on this nonuniform interface, most of them tend to locate on the hydrophobic silicon patches and form mesostructures. Basically, in our experiments, the mesostructures are the result of the decoration with microspheres of a two–dimensional emulsion of silicon oil droplets on water. Thus, the mean

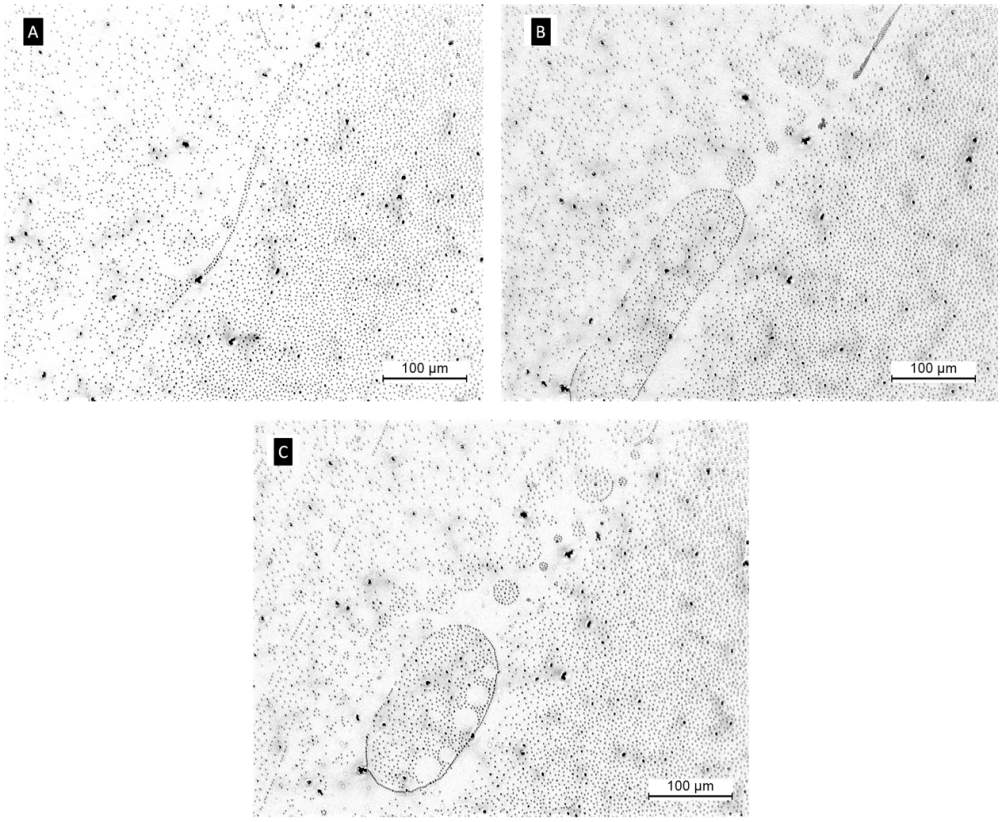

Figure 7.10: Experimental evidence of the spontaneous formation of colloidal mesostructures. There is 5 seconds between each snapshot.

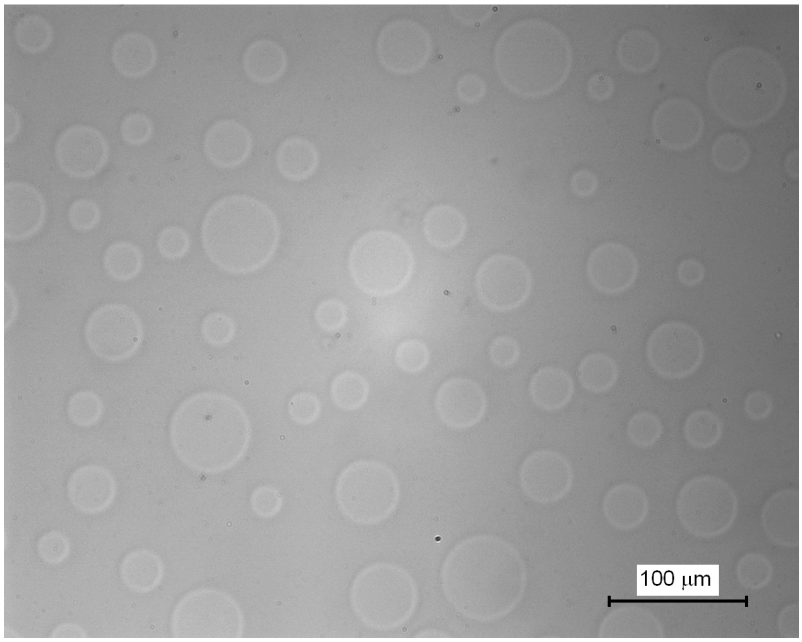

Figure 7.11: Formation of oil drops at the air–water interface. The used dissolution was pure methanol with a silicon oil concentration of 0.05% in volume. The gray profile of the drop has a gradient at its border but is roughly constant at the drop center. This means that the drops must be very flats.

particle distance between the colloidal particles depends on the manner in which they accommodate inside of the hydrophilic and hydrophobic patches at the air-liquid interface. This explains the appearance of circular clusters in mesostructures. We have observed that the most irregular mesostructures (loops) are formed for the largest silicone oil concentration (see figure 7.9), whereas circular clusters are always present for all used concentrations. The patterns of the formed mesostructures are quite similar to that obtained previously by other authors [58, 89, 90, 57, 147, 59].

The formation of oil droplets can be observed in figure 7.11 for which we used a solution of methanol with a concentration of silicon oil of 0.05% in volume, without latex particles. Here, we directly observe the formation of big drops that provokes heterogeneities in surface tension at the interface and that could explain the mesostructures formation.

In short, in our case, the mechanism behind the formation of mesostruc-

tures is not related to a long–range attraction between colloidal particles [149] confined at the air-water interface but to the formation of an oily patched film due to the contamination caused by the silicone oil. This contamination can arise from the coating of the needles and syringes used to deposit and spread the particle solution at the air-water interface. Our results support the suggestion made by Kralchevsky and Denkov [97] on the effect of an oily film in the apparently spontaneous formation of mesostructures on the air–water interface.

7.4 Proposed model

As can be thought when we observe the mesostructure pictures showed in this chapter, even the simplest ring–shaped structure (figures 7.1-A,B,C) is difficult to be explained using an isotropic force. The difficulty is even greater if we try to reproduce more complex structures (figures 7.1-D,E,F).

An heterogeneous interface can induce the appearance of mesostructures, so we decided to simulate the behavior of a colloidal monolayer formed by microspheres spread onto a nonhomogeneous air-liquid interface [142]. The inhomogeneous interface is due to the presence of two liquids with different surface tension. The total potential that a particle experiments is assumed to be composed by only two terms. The first one is due to the repulsive pairwise dipolar force between the partly emergent parts of charged microspheres. The second term depends on the position of the particle at the interface, and it is connected to the interfacial stress caused by the surface tension difference between both liquids. As we will show, this simple potential is able to reproduce the experimental mesostructures, formed by colloidal particles confined at the air–water interface, found by different authors.

7.4.1 Model

Our model for the inhomogeneous interface considers the existence of two domains with different surface tension: the air–water (the largest one) and the air–oily phase, that is located forming lenses. This implies that the so–called spreading coefficient ($S = \gamma_{wa} - \gamma_{wo} - \gamma_{oa}$) is negative, here γ_{wa} and γ_{oa} are the surface tension of the water–air and oil–air interfaces and γ_{wo} is the interfacial tension of the water–oil interface.

For the sake of simplicity we assume that flat lenses represent the oily

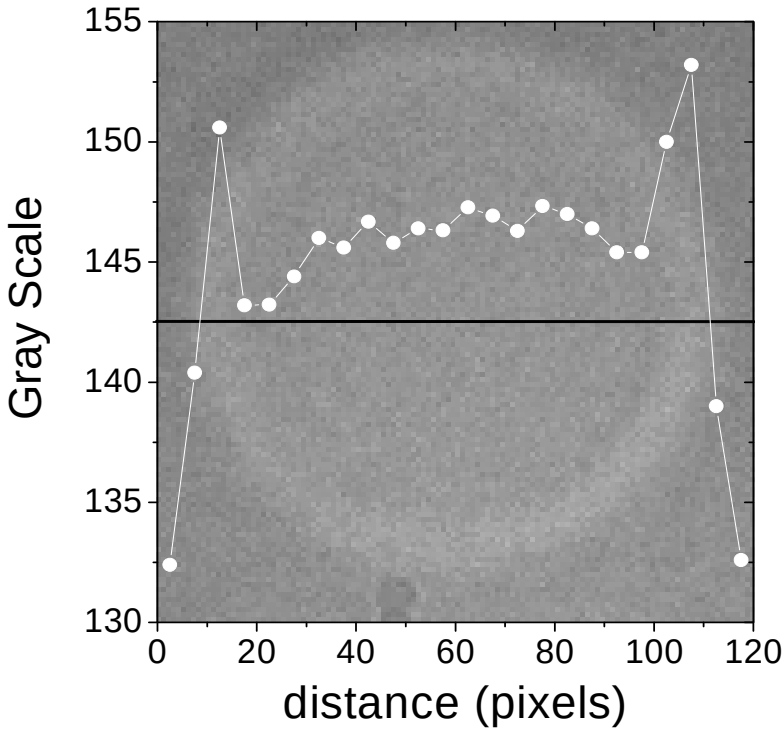

Figure 7.12: Gray profile, at the black line, of the drop used as the background of this graphic. It can be observed that the grayscale values inside the drop remains nearly constant, implying that the drop is flat.

phase. The goodness of this approximation is demonstrated by the analysis of the phase contrast images obtained with the silicon–oil spread at the air–water interface (figure 7.11). So, if we represent the grayscale values along a diameter of a drop (figure 7.12) we found a nearly constant value. This indicates that the optical path for those points is similar and that be the case for the drop thickness. Moreover, we can consider that the oil lenses are thinner than the particle size ($h_{drop} < 600$ nm), because both the particles outside and inside of the drops keep focused simultaneously. According to this model, the interaction between a colloidal particle and an oil droplet can be visualized as the intersection between a sphere and a flat lens (see figure 7.13).

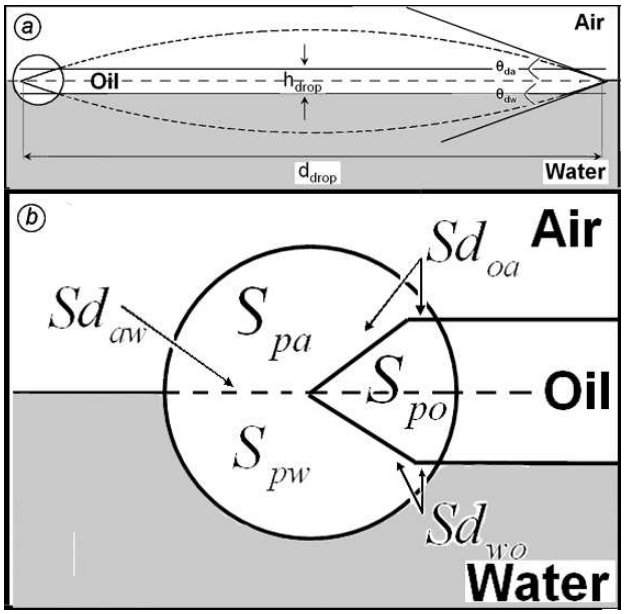

Figure 7.13: . (a) Sketch of the interception of a spherical particle with a flat oil lens both situated at the air–water interface. (b) Representation of the different interfaces those must taken into account to calculate the energy of the particle at the interface using the lens model for the oil droplet.

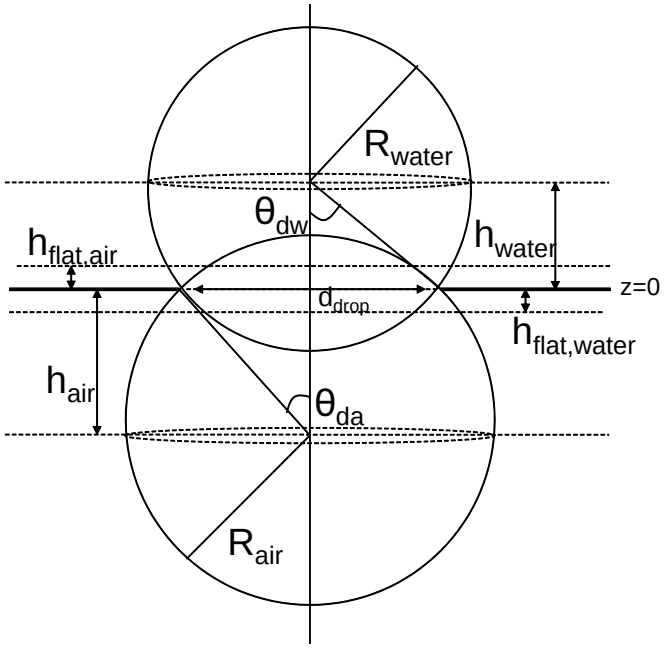

Figure 7.14: Construction of a flat drop through the intersection between two spheres and two planes.

Flat drop model

We represent a drop as the intersection of the lens formed using two spheres of radius R_{air} and R_{water} and two parallel planes at distances $z = h_{flat,air}$ and $z = -h_{flat,water}$ from the interface plane ($z = 0$). That is, the flat drop is composed by the lens part between the two planes (see figure 7.14).

As it is indicated in figure 7.14, the shape of the drop is determined by the angles θ_{da}, θ_{dw}, its diameter d_{drop} and the drop thickness in the air region, $h_{flat,air}$, and in the water region, $h_{flat,water}$. The other parameters can be

obtained using

$$\begin{aligned}
\sin\theta_{da} &= \frac{d_{drop}}{2R_{air}} \\
\cos\theta_{da} &= \frac{h_{air}}{R_{air}} \\
\sin\theta_{dw} &= \frac{d_{drop}}{2R_{water}} \\
\cos\theta_{dw} &= \frac{h_{water}}{R_{water}}
\end{aligned} \tag{7.1}$$

and therefore

$$\begin{aligned}
R_{air} &= 0.5 d_{drop} / \sin\theta_{da} \\
R_{water} &= 0.5 d_{drop} / \sin\theta_{dw} \\
h_{air} &= d_{drop} / (2\tan\theta_{da}) \\
h_{water} &= d_{drop} / (2\tan\theta_{dw})
\end{aligned} \tag{7.2}$$

Interactions

The only direct interaction between particles that we have considered is the dipolar repulsion, V^{dip}, which is strong enough to avoid particle coagulation (section 3.6.2). Any other pairwise interaction is assumed to have a negligible effect.

Colloidal particles are also affected by an external potential, V^{γ}, due to the surface tension inhomogeneities at the interface. The particle energy is different if it is located at the water–air interface, at the oil–air interface, or at the water–oil–air triple contact line. For the sake of simplicity, in our model, we have assumed that flat lenses represent the oily phase. Accordingly, the total interaction potential for a particle placed at position $\vec{r}_i$ is given by

$$V^{total}(\vec{r}_i) = V^{\gamma}(\vec{r}_i) + \sum_{j \neq i}^{N} V^{dip}(|\vec{r}_i - \vec{r}_j|) \tag{7.3}$$

where N is the total number of particles. According to Horozov et al. [79], the dipolar interaction potential (section 3.6.2) at large distances reduces to:

$$V^{dip} = \frac{\pi f_{dip}^2 \sigma^2 P^2 R^4 \sin^4\theta}{4\epsilon\epsilon_0 r^3} \tag{7.4}$$

where σ is the surface charge density of the particle, f_{dip} is the percentage of charges that forms dipoles, P is the dipolar moment of the dipole, R is the particle radius, θ is the particle contact angle, ϵ_0 is the vacuum dielectric permittivity and ϵ is the dielectric constant of the air.

To calculate V^γ, it must be take into account that the energy required to create an interface area S_{ab} between two media "a" and "b" with a surface tension γ_{ab} is given by $V_b = S_{ab} \cdot \gamma_{ab}$. The calculation of V^γ involves the study of how the area of the different interfaces are modified when a particle moves from position $\vec{r}_1$ to $\vec{r}_2$. To help the computation, figure 7.13 the most general case. We have considered flat oily lenses with a maximum thickness $h_{drop} = 2|h_{flat,air}|$ and that $|h_{flat,air}| = |h_{flat,water}|$. These areas depend on this parameter. As figure 7.13 shows, six different interfaces can be distinguished:, $S_{pa}(\vec{r}_i, h_{drop})$, $S_{pw}(\vec{r}_i, h_{drop})$, $S_{po}(\vec{r}_i, h_{drop})$, represent surface areas corresponding to the particle–air, particle–water, and particle–oil interfaces, respectively and analogously, $Sd_{aw}(\vec{r}_i, h_{drop})$, $Sd_{wo}(\vec{r}_i, h_{drop})$ and $Sd_{ao}(\vec{r}_i, h_{drop})$ are the surface area of the air–water, water–oil and air–oil disks that would be created if the particle were removed form the system. Thus, the energy increment of a particle that moves from position $\vec{r}_1$ to $\vec{r}_2$ is given by

$$\begin{aligned} \Delta V &= V^\gamma(\vec{r}_2) - V^\gamma(\vec{r}_1) \\ &= (S^2_{pw} - S^1_{pw})\gamma_{pw} + (S^2_{po} - S^1_{po})\gamma_{po} + (S^2_{pa} - S^1_{pa})\gamma_{pa} \\ &-(Sd^2_{aw} - Sd^1_{aw})\gamma_{aw} - (Sd^2_{wo} - Sd^1_{wo})\gamma_{wo} - (Sd^2_{ao} - Sd^1_{ao})\gamma_{ao} \end{aligned} \tag{7.5}$$

Therefore, the external potential V^γ can be written as

$$\begin{aligned} V^\gamma(\vec{r}, h_{drop}) &= S_{pw}(\vec{r}_i, h_{drop})\gamma_{pw} + S_{po}(\vec{r}_i, h_{drop})\gamma_{po} \\ &+S_{pa}(\vec{r}_i, h_{drop})\gamma_{pa} - Sd_{aw}(\vec{r}_i, h_{drop})\gamma_{aw} \\ &-Sd_{wo}(\vec{r}_i, h_{drop})\gamma_{wo} - Sd_{ao}(\vec{r}_i, h_{drop})\gamma_{ao} \end{aligned} \tag{7.6}$$

7.4.2 Numerical results

Effective potential across the interface V^γ

Table 7.2 shows the constant data values used to compute the external potential $V^\gamma(\vec{r}, h_{drop})$. The values of γ_{aw} and γ_{pa} are the typical for the water–air and polystyrene–air interfaces. The contact angles θ_{pw} and θ_{po} have been

Set	γ_{pw}	γ_{po}	γ_{pa}	γ_{ao}	γ_{ow}	θ_{oa} (°)	θ_{ow} (°)	S_{spread}	h_{drop} 10^{-7} (m)
a	32	14	33	38	38	20	20	−4.62	1.5
b	32	14	33	38	38	20	20	−4.62	3.0
c	32	14	33	38	38	20	20	−4.62	1.5
d	32	31	33	21	53	20	10	−2.97	1.5

Table 7.2: Different set of values used for the surface and interfacial tensions and contact angles of the different interfaces. Surface tensions are expressed in mJ m^{-2}. In all cases, γ_{aw}, d_{drop}, θ_{pw}, and θ_{po} were assumed to be 72 mJ m^{-2}, 7.2x10^{-6} m, 89°, and 60°, respectively.

assigned as fixed values and the others γ values were obtained using the Neumann relationships (see figure 7.15)

$$\begin{aligned} \gamma_{ao}\cos\theta_{ao} &= \gamma_{aw}\cos\theta_{aw} - \gamma_{ow}\cos\theta_{ow} \\ \gamma_{ao}\sin\theta_{ao} &= \gamma_{ow}\sin\theta_{ow} + \gamma_{aw}\sin\theta_{aw} \end{aligned} \tag{7.7}$$

We assume that both menisci of water and oil around the colloidal particle are flat as in our experiments both the Bond numbers ($B = ga^2\Delta\rho/\gamma_{LV}$)), are small at the air–water interface. Here, g is the gravity, $\Delta\rho$ is the density difference between the subphase (water or oil) and the upper phase (air), a the particle radius and γ_{LV} the liquid–vapor surface tension. Therefore, we can approximate $\theta_{aw} = 0°$. Hence, these equations joined with the Young equation 3.1 for the particle at an air–water and at an air–oil interface allow us to determine the unknown surface tension values, γ_{ao}, γ_{ow}, γ_{po}, and γ_{pw}.

For all the cases, the obtained spreading coefficient (S) is negative indicating that the oily phase forms droplets at the air–water interface. The values used for interfacial tensions and contact angles of the oily phase do not correspond to the values of these properties for a particular oil, but they are assumed ad hoc.

Figure 7.16 shows the $V^{\gamma}(\vec{r}, h_{drop})$ potential as a function of the particle distance to the air–water–oil contact line divided by the particle radius. The h_{drop} value affects the external potential as can be seen comparing panels A and B in figure 7.16. Also, figure 7.16C shows the V^{γ} potential for γ_{ao} and γ_{ow} values, so that θ_{oa} and θ_{ow} are slightly different to those used in the cases shown in panels A and B. These changes in the values of the interfacial tensions and contact angles of the air–oil and oil–water interfaces dramatically

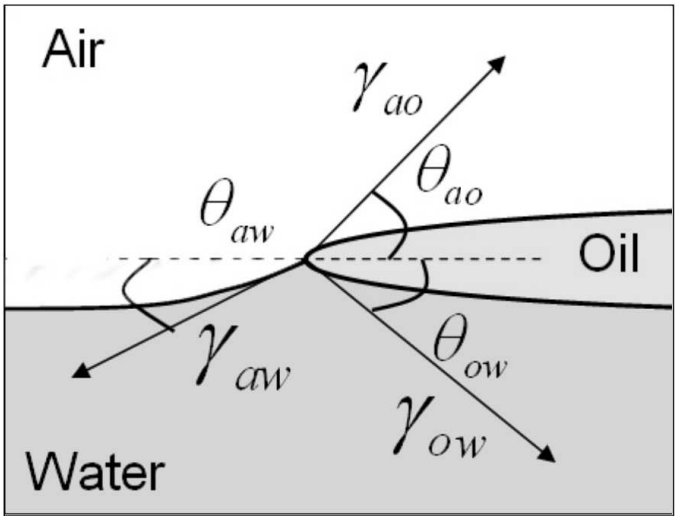

Figure 7.15: Sketch of an oil drop at a fluid–fluid interface.

modify the external potential profile, causing an inversion in the potential experimented by the particle when entering into the oily phase.

As can be seen in figure 7.16B, the energy of a particle inside the oil lens is smaller than the energy outside the drop; so, in principle, the colloidal particles will tend to emigrate to the oil drops. However, due to the different air-water and air-oil surface tensions a minimum is found at $(r - R_{drop})/R_{part} \approx -1.5$, which prevents particle migration till the oil drop center. To remove the particle from this three phase contact line involves a very high–energy cost caused by the creation of a new oil–water interface (S_{wo}). The presence of this minimum can explain the appearance of the colloidal rings found for some liquid mixtures.

7.4.3 Simulations

The simulations were conducted off-lattice using the Monte Carlo method in a two-dimensional simulation cell of dimensions LxL with periodic boundary conditions. In each simulation N spherical particles were randomly placed inside the cell and their surface areas S_{pw}, S_{po}, Sd_{aw}, Sd_{ao} and Sd_{wo} calculated by numerical integration. Then, the total energy was obtained using Eqs. 7.3, 7.4 and 7.6. After that, the particles are displaced independently with a Brownian movement to a new positions. After each particle move-

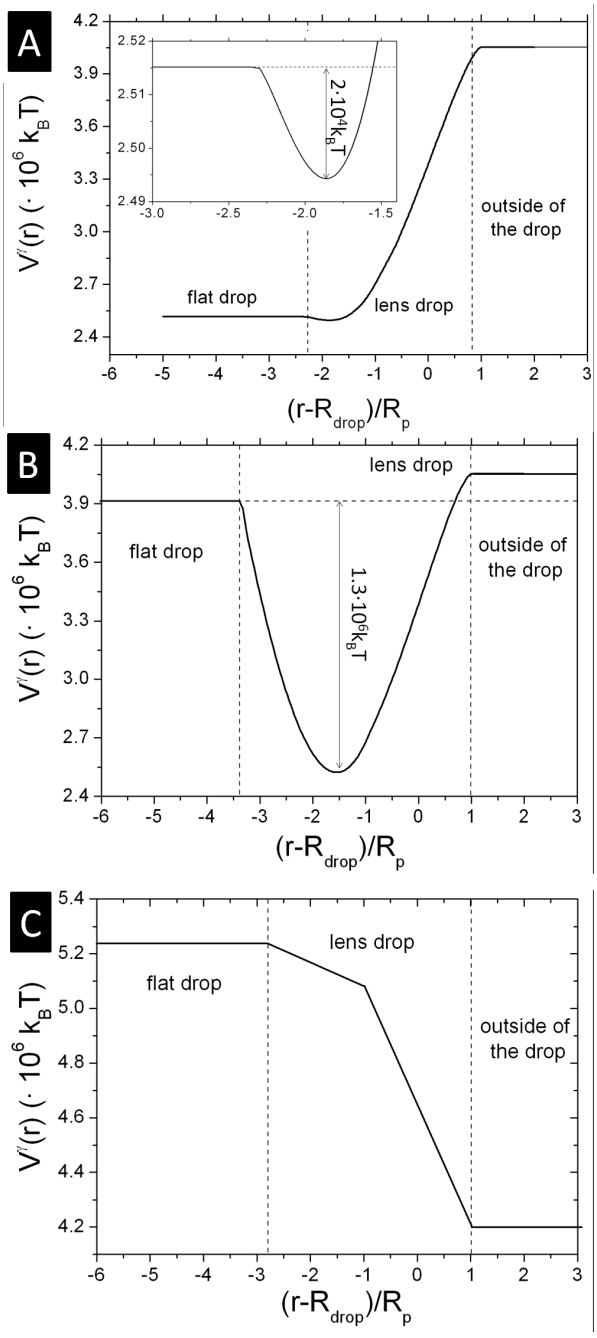

Figure 7.16: V^γ versus the distance of the particle to the oil–water–air contact line reduced by the particle radius. A and B were computed using data sets a and b (Table 7.2) while C is obtained from data set d in table 7.2.

ment, the total energy was calculated and the movement accepted or rejected depending on the differences between the new and the previous energy (like a typical Monte Carlo simulation). The simulation stopped when a stable situation was reached.

Input data for the simulations are as follows: time step ($\Delta t = 4 \times 10^{-4}$ s), number of particles ($N = 300$), fraction of area $\varphi = 0.10$, number of droplets and positions, $\sigma = 6 \cdot 10^{18}$ e^-/m^2 , $f_{dip} = 1\%$, $R = 3 \cdot 10^{-7}$ m, $P = 4.8 \cdot 10^{29}$ C·m assuming a dipole length of 0.3 nm, ϵ_0 and $\epsilon = 1$. The contact angle considered for the particle at the air–water and at the oil–water interface were $\theta_{pw} = 82°$and $\theta_{po} = 15°$, respectively. The surface tensions were $\gamma_{pa} = 34$ mJ/m^2, $\gamma_{aw} = 72$ mJ/m^2, $\gamma_{ao} = 21$ mJ/m^2 and $\gamma_{wo} = 33$ mJ/m^2. γ_{pw} and γ_{po} can be easily obtained using the Young's equation, giving $\gamma_{pw} = 23$ mJ/m^2 and $\gamma_{po} = 14$ mJ/m^2.

7.5 Simulation results

The formation of oil lenses at the air–water interface leads to the existence of a nonhomogeneous interface with hydrophobic (oily lenses) and hydrophilic patches (water surface). When polystyrene microspheres are spread onto this nonhomogeneous interface most of them tend to reach the three phase contact line where they are eventually trapped and form the colloidal rings. Figure 7.17, panels a and b, shows the colloidal rings obtained from simulations using the interaction potential given by eq 7.3. Particles at the air-water interface cannot migrate to the oil–air interface (and vice versa), because they have not enough energy to cross the three phase contact line where the potential V^γ acting on the particle has a minimum (figure 7.16). This further implies that the average interparticle distance depends on particle accommodation inside the hydrophilic and hydrophobic patches at the air-liquid interface. This model explains the appearance of circular rings which are common structures observed in colloidal monolayer experiments. It should be noted that a change in h_{drop} modifies the external potential values (see figure 7.16, panels a and b) but that not affects the ring patterns. The number of colloidal particles that takes part of a ringed pattern depends on h_{drop} as if h_{drop} increases the potential minimum becomes widther and then double or triple rings could be appear. Other mesostructure patterns like circular clusters could be explained if an initial inhomogeneity in the colloidal distribution, due to the turbulent spreading of the particles at the

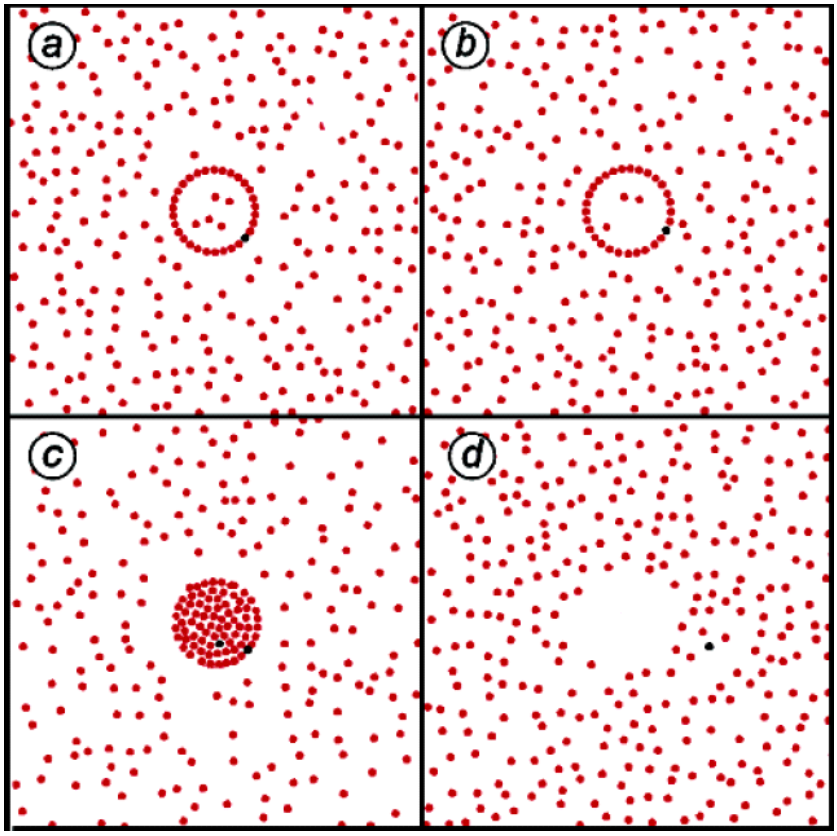

Figure 7.17: Simulated mesostructures at the air–nonhomogeneous liquid interface. (a) and (b) Colloidal rings, (c) Circular clusters, and (d) Voids are obtained using the data parameters showed in lines $a - d$ of Table 7.2, respectively.

interface, is considered. Figure 7.17–*c* shows the structure formed with an initial Gaussian distribution of particles centered on the oil lens. The formation of voids (see figure 7.17–*d*) is reached changing the values (see Table 7.2) of γ_{ao} from 38 to 21 mJ m^{-2}, γ_{ow} from 38 to 53 mJ m^{-2}, γ_{po} from 14 to 31 mJ m^{-2}, and θ_{ow} from 20° to 10°. As can be seen in figure 7.16C, these changes in the surface and interfacial tensions cause an important modification of the external potential, V^{γ}, profile.

In summary, the proposed simple interaction model that take into account the dipolar repulsion between particles and surface tension heterogeneities can explain the formation of most usual mesostructure patterns found in the experiments with colloidal particles.

Chapter 8

Summary and conclusions

This thesis concentrates on the study of the structural and kinetics properties of two–dimensional colloidal systems where the particles interact among them with different kinds of potentials. The questions that we want to answer is: **how modify the interaction potential the structure, kinetics and distribution over the plane of the clusters formed during the coagulation process?**

First, we have studied the order of the aggregates trapped at an interface that is induced by the *Brownian diffusion* of such aggregates and the dependence of this order with the surface packing fraction of particles. In order to do this we have used *Brownian dynamic simulations* where the particles remain irreversibly stick after collision.

Second, we go further and we introduce a medium–range repulsion on the total interaction potential to study the effect of the interaction range over the structure of the aggregates and the kinetic properties of the aggregation process. Again, we used Brownian dynamic simulations where the particles interact with a Yukawa potential. Then, we have studied the effect of varying the range and the interaction between particles in contact over the coagulation process.

Finally, we have studied the origin of a new kind of colloidal structures (mesostructures) that has been reported since the 90's. This mesostructures could appear when colloidal particles are spreading at an liquid–fluid interface (as an air–water interface). We found the experimental conditions that are necessary to obtain such structures and we have showed that the formation of mesostructures is induced by the presence of an contaminating agent which in our case is silicon oil. Moreover, we have developed a simple model based in a

heterogeneous interface in surface tension due to the presence of oil drops at the interface. In order to check this, we have developed a simple Monte Carlo simulation at a heterogeneous interface in surface tension. Those simulations, where particles diffuse in this heterogeneous interface, are able to reproduce the more frequently mesostructures found by other authors.

The following paragraphs briefly summarize the main points of this work.

8.1 Topological order induce by diffusion

By means of Brownian dynamics, we studied the effect of the surface packing fraction on the topological properties of two–dimensional aggregating systems where we assumed the simplest case of freely Brownian diffusive sticking particles without interactions (DLCA). The topological properties have been measured with the help of the *Voronoi construction*. The study of the correlations between non–adjacent cells was achieved by analyzing the system as structured in concentric layers around a given central one. This method allows us to go beyond the internal fractal structure of the clusters and to study the external inter–cluster properties. Indeed, it determines the short and long–range spatial organization of the clusters and the cluster–cluster "interactions" induced by the mutual competition between neighboring depletion regions that occurs when the fractal–like clusters fill up the whole space. The main results of this work where

1.- **We obtained a continuous ordering of the cell structure as aggregation proceeds**. Specifically, clusters tend to adopt a more ordered hexagonal organization in the plane, what topologically means a reduction in both, the second central moment of the number of sides distribution μ_2 and the proportion of defects Λ.

2.- **This ordering is more important for higher particle densities**, where the already small free space existing between growing clusters becomes rapidly shrunk due to the fractal growth.

3.- **This ordering finishes as soon as the scaling of the cluster–size distribution is reached** ($t > t_{sc}$). Since all the studied topological properties ($P(n)$, μ_2, a, $< K_j >$, $< Q_j >$ and Λ) remain constant in this final scaling limit, it can be regarded as a topological invariant state.

4.- **The whole coagulation process lies in a universal topological class** independent on the particle concentration, given by the general relation $a \sim \mu_2^{-0.89}$.

5.- **Colloidal aggregation in two dimensions is only able to produce short–range inter–cluster correlations** (up to the second layer of clusters around a central one, $j = 2$) even for the very high packing fraction of particles. However, the ordering is manifested in the whole shell structure at any topological distance in terms of a decrease of the proportion of defective cells Λ_j.

6.- **The main topological property that controls the degree of structuring at short and long inter–cluster distances is the second central moment** μ_2, which is a measurement of the global order in the whole system.

8.2 Effect of repulsive interaction with non–negligible range

We studied the effect of an interaction potential with a non–negligible range on the kinetic properties and the structure of the aggregates formed in a computer–simulated two–dimensional aggregating system. We have connected the new kinetic region induced by the range of the interaction with the well–known RLCA aggregation regime. Hence, we have a complete description of the kinetic behavior of a two–dimensional aggregating system composed by colloidal particles that interact with a medium–range pairwise repulsive interaction. We have observed that the range of the interaction modifies not only the kinetics of the coagulation process at short times but also the structure of the small aggregates formed in this process. Moreover, although the effect of the interaction range appears only in the first stages of the coagulation, the consequences of this affect the complete evolution of the process. The main results obtained in this work were the following ones

1.- **Two different kinetics regions has been observed in the representation of the *number–average cluster size*** $S_n(t)$**.** The first region appears due to the effect of the non–negligible interaction range and the second one represent the classical RLCA regime.

2.- **Two different regions has been observed also in the mean structure of the aggregates**, depending on the kinetic region where they appear. At short times, the aggregates tend to adopt a linear structure, that correspond to the effect of the non–negligible interaction range. At medium time, the fractal structure characteristic for the RLCA regime is recovered.

3.- **The cluster–cluster interaction potential becomes more repulsive and anisotropic with the increasing of the sizes of the clusters for aggregates with sizes under the critical size** i_0 due to the superposition of the interactions. For aggregates of sizes larger than i_0, not all the monomers that compose these aggregates participate in the total interaction. Therefore, V_{ij} becomes independent on i and j for $i, j > i_0$, the cluster–cluster interaction recovers its isotropy. This transition between anisotropic to isotropic interaction clearly explain the first kinetic region and the arising of linear structures in this region and the transition to the fractal aggregates when the isotropy is recovered.

4.- **A new method has been developed in order to obtain the aggregation rate constants** through the functions $P_{ij} = k_{ij}/k_{ij}^{Br}$ directly from the simulations performed. This method allows us to study the effect of the interaction range over the real coagulation kinetics.

5.- **The kernel found was introduced in the Smoluchowski equation 2.24 and the cluster size distribution were obtained. These functions were compared with the simulation and the agreement is practically perfect.**

8.3 Colloidal mesostructures

The spontaneous formation of the so–called *mesostructures* has been observed in colloidal monolayers trapped at the air–water interface. The distance between particles in these mesostructures is of the order of the particle radius (micrometers), implying that the colloidal interaction potential has a minimum at such distances, which could induce the phase separation of colloidal monolayers in dense and dilute regions. Recently, a great deal of effort has focused on understanding the mechanism behind the phenomenon of

long–range attraction between colloidal particles confined in interfaces which could explain the formation of these structures.

8.3.1 Experimental part

Here, we have shown that the formation of our mesostructures is due to the contamination of colloidal monolayers by silicone oil (poly– (dimethyl-siloxane)), which arises from the coating of the needles and syringes used to deposit and spread the particle solution at the air–water interface. The difference in the interfacial tension of water and silicone oil accounts for the formation of the experimentally observed mesostructures.

1.- **We have shown that the presence of small traces of an oily agent (silicon oil) is able to reproduce all the experimental structures observed by other authors.**

2.- **For first time, we were able to observe the formation of colloidal mesostructures in real time.**

3.- **For small concentrations of silicon oil we observed the formation of rings, circular patterns and voids. When the concentration of oil is increased, it appears loops and other irregular shapes.**

8.3.2 Simulation results

Using computer simulations, we have shown that the formation of colloidal rings, circular clusters and voids is due to the presence of surface tension inhomogeneities at the air water interface. In this case, the total interaction potential was assumed to be composed of only two terms; the first one is due to the (repulsive) pairwise dipolar force between partly immersed charged microspheres, whereas the second depends on the position of the particle at the interface and is connected to the interfacial stress caused by the difference of surface tension between both liquids.

1.- **A simple Monte Carlo simulation was performed to reproduce some of the simulation experimentally obtained.** In this simulation, the particles interact through a dipolar repulsion and a term that take into account the presence of flat oily drops at the air–water interface.

2.- **It is not necessary to introduce any unknown long–range attractive interaction to explain the formation of colloidal mesostructures.**

Chapter 9

Resumen y conclusiones

Esta tesis se centra en el **estudio de propiedades cinéticas y estructurales de sistemas coloidales cuyo movimiento se encuentra confinado en un plano** (sistemas coloidales bidimensionales). En estos sistemas, las partículas pueden interactuar entre ellas a través de diferentes tipos de potenciales de interacción. El principal objetivo planteado en esta tesis consiste en tratar de responder a la pregunta **¿Cómo dependen las propiedades estructurales, las cinéticas y la ordenación de las estructuras formadas durante el proceso de coagulación del potencial de interacción entre partículas?**

En primer lugar, hemos estudiado el **ordenamiento de los agregados** formados en un proceso de coagulación limitado por la difusión Browniana de las partículas, así como la dependencia de dicho ordenamiento de la concentración. Para ello realizamos una serie de simulaciones de dinámica Browniana en la que las partículas permanecen enlazadas de forma irreversible tras una colisión.

El siguiente paso en nuestro trabajo fue introducir en estas simulaciones el **efecto de un potencial de interacción con un alcance no despreciable** para analizar el efecto que dicho alcance posee sobre la estructura de los agregados formados, así como la cinética de coagulación del sistema. De nuevo, empleamos simulaciones de dinámica Browniana donde ahora las partículas interactuarán a través de un potencial tipo Yukawa. Para caracterizar el efecto del alcance, realizamos una serie de simulaciones para distintos valores de dicho alcance.

Finalmente, hemos estudiado el origen de un nuevo tipo de estructuras coloidales (llamadas "mesoestructuras") que pueden aparecer cuando deposi-

tamos partículas sobre una interfaz líquido–fluido (por ejemplo, sobre una interfaz agua–aire). Estas estructuras aparecen por primera vez en la bibliografía a finales de la década de los 90 y a día de hoy no existe un modelo formal capaz de explicar su origen. Nosotros hemos encontrado las condiciones experimentales necesarias para obtener este tipo de estructuras. Además, hemos puesto de manifiesto que **la formación de estas mesoestructuras puede inducirse mediante la presencia de un agente contaminante de tipo oleoso**, que en nuestro caso fue aceite de silicona. En base a estos resultados experimentales, hemos propuesto un sencillo **modelo basado el la presencia de heterogeneidades de energías interfaciales en el sistema** originadas precisamente por la presencia de este aceite. Para comprobar la validez de dicho modelo, implementamos una serie de simulaciones de tipo Monte Carlo modelando esta interfaz heterogénea, donde las partículas se organizan formando estructuras muy similares a las mesoestructuras que con más frecuencia aparecen tanto en nuestros resultados experimentales como en los publicados en la bibliografía.

Los siguientes apartados resumen brevemente las principales conclusiones alcanzadas en este trabajo

9.1 Order Topológico inducido por difusión

Empleando simulaciones de *dinámica Browniana*, hemos estudiado el **efecto de la concentración de partículas sobre las propiedades topológicas en un proceso de coagulación bidimensional limitado por difusión**. Éste es el conocido regimen de agregación DLCA donde las partículas no interactuantes difunden Brownianamente hasta colisionar, tras lo cual, permanecen irreversiblemente agregadas. Las propiedades topológicas de estos sistemas fueron calculadas empleando los llamados diagramas de Voronoi. El estudio de las correlaciones entre celdas (agregados) no adyacentes fue realizado mediante la descomposición del sistema en estructuras de capas concéntricas alrededor de una celda central. Éste método nos permite pasar del estudio de la estructura de los agregados individuales al estudio de como se ordenan los agregados formados sobre el plano. Esta ordenación espacial viene originada por la aparición de regiones de deplección (o de vaciamiento) entre los agregados debido al crecimiento fractal de los mismos que tienden a llenar el espacio. Los principales resultados de este trabajo fueron

1.- **Observamos un ordenamiento continuo de la estructura de cel-**

das a medida que transcurre el proceso de coagulación. Más concretamente, los agregados tieneden a adoptar una estructura más hexagonal en el plano en el que se encuentran. Topológicamente, esto significa tanto una reducción tanto del segundo momento de la distribución del número de lados de las celdas μ_2 como de la proporción de defectos Λ.

2.- **El ordenamiento observado es más importante para el caso de sistemas más concentrados** donde, el ya pequeño espacio libre existente entre los monómeros antes del proceso de coagulación, disminuye rápidamente debido al crecimiento fractal de los agregados.

3.- **El proceso de ordenamiento de los agregados formados termina tan pronto como se alcanza la región de escalado en la distribución de tamaños**($t > t_{sc}$). Debido a que todas las propiedades topológicas estudiadas en este trabajo ($P(n)$, μ_2, a, $< K_j >$, $< Q_j >$ y Λ) permanecen constantes en este límite final de escalado, éste puede verse como un estado topológicamente invariante.

4.- **El proceso de coagulación completo cae en una clase topológica universal**, independiente de la concentración de partículas, dada por la relación general $a \sim \mu_2^{-0.89}$.

5.- **El proceso de agregación en dos dimensionaes solo es capaz de producir correlaciones de corto alcance entre agregados cercanos** (hasta la segunda capa de agregados en torno a uno central, $j = 2$), incluso para el caso de alta concentración de partículas. Sin embargo, el ordenamiento se manifiesta en la estructura de capas completa para cualquier distancia topológica en términos de una disminución de la proporción de defectos topológicos Λ_j.

6.- **La principal propiedad topológica que determina el grado de estructuración a corta y laras distancias entre agregados es el segundo momento de la distribución del número de lados** μ_2, el cual es una medida del orden global del sistema completo.

9.2 Efecto de las interacciones repulsivas de alcance no despreciable

En esta sección estudiaremos el **efecto de un potencial de interacción con un alcance no despreciable sobre las propiedades cinéticas y estructurales de los agregados** formados mediante simulaciones de un proceso de coagulación de dinámica Browniana bidimensional. **Hemos enontrado una nueva región cinética inducida por el alcance de la interacción de tipo repulsivo**, así como **hemos conectado esta nueva región con el conocido regimen de agregación RLCA**. Así pues, tenemos una descripción completa de la cinética de un proceso de coagulación bidimensional formado por partículas coloidales que interactúan a través de un potencial repulsivo a pares de medio alcance. Hemos observado que el alcance de la interacción no solamente modifica a la cinética del proceso de coagulación, sino que también cambia la estructura de los pequeños agregados formados en este proceso. Más aún, aunque el efecto del alcance de la interacción se manifiesta únicamente en los primeros estadios del proceso de coagulación, la consecuencia de esto afecta al completo desarrollo del proceso. Los principales resultados obtenidos de este trabajo fueron

1.- **Se observaron dos regiones cinéticas en la representación del tamaño medio en número $S_n(t)$ frente al tiempo.** La primera región aparece como consecuencia del alcance de la interacción repulsiva mientras que la segunda corresponde al clásico regimen de agregación RLCA.

2.- **Se encontró que las estructuras de los agregados formados en cada una de estas regiones cinéticas son distintas**. A tiempos cortos, el efecto del alcance de la interacción repulsiva provoca que los agregados tiendan a adoptar estructuras lineales. Cuando los agregados son suficientemente grandes, el efecto del alcance de la interacción se vuelve menos importante, recuperando las estructuras fractales características del regimen de agregación RLCA.

3.- **La repulsión agregado–agregado se intensifica con el incremento del tamaño de los agregados involucrados hasra alcanzar un cierto tamaño crítico** i_0 debido a la superposición de las interacciones. Para agregados de tamaño mayor a i_0 no todos los monómeros que componen estos agregados participan en el potencial de interacción total. Así

pues, el potencial de interacción agregado–agregado V_{ij} será independiente del tamaño para $i, j > i_0$ y, a partir de ese momento, tiende a ser más isótropo. Esta transición entre una interacción anisótropa a otra isótropa explica claramente porqué en la primera región cinética las particulas tienden a formar cadenas (potencial anisótropo), que al alcanzar un cierto tamaño recuperan la estructura fractal característica del regimen RLCA (potencial isótropo).

4.- **Hemos desarrollado un nuevo método para obterner el kernel de agregación directamente de las simulaciones** a través de las funciones $P_{ij} = k_{ij}/k_{ij}^{Br}$.

5.- **Los kernels encontrados fueron introducidos en la encuación de Smoluchowski 2.24 obteniendo de su solución tanto el tamaño medio en número de los agregados como su la distribución de tamaños. Estas curvas fueron comparadas con las obtenidas directamente de las simulaciones obteniendo una buena concordancia entre ambas. Esto demuestra que el método empleado es capaz de proporcionarnos un kernel de agregación que nos describe la cinética de crecimiento de los agregados formados**.

9.3 Mesoestructuras coloidales

La formación espontánea de las llamadas mesoestructuras coloidales ha sido observada en sistemas formados por partículas esféricas de poliestireno dispersas sobre una interfaz agua–aire. La distancia entre las partículas que forman estas mesoestructuras es del orden del radio de las mismas (micrómetros), lo cual implica que el potencial de interacción entre coloides posee un mínimo a esta distancia. La presencia de dicho mínimo podría provocar la separación de fases del sistema en regiones densas y regiones empobrecidas de partículas. En los últimos años se ha dedicado un gran esfuerzo en tratar de entender el mecanismo que se esconde tras una posible interacción atractiva de largo alcance que pudiera explicar la formación de estas estructuras.

9.3.1 Parte experimental

En esta sección hemos mostrado que la formación de las mesoestructuras observadas en nuestro laboratorio es debida a la contaminación de las mono-

capas coloidales por un aceite de silicona, el cual procede del recubrimiento de las agujas y de las jeringuillas empleadas para depositar y dispersar las disolución de partículas sobre la interfaz agua–aire. La diferencia entre las energías interfaciales del agua y del aceite de silicona es la responsable de la formación de estas mesoestructuras. Las principales conclusiones a las que hemos llegado en este trabajo fueron

1.- **Hemos demostrado que la presencia de pequeñas trazas de una sustancia oleosa (aceite de silicona) es capaz de reproducir todas las mesoestructuras encontradas experimentalmente en la bibliografía.**

2.- **Por primera vez, hemos sido capaces de observar paso a paso la formación de mesoestructuras coloidales.**

3.- **Para pequeñas concentraciones de aceite de silicona observamos la formación de anillos, patrones circulares y agujeros. Cuando incrementamos la concentración de aceite aparecen lazos y un gran número de formas irregulares.**

9.3.2 Resultados de las simulaciones

El objetivo de esta parte es introducir el potencial de interacción externo procedente del modelo propuesto para explicar la formación de las mesoestructuras y comprobar que es capaz de reproducir la formación de los anillos, patrones circulares y agujeros observados en nuestros experimentos y por otros autores. La presencia de dos líquidos con distinta energía superficial conduce a la formación de lentes de aceite sobre la interfaz agua–aire, lo cual provoca la aparición de heterogeneidades en tensión superficial sobre la interfaz. En las simulaciones realizadas consideramos que el potencial de interacción total está compuesto por dos términos: el primero debido a la interacción dipolar repulsiva entre partículas. Ésta es la interacción más característica en sistemas formados por partículas coloidales atrapadas entre una fase polar y otra apolar. El segundo término del potencial total dependerá de la posición de la partícula sobre la interfaz y es debido a las diferencias en la energía superficial entre los distintos líquidos. Los principales resultados alcanzados fueron

1.- **Se realizaron una serie de simulaciones Monte Carlo capaces de reproducir parte de las mesoestructuras encontradas experimentalmente**.

2.- **No es necesarion introducir ninguna interacción atractiva de largo alcance para explicar la formación de las mesoestructuras coloidales.**

List of Figures

List of Tables

Bibliography

[1] A. Einstein. *Ann. d. Phys.*, 17:549, 1905.

[2] J. Perrin. *Brownian Movement and Molecular Reality.* Taylor and Francis, 1909.

[3] B. V. Derjaguin and L Landau. Theory of stability of highly charged liophobic sols and adhesion of highly charged particles in solutions of electrolytes. *Acta Physicochim URSS*, 14:633, 1941.

[4] E. J. Verwey and j. Th. G. Overbeek. *Theory of the Stability of Lyophobic Colloids.* Elsevier, Amsterdam, 1948.

[5] Z. Hórölgyi, G. Medveczky, and Z. Zrínyi. Experimental study of the aggregate structures formed in the boundary layer of water–air phases. *Colloids Surf.*, 60:79, 1991.

[6] D.J. Robinson and J. C. Earnshaw. Experimental study of colloidal aggregation in two dimensions. i. structural aspects. *Phys. Rev. A*, 46:2045, 1992.

[7] D.J. Robinson and J. C. Earnshaw. Experimental study of colloidal aggregation in two dimensions. ii. kinetic aspects. *Phys. Rev. A*, 46:2055, 1992.

[8] A. Moncho-Jordá, F. Martínez-López, A. E. González, and R. Hidalgo-Álvarez. Role of long-range repulsive interactions in two-dimensional colloidal aggregation: Experiments and simulations. *Langmuir*, 18:9183, 2002.

[9] M. L. Broide and R. J. Cohen. Experimental evidence of dynamic scaling in colloidal aggregation. *Phys. Rev. Lett.*, 64:2026, 1990.

[10] M. Carpineti and M. Giglio. Spinodal–type dynamics in fractal aggregation of colloidal clusters. *Phys. Rev. Lett.*, 68:3327, 1992.

[11] D.J. Robinson and J. C. Earnshaw. Long range order in two dimensional fractal aggregation. *Phys. Rev. Lett.*, 71:715, 1993.

[12] M. Carpineti, M. Giglio, and V. Degiorgio. Mass conservation and anticorrelation effects in the colloidal aggregation of dense solutions. *Phys. Rev. E*, 51:590, 1995.

[13] M. D. Haw, M. Sievwright, W. C. K. Poon, and P. N. Pusey. Structure and characteristic length scales in cluster–cluster aggregation simulation. *Physica A*, 217:231, 1995.

[14] A. E. González and G. Ramírez-Santiago. Spatial ordering and structure factor scaling in the simulations of colloid aggregation. *Phys. Rev. Lett.*, 74:1238, 1995.

[15] A. E. González and G. Ramírez-Santiago. Scaling of the structure factor in fractal aggregation of colloids: Computer simulations. *J. Colloid Interface Sci.*, 182:254, 1996.

[16] J. C. Earnshaw and D.J. Robinson. Topological correlations in colloidal aggregation. *Phys. Rev. Lett.*, 72:3682, 1994.

[17] J. C. Earnshaw and D.J. Robinson. Inter-cluster scaling in two–dimensional colloidal aggregation. *Physica A*, 214:23, 1995.

[18] A. Moncho-Jordá, F. Martínez-López, and R. Hidalgo-Álvarez. Simulations of aggregation in 2d. a study of kinetics, structure and topological properties. *Physica A*, 282:50, 2000.

[19] J. K. G. Dhont. *An Introduction to Dynamics of Colloids*. Elsevier, Amsterdam, 1996.

[20] J Lyklema. *Fundamental of Interfaces and Colloids Science*. Academic Press, London, 1991.

[21] H. Risken. *The Fokker Planck Equation: Methods on Solutions and Applications*. Springer Series in Synergetics. Springer, 2nd edition edition.

[22] Y. Gefen, A. Aharony, B. B. Mandelbrot, and S. Kirkpatrick. Solvable fractal family, and its possible relation to the backbone at percolation. *Phys. Rev. Lett.*, 47:1771, 1981.

[23] T. A. Witten and L. M. Sander. Diffusion–limited aggregation, a kinetic critical phenomenon. *Phys. Rev. Lett.*, 47:1400, 1981.

[24] P. Meakin. Formation of fractal clusters and networks by irreversible diffusion–limited aggregation. *Phys. Rev. Lett.*, 51:1119, 1983.

[25] M. Kolb and R. Jullien. Diffusion limited aggregation with directed and anisotropic diffusion. *J. Phys. (Paris) Lett.*, 45:395, 1984.

[26] D. A. Weitz and M. Oliveira. *Phys. Rev. Lett.*, 52:1433, 1984.

[27] A. Moncho-Jordá, G. Odriozola, F. Martínez-López, A. Schmitt, and R. Hidalgo-Álvarez. The dlca-rlca transition arising in 2d-aggregation: simulations and mean field theory. *Eur. Phys. J.*, 5:471, 2001.

[28] M. V. Smoluchowski. *Phys. Z.*, 17:557, 1916.

[29] P. Meakin. Aggregation kinetics. *Phys. Scr.*, 46:295, 1992.

[30] F. Leyvraz. Scaling theory and exactly solved models in the kinetics of irreversible aggregation. *Phys. Reports.*, 383:95, 2003.

[31] F. Family, P. Meakin, and T. Vicsek. Cluster size distribution in chemically controlled cluster cluster aggregation. *J. Chem. Phys*, 83:4144, 1985.

[32] A. A. Lushnikov. Exact kinetics of sol-gel transition in a coagulating mixture. *Phys. Rev. E.*, 73:036111, 2006.

[33] M. H. Ernst. *Kinetics of clustering in irreversible aggregation.* Amsterdam: North-Holland, 1986.

[34] R. Jullien and R. Botet. *Aggregation and Fractal Aggregates.* World Scientific, Singapore, 1987.

[35] M. H. Lee. *Astrophys. J.*, 418:147, 1993.

[36] G. Odriozola, A. Schmitt, A. Moncho-Jordá, R. Martínez-Leone, and R. Hidalgo-Álvarez. Constant bond breakup probability model for reversible aggregation processes. *Phys. Rev. E.*, 65:031405, 2002.

[37] T. Sintes, R. Toral, and A. Chakrabarti. Dynamical scaling of fractal aggregates in dense colloidal solutions. *Phys. Rev. E.*, 50:2967, 1994.

[38] T. Vicsek and F. Family. Dynamic scaling for aggregation of clusters. *Phys. Rev. Lett.*, 52:1669, 1984.

[39] P. Meakin, T. Vicsek, and F. Family. Dynamic cluster–size distribution in cluster-cluster aggregation: Effects of cluster diffusivity. *Phys. Rev. B*, 31:564, 1985.

[40] G. Odriozola, A. Moncho-Jordá, A. Schmitt, J. Callejas-Fernández, R. Martínez-García, and R. Hidalgo-Álvarez. A probabilistic aggregation kernel for the computer-simulated transition from dlca to rlca. *Europhys. Lett.*, 53:797, 2001.

[41] M. H. Ernst and P. G. J. van Dongen. Scaling laws in aggregation: Fragmentation models with detailed balance. *Phys. Rev. A.*, 36:435, 1987.

[42] E. J. W. Verwey and J. Th. C. Overbeek. *Theory of the stability of Lyophobic colloids*. Elsevier, Amsterdam, 1948.

[43] M. Kolb, R. Botet, and R. Jullien. Scaling of kinetically growing clusters. *Phys. Rev. Lett.*, 51:1123, 1983.

[44] R. Jullien and R. Botet. *Aggregation and Fractal Aggregation*. Word Scientific, 1987.

[45] T. Vicsek. *Fractal Growth Fenomena*. World Scientific, Singapore, 2ï¿½ edition edition, 1992.

[46] R. Jullien. The application of fractals to colloidal aggregation. *Croat. Chem. Acta.*, 65:215, 1992.

[47] T. Vicsek. *Fractal Growth Phenomena*. World Scientific, 1992.

[48] D. J. Robinson and J. C. Earnshaw. Experimental study of colloidal aggregation in two dimensions. iii. structural dynamics. *Phys. Rev. A*, 46:2065, 1992.

[49] M. Lin, H. M. Lindsay, D. A. Weitz, R. Klein, R. C. Ball, and P. Meakin. Universal reaction–limited colloid aggregation. *Phys. Rev. A,*, 41:2005, 1990.

[50] R. Ball, D. Weitz, T. Witten, and F. Leyvraz. Universal kinetics in reaction-limited aggregation. *Phys. Rev. Lett.*, 58:274, 1987.

[51] F. Family, P. Meakin, and T. Vicsek. *J. Chem. Phys.*, 83:4144, 1985.

[52] C. Cametti, P. Codastefano, and P. Tartaglia. Aggregation kinetics in model colloidal systems - a light-scattering study. *J. Colloid Interface Sci.*, 131:409, 1989.

[53] A. Moncho-Jordá, F. Martínez-López, and R. Hidalgo-Á lvarez. The effect of the salt concentration and counterion valence on the aggregation of latex particles at the air/water interface. *J. Colloid interface Sci.*, 249:405, 2002.

[54] R. Aveyard, J.H. Clint, D. Nees, and V.N. Paunov. Compression and structure of monolayers of charged latex particles at air/water and octane/water interfaces. *Langmuir*, 16:1969, 2000.

[55] R. Aveyard, B.P. Binks, J.H. Clint, P.D.I. Fletcher, T.S. Horozov, B.Neumann, V.N. Paunov, J. Annesley, S.W. Botchway, D. Nees, A.W. Parker, A.D. Ward, and A.N. Burgess. Measurement of long-range repulsive forces between charged particles at an oil-water interface. *Phys. Rev. Lett*, 88:246102, 2002.

[56] P. Pieranski. Two–dimensional interfacial colloidal crystals. *Phy. Rev. Lett.*, 45:569, 1980.

[57] J. Ruiz-García, R. Gámez-Corrales, and B. I. Ivlev. Formation of two-dimensional colloidal voids, soap froths, and clusters. *Phys. Rev. E*, 58:660, 1998.

[58] J Ruiz-García, R. Gámez-Corrales, and B. I. Ivlev. Foam and cluster structure formation by latex particles at the air/water interface. *Physica A*, 236:97, 1997.

[59] F. Ghezzi, J. C. Earnshaw, M. Finnis, and M. McCluney. Pattern formation in colloidal monolayers at the air–water interface. *J. Colloid Interface Sci.*, 238:433, 2001.

[60] V. Lowry, M.S. El-Aasser, J.W. Vanderhoff, A. Klein, and C.A. Silebi. Kinetics of agitation-induced coagulation of high-solid latexes. *J. Colloid. Interf. Sci.*, 112:521, 1986.

[61] J.T. Long. *Engineering for Nuclear Fuel Reprocessing, Gordon and Breach Science*. Inc., New York, 1967.

[62] R.J. Pugh and L. Nishkov. *Paper at 28th Conference of Metallurgists*. G.S. Dobby and S.R. Rao, Montreal, 1990.

[63] J.C. Earnshaw. *J. Phys. D*, 19:1863, 1986.

[64] M. Quesada-Pérez, A. Moncho-Jordá, F. Martínez-López, and R. Hidalgo-Álvarez. Probing interaction forces in colloidal monolayers: Inversion of structural data. *J. Chem. Phys.*, 115:10897, 2001.

[65] B.V. Derjaguin. *Kolloid Zei*, 69:155, 1934.

[66] D.Y.C. Chan, J.D. Henry Jr., and L.R. White. The interaction of colloidal particles collected at fluid interfaces. *J. Colloid Interf. Sci.*, 79:410, 1981.

[67] R.J. Hunter. *Foundations of Colloid Science*, volume 1. Clarendon Press, New York, 1987.

[68] M.P. Lyne. PhD thesis, University of British Columbia, 1989.

[69] S. Levine and M.P. Lyne. *Paper at 63rd ACS Colloid and Surface Science Symposium,*. Seattle, 1989.

[70] J. Gregory. Approximate expressions for retarded vanderwaals interaction. *J. Colloid Interf. Sci.*, 83:138, 1981.

[71] J.Th.G. Overbeek. *Proc. Königs Akad. Wetensch. B*, 69:501, 1966.

[72] M.L. Gee and J. Israelachvili. Interactions of surfactant monolayers across hydrocarbon liquids. *J. Chem. Soc. Faraday Trans.*, 86:4049, 1990.

[73] J. Israelachvili and R.M. Pashley. Measurement of the hydrophobic interaction between 2 hydrophobic surfaces in aqueous-electrolyte solutions. *J. Colloid Interf. Sci.*, 98:500, 1984.

[74] N.V. Churaev. *Uspekhi Kollidnoj Khimii, FAN Tashkent*, 70:250, 1987.

[75] H.K. Christenson and P.M. Claesson. Cavitation and the interaction between macroscopic hydrophobic surfaces. *Science*, 239:390, 1988.

[76] J. Israelachvili. *Intermolecular and Surface Forces*. AcademicPress, New York, 2nd edition, 1992.

[77] D.J. Robinson and J.C. Earnshaw. Initiation of aggregation in colloidal particle monolayers. *Langmuir*, 9:1436, 1993.

[78] J. Sun and T. Stirner. Molecular dynamics simulation of the surface pressure of colloidal monolayers. *Langmuir*, 17:3103, 2001.

[79] T. S. Horozov, R. Aveyard, J. H. Clint, and B. P. Binks. Order-disorder transition in monolayers of modified monodisperse silica particles at the octane-water interface. *Langmuir*, 19:2822, 2003.

[80] J. Sun and T. Stirner. Molecular dynamics simulation of compression-induced solid-to-solid phase transitions in colloidal monolayers. 67:051107, 2003.

[81] D.F. Williams. *Ph.D. Thesis*. PhD thesis, University of Washington, 1991.

[82] Z. Hórvölgyi, M. Máté, and M. Zrínyi. On the universal growth of 2-dimensional aggregates of hydrophobed glass-beads formed at the (aqueous-solution of electrolyte)-air interfaces. *Colloids Surf. A*, 84:207, 1994.

[83] D. Stamou, C. Duschl, and D. Johannsmann. Long-range attraction between colloidal spheres at the air-water interface: The consequence of an irregular meniscus. *Phys. Rev. E*, 62:5263, 2000.

[84] P.A. Kralchevsky, N.D. Denkov, and K.D. Danov. Particles with an undulated contact line at a fluid interface: Interaction between capillary quadrupoles and rheology of particulate monolayers. *Langmuir*, 17:7694, 2001.

[85] M. G. Nikolaides, A. R. Bausch, M. F. Hsu, A. D. Dinsmore, M. P. Brenner, C. Gay, and D. A. Weitz. Electric-field-induced capillary attraction between like-charged particles at liquid interfaces. *Nature*, 420:299, 2002.

[86] M. Megens and J. Aizenberg. Like-charged particles at liquid interfaces. *Nature*, 424:1014, 2003.

[87] K.D. Danov, P.A. Kralchevsky, and M.P. Boneva. Electrodipping force acting on solid particles at a fluid interface. *Langmuir*, 20:6139, 2004.

[88] M. Oettel, A. Domínguez, A, and S. Dietrich. Effective capillary interaction of spherical particles at fluid interfaces. *Phys. Rev. E*, 71:051401, 2005.

[89] F. Ghezzi and J. C. Earnshaw. Formation of meso-structures in colloidal monolayers. *J. Phys.: Condens Matter*, 9:L517, 1997.

[90] J. Ruiz-García and B. I. Ivlev. Formation of colloidal clusters and chains at the air/water interface. *Mol. Phys.*, 95:371, 1998.

[91] P.A. Kralchevsky and K. Ñagayama. Capillary interactions between particles bound to interfaces, liquid films and biomembranes. *Adv. Colloid Interf. Sci.*, 85:145, 2000.

[92] M. Abramowitz and J.A. Stegun. *Handbook of Mathematical Functions.* Dover Press., New York, 1974.

[93] P.A. Kralchevsky, V.N. Paunov, I.B. Ivanov, and K. Ñagayama. Capillary meniscus interaction between colloidal particles attached to a liquid-fluid interface. *J. Colloid Interf. Sci.*, 151:79, 1992.

[94] V.N. Paunov, P.A. Kralchevsky, and N.D. Denkov. Lateral capillary forces between floating submillimeter particles. *J. Colloid Interf. Sci.*, 157:100, 1993.

[95] F. Martínez-López, M. A. Cabrerizo-Vílchez, and R. Hidalgo-Álvarez. Colloidal interaction at the air-liquid interface. *J. Colloid Interface Sci*, 232:303, 2000.

[96] F. Ghezzi and J. C. Earnshaw. . *J. Phys.: Condens. Matter*, 9:L517, 1997.

[97] P. A. Kralchevsky and N. D. Denkov. Capillary forces and structuring in layers of colloid particles. *Curr. Opinion Colloid Interface Sci*, 6:383, 2001.

[98] P.A. Kralchevsky, C.D. Dushkin, V.N. Punov, N.D. Denkov, and K. Ñagayama. *Prog. Colloid Polym. Sci.*, 98:12, 1995.

[99] M. Marder. Soap-bubble growth. *Phys. Rev. A*, 36:438, 1987.

[100] J. Stavans and J. A. Glazier. Soap froth revisited - dynamic scaling in the two-dimensional froth. *Phys. Rev. Lett.*, 62:1318, 1989.

[101] J. Stavans. Temporal evolution of 2-dimensional drained soap froths. *Phys. Rev. A*, 42:5049, 1990.

[102] J. J. Chae and M. Tabor. Dynamics of foams with and without wall rupture. *Phys. Rev. E*, 55:598, 1997.

[103] B. Dubertret, K. Y. Szeto, and W. Y. Tam. T1-correlations in two-dimensional cellular systems. *Europhys. Lett.*, 45:143, 1999.

[104] A. Abd el Kader and J. C. Earnshaw. Growth of disorder about point defects in a two-dimensional foam. *Phys. Rev. E*, 58:760, 1998.

[105] W. Y. Tam. Evolution of a single defect in an ideal two-dimensional hexagonal soap froth. *Phys. Rev. E*, 58:8032, 1998.

[106] P. S. Sahni, D. J. Srolovitz, G. S. Grest, M. P. Anderson, and S. A. Safran. Kinetics of ordering in 2 dimensions .2. quenched systems. *Phys. Rev. B*, 28:2705, 1983.

[107] J. C. M. Mombach, R. M. C. de Almeida, and J. R. Iglesias. 2-cell correlations in biological tissues. *Phys. Rev. E*, 48:2598, 1993.

[108] W. Korneta, S. K. Mendiratta, and J. Menteiro. Topological and geometrical properties of crack patterns produced by the thermal shock in ceramics. *Phys. Rev. E*, 57:3142, 1998.

[109] N. Rivier. Statistical crystallography: Structure of random cellular networks. *Phil. Mag. B*, 52:795, 1985.

[110] J. R. Iglesias and M. C. Dealmeida. Statistical thermodynamics of a 2-dimensional cellular-system. *Phys. Rev. A*, 43:2763, 1991.

[111] K. Y. Szeto and W. Y. Tam. *Phys. Rev. E*, 53:4213, 1996.

[112] T. Aste, D. Boosé, and N. Rivier. From one cell to the whole froth: A dynamical map. *Phys. Rev. E*, 53:6181, 1996.

[113] T. Aste, K. Y. Szeto, and W. Y. Tam. Statistical properties and shell analysis in random cellular structures. *Phys. Rev. E*, 54:5482, 1996.

[114] T. Aste. Random walks on disordered networks. *Phys. Rev. E*, 55:6233, 1997.

[115] K. Y. Szeto, T. Aste, and W. Y. Tam. Topological correlations in soap froths. *Phys. Rev. E*, 58:1998, 2656.

[116] K. Y. Szeto, X. Fu, and W. Y. Tam. Universal topological properties of two-dimensional trivalent cellular patterns. *Phys. Rev. Lett.*, 88:138302–1, 2002.

[117] N. Rivier and A. Lissowski. *J. Phys. A:Math. Gen.*, 15:L143, 1982.

[118] F. T. Lewis. *Anat. Records*, 38:341, 1928.

[119] S.F. Edwards and K.D. Pithia. The evolution of liquid foams. *Physica A*, 205:577, 1994.

[120] S. N. Chiu. A comment on riviers maximum-entropy method of statistical crystallography. *J. Phys. A*, 28:607, 1995.

[121] S. N. Chiu. Aboav-weaires and lewis laws - a review. *Materials Characterization*, 34:149, 1995.

[122] D. Weaire. The evolution of the structure of a two-dimensional soap froth. *Philos. Magazine*, 47:L29, 1983.

[123] D. A. Aboav. *Metallography*, 3:393, 1970.

[124] H J Hilhorst. Planar voronoi cells: the violation of aboav's law explained. *J. Phys. A: Math. Gen.*, 39:7227, 2006.

[125] G. Le Caër and R. Delannay. Correlations in topological models of 2d-random cellular structures. *J. phys. A: Math. Gen.*, 26:3931, 1993.

[126] D. A. Aboav. Arrangement of cells in a net. *Metallography*, 13:43, 1980.

[127] J.C. Fernández-Toledano, A. Moncho-Jordá, F. Martínez-López, A.E. González, and R. Hidalgo-Álvarez. Short- and long-range topological correlations in two-dimensional aggregation of dense colloidal suspensions. *Phys. Rev. E*, 71:041401, 2005.

[128] J. C. Fernández-Toledano, A. Moncho-Jordá, F. Martínez-López, and R. Hidalgo-Álvarez. Two-dimensional colloidal aggregation mediated by the range of repulsive interactions. *Phys. Rev. E*, In Press, 2007.

[129] A. E. González, F. Martínez-López, A. Moncho-Jordá, and R. Hidalgo-Álvarez. Concentration effects on two- and three-dimensional colloidal aggregation. *Physica A*, 314:235, 2002.

[130] W. Y. Shih, J. Liu, W. H. Shih, and I. A. Aksay. Aggregation of colloidal particles with a finite interparticle attraction energy. *J. Stat. Phys.*, 62:961, 1991.

[131] R. Delannay and G. Le Caër. Topological characteristics of 2d cellular structures generated by fragmentation. *Phys. Rev. Lett.*, 73:1553, 1994.

[132] K.Y. Szeto and W.Y. Tam. Edge scaling of soap froth. *Physica A*, 254:248, 1998.

[133] A.E. González, F. Martínez-López, A. Moncho-Jordá, and R. Hidalgo-Álvarez. Simulations of colloidal aggregation with short- and medium-range interactions. *Physica A*, 333:257, 2004.

[134] A. J. Hurd and D. W. Schaefer. Diffusion-limited aggregation in 2 dimensions. *Phys. Rev. Lett.*, 54:1043, 1985.

[135] W.H. Press, S.A. Teulkolsky, W.T. Vettering, and B.P. Flannery. *Numerical Recipes*. Cambridge University Press, Cambridge, England, 2nd ed edition, 1992.

[136] A. I. Campbell, V. J. Anderson, and J. S. van Duijneveldt. Dynamical arrest in attractive colloids: The effect of long-range repulsion. *Phys. Rev. Lett.*, 94:208301, 2005.

[137] F. Sciortino, P. Tartaglia, and E. Zaccarelli. One-dimensional cluster growth and branching gels in colloidal systems with short-range depletion attraction and screened electrostatic repulsion. *J. Phys. Chem. B.*, 109:21942, 2005.

[138] A. de Candia, E. Del Gado, A. Fierro, N. Sator, and A. Coniglio. Colloidal gelation, percolation and structural arrest. *Physica A*, 358:239, 2005.

[139] D. J. Robinson and J. C. Earnshaw. *Phys. Rev. E*, 46:2045, 1992.

[140] J. Stankiewicz, M. A. Cabrerizo-Vílchez, and R. Hidalgo-Á lvarez. 2-dimensional aggregation of polystyrene latex-particles. *Phys. Rev. E*, 47:2663, 1993.

[141] J. C. Fernández-Toledano, A. Moncho-Jordá, F. Martínez-López, and R. Hidalgo-Álvarez. Spontaneous formation of mesostructures in colloidal monolayers trapped at the air-water interface: A simple explanation. *Langmuir*, 20:6977, 2004.

[142] J. C. Fernández-Toledano, A. Moncho-Jordá, F. Martínez-López, and R. Hidalgo-Álvarez. Self-assembly in two-dimensions of colloidal particles at liquid mixtures. *Langmuir*, 22:6746, 2006.

[143] A. Kotera, K. Furusawa, and Y. Takeda. *Kolloid Z. Z. Polym.*, 239:677, 1970.

[144] M. C. Wilkinson, J. Hearn, and P. A. Steward. The cleaning of polymer colloids. *Adv. Colloid Interface Sci.*, 81:77, 1999.

[145] Y. Rotenberg, L. Boruvka, and A. W. Neumann. *J. Colloid Interface Sci.*, 93:169, 1983.

[146] C. Tikhomiroff, S. Allais, M. Klvana, S. Hisiger, and M. Jolicoeur. *Biotechnol. Prog.*, 18:1003, 2002.

[147] R. P. Sear, S. W. Chung, G. Markovich, W. M. Gelbart, and J. R. Heath. *Phys. Rev. E*, 59:R6255, 1999.

[148] W. Chen, S. Tan, T. K. Ng adn W. Ford, and P. Tong. Long–ranged attraction between charged polystyrene spheres at aqueous interfaces. *Phys. ReV. Lett.*, 95:218301, 2005.

[149] L. Belloni. *J. Phys.: Condens. Matter*, 12:R549., 2000.

Juan Carlos Fernández Toledano

CONTACT INFORMATION

C/ Fuentenueva s/n
Department of Applied Physics
Facultad de Ciencias.
Granada, 18071 (Spain)

Voice: (+34) 958 246 175
Fax: (+34) 958 958 243 214
E-mail: jucarlos@ugr.es
WWW: http://biocol.ugr.es

RESEARCH INTERESTS

Statistical Mechanics, behavior of colloidal monolayers, interaction potentials, phase transitions, simulations, numerical procedures

EDUCATION

Granada University, C/ Fuentenueva s/n, 18071, Granada, Spain

Ph.D. Physics, January 2008

Diploma de Estudios Avanzados: *"Mesoestructuras y Orden en Monocapas Coloidales"*. Applied Physics department, (2005).

Programa de Doctorado Interuniversitario: *"Ciencia y Tecnología de Coloides e Interfases"*. Applied Physics department, (2002–2003)

Licenciatura en Física, (1997–2002)

Utrecht University, Princetonplein 5, 3584 CC, Utrecht, The Netherlands

Workshop: *"Introduction to Soft Condensed Matter & Advanced Colloid Science"*. (28 Febrero – 11 Marzo, 2005).

Lyon University, CECAM, allé d'Italie, 69007, Lyon, France

Workshop: *"Fluid Phase Behavior and Critical Phenomena from Liquid State Theory and Simulations"*, (05–07, June, 2007)

HONORS AND AWARDS

Premio Hucoa–Erlös al mejor poster, VI GECI y I RICI. Salamanca (2005)

ACADEMIC EXPERIENCE

Granada University, C/ Fuentenueva s/n, 18071, Granada, Spain

Graduate Student **2006**
Asignatura de prácticas de Física de los Procesos Biológicos. 6 creditos

PUBLICATIONS

Chapter of books

"Proteínas Alimentarias y Coloides de Interés Industrial: Long–Range Interactions in 2D Colloidal Systems". J. C. Fernández-Toledano, F. Martínez-López, J. Ruiz-García and R. Hidalgo-Álvarez. I.S.B.N.: 84-472-0884-2. Universidad de Sevilla 2004

"Colloidal Particles at Liquid Interfaces: Theory for interactions in particle monolayers". J.

C. Fernández-Toledano, A. Moncho-Jordá, F. Martínez-López and R. Hidalgo-Álvarez. I.S.B.N.: 13-978-0521-84846-6, Cambridge University Press 2006

International papers

"Spontaneous Formation of Mesostructures in Colloidal Monolayer trapped at the Air/Water Interface: A Simple Explanation". J. C. Fernández-Toledano, A. Moncho-Jordá, F. Martínez-López and R. Hidalgo-Álvarez. *Langmuir* **20**, 6977(2004)

"Short and long range topological correlation in two dimensional aggregation of dense colloidal suspension". J. C. Fernández-Toledano, A. Moncho-Jordá, F. Martínez-López, A. E. González and R. Hidalgo-Álvarez . *Phys. Rev. E* **71**, 041401 (2005)

"Self-Assembly in Two-Dimensions of Colloidal Particles at Liquid Mixtures". J. C. Fernández-Toledano, A. Moncho-Jordá, F. Martínez-López and R. Hidalgo-Álvarez. *Langmuir* **22**, 6746 (2006)

"Two-dimensional Colloidal Aggregation Mediated by the Range of Repulsive Interactions" . J. C. Fernández-Toledano, A. Moncho-Jordá, F. Martínez-López, A. E. González and R. Hidalgo-Álvarez . *Phys. Rev. E* **75**, 041408 (2007)

Conference Presentations

II Conferencia Internacional de Proteínas y Coloides de Interés Industrial. Sevilla (Spain), 4–6 of June 2003. *"Interacciones Atractivas de Largo Alcance en Sistemas Colidales Bidimensionales"*. J. C. Fernández-Toledano, F. Martínez-López, J. Ruiz-García y R. Hidalgo-Álvarez. Poster.

5a Reunión del Grupo Especializado de Coloides e Interfases (GECI). Vigo (Spain), 3–5 of July 2003. *"Sistemas Coloidales Bidimensionales: Estudio de Mesoestructuras"*. J. C. Fernández-Toledano, F. Martínez-López, J. Ruiz-García y R. Hidalgo-Álvarez. Poster.

Cluster-Surface Interactions. Euroconference on Clusters Systems and Nanotubes. Toulon (Francia), 8–13 of May 2004. *"Mesostructure Formation by Silicon Oil"*. J. C. Fernández-Toledano, A. Moncho-Jordá, F. Martínez-López y R. Hidalgo-álvarez. Poster.

XVII Encuentro de Ciencia y Tecnología de Fluidos Complejos. S. Luis de Potosí (Mexico), 5–9 of July 2004. *"Colloidal Aggregation in 2-and 3-D: Experimental Aspects"*. J. C. Fernández-Toledano, A. Moncho-Jordá, F. Martínez-López y R. Hidalgo-Álvarez. Talk.

The 18th Conference of the European Colloid and Interface Society. Almería (Spain), 19–24 of September 2004. *"Topological Correlations in 2D Colloidal Aggregation: Concentration Dependence in DLCA"*. J. C. Fernández-Toledano, A. Moncho-Jordá, F. Martínez-López y R. Hidalgo-Álvarez. Poster.

The 6th Liquid Matter Conference. Utrecht (Netherlands), 1–6 of July del 2005. *"Origin of mesostructures: the effect of heterogeneus in surface tension"*. J. C. Fernández-Toledano, A. Moncho-Jordá, F. Martínez-López y R. Hidalgo-Álvarez. Poster.

6a Reunión del Grupo Especializado de Coloides e Interfases (GECI) y 1 Reunión Ibérica de Coloides e Interfaces (RICI). Salamanca (Spain), 13–15 of July 2005. *"Mesoestructuras coloidales en interfaces aire/agua: efecto de heterogeneidades en tensión superficial"*. J. C. Fernández-Toledano, A. Moncho-Jordá, F. Martínez-López y R. Hidalgo-Álvarez. Poster.

IV Internacional Conference Interfaces Against Pollution (IAP). Granada (Spain). 4–7 of June 2006. *"Colloidal Self-Assembly Induced by Interfacial non-Homogeneities at the Air/Water Interface"*. J. C. Fernández-Toledano, A. Moncho-Jordá, F. Martínez-López and R. Hidlgo-Álvarez. Talk.

The 20th Conference of the European Colloid and Interface Society. Budapest (Hungary), 17–22 of

September 2006. *"Kinetics Effects of Long-Range Interactions in Bidimensional Colloidal Systems"*. J. C. Fernández-Toledano, A. Moncho-Jordá, F. Martínez-López y R. Hidalgo-Álvarez. Poster.

International Workshop on Bubble and Drop Interfaces. Granada (Spain), 25–28 of March 2007. *"Colloidal Mesostructures Induced by Oil Drops at the Air Water Interface"*. J. C. Fernández-Toledano, A. Moncho-Jordá, F. Martínez-López y R. Hidalgo-Álvarez. Talk.

Professional Experience

2000-2001 *Beca de Iniciación a la Investigación: Estudios de Estabilidad en Sistemas Coloidales Bidimensionales*. Grupo de Física de Fluidos y Biocoloides. Granada University, Spain

2002-2003 *Contrato de Investigación Asociado a Proyecto: Estudio de Sistemas Coloidales Bidimensionales. Teoría y Experimentación*. Grupo de Física de Fluidos y Biocoloides. Granada University, Spain. Financiada por el Ministerio de Ciencia y Tecnología. Proyecto MAT1999-0662-C03-02.

2003-2005 *Beca de Formación de Personal Docente e Investigador* llevada a cabo en el grupo de Física de Fluidos y Biocoloides. Granada University, Spain

2005-2007 *Contrato de Formación de Personal Docente e Investigador* llevada a cabo en el grupo de Física de Fluidos y Biocoloides. Granada University, Spain

Computer Skills

- Languages: C++, fortran, some use of Unix shell scripts.
- Applications: Mathematica, Origin, LaTeX, common Windows database, spreadsheet, and presentation software
- Algorithms: Experience programming Monte Carlo, Brownian dynamics and Newtonian dynamics simulations of coagulation processes
- Operating Systems: Unix/Linux, Windows.

Experimental techniques

- Malvern 4700 (photo–correlation spectroscopy–PCS)
- Nephelometre (4, 8 y 18)
- Contatc angle devices: ADSA–P and ADSA–D
- Surface tension devices: pendant drop tensiometer and Langmuir balance
- Confocal microscopy
- Electrophoretic movility: Brookhaven Zeta-PALS and Zeta-sizer IV

languages

Spanish native English good level